Ghent University
Faculty of Engineering
Department of Civil Engineering
Department of Flow, Heat and Combustion Mechanics

Experimental and numerical modeling of heart valve dynamics

Experimentele en numerieke modellering van de hartklepdynamica

ir. Kris Dumont

Supervisors: Prof. Dr. Ir. Pascal Verdonck
Prof. Dr. Ir. Jan Vierendeels

Dissertation submitted to obtain the degree of
Doctor in de Toegepaste Wetenschappen
Academic Year 2004-2005

Experimental and numerical modeling of heart valve dynamics

Experimentele en numerieke modellering van de hartklepdynamica

The cover is designed by b-ART (Bart Dumont).

Supervisors:

Prof. Dr. Ir. Pascal Verdonck

Hydraulics Laboratory
Cardiovascular Research Group
IBiTech
Institute Biomedical Technology
Civil Engineering Department
Faculty of Applied Sciences
UGent, Ghent University
Sint-Pietersnieuwstraat 41
B-9000 Gent, Belgium

Prof. Dr. Ir. Jan Vierendeels

Department of Flow,
Heat and Combustion Mechanics
Faculty of Applied Sciences
Ghent University
Sint-Pietersnieuwstraat 41
B-9000 Gent, Belgium

Exam Commission

Prof. R. Verhoeven (president, Faculty of Engineering, UGent)
Prof. P. Segers (secretary, Faculty of Engineering, UGent)
Prof. W. Flameng (Faculty of Medicine and Health Sciences, KULeuven)
Prof. R. Perrault (Lab. of Aerodynamic Studies, Université de Poitiers)
Prof. A. Redaelli (Dept. of Bioengieering, Politecnico di Milano)
Prof. G. Van Nooten (Faculty of Medicine and Health Sciences, UGent)
Prof. F. van de Vosse (Dep. of Biomedical Engineering, TUEindhoven)
Prof. W. Van Paepegem (Faculty of Engineering, UGent)
Prof. P. Verdonck (Faculty of Engineering, UGent)
Prof. J. Vierendeels (Faculty of Engineering, UGent)

This research was funded by the Institute for the Promotion of Innovation by Science and Technology in Flanders (IWT-01775).

Soon I’ll have the courage
To leave my thoughts behind
I’ll give back all the knowledge
And keep the wisdom precious in my mind

Massive Attack (Three)

Acknowledgements

Since 2000, it has been my privilege to be part of the Hydraulics Lab community, physically rooted at the nice city of Ghent in Belgium. Although I've spent most of the past four years behind a computer doing stuff with heart valves, it is tough for most people to imagine how on earth it is possible to work for more than four years on these small heart valves. In following my own path toward completion of this PhD, I have learned not only about "How Heart Valves Work", but I have learned many lessons; lessons about friendship, about football and victory, about science and innovation of technology, about people and their own culture, and many more. All these lessons made me more mature and they brought me to were I am right now. The last lesson for the completion of this PhD is the writing of a book. The writing of a dissertation can be a lonely and isolating experience, yet it is obviously not possible without the personal and practical support of numerous people.

I thank my supervisors, Professor Pascal Verdonck and Professor Jan Vierendeels for many insightful conversations during the development of the ideas in this thesis. I would like to thank Pascal Verdonck for my journey into Heart Valve Dynamics, for his wisdom, friendship, understanding, and for teaching me how to be a 'successful' researcher. I am particularly grateful to Jan Vierendeels for his thoughtful and creative comments on the complex topic of 'Computational Fluid Dynamics'. I am appreciative and thankful for the support of my dissertation chair, Professor Ronny Verhoeven, and the members of my committee. Professor Patrick Segers raised broad conceptual questions and encouraged me to put more of my own commentary into the dissertation. I am grateful for having had two outstanding experts Professor Guido Van Nooten and Professor Frans van de Vosse as reviewers for my dissertation. I sincerely appreciate the efforts of all who contributed to this work in one way or another: Patke Kishor, Kevin Petersen, Marco Stijnen, Jessa Yperman, Bart Meuris, Willem Flameng.

I would also like to thank more than a dozen colleagues: Stefaan (De Mey), Peter, Stijn, Koen, Fadi, Sunny, Ilse, Tom, Guy, Seba, Lieve, Masanori, Dirk, Stefaan (Bliki), Martin, Marcel, Manuella, Jurgen, Ivo, who provided a source of knowledge, a nice drink or snack during coffee break, a 'listening ear', ... or whatever. I am fortunate to have colleagues who were willing to share their time and expertise to improve my scientific work and writing. Their friendship and professional collaboration meant a great deal to me. Stijn and Sunny dissected the stylistic and grammatical shortcomings of my earlier drafts. To the best of my capabilities, I followed their advice. Their wisdom and compliments are greatly appreciated.

Not least, perhaps, I should thank my girlfriend, Frauke, for her patience and forbearance whilst I have spent hundreds of hours working on it! Futhermore, thank you 'Ma' and 'Pa' for patiently tolerating the rollercoaster ride of moods that accompanied my struggles writing this book. You were there since I was born to share the excitement of my stories, and this sustained me through the highs and the lows. To my dear little sister Tinneke, I want to say 'thanx' for the cooking of the last months and just for spending time with me. I hope you can find your "knight in shiny armour" in the near future. Joren, Anke, Bart and Heidi thanks for the holidays, the drinks, the running-and-biking, the design of the frontpage by b-ART and many more. Special thanks to Paul and Nicole the dear parents of Frauke for providing not only the meat, but more important a lovely daughter. Good luck to their son, Niels alias 'the Hobbit' with his studies. Because of the large families we have it is impossible to mention everybody, but still: 'Thank You!' A special moment of silence to my grand parents who passed away, Vake and Meme. I would like you to know that I love you! To Moeke and Pepe I would like to say: 'Stay with us for many more years!'.

I would like to thank Niek and Marten who have encouraged me during several mountainbike trips. Also, my long standing friends - Simon and Ka(trien& Ber)nard. The conversations in the pubs, the beer and wine, the nice dinners, the parties, the fishing afternoons, the sporting, the biking, ... were very helpful to forget the struggle of the PhD; thanx to the friends of

my parents, the football team ‘Campus’, Koenie, alias ‘the dancer’, Daan and Veerle, Kim and Andy, Marlies and Wim, Nele and Pedro, the “Gidsen”-girls, Glen, Jimmy and Ingrid, Fatima and Jo, Alain and Anne-Greet, Frederik and Caroline and many more. Special thanks to Evy and Wim for their warm welcome upon my arrival in Manhattan, New York. Muchas gracias Isabeeltje y Tine, por todo el tiempo y la fiesta en los lecciones españoles.

Though some of these people may not directly be involved in my thesis writing, the words of all the above and of everybody I forgot to mention were really important for keeping me to work hard and never give up my thesis. The power of language is really amazing, and it can make people from weak to strong. Thanks for all the support!!!

Kris Dumont

Gent, December 2004

Contents

List of Figures

List of Tables

Notations, Symbols and Abbreviations

Haemodynamic Heart Valve Parameters

V_C	[ml]	volume in the compliance chamber of the bioreactor
PLA	[mmHg]	left atrial pressure
PLV	[mmHg]	left ventricular pressure
PLV_{sys}	[mmHg]	maximum left ventricular pressure
PLAO	[mmHg]	aortic pressure
CO	[l/min]	cardiac output
$Q_{fwd,mean}$	[ml/s]	mean forward flow
SV_{fwd}	[ml]	forward stroke volume
T_{fwd}	[s]	duration of the forward flow
VTI	[cm]	velocity time integral
V_{reg}	[ml]	regurgitation volume
V_{leak}	[ml]	leakage volume
V_{close}	[ml]	closing volume
% reg	[%]	percentage regurgitation
$\Delta P, \Delta p$	[mmHg] and [Pa]	pressure difference over the valve the term '(transvalvular) pressure gradient' is often used in clinical studies.
$\Delta P_{fwd,mean}$	[mmHg]	mean pressure gradient during forward flow
$\Delta P_{Doppler}$	[mmHg]	mean Doppler gradient
V_{mean}	[m/s]	mean Doppler velocity
V_{max}	[m/s]	maximum Doppler velocity
V_{CO}	[m/s]	velocity in Central Opening of bileaflet valve, velocity in y-direction
V_{SO}	[m/s]	velocity in Side Opening of bileaflet valve velocity in y-direction
GOA	[cm^2]	geometric orifice area
EOA	[cm^2]	effective orifice area
EOA_{Gorlin}	[cm^2]	EOA calculated with the Gorlin equation
$EOA_{continuity}$	[cm^2]	EOA calculated with continuity equation
PI	[-]	performance index
θ	[-]	orifice constant
SS	[Pa]	shear stress

Dimensionless numbers

Re	Reynolds number
Sr	Strouhal number

CFD Algorithm Parameters

θ	[rad] or [degrees]	angle of the (stiff) valve leaflet, or of a segment of the flexible leaflet
I	[kg·m^2]	moment of inertia
M	[N·m]	moment of forces on the valve leaflet
ρ	[$\frac{kg}{m^3}$]	density of fluid or leaflet material
μ	[Pa·s], [$\frac{kg}{m \cdot s}$]	dynamic viscosity of the fluid
T_p	[s]	time period of one flow cycle
u, U	[m/s]	velocity in x-direction
v, V	[m/s]	velocity in y-direction
h	[m]	height (or characteristic distance)
r	[m]	radius
l	[m]	length of the valve leaflet
Δl	[m]	length of a segment of the leaflet
t	[m]	thickness of the valve leaflet
EI	[Pa]	stiffness of the valve material
k_s	[N·m/rad]	stiffness of the torsional spring
$k_{s,hinge}$	[N·m/rad]	stiffness of the hinge

Quantaties

$\overrightarrow{\boldsymbol{a}}$	physical vector
$\underline{a}$	column vector
A	matrix
$\underline{\overline{\boldsymbol{A}}}$	tensor

Operations

$\frac{\partial a}{\partial t}$	time derivative
$\dot{a}$	time derivative (velocity)
$\ddot{a}$	double time derivative (acceleration)
$\overrightarrow{\boldsymbol{a}} \cdot \overrightarrow{\boldsymbol{b}}$	inner vector product
$A \cdot B$	inner matrix product
A^T, $\underline{a}^T$	transposition
A^{-1}, $\underline{a}^{-1}$	inversion
$\int_S ...da$	surface integral
$\int_V ...da$	volume integral

Preface

The first clinical use of a cardiac valvular prosthesis took place more than 50 years ago, when Dr. Charles Hufnagel implanted the first artificial caged ball valve in the descending aorta of a patient to treat aortic insufficiency. Since then, it has become clear that quality of life can be improved if a diseased heart valve is replaced by a prosthetic device. Studies on the medical complications in currently used substitutes involve many expensive and time-consuming experiments. Too often, the development of improved prostheses or new concepts is based on empirical knowledge and understanding.

Existing artificial (biological or mechanical) heart valves are studied in animal and clinical studies and in experimental *in vitro* studies. Experimental models use mock loops or pulse duplicator systems to mimick the physiological environment of the left or right heart in a controllable manner. Heart valves can be tested under standardized hydrodynamic conditions and thus they can be compared more accurately and subject independent. Important design criteria of heart valves are related to the behavior of the valve in the flow field. In particular, pressure gradients should be as low as possible. Stagnation, recirculation zones and shear stresses are to be minimized in order to prevent platelet activation and initiation of coagulation.

In vitro testing implies that prototypes of the valves are already available at the time of testing. In the course of the design process, valves are computer designed and virtual valve prototypes are available in an early stage of the design process. The challenge remains, however, to test the haemodynamic performance of these virtual prototypes. To do so, advanced computational algorithms, which take into account the continuous and full interaction between the flow and the valve leaflets (Fluid-Structure Interaction), are required. They may specifically be helpful in obtaining insight in system responses, which are difficult to capture experimentally.

In this dissertation it will be demonstrated that computational fluid dynamics or CFD simulations can be used to study the complex valve hydrodynamics in detail. The developed algorithms will be applied on two cases. First, it will be shown that the CFD code allows to simulate the behavior of existing numerical valves, such as bileaflet valves, in a 3D flow field. As such, CFD can be a tool for valve design prior

to manufacturing prototypes for detailed testing. In future, numerical models will be a major research tool to unravel the haemodynamics associated with thrombolytic and hemolytic events of new and existing mechanical heart valves. Computer methods may help estimating blood damage in different heart valve designs. As such, they can help in the development of a heart valve that doesn't require any anticoagulation therapy. It's a long way before computers, if ever, will replace animal testing. Nevertheless, together with better experimental testing, numerical modeling integrated into the clinical research may help in significantly reducing animal experiments.

Secondly, there are new developments in tissue engineering (TE), where big effort is done to produce viable and durable tissue engineered valves. A critical point in the production process is the maturation and conditioning of TE valves in a bioreactor. It is important to know and to control the forces exerted on the leaflet and cells throughout the growing process. Here also, CFD can play a major role. From CFD perspective, the challenging task is to model the dynamic interaction of the flexible valve leaflet with the surrounding blood and to calculate the local deformations and stresses in the structure. However, the large differences in material properties of the fluid and structure and the finite motion of the leaflets complicate blood-valve interaction modeling. Until now, this has impeded numerical analysis of valves operating under physiological conditions. With the presented computer methods, the shear stress on the cells of a tissue engineered heart valve construct can be calculated. This could play a key role in the successful development of a tissue engineered heart valve.

The dissertation is structured as follows. Part **A** contains all the introductory chapters. In the first chapter heart valve anatomy, physiology and histology are explained. In the second chapter heart valve diseases, diagnosis, treatment and tissue engineering are described. The third chapter gives an engineering perspective on the testing and performance of heart valve constructs.

Subsequently, part **B** concentrates on experimental *in vitro* testing and modeling of heart valves. Two more chapters focus on a mitral bileaflet heart valve (On-X) and on an aortic monoleaflet heart valve (Omnicarbon), respectively. The third chapter

of part **B** investigates a newly developed bioreactor environment for the creation of a viable tissue engineered heart valve.

The main goal of these chapters is to familiarize the reader with fluid dynamic valve testing and to provide some background on (i) performance estimation as used in this field of research, and (ii) the requirements of bioreactor systems as used in tissue engineering.

The major achievements of this work are within the domain of numerical modeling, both of mechanical and biological heart valves. These novel contributions are assembled in part **C**, which is the core of this PhD. A first study presents the algorithm, followed by a 2D validation study. The model is then applied on a 3D realistic mechanical heart valve (ATS) in the next two chapters. The final chapter gives a detailed explanation of a 2D flexible heart valve numerical model.

The developed methods are discussed with attention for improvement of some critical points. It is our believe that the experimental and numerical models presented in this dissertation will be useful as an analysis tool to improve existing valve prostheses and to develop new prosthetic valve concepts leading to more advanced heart patient care and cure.

Part A.

Introduction

Chapter I

Anatomy and physiology of heart valves

Scientific knowledge of the heart dates back almost as far as the beginnings of recorded history. Among the first people to investigate and write about the anatomy of the heart was the Greek physician, Erasistratus, around 250 BC. Erasistratus described the appearance of the heart and the four valves inside it. Although he correctly deduced that the valves prevent blood from flowing backward in the heart, he did not take into account that the heart was a pump. Claudius Galenus (129-201 AD), a Greek-born Roman physician, recognized that the heart was made of muscle, but he believed that the liver was responsible for the movement of blood through the body. Leonardo da Vinci (1452-1519 AD) made a number of advances in the understanding of blood flow. He deduced that eddy currents help heart valves to close, but he was not aware of a closed blood circulatory system. An important milestone was William Harveys discovery (17th century) of the pumping function of the heart and the circulation.
Nevertheless, now nearly 400 years later, an accurate quantitative description of cardiac function is still a challenge. In this chapter, the anatomy and physiology of the normal heart, heart valves and the blood are introduced.

I.1. The human heart and circulation

The human heart acts like a pump which provides the circulation of blood in the human body. To achieve an efficient circulatory system that allows sufficient gas exchange through the lungs and supplies the organs with heat and oxygen, the human circulatory system consists of two circuits connected in series (figure I.1(a)). The largest loop is the systemic circulation that is maintained by the left side of the heart and provides oxygen rich blood to the muscles, tissue and the organs. After the

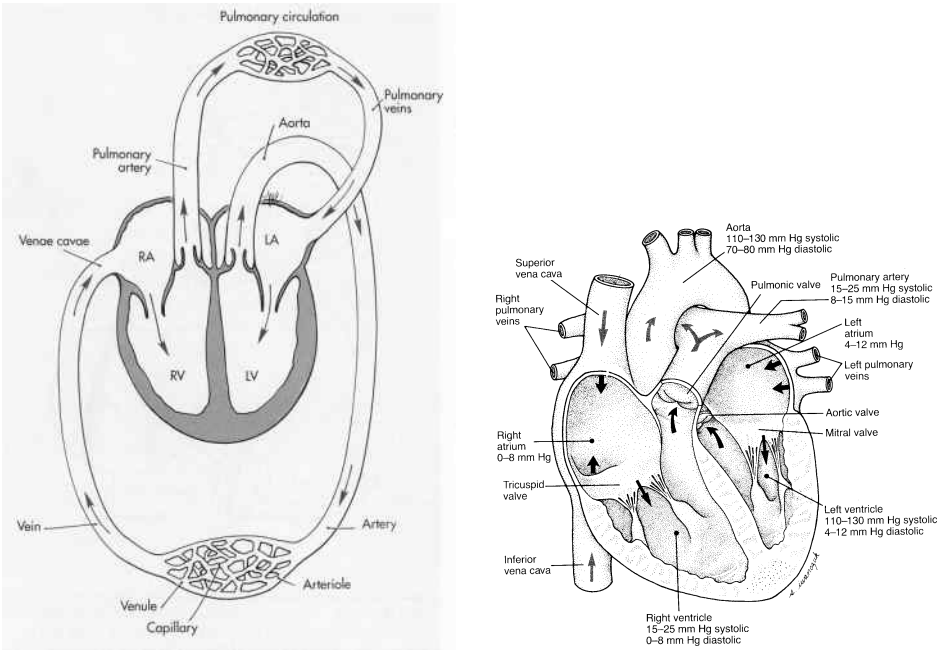

(a) The sequence of blood flow in the circulation.[1]

(b) Anatomy of the heart and governing pressures.[2]

Figure I.1.: The heart and circulation.

blood has passed the organs, it flows into the right side of the heart. The right heart subsequently pumps the blood through the pulmonary circulation. The main function of this circulation is to pass blood through the lungs where it is oxygenated.[3]
Looking at the heart in somewhat more detail, it is divided into four cavities or 'chambers' - two atria (left and right) and two ventricles (left and right) - each closed off by a one-way valve (figure I.1(a)). The left and right side of the heart are separated by the septum. The upper and lower caval veins (venae cavae) collect the blood into the right atrium (RA) from where it passes through the *tricuspid valve* into the right ventricle (RV). Contraction of the right ventricle squeezes the blood through the *pulmonary (pulmonic) valve* towards the lungs where the oxygenation takes place. Via the pulmonary veins, the blood reaches the left atrium (LA), passes through the *mitral valve* and fills the left ventricle (LV). With the following contraction, the blood is squeezed through *the aortic valve* into the aorta and the rest of the systemic circulation (figure I.1).[5]
In the course of a day, the heart contracts and expands on average 100,000 times, pumping approximately 8,000 liters of blood.[6] By opening and closing in a synchro-

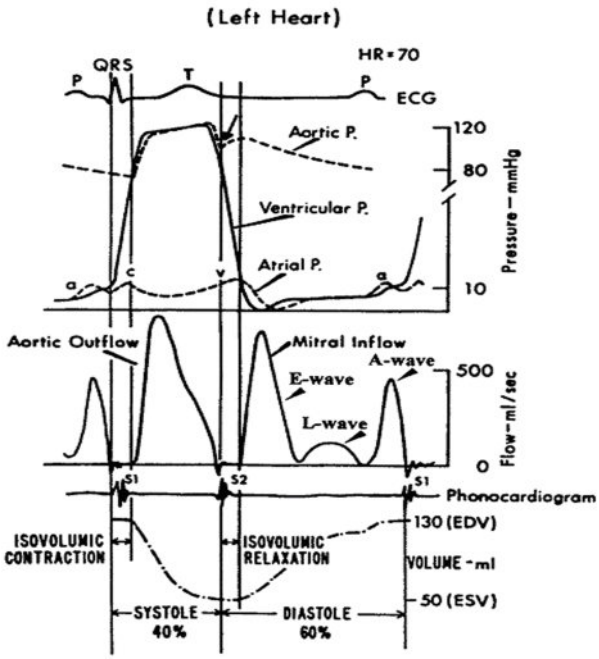

Figure I.2.: Left ventricular heart cycle with from top to bottom: ECG, pressure, flow velocity, volume.[4]

nized manner, the four valves ensure the one-way flow of the blood in the human circulation.

I.2. The cardiac cycle

While pumping blood through the circulatory system, the heart goes through alternating phases of filling and ejection. Both atria and ventricles work synchronously, but the atria and ventricles go through different phases. Hereafter the phases for the left heart will be discussed. In the right heart, the exact same phases occur but at lower pressures (figure I.1(b)).

The cardiac cycle can be divided into a systolic (ventricular contraction) and diastolic (ventricular relaxation) time interval (figure I.2).

During the isovolumic systolic contraction of the left ventricle (LV), pressure rises from 10 to around 80 mmHg. During this phase both the aortic and mitral valve are closed. When the ventricular pressure rises above aortic pressure, the valve opens and blood is ejected from the LV into the aorta. The aortic velocity profile shows a maximum velocity of about 1 to 1.4 m/s. The ventricular and aortic pressures

further rise to 120 mmHg.
The diastolic portion of the heart cycle can be subdivided into four phases: (1) isovolumetric relaxation, (2) rapid or early filling (E-wave), (3) diastasis (L-wave) and (4) atrial contraction (A-wave). In the first phase, between the time of aortic valve closure and mitral valve opening, LV pressure drops exponentially from the aortic pressure level to a pressure of a few mmHg existing in the left atrium (LA). The next phase, i.e. early filling (E-wave), begins when pressure in the left ventricle (LV) falls below that in the LA, opening the mitral valve and the LV to start filling. The third phase is diastasis (L-wave), with little extra filling of the atrium. The fourth phase or atrial contraction of the left atrium (A-wave), contributes for an extra 15 to 25 % of the LV filling.[5] The mitral velocity profile has a first peak of 0.7 m/s (E-wave) in early diastole and a second increase of velocity 0.5 m/s following the atrial contraction (A-wave).

I.3. How valves function

The upper chambers of the heart, the atria, are anatomically separated from the lower chambers or ventricles by a fibrous ring. The four cardiac valves are embedded within this ring. All valves have thin flaps, called leaflets or cusps, that open to let the blood through and close to prevent it from flowing backward (figure I.1).

I.3.1. Atrioventricular valves

The atrioventricular valves, i.e. the mitral and tricuspid valve, are situated between the atrial and ventricular chambers. The mitral (figure I.3(a)) and tricuspid valve leaflets are connected by chords (chordae tendineae) to muscle bundles or papillary muscles in the chamber walls. Contraction of these muscle bundles during the ejection phase pulls the chords to open the valve and also prevents the valve leaflets from flipping upward into the atria.

I.3.2. Semilunar valves

The semilunar valves, i.e. aortic and pulmonary valves, are flaps of connective tissue reinforced by fibers. They are shaped like half a moon, hence the name semilunar. The aortic (figure I.3(b)) and pulmonary valves have no chords but consist of flaps

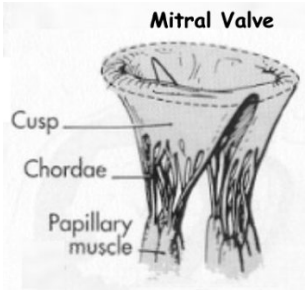

(a) Mitral valve.

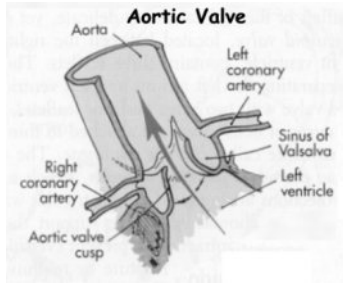

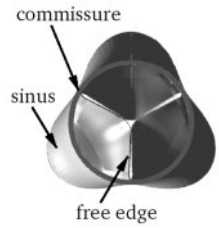

(b) Aortic valve.

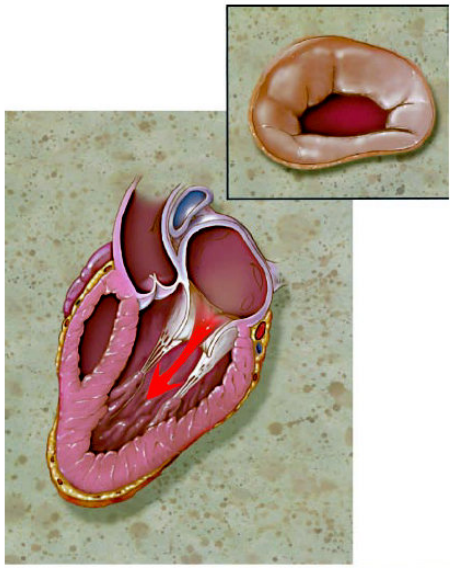

(c) In normal individuals, the mitral valve opens to allow blood to flow into the left ventricle.

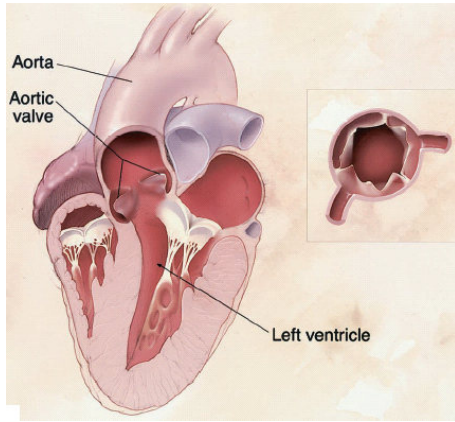

(d) In the normal individual, the left ventricle contracts and fully opens the aortic valve.

Figure I.3.: Left ventricular heart valves.[1,7]

of tissue or cusps at the exit from the chamber, which are pushed open by the flow of blood and fall back together to close off the ventricle once the blood has been ejected. Because of their structural design, they are less likely to experience any form of prolapse. Each cusp has a margin that is attached to the wall of the aorta or pulmonary artery and another free margin. The cusps are positioned so that a portion of their free margin overlaps the adjacent cusp, i.e. the lunulea (coaptation).[7] This mechanism is of great importance in maintaining valve competence and preventing backwards leak of blood into the ventricle. The point where two adjacent cusps meet at the wall of the artery is called a commissure. Since there are three cusps, a semilunar valve normally has three commissures. The aortic cusps

are named according to the coronary artery which arises above it. There is a right coronary cusp, a left coronary cusp, and a non-coronary cusp which is unrelated to a coronary artery. The aortic heart valve furthermore consists of three sinus cavaties, i.e. the sinuses of Valsalva (figure I.3(b)). These sinuses are a widening of the aortic wall. The pulmonary valve also has three cusps, named according to their position - anterior, left and right posterior cusps. The aortic valve has been thought of as a passive structure where all of its mobile components move only as a results of blood pressure and flow. It has been shown, that the commissures move outward in a passive response to pressure resulting in an increase of the aortic valve radius. This outward movement of the commissures initiates valve opening.[8,9]

I.4. Histology of heart valves

It is widely believed that all heart valves are simple structures contributing to the unidirectional flow of blood and responding to pressure gradients across the valve.[10] It is now becoming apparent, however, that heart valves have a complex structure optimized for an active performance in the microenvironment in which they are placed.[11]

It is thus important to consider the histology of natural heart valves. The principal cell types in the native heart valve are the valvular interstitial cells (VICs) and valvular endothelial cells (VEC).[10,12,13] They are embedded into the heart valve extracellular matrix.

I.4.1. Valvular interstitial cells

VICs mediate ongoing extracellular matrix (ECM)[14] repair and remodeling. This regenerative process appears to be vital to normal valve function.[15,16] Moreover, the integrity of collagen and other ECM components (i.e., elastin and proteoglycans) is the principal determinant of the durability of heart valves. Structural deterioration of native and biological substitute valves is ultimately mediated by chemical (enzymatic) and mechanical damage to collagen. The quality of valvular ECM depends on the condition of VICs and their ability to adapt to environmental need. The VICs of nearly all current bioprosthetic valve substitutes become nonviable during pro-

cessing. Thus, in a tissue valve without any viable cells, ECM damage that occurs during substitute valve function after implantation cannot be repaired.[17]

I.4.2. Valvular endothelial cells

VECs form a monolayer on the leaflet surface that constitutes the primary interface between the bloodstream and inner valve tissue. Whilst there is significant data on the various functions of vascular endothelium,[18] the specific role of valve endocardium remains unclear and has not been widely studied. However, it seems reasonable that the VECs minimally act to maintain a nonthrombogenic valve surface, similar to the vascular endothelium.[19]

I.4.3. Heart valve extracellular matrix

The principal components of the valve extracellular matrix (ECM) are the fibrous macromolecules (i) collagen and (ii) elastin, (iii) proteoglycans and (iv) glycoproteins, each component conferring unique physical and mechanical properties.[20]
Each of the three major structural valve components (collagen, elastin and proteo-

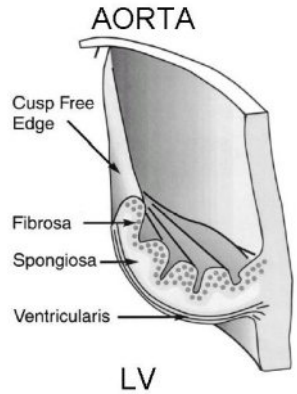

Figure I.4.: Aortic valve histology.[21]

glycans) constitutes a significant proportion of each of the three morphologically distinct and functionally significant layers of the valve leaflet matrix.[22] These layers are termed the fibrosa, spongiosa, and ventricularis.[23] Finally the valve leaflet is covered by an endothelial cell layer.

- *Fibrosa.* The fibrosa layer forms the load-bearing fibrous backbone of the valve leaflet, consisting of sheets of collagen bundles.[20] They are mainly arranged parallel to the cuspal free edge[24] as shown in figure figure I.4.[21] The collagen fibers are highly folded in radial direction and when stretched they are simply unfurling their coils. Furthermore, the collagen on its own is not highly deformable (extensible).[21]

- *Spongiosa.* The central located spongiosa is composed of loosely arranged collagen and glycosaminoglycans (GAGs). The spongiosa appears to lubricate relative movement between the fibrosa and the ventricularis and dissipate energy by acting as a shock absorber during closure.[20]

- *Ventricularis.* The ventricularis layer is much thinner than the other two layers, and is abundant in radially aligned elastic[20] fibres as shown in figure I.4.[21] Elastic fibres, i.e. elastin, allow tissues to withstand repeated deformation.[25] Elastin is believed to be responsible for maintaining the aortic valve collagen fibre architecture (mainly in the fibrosa) in its neutral corrugated state.[26]

Structural components of the ECM, such as collagen and Glycosaminoglycans (GAGs), have major roles in valvular degeneration and calcification of bioprosthetic heart valves. In particular the GAGs located in the spongiosa layer of the heart valves are extremely important for mechanical properties.[20] Their rigidity provides structural integrity to cells and provides channels between cells that permit cell migration. The elastin fibers permit distension of the aortic wall and leaflets while the collagen bundles provide tensile strength, limit distension and prevent disruption. This organization controls the distribution and magnitude of tensile stress.[27]

I.5. Mechanical properties of the aortic valve leaflets

Recent morphologic observations of elastin structures in aortic valves suggest that elastin is mechanically coupled to collagen. Since the mechanical stiffness of elastin is considerably lower than that of collagen, and aortic valves contain relatively little elastin, the mechanical importance of elastin in heart valve function is not clear.[21] Examining the tension/strain curves,[21] it can be seen that in the radial direction (figure III.9), the ventricularis appears to dominate the elastic response of the elastin fibers in the low-strain region. At these low strains, the fibrosa does not contribute

any tension since its collagen fibers are highly folded in radial direction and is simply unfurling its coils. In the circumferential direction (figure III.9), a similar pro-

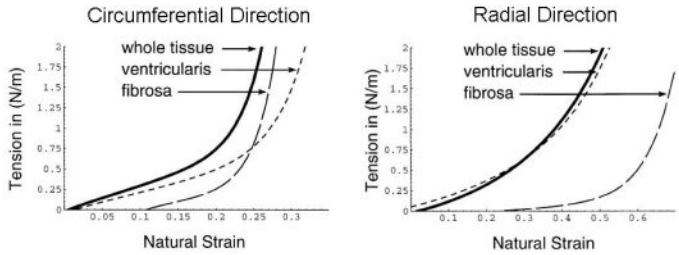

Figure I.5.: Mechanical properties of the aortic valve layers.[21]

cess occurs, but to a lesser extent. Below strains of 0.15, the fibrosa has little effect; between 0.15 and 0.25, the fibrosa and the ventricularis contribute almost equally, and above strains of 0.25 and loads of 2.0 N/m, the fibrosa begins to dominate, because the collagen fibers are fully unfolded.

Elastin tends to dominate the distensibility curves of the radial ventricularis, but participates very little in the fibrosa. The low but significant tension produced by the elastin structures of the aortic valve, together with previously observed elastin morphology as well as the measurable preload of elastin, suggest that the purpose of elastin in the aortic valve leaflet is to maintain a specific collagen fiber configuration and to return the fibers to this state, once external forces have been released.[21,26] Furthermore Lee and Vesely et al.[27] showed that damage to elastin *in vivo* will enable the collagen network to elongate, reducing valve cusp extensibility and increasing stiffness. Damage to elastin may therefore contribute to the degeneration and failure of prosthetic valves.[27,28]

The modulus of Young E for normal aortic valve leaflets found in literature is between $1 \cdot 10^6$ N/m^2 and $2 \cdot 10^6$ N/m^2.[29,30,31,32] The thickness of the leaflet varies between 0.2 and 1.4 mm,[29,33] but most researchers use about 0.6 mm as a standard leaflet thickness for aortic valve.[31,32,34]

I.6. Rheology of blood

So far, the properties of the fluidum at hand have not been addressed. For experimental and numerical studies it is important to consider the properties of the fluid as they influence the behavior of the heart and valves.

Blood is a concentrated suspension of blood cells in plasma. The properties of blood are governed by the concentration of red blood cells (hematocrit or Ht). The viscosity of blood increases with the concentration of red blood cells.[35] The discussion on the properties of blood in this section is limited to physiological values of Ht (30-50%). Furthermore Fahraeus and Lindqvist[36] observed a decrease in the blood viscosity in tubes with small diameters ($<500\mu$m). Since heart valves have bigger diameters, the so-called Fahraeus-Lindqvist effect is not further discussed.
Figure I.6 demonstrates the shear-thinning behavior of blood. At low shear rates ($\dot{\gamma} < 10s^{-1}$), the red blood cells tend to aggregate. This aggregation of red blood cells increases the viscosity. If shear rate is increased, the aggregates break up and the

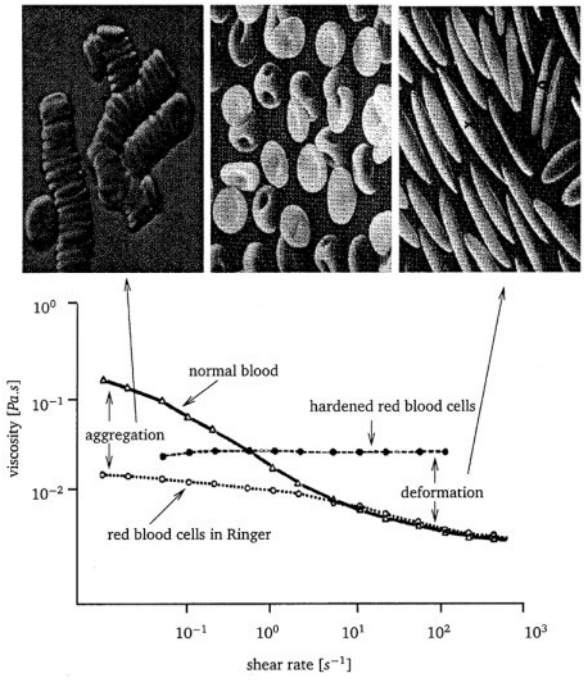

Figure I.6.: Viscosity in steady shear of normal blood, blood with hardened red blood cells (no deformation) and blood in Ringer solution (no aggregation).[37,38,39]

red blood cells align with the flow. The higher shear rates are deforming the red blood cells and eventually decreasing the viscosity.[37]
In the literature on blood flow in large arteries and heart valves, blood is generally modeled as a Newtonian fluid (fluid with a constant viscosity value) with the high shear rate limit viscosity of blood ($\mu=\mu_\infty$).[29,40,41,42,43] When studying low levels of shear such as pertain to recirculation regions and vortices populating a heart valve

wake, the blood non-Newtonian characteristics overwhelm its Newtonian high shear characteristics. In these cases it is valuable modeling the blood as a non-Newtonian fluid.[44,45] The Cross and Carreau model is commonly used for the modeling of the shear rate dependent viscosity of blood.[45,46,47,48,49,50,51]

$$\mu = \mu_\infty + (\mu_o - \mu_\infty) \cdot [1 + K \cdot \dot{\gamma}^a]^{\frac{n-1}{a}} \tag{I.1}$$

where μ_o=0.1072 10^{-3} mPa·s, μ_∞=3.5 mPa·s, n=0.3568, K=2.6502, a=2 and $\dot{\gamma}$ the shear rate in 1/s.[52] The Casson and the power-law model are other models which can be used for the modeling of the non-Newtonian behavior of blood in the low shear rate region.[53]

Chapter II

Heart valve disease and treatment

Surgical replacement of diseased human heart valves by mechanical and tissue valve substitutes is now commonplace, with approximately 93,000 valve replacements done each year in the US[54] and 275,000 worldwide.[17] Although survival and quality of life are enhanced for many patients, prosthesis-associated complications[55] and failure are still frequent and have a great impact on patient outcome.[17] In an attempt to further reduce the incidence of complications, new valve designs continue to be developed. Yet to understand the future of valve replacement therapy it is important to understand the nature of natural heart valve diseases and the history of artificial heart valve development.[55]

II.1. Causes of heart valve disease

Some diseases of the valves take 20 to 30 years to develop, and by the time a patient becomes aware of the symptoms, the condition has often progressed to an advanced and sometimes irreversible stage. Many damaged valves, however, may not cause any trouble at all, and people with one or more abnormal valves can go through a normal life[6] without ever being diagnosed for valve dysfunction. The causes of heart valve damage vary depending on the type of disease present, and may include the following:

- *Rheumatic Fever.* In the past, heart valve disease was usually caused by rheumatic fever, an inflammatory condition that often starts with a strep throat (a streptococcal bacterial infection). Damage is caused not by the bacteria themselves, but by an autoimmune response - a process in which the body, mistakenly begins to damage its own tissues.[6]

- *Infective Endocarditis.* Infective endocarditis is an infection of the endocardium, the lining that covers the inner wall of the heart chambers and heart

valves caused by *bacteria*, *viruses*, *fungi*, or other infectious agents. The infection can cause vegetations on the heart valves.[6]

- *Myxomatous Degeneration.* In the elderly, one of the most common causes of heart valve disease is a process called myxomatous degeneration, which usually affects the mitral valve. This dysfunction stems from a series of metabolic changes. The valve's tissue loses its elasticity, becomes weak, and becomes covered by deposits. The chords that control the opening and closing of the valve may break off[6] (not only in myxomatous disease).

- *Calcific Degeneration.* Another common cause of heart valve disease in the elderly is calcific degeneration, a process in which calcium deposits build up on the valve. This type of tissue degeneration usually causes aortic stenosis, a narrowing of the aortic valve.[6]

- *Congenital Anomalies.* Heart valve disease may also result from congenital abnormalities, problems that are present from birth. The most common congenital defect is a misshapen aortic valve, which has two leaflets instead of three and is therefore referred to as bicuspid.[6]

- *Other Causes.* Finally, heart valve disease may be a result of other heart disease, particularly coronary artery disease or a heart attack. These conditions can cause injury to one of the papillary muscles that support the valves, or annulus dilatation so that it doesn't close properly.

II.2. Diagnosis

Cardiac auscultation remains the most widely used method of screening of heart disease. While almost no sound is heard when blood flows through a normal valve, its passage through a diseased valve creates a whooshing noise, referred to as a murmur.[56,57] The production of murmurs is due to 3 main factors: (1) high blood flow rate through normal or abnormal orifices; (2) forward flow through a narrowed or irregular orifice into a dilated vessel or chamber; or (3) backward or regurgitant flow through an incompetent valve.
To further define the type of valve disease and extent of the valve damage, physicians may use any of the following diagnostic procedures:

- *Electrocardiogram (ECG).* The absence of ventricular hypertrophy, atrial abnormality, arrhythmias, atrio-ventricular conduction abnormalities, prior myocardial infarction, and evidence of active ischemia on the ECG provides useful negative information at a relatively low cost.

- *Chest X-ray.* Chest X-ray often yields qualitative information on cardiac chamber size, pulmonary blood flow, pulmonary venous pressures, pulmonary vascular redistribution, and cardiac calcification in patients with cardiac murmurs.[57]

- *Transthoracic Echocardiography.* A major diagnostic tool in assessing valve disorders is echocardiography, a non-invasive and painless procedure. Standard echocardiography may indicate abnormal valve motion and morphology. With Doppler echocardiography, the detected velocity reflects the severity of stenotis and regurgitation of the valves.[56,57]
  Figure II.1 shows normal Doppler echocardiographic flow profiles for the aortic (figure II.1(a)) and the mitral (figure II.1(b)) valve.

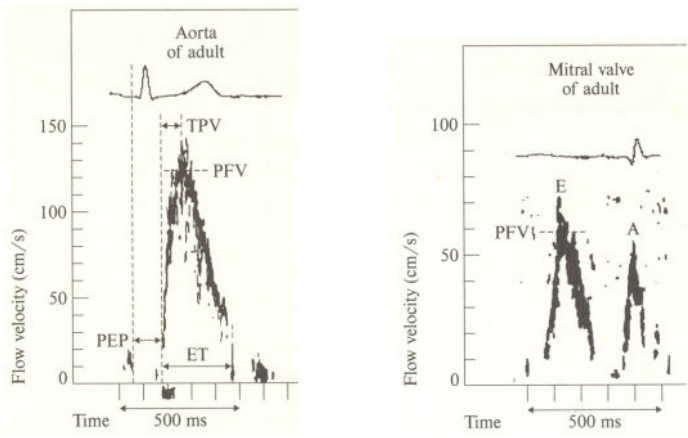

(a) Normal aortic Doppler profile.

(b) Normal mitral Doppler profile.

Figure II.1.: Aortic and mitral Doppler profiles.[58,59]

- *Cardiac Catheterization.* A thin (hollow) catheter is inserted into one of the patient's arteries (**arterial** catheterization) and guided to the heart. When the catheter is in place, a chemical dye is injected through the tube. The dye shows up on the X-ray, allowing physicians to visualize the inside of the

left heart, to see whether all the blood is flowing in the proper direction or if there is any backflow, and to assess the performance of natural or prosthetic valves.[6]

In the **venous** system, a catheter is seen coming from a vein in the neck and enters the right-sided heart chambers. In the **arterial** system, a catheter is seen coming from an artery in the leg and enters the left-sided heart chambers.[60]

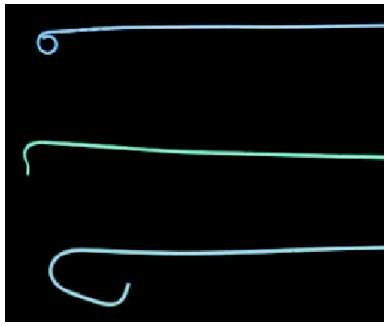

(a) Typical catheters used for pressure measurements and angiography.

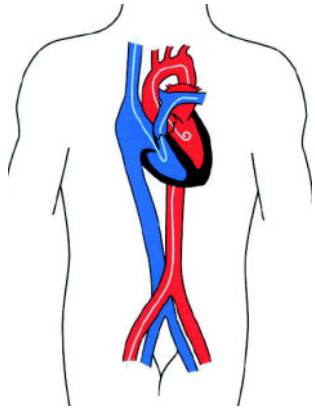

(b) Cardiac catheterization in clinical practice.

Figure II.2.: Invasive Catheterization.[60]

II.3. Types of heart valve disease

The mitral (figure I.3(a)) and aortic (figure I.3(b)) valves are the most common sites of heart valve disease, because of their location on the left side of the heart. The left chambers have a greater workload, because they pump blood to the entire body, whereas the right chambers push blood only to the lungs, which is an organ with low resistance and flow. Any abnormality in the mitral and aortic valve is more likely to produce symptoms and be quickly noticed by both patients and physicians.

Two major problems may arise in the functioning of the valves: they may fail either to open fully or to close completely. The narrowing of a valve, called **stenosis**, occurs when the leaflets become rigid, thickened, or fused together, reducing the opening through which the blood passes from one chamber to another. As flow is obstructed, the blood accumulates in the chamber, forcing the heart to work harder

in order to pump the blood. When the valve fails to close properly - a condition referred to as **insufficiency** or **regurgitation** - a portion of the ejected blood flows backward. For example, if the aortic valve is unable to close properly, some of the blood that is pumped forward from the left ventricle into the aorta leaks back into the ventricle during ventricular diastole. In severe cases, as much as 90 percent of the entire pumped volume may flow back.[6]

In some cases, stenosis and insufficiency may occur together. This happens when the leaflets have become shrunken and stiff with the valve fixed in a halfopen position.

Valvular stenosis and insufficiency can gradually wear out the heart. At first, the heart muscle dilates and thickens. This enables it to compensate for the extra workload and allows the heart to supply an adequate amount of blood to the body. Eventually, however, the enlarged heart may grow weaker and become unable to pump blood as efficiently as before.[6]

The major complication resulting from heart valve disease is congestive heart failure, a condition that occurs when the heart is unable to pump out an adequate volume of blood. The heart's weak pumping action leads to a buildup of fluid (congestion) in the lungs and other tissues such as the legs, feet, ankles and the abdomen. The 'water' in the lungs makes breathing difficult and in the legs, for instance, it causes obvious swelling (edema).

II.3.1. Mitral valve prolapse

This condition is also known as click-murmur syndrome, floppy-valve syndrome and balloon mitral valve. Mitral valve prolapse means that one or both of the valve cusps may be enlarged, and sometimes the supporting chords and muscles are too long. Instead of closing evenly, one or both of the cusps prolapse or bulge out into the left atrium.[61] Depending on the degree of the deformity, the prolapse can lead to mitral regurgitation. Mitral valve prolapse is the most common type of mitral valve disorder, and perhaps the best known to the general public.

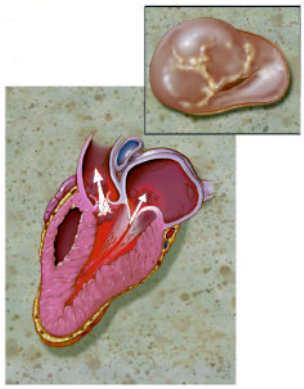

(a) In the patient with mitral regurgitation, the valve does not close completely.[61]

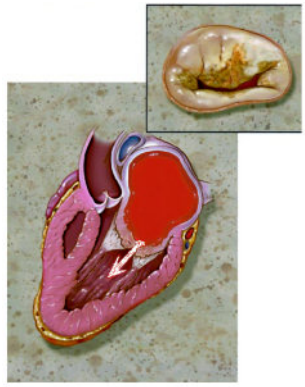

(b) In patients with mitral valve stenosis, the valve has a restricted opening.[61]

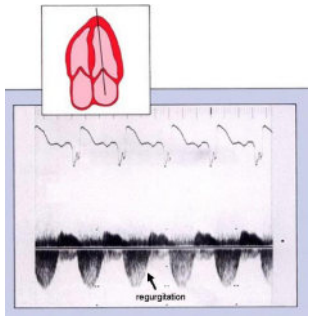

(c) Doppler recording of typical mitral regurgitation from the apex (Scale marks = 2 m/s).[62]

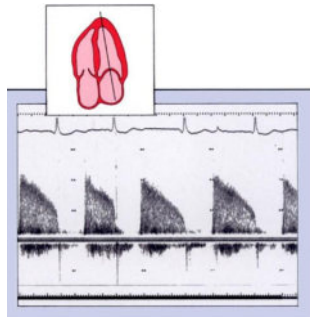

(d) Typical diastolic pattern of mitral stenosis using Doppler. Note early diastolic velocity rises to 2 m/s (Scale marks = 1 m/s).[63]

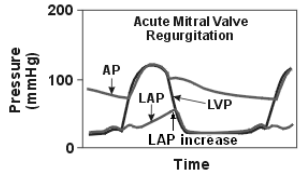

(e) Mitral insufficiency: during ventricular contraction (systole), the left ventricle eject into the left atrium as well as into the aorta, thereby increasing LAP.

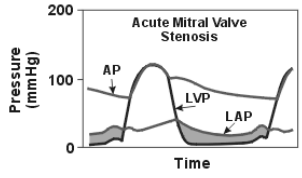

(f) Mitral stenosis: during ventricular filling (diastole), LAP exceeds LVP (gray area: pressure gradient generated by stenosis).

Figure II.3.: Mitral regurgitation and mitral stenosis.

II.3.2. Mitral regurgitation

Mitral regurgitation (figure II.3(a)) is most often caused by annulus dilatation or by a dysfunction of the papillary muscles that control the closing of the valve, or by a rupture of the chordae tendineae. A heart attack may result in mitral insufficiency if a portion of the heart that supports the position of the valve is disrupted. Prolapse of the mitral valve (figure II.3(a)) may also be associated with insufficiency. In rare cases, insufficiency is a result of a congenital defect or disorder.[61]
If a great deal of leakage occurs between the atrium and ventricle and when this persists over long periods, pressure will build up in time in the lungs and shortness of breath will occur.
The full spectral profile of mitral regurgitation obtained by Doppler echocardiography commonly reaches peak velocities of between 3 and 6 m/s, depending on the systolic pressure gradient between the two chambers. The profile is usually quite symmetric, as seen in figure II.3(c). The opening and closing motions of the mitral valve will sometimes result in sharp spikes on the spectral velocity recording because the rapidly moving valves will also render a Doppler signal.[62]
In mitral regurgitation (figure II.3(e)), blood flows back into the left atrial chamber during systole. There is also a large increase of the atrial pressure at the end of the systole (figure I.2 and II.3(e)). The regurgitant flow reduces the net stroke volume of the ventricle into the aorta and causes an enlargement of the proximal atrial chamber and an increase in atrial pressure. The atrium will compensate by increasing its force of contraction through the Frank-Starling mechanism in order to enhance ventricular filling. However, the increased atrial pressure can lead to pulmonary congestion and edema.

II.3.3. Mitral stenosis

Mitral stenosis (figure II.3(b)) is a narrowing or blockage of the mitral valve.[61] The narrowed valve causes blood to backup in the left atrium instead of flowing into the left ventricle and results in an increase in the pressure in the left atrium. This pressure is transmitted back through the pulmonary veins, causing congestion of the lungs. Mitral stenosis can be aggravated by atrial fibrillation, a condition in which the atrium weakens and contracts with irregular movements instead of a coordinated pumping action and loses its transport function. Mitral stenosis may

also be associated with aging and a buildup of calcium on the ring around the valve where the leaflet and heart muscle meet.
The normal mitral valve area is 4-6 cm^2, and severe mitral stenosis is present with valve areas smaller than 1.5 cm^2.
The typical echocardiographic spectral recording of mitral stenosis demonstrates spectral broadening in diastole, with peak flow in early diastole and a progressive but slowed diastolic descent (figure II.3(d)).[63]
Mitral valve stenosis results in the left atrial (LA) pressure being much greater than left ventricular (LV) pressure during diastolic filling (shaded gray in figure II.3(f)). The high resistance across the stenotic mitral valve causes blood to back up into the left atrium and reduces filling (end-diastolic volume) of the left ventricle despite the elevated LA pressure. The reduced ventricular filling (decreased preload) can result in reduced ventricular stroke volume by the Frank-Starling mechanism. If the stroke volume drops significantly, the reduced cardiac output may result in a reduction in aortic pressure. The increase in LA pressure can result in pulmonary congestion and edema because of increased pulmonary capillary hydrostatic pressure.

II.3.4. Aortic regurgitation

In its acute form, aortic regurgitation (figure II.4(a)) usually occurs as a result of an infection that destroys the valve's leaflets. The chronic form, which is more common, is usually a consequence of widening of the aorta in the region where it connects to the valve. Sometimes the ascending aorta may be widened due to a genetic disorder, such as Marfan syndrome, a congenital connective tissue disease.[64]
Aortic regurgitation, unlike other valve abnormalities, often produces no symptoms for many years. Shortness of breath, sometimes accompanied by chest pain and ankle swelling, may be noticed after many years if the condition is not severe. The constant regurgitation of blood results in a dilation or enlargement of the left ventricle.
The Doppler evaluation of aortic insufficiency appears as a high frequency turbulent jet with spectral broadening and flow toward the transducer as noted in figure II.4(c).[62]
In the case of aortic regurgitation, blood flows back into the left ventricle chamber after ejection is complete. This leads to an increase in diastolic volume and pressure, which causes the ventricle to contract more forcefully (Frank-Starling mecha-

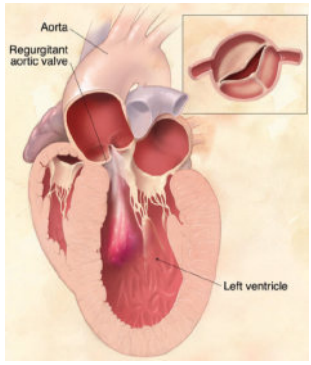

(a) In this patient with aortic regurgitation, the abnormal aortic valve does not close fully.[64]

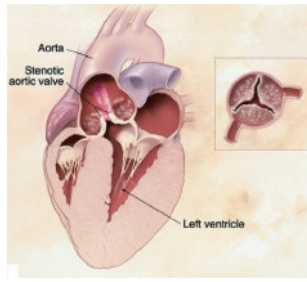

(b) In this patient with aortic stenosis, there is an abnormal calcified aortic valve that cannot open fully.[64]

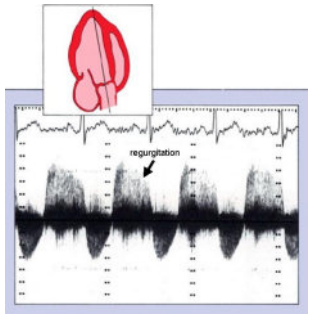

(c) Aortic insufficiency is recorded as diastolic flow toward the transducer with a peak velocity of 3 m/s (Scale marks = 1 m/s).[62]

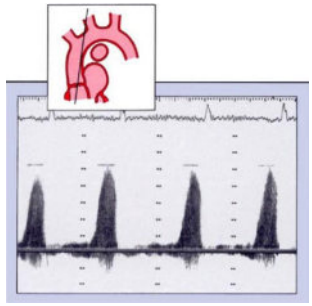

(d) Typical aortic systolic velocity recording in a patient with aortic stenosis. Note that the peak velocity is almost 5 m/s (Scale marks = 1 m/s).[63]

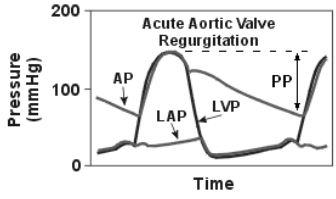

(e) Aortic insufficiency: during ventricular relaxation (diastole), blood flows backwards from the aorta into the ventricle. Aortic pulse pressure and LAP increase.

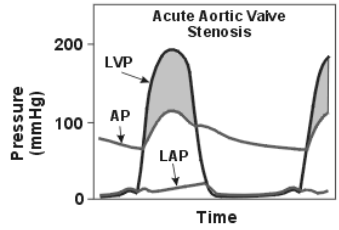

(f) Aortic stenosis: during ventricular ejection (systole), LVP exceeds AP (gray area: pressure gradient generated by stenosis).

Figure II.4.: Aortic regurgitation and aortic stenosis.

nism) thereby increasing the stroke volume to help compensate for the regurgitation. If there is significant regurgitation across the valve, the rate of decline in pressure (pulse pressure PP) within the aorta will be greater as illustrated in the figure II.4(e). This results in a characteristic widening of the aortic pulse pressure.

II.3.5. Aortic stenosis

There are three major causes of aortic stenosis: calcific degeneration or deposits of calcium on the valve (in elderly), congenital abnormality (uncommon), and rheumatic fever. The disorder is recognized by a characteristic murmur; which can become quite loud and is usually easily recognized with a stethoscope.

Stenosis of the aortic valve (figure II.4(b)) obstructs the flow of blood from the left ventricle, causing it to thicken (hypertrophy) and/or enlarge (dilation) and eventually weaken over time. At rest, the ventricle can compensate for the presence of the stenosis by pumping harder, but during physical exertion it may not be able to maintain a sufficient output of blood to the organs and the brain. Fainting may result.[64]

The normal aortic valve area is 2.6-3.5 cm^2 in adults. Valve areas of 1.0 cm^2 or smaller are considered as severe aortic stenosis.

A Doppler velocity pattern of a patient with severe aortic stenosis is shown in figure II.4(d). In this condition, there is marked spectral broadening, delayed systolic peaking, and a marked increase in velocity. In this patient, the peak systolic velocity is almost 5 m/s.[63]

Aortic valve stenosis (figure II.4(f)) is characterized by the left ventricular pressure being much greater than aortic pressure during left ventricular ejection (shaded gray in figure). The pressure gradient across the stenotic lesion results from both increased resistance (related to narrowing of the valve opening) and turbulence distal to the valve. The magnitude of the pressure changes is determined by the severity of the stenosis and the flow rate across the valve.

II.3.6. Tricuspid and pulmonary stenosis and regurgitation

These disorders account for less than 5 percent of valve disease. Abnormalities of the tricuspid valve are generally caused by rheumatic fever or metabolic abnormalities affecting the heart (a secondary cause to longstanding and severe mitral disease). Among the major symptoms they produce are edema and fatigue. Pulmonary steno-

sis - are also rare and are primarily due to congenital defects. Children born with a severely narrowed pulmonary valve may require immediate surgical intervention for survival.

II.4. Treatment

II.4.1. Drugs

No drugs can cure severe valve diseases. The major function of drugs administered in valve disorder are to reduce the severity of symptoms, possibly reduce the workload of the heart, and/or prevent complications.[6,57] Without being exclusive, the following categories represent the most commonly applied types of drugs.

- *Vasodilators*: dilate venes and peripheral arterioles, reduce the vascular resistance against which the heart must pump, and decrease the workload of the heart. They are used to treat congestive heart failure associated with heart valve disease (usually valve insufficiency).
- *Diuretics*: lower the salt and fluid levels in the body and reduce intra- and extra-vascular volumes. Diuretics also reduce swelling and ease the heart's workload by decreasing the volume of blood that needs to be pumped.
- *Anticoagulants*: prevent formation of blood clots. These include medications such as warfarin and heparin.
- *Antiarrhythmics*: maintain a regular heartbeat and slow down rapid heart rhythms.

II.4.2. Balloon valvuloplasty

This relatively new technique is increasingly used as an alternative to surgical repair of valve stenosis. Balloon valvuloplasty is a procedure in which a balloon catheter with a small deflated balloon at the tip is inserted through the skin into a blood vessel, and then is threaded up to the opening of the narrowed heart valve. The balloon is inflated, which stretches the valve open. This procedure relieves some valve obstructions. While somewhat less effective than surgery, it is a less invasive pro-

cedure. Balloon valvuloplasty may relieve many of the symptoms of valve disease, but it will not cure valve disease.[6]

II.4.3. Surgical repair

The surgeon will always try to repair a damaged valve, however this requires normal valve tissue.
For mitral and tricuspid valve disease, the surgeon is able to open fused leaflets, remove calcium deposits, repair floppy leaflets so they close normally, tighten the chords and support an enlarged annulus by attaching a ring or band (annuloplasty). Bicuspid aortic valve disease (two leaflets instead of three) is a common type of aortic valve disease. When there is a leak, the surgeon may be able to reshape the aortic valve leaflets, allowing the valve to open and close more easily.
In the majority of cases, however, a severely stenotic calcific valve (with no normal tissue) has to be replaced.[6]

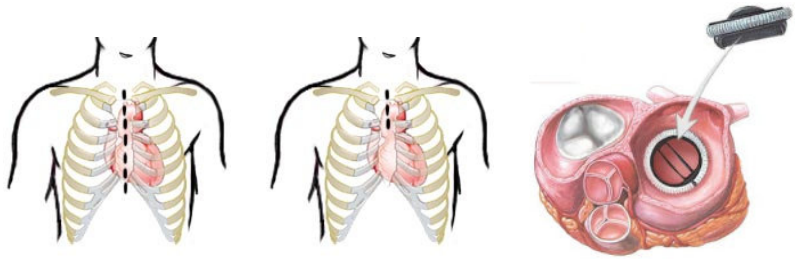

(a) Traditional open heart surgery. (b) Minimal invasive heart surgery. (c) Heart valve replacement.

Figure II.5.: Heart valve surgery and heart valve replacement.

II.4.4. Valve replacement surgery

This type of surgery is usually recommended when the valve is severely damaged and potentially life-threatening.[6]
Valve replacement requires open heart surgery (figure II.5). During *traditional heart valve surgery*, a surgeon will medically open the entire sternum (breastbone) to get direct access to the heart. The surgeon then repairs or replaces the abnormal heart valve or valves. *Minimally invasive heart surgery* is an alternative approach performed through a smaller incision. The incision is only a few centimeters instead

of the 15 to 25 centimeters required for traditional heart surgery.
Artificial valves are carefully sutured or sewn into the valve annulus after removal of the diseased valve, completely replacing the natural valve. There are two types of prosthetic valves that can be used to replace the original valves: mechanical (figure II.6) and biological (bioprosthetic) (figure II.8) valves.

(a) Caged ball valve.

(b) Tilting disc (monoleaflet) valve (Omnicarbon).

(c) Bileaflet valve (ATS Open Pivot).

Figure II.6.: Mechanical valve types.

II.4.4.1. Mechanical valves

Charles Hufnagel successfully implanted a human patient in 1952[65] with a *caged-ball valve* (figure II.6(a)); the valve was placed in the descending aorta. Starr-Edwards[66,67] was the first to replace a patient's mitral valve with a *caged-ball valve* (figure II.6(a)) in 1960. The cage-ball valve consists of a metal ring covered in Dacron and a thin metal cage. Inside the cage is a ball, which exactly fits the dimension of the ring. Blood flowing in the correct direction pushes the ball away from the ring towards the cage and flows by uninterrupted. When the blood flows in the opposite direction, it pushes the ball back into the ring, creating a tight seal that prevents leaking. The *tilting disc valves* work somewhat along the principle of a hinged door that is opened. Mechanical valves make a clicking noise with each heartbeat.
The mechanical valves, currently most in use, are *bileaflet valves* and *single tilting disc valves* (figure II.6).[68]
The following mechanical heart valves are studied in further detail in this work:

- *Omnicarbon Monoleaflet Valve.* The Omnicarbon cardiac valve is a monoleaflet prosthesis (figure II.6(b)) that basically consists of a ring and a curved freely-rotatable disc, which is retained by two shields extending from the ring. The Omnicarbon valve is particularly appropriate for ultrasound visualization

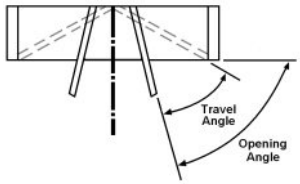

(a) Opening angle and travel angle of the leaflet in a mechanical bileaflet valve.

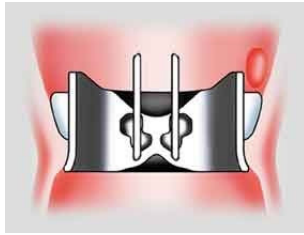

(b) On-X shaped orifice with flared inlet.

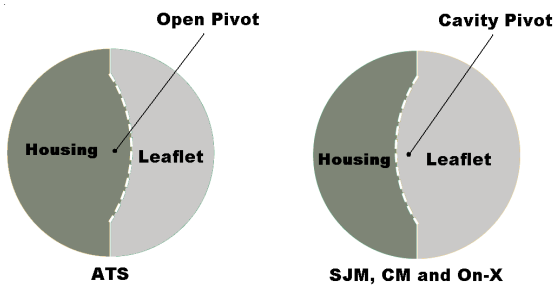

(c) Bileaflet hinge design.

Figure II.7.: Design of bileaflet mechanical heart valves.

because of its simple geometric shape and the absence of inner structures. Its hingeless design produces central flow of blood. The disc opens to a maximum angle of 80° at maximum cardiac output rate. An adequate opening angle of approximately 60°-70° is expected at normal cardiac output at rest. Leakage flow is relatively low because of the presence of a disc seat on the housing ring where the disc closes at 12° angle. The seat eliminates the open gap which exists in other valve designs. Further motion of the disc beyond its 12° position is wasted energy and does not benefit the flow process. The travel angle thus varies between 48°-68°.

- *On-X Bileaflet Valve.* Bileaflet valves have two semicircular leaflets that pivot in hinges integrated into the flange. Typical design characteristics of the On-X valve are a shaped orifice with flared inlet design (figure II.7(b)) to reduce inlet turbulence, an elongated body to reduce exit losses, thinner leaflets and a supra-annular sewing ring for small aortic valves.[69,70,71] The main effect of its design is an enlarged valve area available for flow, as compared to other equally sized prosthetic valves. The travel angle of these valves is 50°.

Table II.1.: Opening and travel angles.

Maximum and Observed Opening and Travel Angles[73]					
Mechanical Valve Type	Maximum Opening Angle [degrees]	Observed Opening Angle [degrees]	Maximum Travel Angle [degrees]	Observed Travel Angle [degrees]	Pivot Type
SJM HP	85	85	60	60	Cavity Pivot
CM	78	78	53	53	Cavity Pivot
On-X	90	81.6	47	38.6	Cavity Pivot
ATS	85	74.8	60	49.8	Open Pivot

SJM HP: St. Jude Medical Haemodynamic Plus Series, Inc., St. Paul, MN, USA

CM: CarboMedics, Inc., Austin, TX, USA

On-X: Medical Carbon Research Institute, Austin, TX, USA

ATS: Advancing the Standard, ATS Medical, Inc., Minneapolis, MN, USA

- *ATS Open Pivot Bileaflet Valve.* The ATS valve (ATS Medical, Minneapolis, MN, USA) is a pyrolytic carbon, open pivot, low-profile cardiac prosthesis (figure II.6(c)). The theoretical opening angle of the ATS valve is 85°with 60° angle of travel. Specific to this valve is its open pivot design, in which the convex pivot and stops are located on the inner circumference and extended in the flow field.[72]

Table II.1 gives a summary of the opening and travel angles of four types of bileaflet valves. Note that, for some valves, the theoretical opening angle is not reached while operating *in vivo*. Data in table II.1 are from an *in vitro* study done by Feng et al.[73] Besides the difference in opening and travel angles, there is also a difference in the design of the hinge region. Figure II.7(c) explains the difference between an “Open Pivot” hinge and a “Cavity Pivot” hinge. In the “Open Pivot” hinge, the valve leaflet rotates over a circular ‘bulb’ made *on* the housing, while the leaflet rotates in a ‘hole’ made *in* the housing of valve with a “Cavity Pivot” hinge. The ATS valve is the only valve based on the Open Pivot Hinge mechanism.

The mechanical valves have the advantage of durability: they may often last a lifetime.[55] On the rare occasions that a mechanical valve does fail, it may do suddenly and cause the heart to fail. The most important disadvantage is that the patient will have to follow a lifetime regimen of anticoagulants such as warfarin to prevent blood

clots causing valve thrombosis.[68] Taking anticoagulants also places some restrictions on the patient's activity; contact sports or other activities that could result in bruising or internal bleeding usually have to be avoided.

II.4.4.2. Biological or bioprosthetic valves

Bioprosthetic valves (figure II.8), also known as tissue valves, can be categorized as heterografts, homografts, or autografts. Heterograft valves (also called xenografts) are either whole porcine aortic valves or hand-fabricated valves made from bovine pericardial tissue. Homograft valves are human aortic valves harvested from cadavers and cryogenically preserved. Autografts are used solely in the Ross procedure, where the native pulmonary valve is used to replace the aortic valve and in which the pulmonary valve is replaced with a homograft.[74]
Biological valves do not ordinarily require the patient to take anticoagulant medication for more than six to eight weeks following surgery. The disadvantage of these replacement valves is that they do wear out and may have to be replaced after about ten to fifteen years.[75] Mostly, they wear out gradually, so there is little risk of a sudden episode of heart failure. Bioprosthetic valves degenerate more slowly in elderly patients than in the young. In contrast the risk of anticoagulation related complications may be higher in the very elderly.
In so called stented bioprostheses, porcine or bovine pericardial leaflets are mounted onto a fixed plastic or metallic frame or stent (figure II.8(a)). Nonstented or stentless aortic bioprostheses (figure II.8(b)), where this metal frame is absent, have been the focus of numerous studies in the last decade.

(a) Stented valve. (b) Stentless valve.

Figure II.8.: Stented versus stentless valve.

Stentless heart valves Compared with stented valves, stentless valves are thought to offer superior haemodynamics, with a higher effective orifice area[76] (figure II.9(a)), possibly yielding to survival advantage.[77] Nonstented bioprostheses have been associated with lower pressure gradients, at rest and exercise, than stented bioprostheses or mechanical valves.[76] Their durability is as yet undetermined,[78] although their design may overcome some of the disadvantages stemming from the presence of a rigid stent and the resulting forces on the valve leaflets[79,80] (figure II.9(b)). Furthermore the leaflet opening behavior changes in presence of stent (figure II.9(c)), resulting in different stress distribution in the valve leaflet.[81,8]

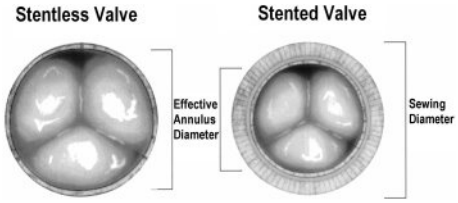

(a) Effective annulus diameter for stented and stentless valves.[82]

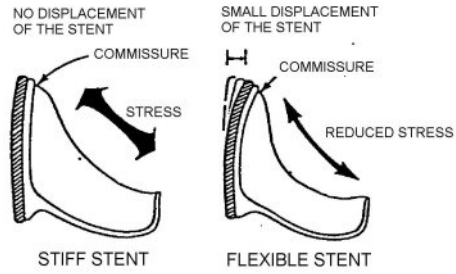

(b) Reduced stress distribution in valve leaflets.

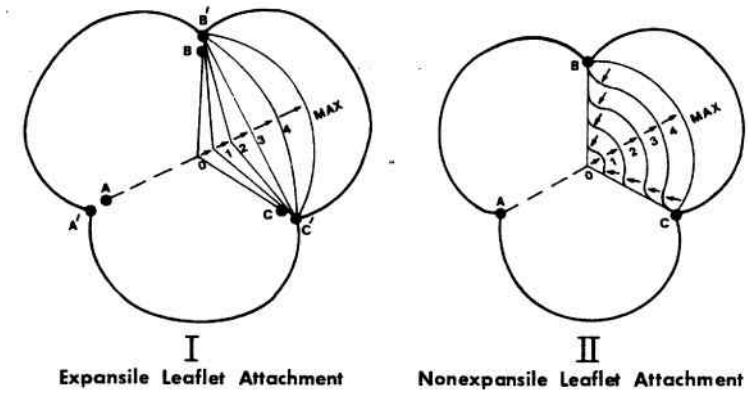

(c) Leaflet profiles during opening for expansile (I) and nonexpansile (II) leaflet attachments.[8]

Figure II.9.: Why stentless heart valves?

II.5. Recent developments: progress towards a tissue engineered heart valve

An underlying problem with all current methods of heart valve replacement is that the non-living material lacks an intrinsic repair system that can recondition the valve after structural injury.[22] Optimal valve replacement tissue should be biocompatible whilst exhibiting growth and reparative capabilities.[83] The relatively new field of Tissue Engineering (TE) may offer a solution to heart valve replacement.[84] Current strategies in this field of tissue engineering are: (i) transplantation of constructs containing specific cell types to the site of injury following an *in vitro* conditioning period (*in vitro* colonization approach), or (ii) constructs which will recruit endogenous progenitor or differentiated cells from the surrounding tissue (*in vivo* colonization approach).[22] Either of these constructs, theoretically, could functionally integrate with the host tissue and encourage tissue regeneration. A thorough knowledge of normal heart valve development and functional tissue composition is an essential prerequisite to establish the desired structural makeup of a tissue-engineered alternative.[17]

II.5.1. Tissue engineering approach to heart valve replacement

In the following the most important parameters which need to be considered for the creation of a tissue engineered heart valve (TEHV) are described.

Cells To create a functional and durable TEHV, the establishment of cultured cells is a priority. To avoid rejection, cells are ideally autologous.[85] However, in diseased states or with geriatric patients, autogeneic cells may not be an appropriate transplantation source.[86] At present, autologous cells are unavailable 'off-the-shelf'.[87] Another cell source may be stem cells, but currently ethical issues make it impractical to use these cells for research purposes. However, the stem-cell approach shows great potential for future TE-applications.[88]

Scaffolds The traditional concept of tissue engineering involves the use of three-dimensional scaffolds as cell transplant devices to replace the extracellular matrix.

The cells can be seeded on a biodegradable polymeric scaffold[89,90,91] or on an acellularized bio-matrix.[92]

Signals Successful tissue regeneration is not achieved 'simply' by combining cells and scaffolds.[22] A key challenge in tissue engineering is to understand quantitatively how cells respond to molecular and biomechanical signals and integrate multiple inputs to generate a given response, and to control nonspecific interactions between cells and a biomaterial, so that cell responses specifically follow desired receptor-ligand interactions.[17]
In vitro methods of mechanical stimulation or physical signaling have been shown to improve cell and tissue growth. This has led to the design and development of bioreactor systems mimicking the environment on the transplant site.[22,93]

II.5.2. Bioreactor technologies

A bioreactor aims to mimic the complex *in vivo* environment, including all natural stimuli that have impact on cell growth and differentiation. In a classic general cell culture bioreactor system,[94] these stimuli can be divided into 4 different basic aspects: (i) the matrix or scaffold in or on which cells grow, (ii) the biochemical and physiological composition of the medium, (iii) the composition of the gas phase and (iv) the incubation temperature. All of these stimuli are of great importance for cell differentiation and proliferation. A more modern approach is to create an *in vitro* environment that not only embodies the 4 above-mentioned aspects but also includes a mechanical stimulus. The involved cell cultures have a controlled delivery of a mechanical input like hydrostatic pressure, fluid shear stress or substrate strain. This mechanic signal is translated by the cell membrane and membrane proteins to the cytoskeleton.[95] Many studies have shown that cell and tissue growth is enhanced in response to mechanical stresses under fluid flow as compared to that under static incubation conditions. These studies define a bioreactor as *"a system that simulates physiological environments for the creation, physical conditioning, and testing of cells, tissues, precursors, support structures, and organs* in vitro*"*.[93,95,96,97,98] The bioreactor system allows for a tissue construct to be s(t)imulated in a controlled environment. Fluid flow, to provide biochemical and mechanical stimulation, is controlled in terms of composition, flow rate, pressure, and temperature. A mechanical force can be applied and controlled to provide direct mechanical stimulation. Pul-

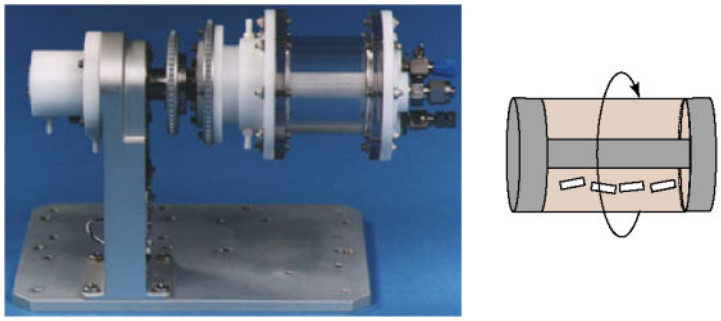

Figure II.10.: Rotating-wall vessels provide a dynamic culture environment to the constructs, with low shear stresses and high mass-transfer rates.[101]

satile forces, pressure, flow rate, shear stress, frequency and stroke volume are extremely important design considerations. The biochemical environment is equally important in the design of a bioreactor. The transfer of nutrients to the cells and removal of waste products is necessary for the healthy development of tissue.[93]
Today there are a number of different types of bioreactors available including static, dynamic, and biomimetic systems. The evolution of the bioreactor is described in the following, originating with static culture flasks, the biomimetic bioreactors of today and the future devices of tomorrow.[93]

Static systems The static flask system is the simplest type of bioreactor and consists of a flask with tissue constructs fixed in place in a culture medium.[99] In these systems tissue constructs may be grown in a static environment or a mixed environment by employing the use of a magnetic stirrer. The use of static systems can lead to structurally inadequate nonuniform tissue constructs.[94,100]

Dynamic systems Since physical stimuli have been shown to modulate tissue development, the design of bioreactors has been motivated to expose growing tissues to mechanical forces. One such system that employs the benefit of a low shear stress environment is a rotating wall vessel (figure II.10) wherein cells are grown in a microgravity environment.[102,103,104,105,106] It has been shown that engineered cardiac tissues grown in rotating vessels are structurally and functionally superior to constructs grown in static or mixed flasks.[94,100,101,107,108]

Biomimetic systems Based on the fact that physical stimuli improve cell and tissue growth, Niklason et al. developed a bioreactor to closely mimic *in vivo* con-

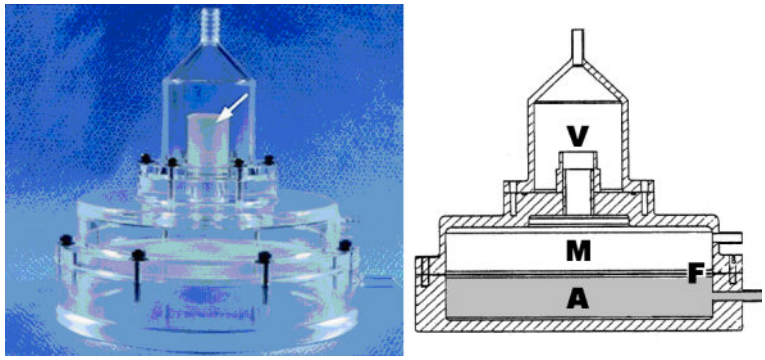

Figure II.11.: Photograph and schematic diagram of pulsatile bioreactor developed by Hoerstrup et al.;[97] (V) tissue engineered heart valve, (F) flexible membrane, (A) air chamber and circuit, (M) culture medium circuit.

ditions.[95] This perfusion system provides intraluminal pressure and pulsatile flow to four bioreactors, each of which contains one tissue-engineered vessel. Gas exchange is provided via a reservoir bag, and the pressure is monitored constantly.
The development of an optimal system for tissue engineering heart valves (figure II.11) and small diameter vascular grafts under pulsatile flow conditions is currently an innovative research topic.[17,96,97,109]

II.5.3. Current progress towards a Tissue Engineered Heart Valve

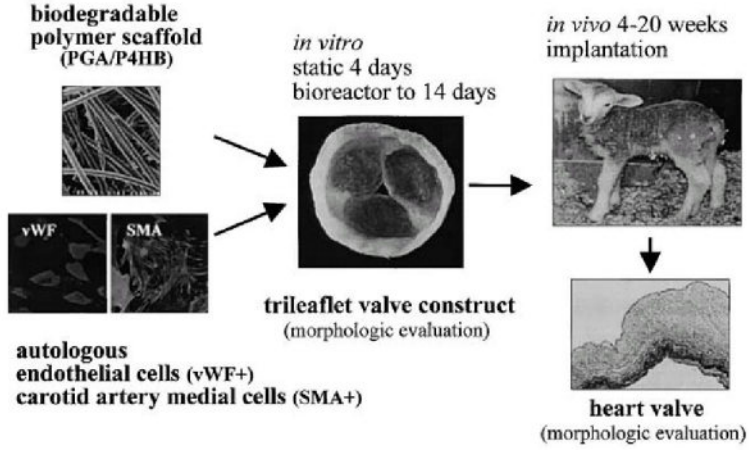

Figure II.12.: Experimental design for preparing and evaluating a tissue engineered heart valve.[110]

Design of tissue-engineered heart valves is difficult due to the complex nature of the dynamic mechanical environment in which they must perform.[93] The heart valve must open and close at a frequency of approximately 1 Hz. In addition, they are also exposed to bending stresses and high shear stresses associated with blood flow.[111] Sodian et al.[112] created a trileaflet heart valve from a porous biodegradable scaffold. Results indicated that the cultured cells appeared to be viable and that extracellular matrix formation was induced after pulsatile flow exposure.[112]

The TE valves were grown in an *in vitro* pulse duplicator[97] system under gradually increasing flow and pressure conditions, thereby providing physical signals to the developing tissues comparable to those encountered *in vivo*. After 14 days of *in vitro* culture, the valves grown in the bioreactor showed significantly higher formation of matrix proteins, a more organized histological structure, and more favorable mechanical properties than did constructs grown under static culture conditions. Six of these valve constructs were then implanted into the pulmonary position of sheep for *in vivo* evaluation. Echocardiography showed functioning valves up to 20 weeks.

Hoerstrup fabricated trileaflet heart valves using polyglycolic-acid (PGA) scaffolds coated with poly-4-hydroxybutyrate (P4HB).[110] In all of the tissue engineered heart valves grown in the bioreactor,[97] synchronous opening and closing of the leaflets was observed. All leaflets were intact, mobile, pliable, and competent during valve closure compared to those grown in static culture, which were fragile and began to lose structural integrity after 14 days. Histology of the TE leaflets revealed cellular tissue organized in a layered fashion with a dense outer layer and lesser cellularity in the deeper portions after 14 days in the pulse duplicator. Formation of extracellular matrix was demonstrated as predominantly GAGs and some collagen.[110] Smooth muscle cells were detectable throughout the tissue. The static controls showed less tissue formation and organization at all time points. Additionally, the tissue grown in the bioreactor had a confluent smooth surface with cell orientation in the direction of flow, while a rough surface was observed for the static grown tissues. There was mild to moderate valve regurgitation present at 16 and 20 weeks that was due to central noncoaptation. This may result from shrinkage of the cuspal tissue during the process of scaffold bioabsorption and/or the observed increase of the inner diameter of the valve constructs in accordance with the sheep pulmonary artery growth (4 mm over the 5-month time period).[110]

Ideally, when tissue engineering techniques will be introduced in future clinical rou-

tine, the schedule for a patient diagnosed for valve disease may be (1) cell harvest by a bone marrow puncture under local anesthesia; (2) differentiation and expansion of the cells; (3) tissue engineering of a heart valve prosthesis *in vitro*; and (4) following yet to be defined quality criteria (biochemical, histological, bio-safety, etc.) implantation of a living autologous prosthesis into the patient.[113]

Chapter III

Haemodynamic assessment of prosthetic heart valves

III.1. Parameters derived from flow and pressure data

III.1.1. Cardiac output

The performance of a valve depends on the flow passing through it. When evaluating a valve, an important parameter is thus the total flow rate through the valve. During each cardiac cycle, a volume of blood, i.e. the stroke volume (SV), is ejected. The amount of cardiac cycles or beats per minute (bpm) is defined as the heart rate (HR). The volume of blood ejected by the ventricles per minute is called the cardiac output (CO). Cardiac output in humans varies between 4-6 l/min at rest to 20-35 l/min during exercise, with heart rate variations from 40-70 bpm at rest to 170-200 bmp during exercise and SV from 60-125 ml during rest to 100-200 ml during exercise. A well trained person develops a larger CO with a lower HR, and thus his heart delivers a larger SV.[5] The stroke volume (SV [ml]), times the number of beats per minute (heart rate, HR), equals the cardiac output (CO [l/min]; equation III.1).

$$CO = SV \cdot HR \tag{III.1}$$

Changes in either stroke volume or heart rate will alter cardiac output. The SV can be calculated from velocity measurements over the valve (equation III.2) as

$$SV = VTI \cdot A \tag{III.2}$$

with VTI, the velocity time integral (VTI [cm]) and A the valve area in [cm^2]. The VTI = $\int v \cdot dt$ is obtained from the Doppler velocity-time curve as the area under the velocity curve.

III.1.2. Pressure gradient

The resistance of the valve against the flow can be quantified by pressure/energy losses over the valve.

Pressure gradient from catheterization A dynamic systolic gradient between left ventricular and aortic pressures is evident. Assuming proper alignment of the pressure tracings, a series of instantaneous pressure differences can be measured, and the mean systolic gradient ΔP_{mean} can be calculated. The gradient ΔP_{peak} between the peak systolic left ventricular pressure and the systolic aortic pressure can also be determined, even though these two peaks are non-simultaneous. Note that the maximum instantaneous gradient ΔP_{max} is always larger than the peak-to-peak gradient. Similar gradients can be determined for the mitral valve during ventricular filling (diastole).[114]

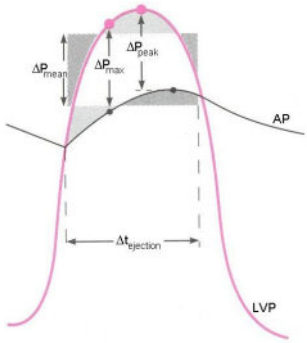

(a) Pressure gradient from catheterization; LVP: left ventricular pressure, AP aortic pressure.[114]

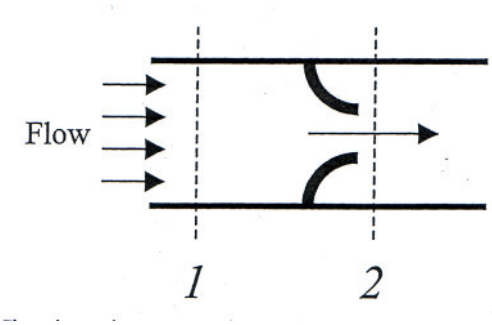

(b) Flow through a stenosis. The pressure drop between points 1 and 2 is calculated from velocity measurements at point 2 (assuming that it is much greater than the velocity at point 1) using the simplified Bernoulli equation.[115]

Figure III.1.: Pressure gradients in heart valves.

Pressure gradient from Doppler measurements The simplified Bernoulli equation is derived from the Bernoulli equation based on the assumptions that the flow through the stenosis is laminar and inviscid (viscous forces negligible). Bernoulli's hydraulic formula states the conservation of mechanical energy between two points

along a streamline (figure III.1(b)):[115]

$$P_1 - P_2 = \frac{1}{2} \cdot \rho(v_2^2 - v_1^2) + \rho g(z_2 - z_1) + \rho \int_1^2 \frac{dv}{dt} ds \qquad \text{(III.3)}$$

where P_1 [Pa], v_1 [m/s], z_1 [m] are the pressure, velocity, and height from a reference level at the upstream location, and P_2 [Pa], v_2 [m/s], z_2 [m] are the pressure, velocity, and height at the downstream location. The integral term accounts for the flow acceleration or deceleration between the two locations. If the equation is applied at peak systolic velocity, this term becomes zero, because the derivative becomes zero. When further applied on two points along a stream line located at the same height, one finds that:[115]

$$P_1 - P_2 = \frac{1}{2} \cdot \rho(v_2^2 - v_1^2) \qquad \text{(III.4)}$$

When the downstream velocity is much higher than the upstream velocity ($v_2 >> v_1$), v_1^2 can be neglected. Filling in the value of ρ of blood at 37°C (1060 kg/m^3) and converting pressure from Pa to mmHg (133 Pa = 1 mmHg) results in a factor of about 4, in the so-called simplified Bernoulli equation:[115]

$$\Delta P_{\text{Doppler}}\ [\text{mmHg}] \quad = \quad 4 \cdot v_2^2 \quad \text{and} \quad v_2 \text{ in } [\text{m/s}]$$

where ΔP is in [mmHg] and v_2 is in [m/s].[115] This equation has found wide application clinically in determining pressure drops across severe stenosis from noninvasive velocity measurements with Doppler ultrasound.

The Bernoulli equation is not valid in cases in which viscous forces are significant, such as in long constrictions with a small diameter, or in flow with separation regions. In addition, it does not account for turbulent energy losses in cases of severe stenosis. Such losses should be taken into account, because they reduce the energy content of the fluid.[115]

In normal individuals, there is a very slight (1-2 mmHg) pressure difference between the left ventricle and aorta during ejection that helps drive the blood across the aortic valve. In contrast, very high pressure gradients are observed in patients with a stenotic valve. We refer to figures II.4(d) and II.3(d) where a pressure gradient ΔP of $4 \cdot (5\ \text{m/s})^2$ = 100 mmHg occure in the case of a severe aortic stenosis and $4 \cdot (2\ \text{m/s})^2$ = 16 mmHg in the case of a mitral stenosis.

III.1.3. Effective orifice area and performance index

When blood is flowing through an orifice with cross section area A [m^2], convergence of streamlines make that only part of the cross section is effectively used for flow passage. This is particularly important in valve dynamics where the effective valve area should be maximized to avoid high velocities, turbulence, shear, and associated high pressure drops. The effective orifice area (EOA) is the standard parameter for the clinical assessment of the severity of the valve stenosis. It is also a parameter that can be used to compare performance of different mechanical and biological valve prostheses. As demonstrated in figure III.2, the flow through the valve is narrowing, using only the EOA, i.e. a fraction of the total geometric orifice area (GOA). The effective orifice area (EOA [cm^2]) is calculated - based on the continuity equation - as the ratio of forward stroke volume and VTI:

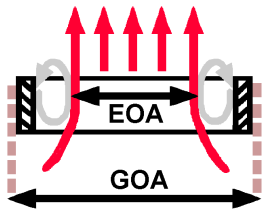

Figure III.2.: Geometric and effective orifice area (GOA and EOA).

$$EOA_{Continuity} = \frac{SV}{VTI} \tag{III.5}$$

Besides the continuity equation, the Gorlin equation provides an alternative way to calculate the effective orifice area (EOA_{Gorlin}). With Q the flow rate [m^3/s] and v the maximal velocity [m/s] in the vena contracta, the EOA is given by

$$EOA = \frac{Q}{C_1 v} \tag{III.6}$$

where C_1 is a coefficient to adjust for the velocity profile in the vena contracta. Through the orifice, there is a conversion of potential energy to kinetic energy, and this conversion is described by:[115]

$$v = C_2 \cdot \sqrt{2 \cdot g \cdot \Delta h} \tag{III.7}$$

with the pressure head across the orifice $\Delta h=\Delta z+\frac{\Delta P}{\rho g}$ and where C_2 is a coefficient to adjust for loss in the conversion of energy from potential to kinetic energy. With $\Delta z=0$ and assumption of $C_1 \cdot C_2=1$, the formula can be written as:

$$EOA = \frac{Q}{v} = \frac{Q}{\sqrt{2\frac{\Delta P}{\rho}}} = \frac{Q}{\sqrt{2\frac{\rho_{Hg} \cdot g \cdot \Delta h_{Hg}}{\rho}}} \tag{III.8}$$

The commonly used SI units [m^2], [m^3/s], [Pa] are converted into clinical used units [cm^2], [ml/s], [mmHg] for the area, the flow and pressure respectively.

$$\begin{aligned} EOA\ [cm^2] &= 10^4 \cdot EOA\ [m^2] \\ Q\ [ml/s] &= 10^6 \cdot Q\ [m^3/s] \\ \Delta P\ [mmHg] &= 10^3 \cdot \Delta h_{Hg}\ [mHg] \end{aligned} \tag{III.9}$$

$$\begin{aligned} \rho_{Hg} &= 13600\ [kg/m^3] \\ g &= 9.81\ [m/s^2] \end{aligned} \tag{III.10}$$

Combining equations III.8 and III.9 results in:

$$EOA \cdot 10^{-4} = \frac{Q \cdot 10^{-6}}{\sqrt{2\frac{\rho_{Hg} \cdot g \cdot 10^{-3} \cdot \Delta P}{\rho}}} \tag{III.11}$$

And thus finally the Gorlin equation can be written as:

$$EOA_{Gorlin} = \frac{Q}{51.6\sqrt{\Delta P}} \tag{III.12}$$

with EOA in [cm^2], ΔP in [mmHg] and the mean forward flow $Q_{fwd,mean}$ in [ml/s], calculated as the ratio of the "positive" area under the flow curve (forward stroke volume SV) divided by the duration of forward flow.
EOA_{Gorlin} is a fraction θ of the available geometric orifice area GOA, with θ known as the orifice constant, so that $EOA_{Gorlin} = \theta \cdot GOA$.
The performance index (PI [-]) of the valve is calculated as the ratio of the effective orifice area and the geometric orifice area (GOA):

$$PI = \frac{EOA}{GOA} = \theta \tag{III.13}$$

III.1.4. Regurgitation

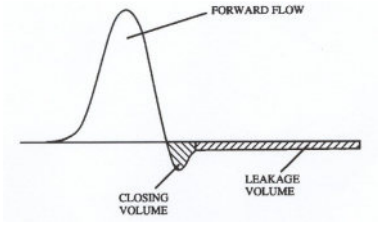

Figure III.3.: Flow cycle divided into forward flow, closing volume, and leakage volume.[55]

Regurgitation is reversed flow through the 'one way' valve. The percentage of regurgitation (% reg) in relation to the total SV is calculated as

$$\%\ \text{reg} = \frac{V_{reg}}{(V_{reg} + SV)} \quad . \tag{III.14}$$

V_{reg} [ml] is the total volume of regurgitation and can be split into V_{close} and V_{leak}. V_{close} is the volume of regurgitation due to the closing of the valve. V_{leak} is the volume of regurgitation due to leakage of the closed valve.

III.1.5. Flow patterns and shear stresses

Laminar and turbulent flow The Reynolds number (Re; equation III.15) is a quantity that engineers use to assess whether a fluid flow is laminar or turbulent. This is important, because increased mixing and shearing occur in turbulent flow. This results in increased energy losses which affects the efficiency of heart valves. A good example of laminar and turbulent flow is the rising smoke from a cigarette. The smoke initially travels in smooth, straight lines (laminar flow) then starts to "wave" back and forth (transition flow) and finally seems to randomly mix (turbulent flow). The dimensionless Reynolds number Re [-] is defined as:

$$\text{Re} = \rho \frac{U\ D}{\mu} \tag{III.15}$$

with ρ the density of the fluid (kg/m^3), U the velocity of the flow (m/s), D the diameter of the vessel (m) and μ the dynamic viscosity of the fluid (mPa·s). Figure III.4 demonstrates the different flow regimes in function of Re for the flow in a straight

tube. Generally, a fluid flow is laminar in a stiff tube from Re = 0 to some critical value (Re $<$ 2000) at which transition flow begins. Transition flow is fluctuating

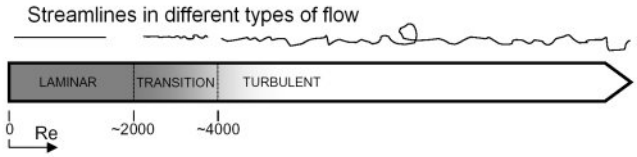

Figure III.4.: Diagram of flow regimes in pipe flow.

between laminar and turbulent flow (2000 $<$ Re $<$ 4000). The fluid flow becomes unstable for higher Reynolds numbers (Re $>$ 4000). In turbulent flow, there is increased mixing that results in viscous losses which are generally much higher than those in laminar flow.[116] The Reynolds number can reach up to 4500 at peak flow in the normal aortic valve.
The Strouhal number gives an indication of a steady or transient regime of the flow. The Strouhal number is defined as

$$\mathrm{Sr} = \frac{\mathrm{D}}{\mathrm{T_p} \cdot \mathrm{U}} \tag{III.16}$$

with T_p the period of time of the observed flow phenomena. A very small Strouhal number (Sr$<<$1) is considered quasi-steady. For Strouhal number close to one the flow is considered transient.

Shear stresses As blood flows through a vessel or valve, it exerts a physical force on the vessel wall or the valve leaflet. This force can be resolved into two principal vectors. Shear stress, being tangential to the wall, represents the frictional

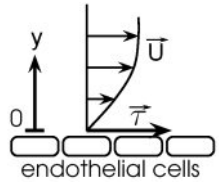

Figure III.5.: Shear stress represents the frictional force exerted by the flowing blood on the endothelial surface of the wall.

force exerted by the flowing blood at the endothelial surface of the wall. The shear stress on the vessel wall or on the valve leaflet is normally called wall shear stress

or WSS. Normal stress, or pressure, is perpendicular to the wall. In case of laminar flow shear stress is calculated with equation III.17.

$$\overrightarrow{\tau}_{\text{laminar}} = \mu \cdot \frac{\partial \overrightarrow{\text{U}}}{\partial \text{y}} = \mu \cdot \dot{\gamma} \qquad \text{[Pa] or [N/m}^2\text{]} \qquad \text{(III.17)}$$

with μ the dynamic viscosity of the fluid, $\overrightarrow{\boldsymbol{U}}$ the velocity vector and $\dot{\gamma}$ the shear rate. Turbulence in the blood system increases resistance to flow, resulting in higher pressure gradients. Turbulent shear stresses are calculated in a slightly different manner, as shown in equation III.18:[44]

$$\overrightarrow{\tau}_{\text{turbulent}} = \mu \cdot \frac{\partial \overrightarrow{\text{U}}}{\partial \text{y}} - \rho \overline{\text{u}'\text{v}'} \qquad \text{(III.18)}$$

with u' and v' the turbulent fluctuations of the velocities u and v respectively.
The vascular and valvular endothelial cells are subjected at all times to shear forces that act on the vessel surface as a result of the flow of viscous blood. Fluid shear stress regulates endothelial phenotype by altering its gene expression profile, including growth factors.[117,118] Fluid shear stress transforms polygonal, cobblestone-shaped endothelial cells of random orientation into fusiform endothelial cells aligned in the direction of flow (figure III.6(b)). High shear stress (>40 N/m^2) can cause direct endothelial injury.[117] Low and oscillating shear stress regions (< 0.4 N/m^2) can lead to atherosclerotic lesions (plaque), mainly in arterial bifurcations and in coronary arteries.[117]
High shear stresses in the blood may create platelet activation[119,120] leading to thrombosis,[121] and the subsequent risk of embolism. Blood platelet damage starts

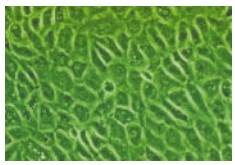

(a) Low arterial haemodynamic shear stress ($\tau \sim$ 0-0.4 N/m^2).[117]

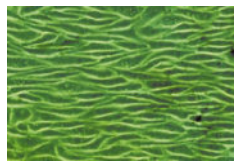

(b) Physiologic arterial haemodynamic shear stress ($\tau >$ 1.5 N/m^2).[117]

Figure III.6.: Transformation of endothelial cell morphology by fluid shear stress: aortic endothelial cells exposed to physiologic shear stress (1.5 N/m^2, right panel) for 24 hours align in the direction of blood flow while those exposed to low shear stress.[117,118]

to occur at shear stress values of 10 N/m^2.[122] Furthermore, the magnitude, exposure time, and spatial distribution of the shear stresses coincide with damage to red blood cells. Shear stresses above 200 N/m^2 will cause hemolysis.[123, 124, 125] Hemolysis can also occur at lower shear stress values if there is a long exposure time.[44, 126] Therefore recirculation zones in prostethic heart valves are to be avoided, unless they are washed out every next heart beat,[127] so that the residence time of particles remains limited. *In vitro* studies of aortic prosthetic heart valve designs have distinctly revealed shear stress values sufficiently high to cause lethal or sublethal damage to blood cells.[128, 129]
Shear stress can not be measured directly *in vitro* nor *in vivo* on a moving heart valve leaflet. For that reason the technique of computational fluid dynamics can be used, to estimate the shear stress.

III.2. *In vitro* measurements

Heart valve studies are often performed based on clinical or animal studies. An *in vitro* setup provides a way to test heart valves in a controlled environment. Furthermore animal studies are minimized due to these models.
A pulse duplicator system PDS[73, 130, 131] is a hydraulic model of the human left heart, connected to a windkessel model of the human systemic circulation.[132] Figure III.7(a) shows an example of PDS of the Hydraulics Laboratory (UGent). As a test fluid, a mixture of 40% glycerine - 60% water is commonly used to simulate the dynamic viscosity of 3.0 mPa.s of the blood. The fluid enters the model from a controllable preload reservoir representing the lungs(9) via 2 rigid pulmonary veins(8). The fluid reaches the left ventricle (LV)(2) through the mitral valve(5). The left ventricle ejects through the aortic valve(15) into the afterload system that consists of an air chamber(16) or 'windkessel' and a hydraulic resistor(13). This air chamber represents the elastic function or compliance of the large arteries. The resistor mimicks the hydraulic function of the arterioles and capillaries. A venous reservoir(12) guarantees a constant venous pressure of 5 mmHg. Both the preload lung (9) and the venous reservoir have an overflow system, with the overflows ending in a central buffer reservoir (11) out of which the test fluid is pumped (10) continuously into the lung reservoir.
The left ventricle is represented by an anatomically shaped silicone sac, mounted in

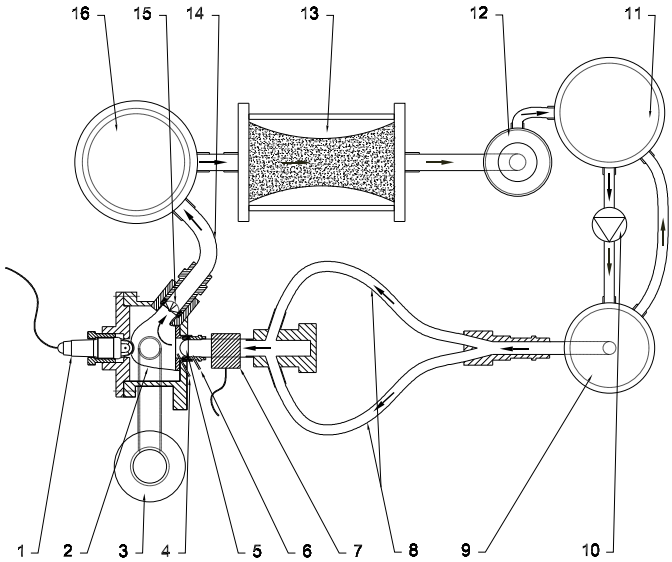

(a) Hydraulics Laboratory Pulse Duplicator System.[130,133]

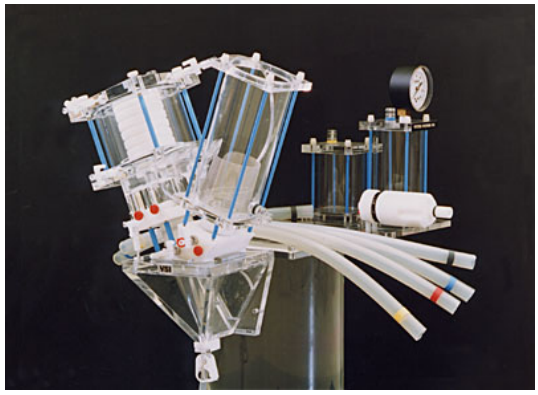

(b) Vivitro Pulse Suplicator System.[131]

Figure III.7.: Pulse duplicator heart models.

a Perspex housing. It is surrounded by water and connected to an external circuit, consisting of Perspex cylindrical reservoirs [(3)]. Pressurized air is delivered to this external circuit and controls the contraction and relaxation of the cardiac chamber. The PDS is computer controlled: a target left ventricular pressure curve is sent to the computer system and a feed-back system controls the amount of pressurized air delivered to the system such that the target curve is respected as closely as possible.[130,133] Physiological parameters such as the heart rate, the stroke volume and

the pressure levels can be varied with these PDS systems. A picture of a comparable commercially available system is shown in figure III.7(b).[131] These artificial heart models can be used to test different types and sizes of artificial heart valves. Pressure, flow and even Doppler measurements[130,133] made with these systems make it possible to estimate the hydrodynamic performance of artificial heart valves in a controllable *in vitro* environment.[134,135]

III.3. Results from clinical and experimental heart valve studies

The following section gives a short overview of some clinical and experimental studies. It is not the intention to give a detailed literature study, but to give the reader an idea of heart valves examinations and how these heart valves will perform.

III.3.1. Pressure gradient in experimental and clinical studies

Results[73] from *in vitro* experiments done by Feng et al[73] are displayed in figure III.8(a). The SJM HP (St. Jude Medical Hemodynamic Plus) and On-X valves produced the lowest mean positive pressure drop, and the CM (CarboMedics) valve produced the highest under every condition. The differences in these pressure drops were related to the geometric orifice diameter and the degree of valve opening. That the On-X valve produces the smallest pressure drop is mainly due to its larger internal orifice diameter and the parallel opening of its leaflets. The SJM HP valve also benefits from a larger internal orifice diameter and a large opening angle. The ATS valve has a lower mean positive pressure drop than the CM valve in pulsatile flow despite the findings that its maximal opening angle is less than that of the CM valve. Furthermore, it can be observed from figure III.8(a), that the pressure drop over the valves increases with the cardiac output.

In the clinical setting, this maximum pressure gradient cannot be measured invasively because it is not possible to position a catheter across or between mechanical prosthetic valve leaflets in patients.[136] Doppler gradients across the central orifices are significantly higher than the transvalvular and net catheter pressure gradients measured across the valve (figure III.8(b)). These differences are due to downstream pressure recovery (figure III.8(c)).[136,137] This pressure recovery is demonstrated in

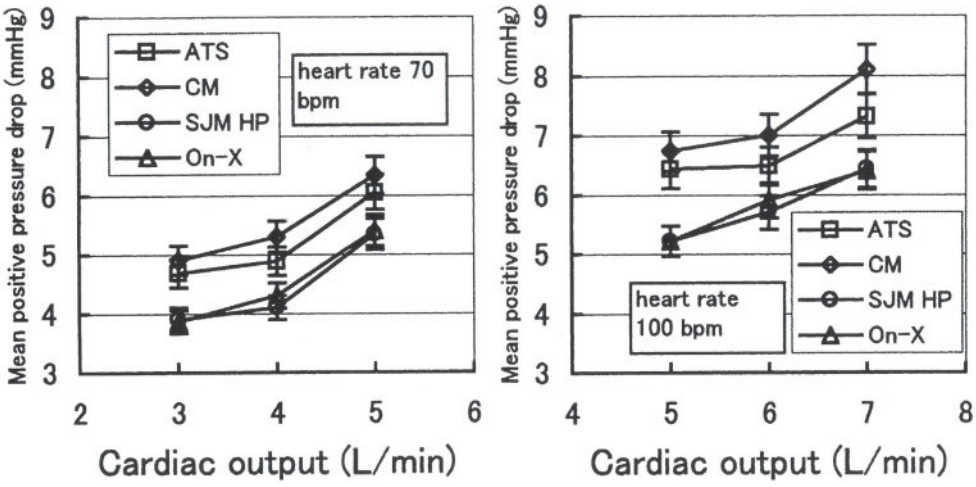

(a) Example of pressure gradient measurements.[73]

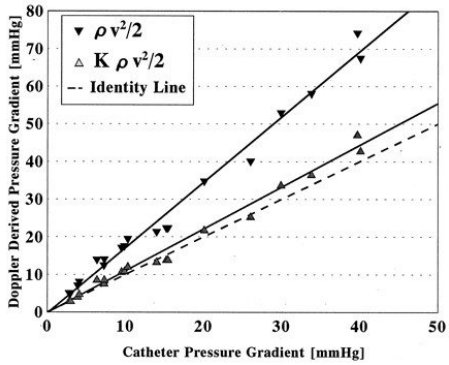

(b) Correlation between catheter transvalvular pressure gradients and Doppler-derived pressure gradients without and with incorporating a pressure loss coefficient K=0.64 in the simplified Bernoulli equation.[136]

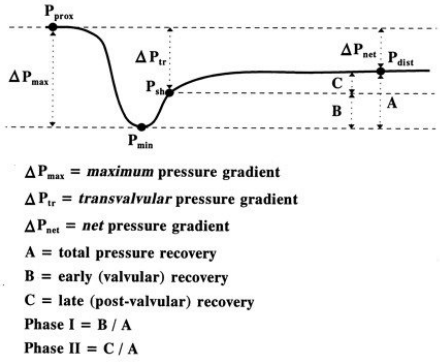

(c) Schematic representation of a centerline pressure profile showing the locations where pressures were read out for comparison; this also illustrates the calculations of maximum, net, and transvalvular pressure gradients as well as the two phases of downstream pressure recovery.[136]

Figure III.8.: Pressure gradient.

figure III.8(c), which gives the pressure at a certain time along the axis of the valve. The pressure shows a drop, but recovers at a certain distance downstream the valve, due to conversion of kinetic energy into potential energy upon deceleration of the flow through the valve.

III.3.2. Effective orifice area

Many clinical and experimental studies are done in order to estimate the EOA. From the EOA one can calculate the performance index PI and this provides clinicians and engineers of a way to compare different types of heart valves. The higher the PI, the better the hydrodynamic performance is of the studied heart valve. This means the contraction of the flow through the valve is minimized and the flow utilizes a high percentage of the available geometric orifice area. Bech-Hanssen et al. showed similar effective orifice areas *in vitro* for St Jude Medical and Omnicarbon valves (figure III.9).[138]

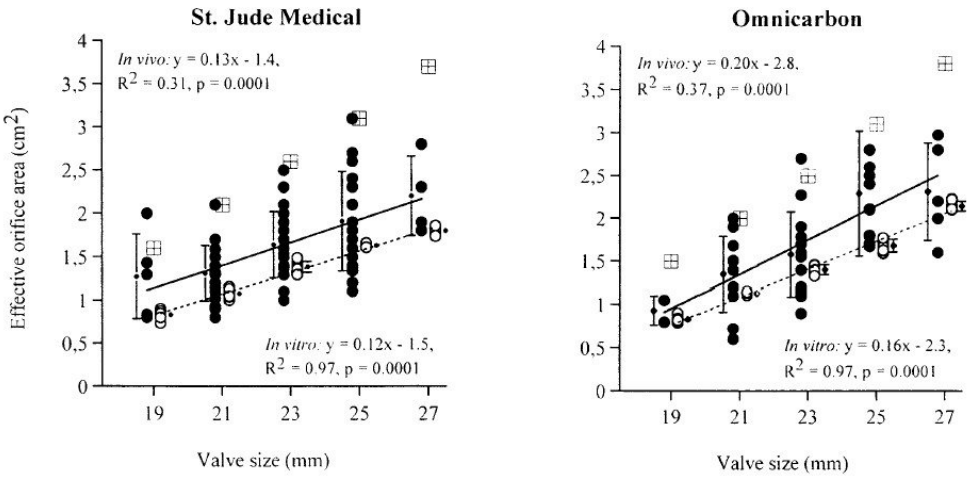

Figure III.9.: Effective orifice area of two different mechanical valve types.[138] Results are shown for the *in vivo* (black o) and *in vitro* (open o) studies. Bars indicate mean ± SD. Boxes show the geometric orifice area.

III.3.3. Regurgitation

Figure III.10 gives an example of data on regurgitation of different types of bileaflet valves.[73] As reported by Wu et al.,[139] the closing volume - expressed as a percentage of the forward flow volume - increased with decreasing cardiac output. The closing volumes shown in figure III.10 of the valves are within the acceptable range ($<8\%$).[73] The SJM HP valve under the low cardiac output condition at 100 bpm showed a somewhat higher closing volume of 11.4%.

Closing volume is believed to be proportional to opening angle of the mechanical heart valve (figures II.7(a) and III.10).[73] We refer to table II.1 which summarizes

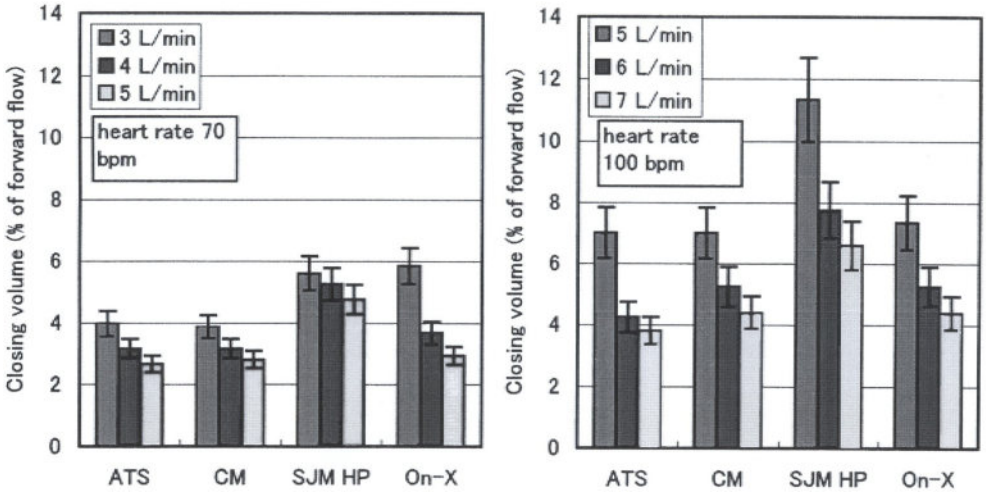

Figure III.10.: Closing volumes of different bileaflet heart valves (ATS: Advancing The Standard, CM: Carbomedics, SJM HP: St. Jude Medical Hemodynamic Plus, On-X) studied in mitral position in an experimental setup at 70 beats/min and at 100 beats/min.[73]

the maximum and observed opening and travel angles of mechanical bileaflet valves used in their study. Figure II.7(a) defines the opening and travel angle of a bileaflet valve. One can see that the SJM HP valve presents the maximum opening angle as well as, consistently, the largest closing volume, under each drive condition. Correspondingly, the smaller opening angles for the CM and ATS valves gave rise to the smallest closing volumes. Although the On-X valve has a parallel-opening leaflet design (opening angle of 90°), the closing volume remained low because the actual non-fully open and the original small travel angle design minimizes the volume that is swept during closure. As a result, the On-X valve generally presents as small a closing volume as does the CM valve.[73]

III.3.4. Flow patterns and shear stresses

The caged ball valve Natural heart valves allow blood to flow straight through the center of the valve. This property, known as central flow, keeps the amount of work done by the heart to a minimum. With non-central flow, the heart works harder to compensate for momentum lost to change the direction of the fluid. Caged-ball valves completely block central flow (figure III.11(a)); blood therefore requires more energy to flow around the occluder. In addition, collisions with the occluder ball caused damage to blood cells. Caged-ball valves are also notorious for stimulating thrombosis, requiring patients to take lifelong prescriptions of anticoagulants.

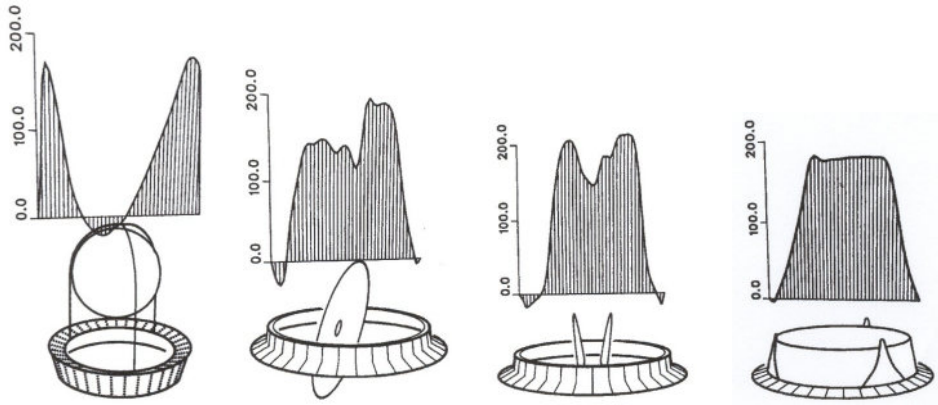

(a) Caged ball valve. (b) Tilting disc valve. (c) Bileaflet valve. (d) Bioprosthesis.

Figure III.11.: Velocity profiles in cm/s based on *in vitro* measurements on 27 mm aortic valve designs. Measurements were done downstream the valve on a centerline at peak systole, at a cardiac output of 6 l/min and a heart rate of 70 beats/min.[55]

High turbulent shear are observed at the edges of the jet (figure III.12(a)). The intensity of turbulence during peak systole does not decay very rapidly downstream of the valve. Elevated shear stresses occurred during most of systole.[55] This type of valve is no longer used in patients nowadays.

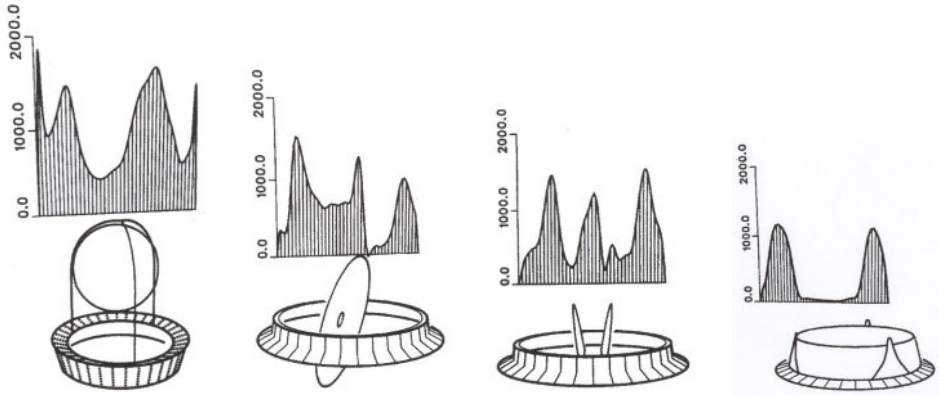

(a) Caged ball valve. (b) Tilting disc valve. (c) Bileaflet valve. (d) Bioprosthesis.

Figure III.12.: Turbulent shear stress profiles in $0.1 \cdot N/m^2$ based on *in vitro* measurements on 27 mm aortic valve designs. Measurements were done downstream the valve on a centerline at peak systole, at a cardiac output of 6 l/min and a heart rate of 70 beats/min.[55]

The monoleaflet tilting disc valve This valve design allows more central flow while still preventing backflow. However, flow is not completely central (figure III.11(b)), because the blood has to make a significant directional change to flow

around the occluder disc. Newer models of monoleaflet valve improves this shortcoming.
In the major orifice region (figure III.12(b)), high turbulent shear stresses are confined to narrow regions at the edges of the major orifice jet. During the acceleration and deceleration phases the turbulent shear stresses are relatively low.[55] High turbulent shear stresses are more dispersed in the minor orifice than those in the major orifice regions as shown in figure III.12(b).

The bileaflet valve These valves provide the closest approximation to central flow yet achieved in a mechanical heart valve (figure III.11(c)). The two leaflets block flow to some extent, leading to a three-part flow pattern. High turbulent shear stresses occure at locations immediately distal to the valve leaflets[55] (figure III.12(c)).

Biological valves Biological valves, optimally mimick native heart valves and provide nice central flow (figure III.11(d)).Turbulent shear stress measurements during deceleration phase showed low shear stresses spread out over a wide region.[55] During peak systole, the high turbulent shear stresses were confined in a narrow region (figure III.12(d)).

III.4. Computational fluid dynamics and fluid-structure interaction of heart valves

With the advent of high speed computers and the development of computational fluid dynamic (CFD) analysis algorithms, fluid dynamic simulation of the valve function provides a viable alternative for the detailed analysis of the haemodynamics of prosthetic heart valves. Recently, realistic simulations have become possible, modeling the leaflet motion including the fluid-structure interaction (FSI)[140, 141, 142] during the opening and closing phases. These new fluid-structure interaction (FSI) algorithms will be a major engineering tool available to unravel the haemodynamics associated with thrombolitic and hemolytic events of existing and new prosthetic heart valves. Within the context of clinical application, stenotic and/or incompetent valve performance can be studied with respect to the associated medical complications using computational models.[29, 30, 81, 143] In general, these models can be used

to study and resolve problems associated with failure and medical complications of diseased valves and currently used prosthetic devices.[29,30,81,143]

III.4.1. Computational fluid dynamics

Computational Fluid Dynamics is the analysis of systems involving fluid flow, heat transfer and associated phenomena such as chemical reactions by means of computer-based simulation. The technique is very powerful and spans a wide range of industrial and non-industrial application areas. Increasingly CFD is becoming a vital component in the design of industrial products and processes.[144]
The equations governing the fluid flow problem are the continuity (conservation of mass) and the Navier-Stokes (conservation of momentum). These equations form a system of coupled non-linear partial differential equations (PDEs). Because of the non-linear terms in these PDEs, analytical methods can yield very few solutions. CFD is the art of replacing the differential equation governing the fluid flow, with a set of algebraic equations (the process is called discretization), which in turn can be solved with the aid of a digital computer to get an approximate solution. The well known discretization methods used in CFD are Finite Difference Method (FDM), Finite Volume Method (FVM) and Finite Element Method (FEM). A thorough explanation of these techniques falls beyond the scope of this work.

III.4.2. Fluid-structure interaction methods

Fluid-structure interaction or FSI involves the dynamic interaction between an elastic deformable structure and a fluid. This computational technique can be used for studying biofluid dynamics problems, e.g. the coupled motion of the blood filling the ventricles of the heart, the muscles of the heart wall, and the leaflets of the cardiac valves.[29,145,142]
There are different ways to tackle a coupled interaction problem. One possibility is to develop new software and solution methods for each of these coupled applications. This is referred to as a monolithical approach,[146] or sometimes as the direct method.[147] On the other hand, one may assume that the methods and software systems which have been developed for either fluid or structural applications will continue to be used separately. Therefore we consider partitioned methods[148] - also known as iterative methods[147] for fluid-structure interaction, i.e. separate solvers

are used for the fluid and the structure.[149]
Furthermore, different numerical methods have been developed to tackle the complex FSI problems: the Immersed Boundary Method, the Fictitious Domain Method and Arbitrary Lagragian Eulerian or ALE based FSI Method.

III.4.2.1. Immersed boundary method

In designing the original immersed boundary method, Peskin[145] realized the advantages of describing the fluid variables and the immersed objects in different ways. The fluid variables are described in what is known as an *Eulerian* manner. One focuses on each point in space and asks how the fluid variables change with time at that point in space. On the other hand, the objects are described in what is called a *Lagrangian* manner. The location of each material point is tracked as time advances and the system evolves. The state of the system at any time is given by the fluid velocity and pressure fields, and by the locations of the Lagrangian points which constitute the immersed objects. The essence of how the Immersed Boundary method computes the change in the system over a short time interval (or timestep) is as follows: from the Lagrangian description of each immersed object, it is determined how much the object has been deformed at the beginning of the timestep, and from this elastic forces generated within the object are calculated. Since the object is in direct contact with the fluid, these forces affect the fluid motion. To calculate the effect of these forces on the fluid, they are transmitted from the elastic objects to the fluid, and their contribution is added in the fluid dynamics equations which drives the fluid motion.

III.4.2.2. Fictitious domain method

The fictitious domain (FD) method is based on the imposition of velocity constraints associated with rigid internal boundaries by means of Lagrange multipliers.[150,151] It has similarities with the so-called immersed boundary technique of Peskin and McQueen,[145] in which at a number of control points (at the intersection of fluid and solid), tension forces are imposed pointwise and distributed to neighboring nodes. It gained popularity to solve the fluid-structure interaction of the flexible aortic heart valve over the last years. De Hart et al.[29,30,81] studied a 3D model of the aortic valve with this method. However, the accuracy of the pressure and wall shear stress in the

vicinity of the solid is poor. Therefore, a mesh adaptation algorithm is applied, which locally adapts the fluid mesh to the position of the solid mesh every time step.[152]

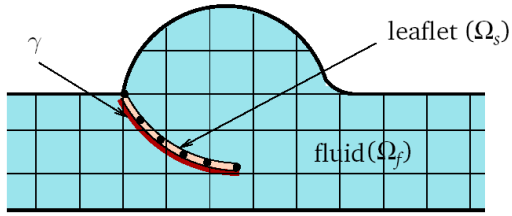

(a) Traditional fictitious domain mesh: alignment of interface with the structure, which is positioned arbitrarily in the fluid mesh.[29]

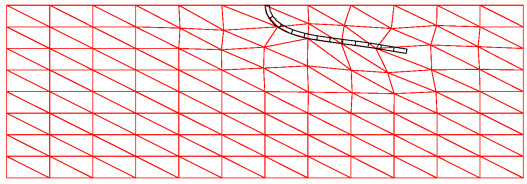

(b) Adaptation of the fluid mesh by shifting nodes.[152]

Figure III.13.: The fictitious domain method.

III.4.2.3. Remeshing methods combined with arbitrary Lagrangian Eulerian method

In an Eulerian setting, the fluid is described using a fixed mesh. The Lagrangian formulation is what we normally associate with FEM for structural mechanics. It is a formulation where the numerical grid follows the motion of the material. Each element represents the same piece of material through out the whole simulation. This method is suitable for solid structures undergoing limited deformations. Severely distorted elements can lead to bad or non-useful results. The applicability of the Lagrangian formulation is somewhat limited in general applications involving gases and liquids. However, the Eulerian and Lagrangian formulations are, at first sight incompatible.

The arbitrary Lagrangian-Eulerian (ALE) formulation,[153,154] effectively combines these two formulations and is often applied for fluid-structure interaction simulations. In the arbitrary Lagrangian-Eulerian (ALE) method, the computational mesh

is allowed to move in space in an arbitrary way conform to the body motion.[155] Fig-

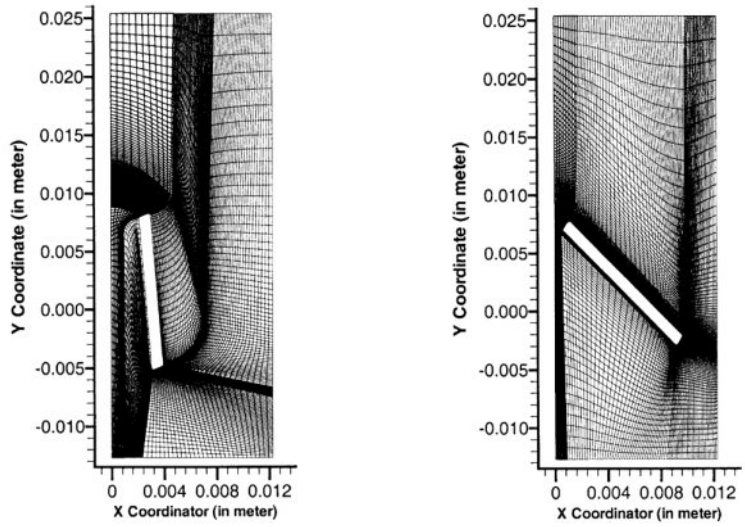

Figure III.14.: Computational mesh for closure dynamic simulation: Mesh for fully open position and with the leaflet at 27.21°.[141]

ure III.14 demonstrates that it requires a continuous adaptation of the mesh without modification of the mesh topology.

III.4.3. Numerical modeling of heart valves

III.4.3.1. Mechanical heart valve modeling

Several studies have been reported on the computation of recirculation regions[127,156] and wall shear stresses in the clearance region[157] with the leaflets of the mechanical valve in a fixed position (figure III.15).[158,159,160] These studies neglected the interplay between the flow field and the leaflet motion. In other studies, however, the fluid flow has been coupled to the leaflet motion from the fully open to closed position using prescribed valve motion in a simplified flow domain.[155] Such a specification avoids the complex problem of the leaflet-fluid interaction during the valve closure.

One of the important requirements of an accurate simulation of valve function is the development of a validated fluid-structure interaction (FSI) algorithm for the prediction of the leaflet motion resulting from the fluid stresses acting on that same leaflet. Several attempts on the development of a FSI algorithm for mechanical heart valve function have been reported recently. These studies have been restricted to two-

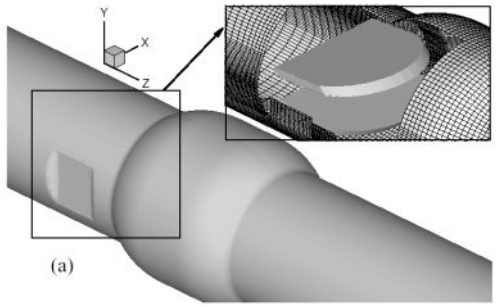

Figure III.15.: Geometry and coordinate definitions of the modeled bileaflet mechanical heart valve: the symmetric aorta with the inset showing the two leaflets. Calculations are carried out for the full three-dimensional valve geometry under steady inflow conditions.[158]

dimensional analysis (figure III.14)[51,141] with the leaflets in the closed position and a complete three-dimensional FSI algorithm for valve functional simulation is yet to be developed.

These simulations can be used to analyze the details of the fluid dynamic stresses in the regions of interest with the mechanical valve prostheses where detailed experimental measurements are impractical. Leaflet behavior and variations of shear stresses with time and space can also be obtained. Also the regurgitation flows can be calculated. The maximum shear stress, an important issue for valve haemodynamic analysis, has been found in the vicinity of the contact point where a leaflet contacts with housing in the final stage of the closing phase.[51,141] Such regions include the peripheral clearance region between the leaflet edge and the valve housing as well as the hinge area where the leaflets and the housing interact.

III.4.3.2. Bioprosthesic heart valve modeling

Many numerical structural models have been developed that describe the behavior of the aortic valve ignoring its interaction with the blood.[161,162,163,164,165] The opening and closing behavior of this valve during systole involves, however, a strong interaction between blood and the surrounding tissue. Several attempts have been made to analyze the valve kinematics using numerical fluid-structure interaction models. Horsten et al.[167] modeled the interaction of a two-dimensional leaflet with a rigid channel flow. Peskin and McQueen et al.[145] developed a three-dimensional model including the surrounding vessel walls (figure III.16(a)). However, these models used simplified descriptions for the structures and were only applicable for relatively low, non-physiological Reynolds numbers. Fluid-structure simulation of

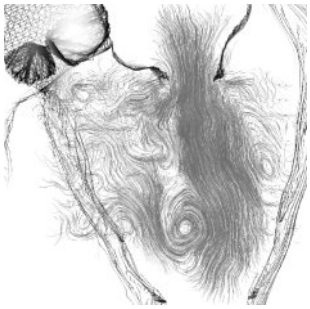

(a) Section through the model left ventricle showing streamlines of ventricular filling. The closed aortic valve is at the top left side, and the open mitral valve is at the top right.[145]

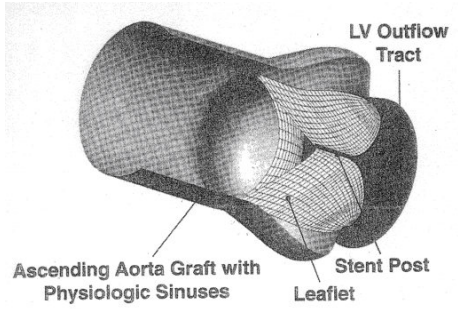

(b) Three-dimensional coupled fluid-structure simulation of pericardial bioprosthetic aortic valve function.[166]

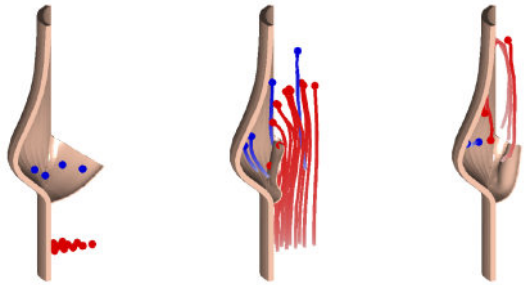

(c) A three-dimensional analysis of a fiber-reinforced aortic valve prosthesis.[30,81,143]

Figure III.16.: Fluid-structure interaction modeling of bioprosthesic heart valves.

a bioprosthetic aortic valve functioning is performed by Makhijani et al. (figure III.16(b)),[166] where the leaflet structure has a much higher resistance to bending compared to the natural leaflets. A physiological more realistic fluid-structure interaction model of the natural valve (figure III.16(c)), accounting for the phenomena occurring during systolic phase, has been developed by De Hart et al.[30,81,143]

In case of bioprosthetic valves, these simulations can be used to compute the magnitude and the location of regions of high stress and shear concentrations where structural disintegration of the leaflets is suspected. Design parameters, such as commissural height, free edge length, leaflet/root fixation, leaflet fiber-reinforcement, sinus depth and height, and aortic root compliance, can computationally be optimized depending on the patients characteristics.[7]

Conclusion

With this introductory part, we have tried to provide sufficient background that should allow the reader to situate the following chapters, containing new contributions to the field of heart valve research.
In this thesis different types of mechanical heart valves have been studied using experimental and numerical models. The On-X bileaflet mitral valve and the Omnicarbon monoleaflet aortic valve were tested with the pulse duplicator of the Hydraulics Laboratory (UGent). Furthermore a prototype of a bioreactor pulse duplicator system has been developed for the testing and creation of a tissue engineered heart valve.
A numerical model for the simulation of mechanical heart valves was developed and validated for a 2D aortic valve model. The model is based on the commercial Fluent software, which uses the finite volume method. The software uses a dynamic mesh model based on the ALE and local remeshing to adapt the mesh in FSI problems. Therefore we developed a partitioned method or iterative methods for fluid-structure interaction. The model has been used for the 3D modeling of the ATS Open Pivot heart valve.
Finally, a 2D FSI model of flexible heart valve has been developed. We believe that this model has great potential for helping to set up a protocol for the growing of a Tissue Engineered heart valve construct.

Part B.

In vitro studies of heart valves

Chapter IV

Mock loop testing of On-X® prosthetic mitral valve with Doppler echocardiography

The contents of this chapter is published in Artif Organs 2002;26(10), 872-878.
Mock loop testing of On-X® prosthetic mitral valve with Doppler echocardiography
Verdonck P, Dumont K, Segers P, Vandenberghe S, Van Nooten G

Abstract

Previous *in vitro* testing mainly in aortic position and clinical experience often based on Doppler echocardiographic observations demonstrated an excellent haemodynamic behavior of the On-X valve. However, integrative studies including simultaneous haemodynamic pressure and flow measurements and Doppler echocardiography are lacking. Using our computer controlled mock loop system, two samples of the Mitral 27/29 and one sample of the Conform-X Mitral 25/33 are tested in mitral position. Data include transvalvular pressure gradient and flow as well as transthoracic Doppler echocardiography. The valves were tested in 3 pressure conditions (ventricular systolic pressure of 100, 130, and 160 mmHg) at three different heart rates (60, 100, and 140 beats/min). In addition, ventricular pressure conditions simulating fibrillation were imposed. Both valve types show similar hydrodynamic characteristics and have an effective orifice area of 2.1 cm^2 and a performance index of 0.56 for a cardiac output of 3.5 l/min. Regurgitant volumes remain below 6 ml.

IV.1. Introduction

Previous *in vitro* testing[69, 70, 71, 168, 169] of the On-X prosthetic heart valve (figure IV.1), mainly in aortic position and Doppler echocardiography based observations in clinical practice demonstrated excellent hydrodynamic characteristics of the valve. Typical design characteristics of the On-X valve are a shaped orifice with flared inlet design to reduce inlet turbulence, an elongated body to reduce exit losses, thinner leaflets, and a supra-annular sewing ring for small aortic valves.[69, 70, 71] The main effect of its design is an enlarged valve area available for flow, as compared to other equally sized prosthetic valves.

Integrative studies on the On-X mitral valve, linking transvalvular Doppler echocardiographic flow velocity measurements to transvalvular volume flow and pressure gradients are lacking. Therefore, the aim of this study was to perform hydrodynamic tests of the On-X valve in mitral position in a mock loop in mitral position using both standard hydrodynamic measurements (pressure and flow) as well as Doppler echocardiography.[130, 133]

IV.2. Materials and methods

IV.2.1. Valves tested

Three valves were provided by the manufacturer (Medical Carbon Research Institute MCRI^{TM}, LLC, Address: 8200 Cameron Road, A-196, Austin, TX 78754,

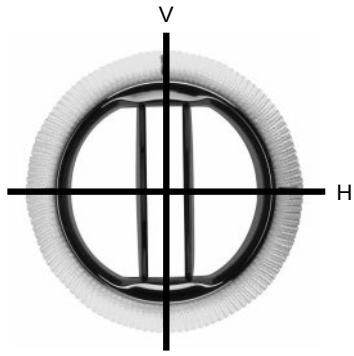

Figure IV.1.: Top view of an On-X prosthetic heart valve with indication of the scan-planes of the Doppler probe (V: vertical, H: horizontal).

USA) for *in vitro* testing: two On-X Mitral 27/29 (valve A and C) and one On-X Conform-X Mitral 25/33 (valve B). The Conform-X type is a newer valve type with a modified sewing ring. It is a "one size fits all" valve, suitable for orifice areas of 25 to 33 mm. The other valves are standard On-X valves for orifices of 27 to 29 mm. The geometric orifice area of these 3 valves is the same, as well as the travel angle of 50°.[169] Dimensions of the valves are given in table IV.1.

Table IV.1.: On-X valve specifications.

On-X cardiac valve specifications [mm]					
Valve Size Descriptor	Tissue annulus Diameter	Internal annulus	Geometric orifice diameter: OD_{mean}	Disc height at hinge: $h_{leaflet}$	Disc thickness: $\Delta_{leaflet}$
27/29	25	23.40	21.80	20.60	0.86
Conform 25/33	27	23.40	21.80	20.60	0.86

On-X cardiac valve areas [cm^2]		
Valve size descriptor	Geometric orifice area (OA)	Orifice area without disc
27/29	3.74	4.10
Conform 25/33	3.74	4.10

IV.2.2. Pulse Duplicator System: measuring haemodynamic data and transthoracic visualization of transmitral flow.[130,133,170]

The valves were mounted in our pulse duplicator system (PDS) in mitral position (figure IV.2; note that the numbers between brackets $^{(\ldots)}$ refer to the numbers in the figure). The PDS is a hydraulic model of the human left heart,[130,133] connected to a windkessel model of the human systemic circulation.[132] The test fluid (40% glycerine - 60% water mixture with a dynamic viscosity of 3.0 mPa.s) enters the model from a controllable preload reservoir representing the lungs $^{(9)}$ via 2 rigid pulmonary veins $^{(8)}$. The fluid reaches the left ventricle (LV) $^{(2)}$ through the mitral valve $^{(5)}$. The left ventricle ejects through the aortic valve $^{(15)}$ (bioprosthesis) into the afterload system that consists of an air chamber $^{(16)}$ or 'windkessel' and a hydraulic resistor $^{(13)}$. A venous reservoir $^{(12)}$ guarantees a constant venous pressure of 5 mmHg. Both the preload lung $^{(9)}$ and the venous reservoir have an overflow

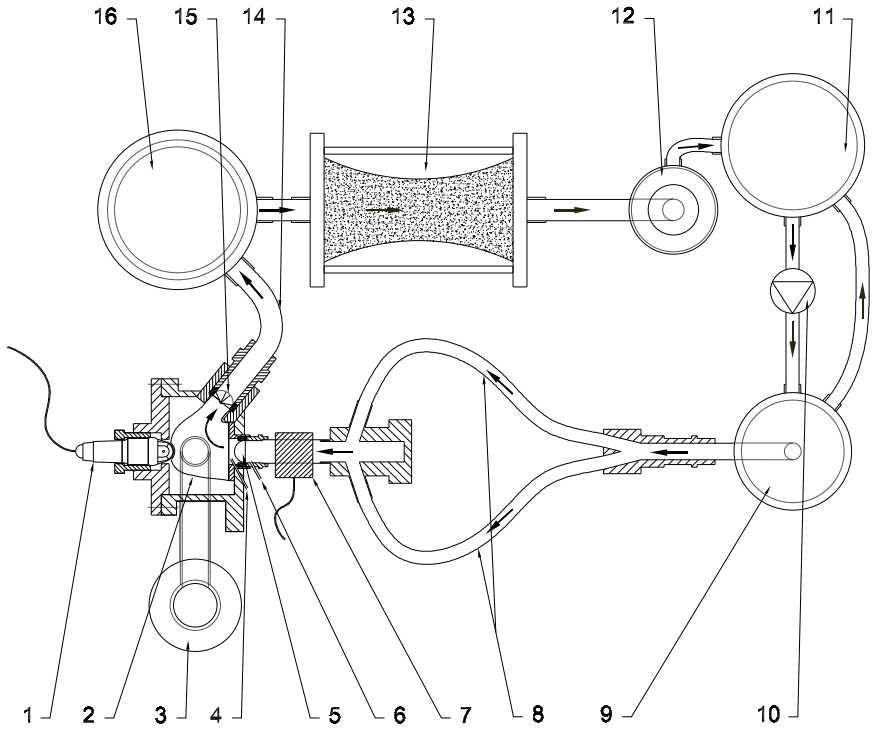

Figure IV.2.: Pulse Duplicator System: measuring haemodynamic data and transthoracic Doppler echocardiographic data.

system, with the overflows ending in a central buffer reservoir (11) out of which the test fluid is pumped (10) continuously into the lung reservoir.

The left ventricle is an anatomically shaped silicone sac, mounted in a Perspex housing. It is surrounded by water and connected to an external circuit, consisting of Perspex cylindrical reservoirs (3). Pressurized air is delivered to this external circuit and controls the contraction and relaxation of the cardiac chamber. The PDS is computer controlled: a target left ventricular pressure curve is sent to the system and the feed-back system controls the amount of pressurized air delivered to the system such that the target curve is respected as closely as possible.[130,133]

Left ventricular pressure was measured with a 6 French pigtail catheter inserted in the LV via an access port (4), 3 cm distal to the valve. Left atrial (LA) pressure was measured 3 cm proximal to the valve via a short cannula (6). Both were then connected to a piezo-electric pressure transducer (Ohmeda, Ghent, Belgium). In

this setting, transmitral flow velocities could be visualized with a 3.25 MHz ultrasound probe mounted in position (1) (figure IV.1). This viewpoint corresponds to the *in vivo* transthoracic apical window. Volume flow was measured with an ultrasonic flow meter (7) (H16C flow probe, Transonic Systems Inc., Ithaca, NY, USA) mounted on the rigid tube (figure IV.2).
Valves were tested at 60, 100, and 140 beats/min and for 3 levels of LV systolic pressure (100 mmHg, 130 mmHg, and 160 mmHg). We further applied an irregular LV target pressure to study valve dynamics in simulated conditions of ventricular fibrillation.

IV.2.3. Haemodynamic data and transthoracic flow visualization

IV.2.3.1. Parameters derived from the haemodynamic data

Data were measured with the PDS and consist of pressures upstream (atrial) and downstream (ventricular) of the valve, and transvalvular flow with the Transonic flow probe mounted on the rigid atrial inflow. Data were sampled using Labview Software and a multifunction National Instruments data acquisition card (PCI 6024E, National Instruments, Texas, USA) also used for controlling the pulse duplicator system. For all heart rates, 1024 samples were taken at 200 Hz. After calibration of pressure and flow, one averaged cycle was calculated, further used for subsequent analysis. Figure IV.3(a) shows an example of averaged LA and LV pressure and according flow cycle. The data shown in figure IV.3(a) are signals filtered by use of a low-pass filter. This has no effect on calculated indices, as they were derived from mean pressure values which are not affected by the filter. All data have been analyzed and parameters derived using customized software, written in Matlab (Matlab 5.3, The Mathworks, Inc., Natick, MA, USA). LV systolic pressure (PLV_{sys} [mmHg]) is the maximum value of LV pressure. Cardiac output (CO [l/min]) was calculated as the average of the flow wave. Systolic and diastolic periods were determined from the flow curve as the periods of backward (regurgitation) and forward flow, respectively. Mean forward flow ($Q_{fwd,mean}$ [ml/s]) was calculated as the ratio of the "positive" area under the flow curve (forward stroke volume SV_{fwd}) divided by the duration of forward flow. Regurgitant volume (V_{reg} [ml]) is the "negative" area under the flow curve. V_{reg} is further split into the closing volume (V_{close}) and the leak volume (V_{leak}), based on visual identification of the inflection

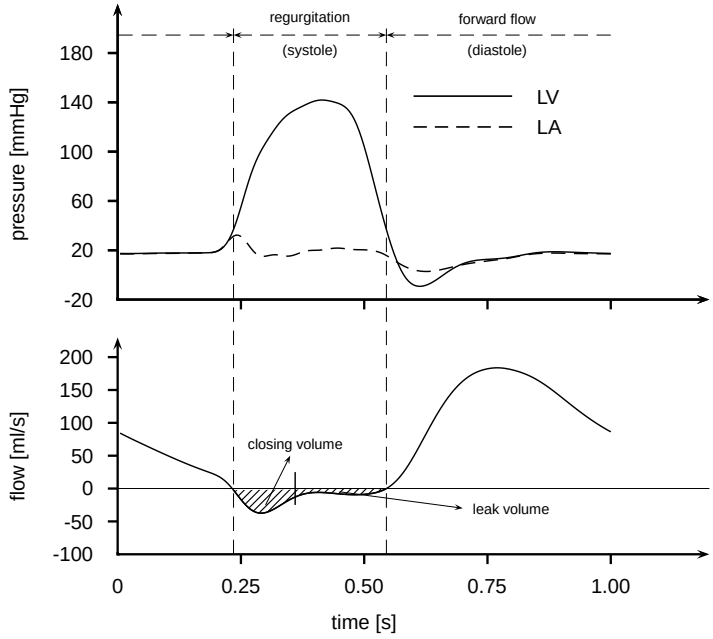

(a) Averaged Pressure and Flow Cycle

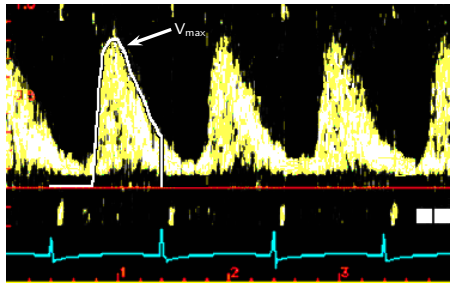

(b) Continuous Wave Doppler Measurement

Figure IV.3.: (a) Example of an averaged pressure and flow cycle for a bileaflet valve, measured at 60 beats/min, (b) velocity contour and maximum velocity (V_{max}) drawn manually on Continuous Wave Doppler Data.

point in the flow signal (figure IV.3). The pressure difference (ΔP [mmHg]) is the instantaneous difference of LA and LV pressure. The mean ($\Delta P_{fwd,mean}$) value during systole has been derived.

IV.2.3.2. Parameters derived from the transthoracic flow velocity measurements

The valve and transmitral flow were visualized using the 2D ultrasound echo (2D), Continuous Wave Doppler (CW), Colour M-mode (CMM) and 2D colour flow (2D colour) modalities on the Vingmed CFM 800 machine with the 3.25 MHz cardiac probe in the transthoracic window and a vertical scan plane (indicated as "V" in figure IV.1). Velocities (CW) were measured with the scan line through the center of the valve. All data were stored on videotape and a colour M-mode and continuous wave Doppler image were digitally stored on optical disc for off-line analysis. Doppler data were analyzed using the Vingmed CFM 800 on-board data analysis software package (EchoPAC 5.4.4, GE Vingmed). The images allowed analyzing the forward flow through the mitral valve. The maximum velocity contour was manually traced (figure IV.3(b)), with the area under the curve yielding the velocity time integral (VTI [cm]). The onset of the forward mitral inflow was taken as the point where the extrapolated slope of the early filling phase crossed the time axis. The end of filling was determined by the ECG signal, indicating the onset of ventricular contraction (and thus the end of diastole). The software further gives maximum (V_{max} [m/s]) and mean velocity (V_{mean} [m/s]) during forward flow. For each condition, three cardiac cycles were analyzed. All values given in the text are averaged.

IV.2.3.3. Valve performance indices derived from haemodynamic and echocardiographic data

The percentage of regurgitation (% reg) is calculated as

$$\%reg = \frac{V_{reg}}{(V_{reg} + SV_{fwd)}} \tag{IV.1}$$

The effective orifice area (EOA [cm^2]) is calculated - based on the continuity equation - as the ratio of forward stroke volume and VTI:

$$EOA = \frac{SV_{fwd}}{VTI} \tag{IV.2}$$

The performance index (PI [-]) of the valve is calculated as the ratio of the effective orifice area (EOA) and the geometric orifice area (OA):

$$PI = \frac{EOA}{OA} \tag{IV.3}$$

The mean Doppler velocity and the simplified Bernoulli equation are used to calculate an estimated value of the forward pressure difference ($\Delta P_{Doppler}$):

$$\Delta P_{Doppler} = 4 \cdot V_{mean}^2 \tag{IV.4}$$

Besides the continuity equation, the Gorlin equation provides an alternative way to calculate the effective orifice area (EOA_{Gorlin}). The Gorlin equation is based on the fundamental hydraulic law of flow through an orifice and couples the flow through the valve orifice to the Doppler pressure gradient over the valve. With mean flow through the valve $Q_{fwd,mean}$ expressed in [ml/s] and Doppler gradients $\Delta P_{Doppler}$ expressed in [mmHg], the general formulation is given as:

$$EOA_{Gorlin} = \frac{Q_{fwd,mean}}{51.6 \cdot \sqrt{\Delta P_{Doppler}}} \tag{IV.5}$$

EOA_{Gorlin} is a fraction θ of the available geometric orifice area OA, with θ known as the orifice constant. The constant 51.6 is obtained from $\sqrt{2 \cdot 981} \cdot \sqrt{1.36}$, with 981 being the gravity constant in cm/s^2 and 1.36 resulting from converting cmH_2O into mmHg.
It is clear that the orifice constant θ is comparable to the performance index PI.

IV.3. Results

For all valves and heart rates, PLV_{sys} was regulated to 3 different levels (100, 130, and 160 mmHg). To process the data, we pooled the data obtained at the different pressure levels, yielding an average PLV_{sys} of 129 ± 22 mmHg. Cardiac output throughout these experiments was in the range 3.0 - 4.1 l/min (average value 3.54 ± 0.28 l/min). $\Delta P_{fwd,mean}$ was 1.4 ± 1.2 mmHg for $Q_{fwd,mean}$ of 88 ± 10 ml/s. Transthoracic Doppler-data are summarized in figure IV.4, showing V_{max} (figure IV.4(a)), V_{mean} (figure IV.4(b)) and VTI (figure IV.4(c)). V_{mean} is about constant for the different pressure and heart rate settings (as expected seen the relatively

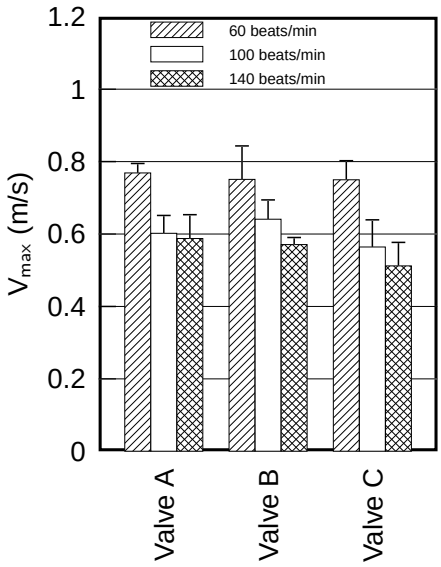

(a) Mean value and standard deviation of maximum velocity (V_{max}).

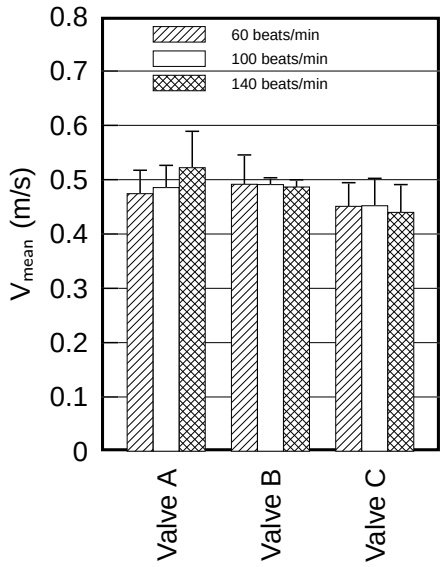

(b) Mean value and standard deviation of mean velocity (V_{mean}).

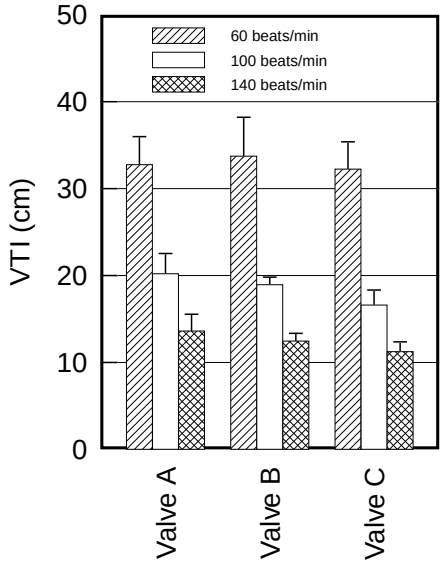

(c) Mean value and standard deviation of velocity time integral (VTI).

Figure IV.4.: Velocity data for three samples (A, B, C) of the On-X valve in mitral position, for three heart rates (60, 100, and 140 beats/min), and averaged for the different pressure levels.

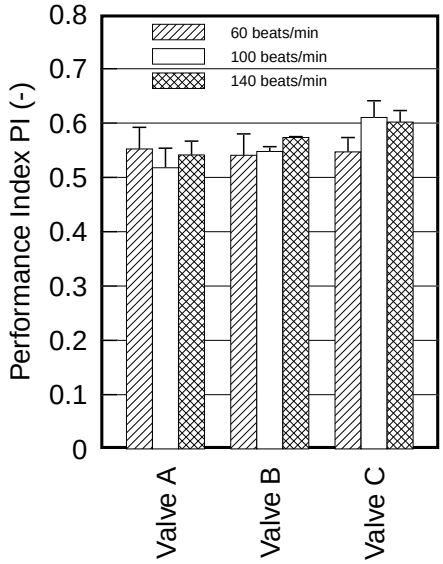

Figure IV.5.: Mean value and standard deviation of the performance index (PI) for On-X valve in mitral position for three samples (A, B, C), three heart rates (60, 100, and 140 beats/min), and averaged for the different pressure levels.

constant cardiac output), but V_{max} tends to be lower for the higher heart rates.

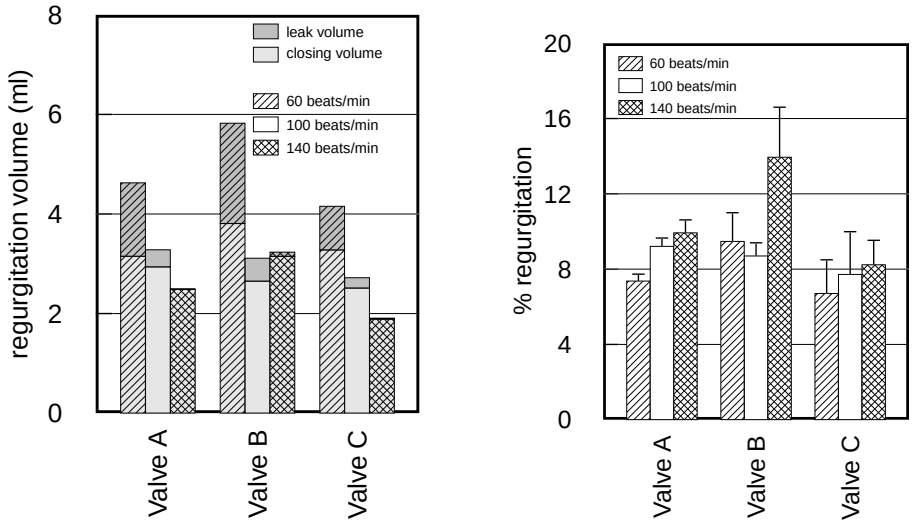

(a) Regurgitation volume.

(b) Mean value and standard deviation of % regurgitation.

Figure IV.6.: Regurgitation for On-X valve in mitral position for three different samples (A, B, C), for three different heart rates (60, 100, and 140 beats/min), and averaged for the different pressure levels.

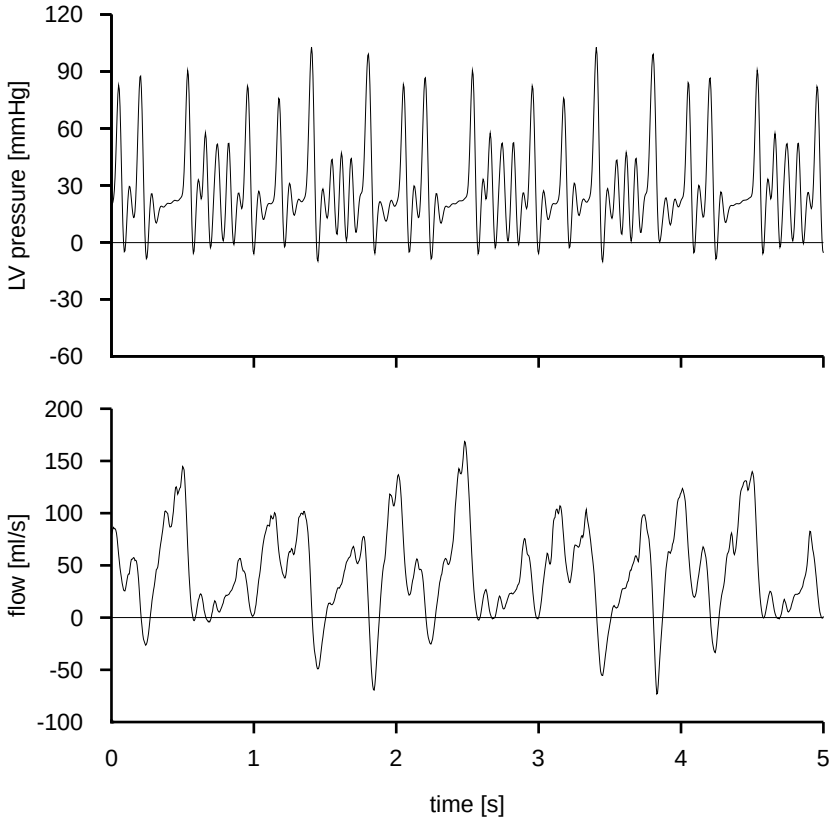

Figure IV.7.: Simulated fibrillation conditions for valve sample A.

VTI decreases with increasing heart rate, as anticipated. All three samples yield comparable results. $\Delta P_{Doppler}$, calculated with the simplified Bernoulli equation, is 0.92 ± 0.17 mmHg (range 0.59 - 1.39 mmHg). The effective orifice area calculated with the continuity and the Gorlin equation is given in Table IV.2. The values for both equations are in the same range (EOA = 2.1 ± 0.1 cm^2; EOA_{Gorlin} = 1.8 ± 0.2 cm^2), but EOA_{Gorlin} is systematically lower. The overall average θ is 0.48 ± 0.05 and PI is 0.56 ± 0.04. Valve-specific data for PI are shown in figure IV.5. Regurgitation data (V_{reg} and %reg) are presented in figure IV.6, with V_{reg} split into V_{close} and V_{leak}. Overall, V_{reg} remains lower than 6 ml (average 3.5 ± 1.2 ml), with V_{close} = 2.9 ± 0.7 ml and V_{leak} = 0.6 ± 0.7 ml.

As an example, figure IV.7 gives the hydrodynamic data (PLV and flow) as measured in the fibrillation simulation sequences for valve sample A. Similar data have been measured for the other two samples. Due to the low transvalvular pressure gradients

Table IV.2.: The effective orifice area (mean value and standard deviation) calculated according to continuity equation (EOA) and to the Gorlin equation (EOA_{Gorlin}).

Heart Rate [beats/min]	Effective Orifice Area Continuity Equation (EOA) [cm^2]	Gorlin Equation (EOA_{Gorlin}) [cm^2]
60	2.05 ± 0.12	1.99 ± 0.10
100	2.09 ± 0.18	1.77 ± 0.09
140	2.14 ± 0.12	1.61 ± 0.12

and the low pressure differences needed for opening and closing of the valve, the valve seems to close several times (presence of backflow in the flow data) within this fibrillation sequence, which is confirmed by echocardiographic images of the valve movement.

IV.4. Discussion

Overall, our data confirm the excellent hydrodynamic performance of the On-X valve as reported in earlier studies.[69,71,169,171,172] In this study, considering different valve types (the standard mitral 27/29 and Conform 25/33) but of the same size, we cannot discriminate between the different valve samples from a fluid-dynamic point of view.

This observation is no surprise, given the fact that the geometric orifice area is the same for the three valves. Furthermore, the connection between the left atrium and the left ventricle in the pulse duplicator system generates a “tunnel-like” effect. As such, the valves were mounted in a short tube and it was not possible to observe the potential hydraulic effect of the geometrical difference between standard 27/29 On-X valves and 25/33 conform-X valve.

During forward flow conditions, measured mean pressure gradients are lower than 3 mmHg for cardiac outputs between 3.3 and 3.8 l/min. The Doppler-derived mean pressure gradients are lower than 1.4 mmHg for the same flow conditions. This value is lower than the 4.5 mmHg reported by Chambers et al.,[169] probably due to the relatively low cardiac output in the pulse duplicator system (cardiac output used by Chambers er al.[169] was 5.9 ± 2.6 l/min). For all pulsatile flow conditions, forward maximum velocities remained below 1 m/s, with mean velocities in the order

of 0.5 m/s. As expected, the velocity time integral decreases with heart rate due to the reduced time that is available for left ventricular filling.
The effective orifice area, calculated with the continuity equation, was between 2 and 2.3 cm^2. This value is in agreement with *in vivo* patient data: 2.2 ± 0.5 cm^2 for the 27/29 On-X mitral valve.[168,169] As Chambers et al., we found that methods to calculate effective orifice area are not interchangeable. Using the Gorlin equation, EOA is estimated about 0.2 cm^2 lower (table IV.2) than using the continuity equation (overall average 1.79 cm^2). There was no correlation between both parameters, but this may again be due to the fact that data are within a narrow range and form a cluster of data points.
The performance index was calculated as the ratio of the effective orifice area (continuity equation) and the geometric orifice area as given in table IV.1. Values range from 0.49 to 0.65. Again, there was no difference between the samples. The performance index given by Chambers et al. was 0.38, but they calculated PI using the available tissue annulus (5.72 cm^2). Using the same definition and reference value, we found an average performance index of 0.37.
The total regurgitant volume was lower than 6 ml, the closing volume being the most important contributor (between 2 and 4 ml). For heart rates of 140 beats/min, we found no significant leak volume. On average, the leak volume was 0.6 ± 0.7 ml. The average percent regurgitation was 9 ± 2%.
We tested the On-X valves during a sequence of fibrillation, simulated by applying an irregular and low left ventricular driving pressure (see figure IV.7). Quantitative analysis of haemodynamic and Doppler echocardiographic data is difficult due to the irregularity of the signals, and data are strictly qualitative.

IV.5. Conclusion

In conclusion, the On-X Mitral 27/29 and On-X Conform-X Mitral 25/33 show an excellent hydrodynamic performance. Effective orifice area is 2.1 cm^2 and the performance index 0.56 for a cardiac output of 3.5 l/min. Regurgitation volumes are below 6 ml. We did not observe any difference in hydrodynamic performance between the standard On-X valve and the On-X Conform valve. Data are in agreement with reported *in vitro* and clinical data.

Chapter V

Omnicarbon® 21 mm aortic valve prosthesis *in vitro* hydrodynamic and Doppler echocardiographic study

---

The contents of this chapter is published in Int J Artif Organs 2002;25(8):783-790.
Omnicarbon® 21 mm Aortic Valve Prosthesis *in vitro* Hydrodynamic and Echo-Doppler Study
Dumont K, Segers P, Vandenberghe S, Van Nooten G, Verdonck P

Abstract

The aim of this study was to perform combined hydrodynamic and Doppler echocardiographic tests of the Omnicarbon 21 mm cardiac valve in aortic position in our Pulse Duplicator System for simultaneous assessment of valve performance and valve leakage data. During forward flow conditions, measured mean pressure gradients are between 4.5 and 20.2 mmHg (11.9 ± 4.4 mmHg) for cardiac outputs between 3.6 and 5.3 l/min (4.5 ± 0.4 l/min). Doppler-derived mean pressure gradients are between 2.0 and 17.0 mmHg (9.3 ± 3.9 mmHg) for the same flow conditions. Effective orifice area is 1.31 ± 0.08 cm^2 and the performance index is 0.74 ± 0.04, using the actual geometric orifice area, and 0.38 ± 0.02, using the tissue annulus diameter, for a cardiac output of 4.5 ± 0.4 l/min. Regurgitation volumes are below 3 ml. There is a trend to an effect of valve orientation on haemodynamics.

V.1. Background and aim of the study.[173,174,175,176,177]

The Omnicarbon cardiac valve is a monoleaflet prosthesis that basically consists of a ring and a curved freely-rotatable disc, which is retained by two shields extending from the ring. The Omnicarbon valve is particularly appropriate for ultrasound visualization because of its simple geometric shape and the absence of inner structures. Its hingeless design produces central flow of blood. The disc opens to a maximum angle of 80° at maximum cardiac output rate. An adequate opening angle of approximately 60°-70° is expected at normal cardiac output at rest. Leakage flow is relatively low because of the presence of a disk seat on the housing ring where the disc closes at 12° angle. The seat eliminates the open gap which exists in other valve designs. Further motion of the disc beyond its 12° position is wasted energy and does not benefit the flow process. The aim of this study was to perform combined hydrodynamic and Doppler echocardiographic tests of the Omnicarbon 21 mm cardiac valve in aortic position in a Pulse Duplicator System (PDS).[130,133] The PDS was designed to study prosthetic heart valves in mitral and aortic position using both standard hydrodynamic measurements (pressure and flow) as well as Doppler echocardiography.

V.2. Materials and methods

Three samples of the Omnicarbon 21 mm cardiac valve were provided by the manufacturer (MedicalCV Inc.). Valve dimensions are summarized in Table V.1. The valve model is designed to be implanted intra-annularly, hence its size represents the outside diameter including the suture ring.

V.2.1. Pulse Duplicator System

The PDS (figure V.1) is a hydraulic model of the human left heart, connected to a windkessel model of the human systemic circulation. The test fluid (40% glycerine - 60% water mixture with a dynamic viscosity of 3 mPa·s at room temperature) enters the model from a controllable preload reservoir (5) representing the lungs. The fluid enters the left ventricle (LV) (6) through the mitral valve (8). The left ventricle ejects through the aortic valve into the afterload system that consists of an air chamber ("windkessel") (3) and a hydraulic resistance (4). A venous reservoir

Table V.1.: Omnicarbon cardiac valve.

Omnicarbon Cardiac Valve Specifications [mm]				
Tissue Annulus Diameter	Internal Annulus	Geometric Orifice Diameter: OD_{mean}	disc height at hinge: $h_{leaflet}$	disc thickness: $\Delta_{leaflet}$
21	16	15	1.39	0.8
Omnicarbon Cardiac Valve Areas [cm^2]				
Geometric Orifice Area (OA)		Orifice Area Without Disc		
1.77		1.88		

guarantees a constant venous pressure of 5 mmHg. Both the preload lung and the venous reservoir have an overflow system, with the overflows ending in a central buffer reservoir out of which the test fluid is pumped continuously into the lung reservoir. The left ventricle is a silicone sac, mounted in a Perspex housing. It is surrounded by water and connected to an external circuit [(2)], consisting of Perspex cylindrical reservoirs. Pressurized air is delivered computer-controlled to this external circuit and regulates the contraction and relaxation of the cardiac chambers. The Omnicarbon valves were tested in aortic position [(7)]. Measurements were done with the valves in “vertical” position and “horizontal” position (figure V.2).

V.2.2. Data handling

Data were averaged per pressure level or, when appropriate, per heart rate. Multivariate analysis indicated no significant differences between results with the valve in horizontal or vertical position. Therefore, these data were pooled for the analysis of most results, except for the analysis of forward pressure gradient-flow relations.

V.2.3. Pressure and flow data

Left ventricular and aortic pressure and flow were measured using Labview Software and a multifunction National Instruments data acquisition card (PCI 6024E, National Instruments, Texas, USA). For all heart rates, 1024 samples were taken at 200 Hz. These data are further analyzed and parameters derived using customized software, written in Matlab (Matlab 5.3, The Mathworks, Inc., Natick, MA, USA).

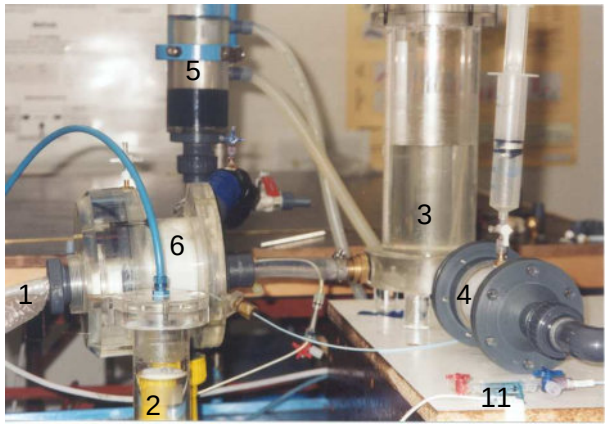

(a) Experimental setup with windkessel model.

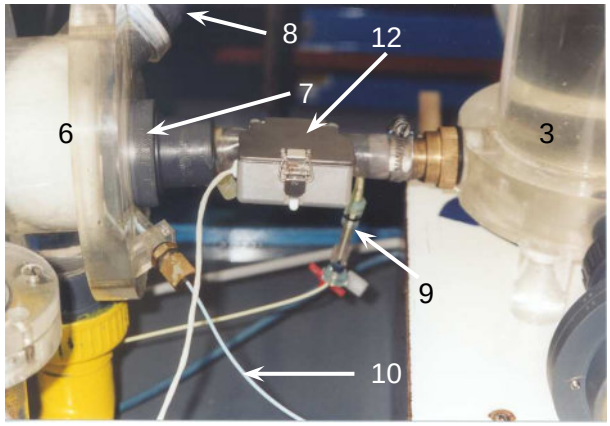

(b) Measurement equipment.

Figure V.1.: Pulse Duplicator System and simultaneous measurement of data.

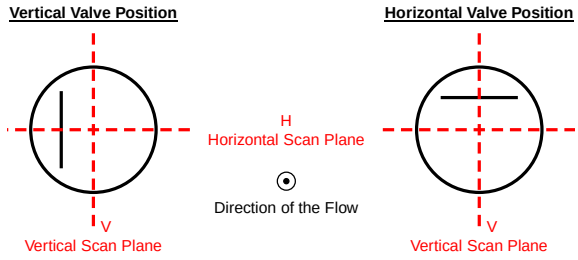

(a) Omnicarbon monoleaflet valve. (b) Orientation of the Omnicarbon monoleaflet valve.

Figure V.2.: Schematic drawing of the open Omnicarbon valve in the “vertical” and “horizontal” position with indication of the vertical (V) and horizontal (H) echo-Doppler scan planes.

After calibration of pressure and flow, one averaged cycle was calculated. Signals were aligned in time to account for time delays in the fluid-filled 6 Fr pigtail catheter, and these data were further used for subsequent analysis. Figure V.3 shows an example of averaged LV and aortic pressure and according flow cycles. From these data

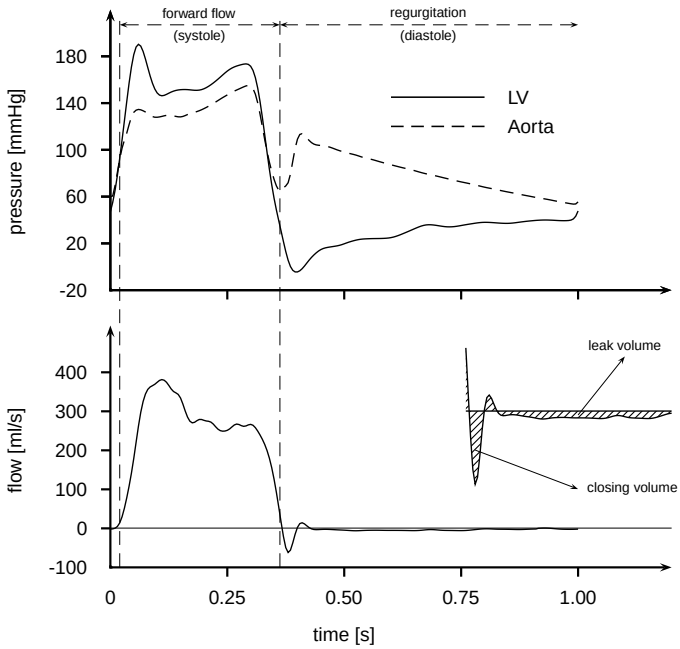

(a) Averaged pressure and flow cycle.

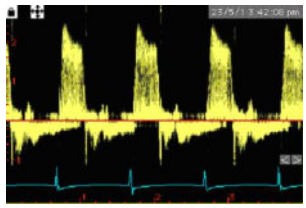

(b) Continuous wave Doppler measurement.

Figure V.3.: Example of an averaged pressure and flow cycle for an Omnicarbon valve (valve A) measured in vertical position at 60 beats/min and aortic systolic pressure of 150 mmHg.

the following numbers were derived. Cardiac output (CO) was calculated as mean flow and though expressed in l/min. Systolic and diastolic flow periods were determined from the flow curve as the periods of forward and backward (regurgitation) flow, respectively. Mean forward flow ($Q_{fwd,mean}$) was calculated as the ratio of the

positive area under the flow curve (Forward Stroke Volume SV_{fwd}), divided by the duration of forward flow (T_{fwd}). The reguritation volume (V_{reg}), i.e. the "negative" area under the flow curve, was further split into the closing volume (V_{close}) and the leak volume (V_{leak}). The pressure difference (ΔP) was the instantaneous difference of LV and aortic pressure. The mean ($\Delta P_{fwd,mean}$) during systole was derived.

V.2.4. Continuous wave Doppler data

Doppler data were analyzed using the Vingmed CFM 800 on-board data analysis software package (EchoPAC 5.4.4, GE Vingmed, $^{(1)}$ in figure V.1). The images allowed analyzing the forward flow through the aortic valve. The maximum velocity contour was manually traced, with the area under the curve yielding the velocity time integral (VTI). The software further yielded maximum (V_{max}) and mean velocity (V_{mean}), the latter being calculated as the ratio of VTI and T_{fwd}. For each condition, three cardiac cycles were analyzed. All values given in the text are averaged.

V.2.5. Derived parameters

The percentage of regurgitation (%reg) is calculated as

$$\%reg = \frac{V_{reg}}{V_{reg} + SV_{fwd}} \tag{V.1}$$

The effective orifice area (EOA [cm^2]) is calculated - based on the continuity equation - as the ratio of the forward stroke volume (SV_{fwd}) and VTI:

$$EOA = \frac{SV_{fwd}}{VTI} \tag{V.2}$$

The mean Doppler velocity and the simplified Bernoulli equation can be used to estimate the forward pressure difference ($\Delta P_{Doppler}$):

$$\Delta P_{Doppler} = 4 \cdot V_{mean}^2 \tag{V.3}$$

Besides the continuity equation, the Gorlin equation provides an alternative way to calculate the effective orifice area (EOA_{Gorlin}):

$$EOA_{Gorlin} = \frac{Q_{fwd,mean}}{51.6 \cdot \sqrt{\Delta P_{Doppler}}} \tag{V.4}$$

Finally, the performance index (PI [-]) of the valve is calculated as the ratio of the effective orifice area (EOA) and the geometric orifice area (OA):

$$PI = \frac{EOA}{OA} \tag{V.5}$$

Depending on how the geometric orifice area is defined, different values are obtained (table V.2). We calculated the performance index using a measured value for the geometric orifice (1.77 cm^2), giving PI_{geo}, and a value calculated from the tissue annulus diameter (21 mm, yielding an area of 3.46 cm^2), giving PI_{tissue}.

V.3. Results

Overall, cardiac output is 4.5 ± 0.4 l/min (table V.2). The mean pressure gradient

Table V.2.: Summary of data for Omnicarbon cardiac valve, valve size 21 mm

Summary of the Experimental Data of the Omnicarbon Study

Pressure Level [mmHg]	Cardiac Output [l/min]	Effective Orifice Area Continuity Equation [cm^2]	Effective Orifice Area Gorlin Equation [cm^2]	Performance Index using Tissue Annulus Diameter [-]	Performance Index using Geometric Orifice Area [-]
100	4.00 ± 0.274	1.30 ± 0.083	1.26 ± 0.080	0.38 ± 0.024	0.74 ± 0.047
125	4.49 ± 0.215	1.32 ± 0.063	1.28 ± 0.061	0.38 ± 0.018	0.75 ± 0.036
150	4.89 ± 0.228	1.32 ± 0.089	1.27 ± 0.086	0.38 ± 0.026	0.74 ± 0.050
Overall Average	4.50 ± 0.436	1.31 ± 0.078	1.27 ± 0.076	0.38 ± 0.023	0.74 ± 0.044

over the valve is 11.9 ± 4.4 mmHg and is function of flow (values between 4.5 - 20.2 mmHg) (figure V.4). Figure V.4(b) shows in more detail the relation between measured mean pressure drop over the valve, and the mean forward flow through the valve. A 2nd order polynomial was fitted to the data points. The regression line through the data measured with the valve in vertical position being above the regression line through the "horizontal" data. For example, for a $\Delta P_{fwd,mean}$ of

10 mmHg the difference in $Q_{fwd,mean}$ between vertical and horizontal position is 30 ml/s (193 vs. 163 ml). Multivariate analysis, however, indicated no significant difference between results in horizontal and vertical position. The Doppler-gradient calculated from V_{mean} and using the simplified Bernoulli equation, are systematically lower than the measured pressure gradient (figure V.4(a)) (mean difference 2.6 mmHg). Regurgitation volume and % regurgitation are given in figure V.5 for three

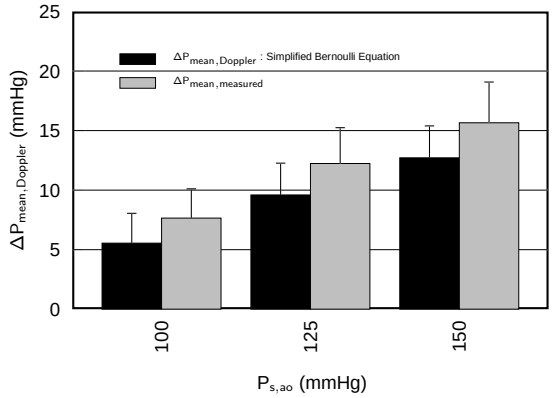

(a) $\Delta P_{mean,Doppler}$ calculated using the simplified Bernoulli equation and $\Delta P_{mean,measured}$.

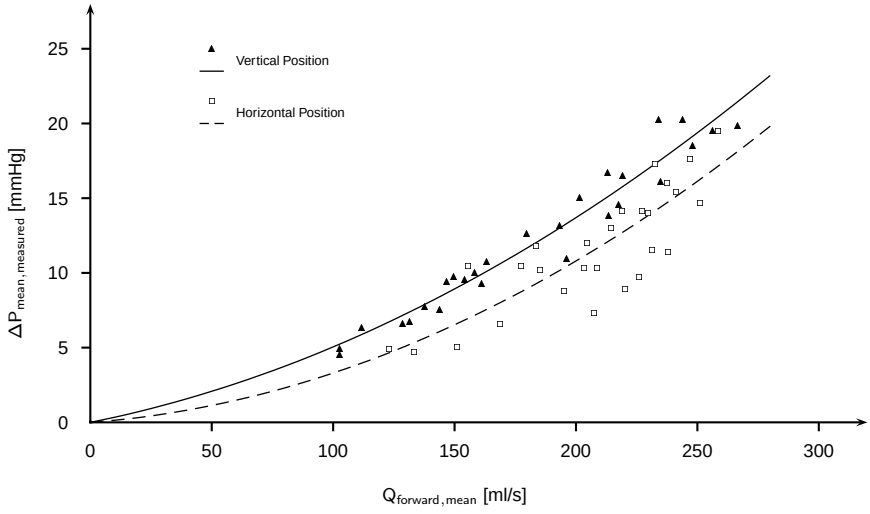

(b) Relation between forward pressure gradient $\Delta P_{fwd,mean}$ and flow $Q_{fwd,mean}$ for vertical and horizontal position of the valve.

Figure V.4.: Comparison of $\Delta P_{mean,Doppler}$ and $\Delta P_{mean,measured}$ (a), relation between forward pressure gradient $\Delta P_{fwd,mean}$ and flow $Q_{fwd,mean}$ (b).

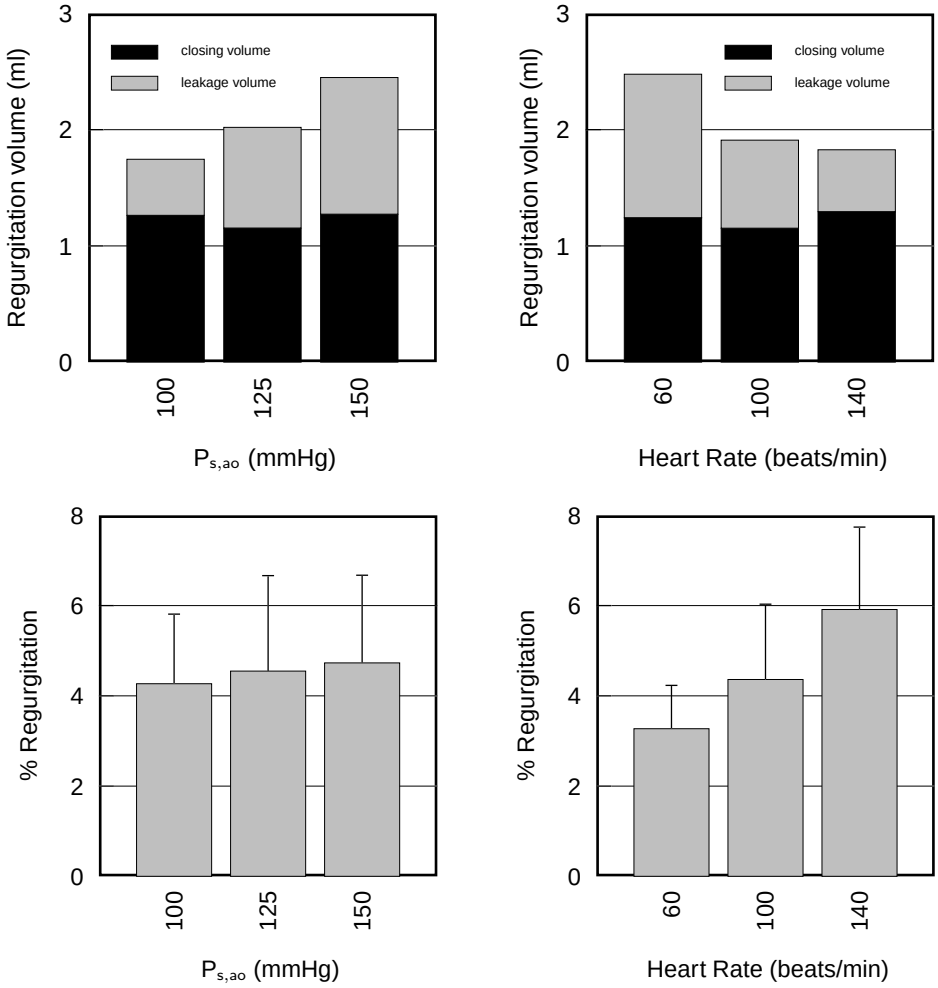

Figure V.5.: Valve leakage based on flow data per pressure level and per heart rate.

different heart rates and three different pressure levels. Closing volume is rather constant and between 1 and 1.5 ml. Total regurgitating volume is lower than 3 ml. The leakage volume increases with systolic pressure and decreases with the heart rate. The percentage regurgitation is less than 6%. Doppler velocities and VTI are shown in figure V.6. Maximal velocities are between 2 and 2.5 m/s; mean velocities (averaged over the period of forward flow) around 1.5 m/s. The Velocity Time Integral (figure V.6) strongly depends on heart rate; for this reason, data were averaged per heart rate and per aortic pressure level.

The effective orifice area of the valve was calculated using the continuity equation and the Gorlin equation, respectively (table V.2). For the standard “continuity-

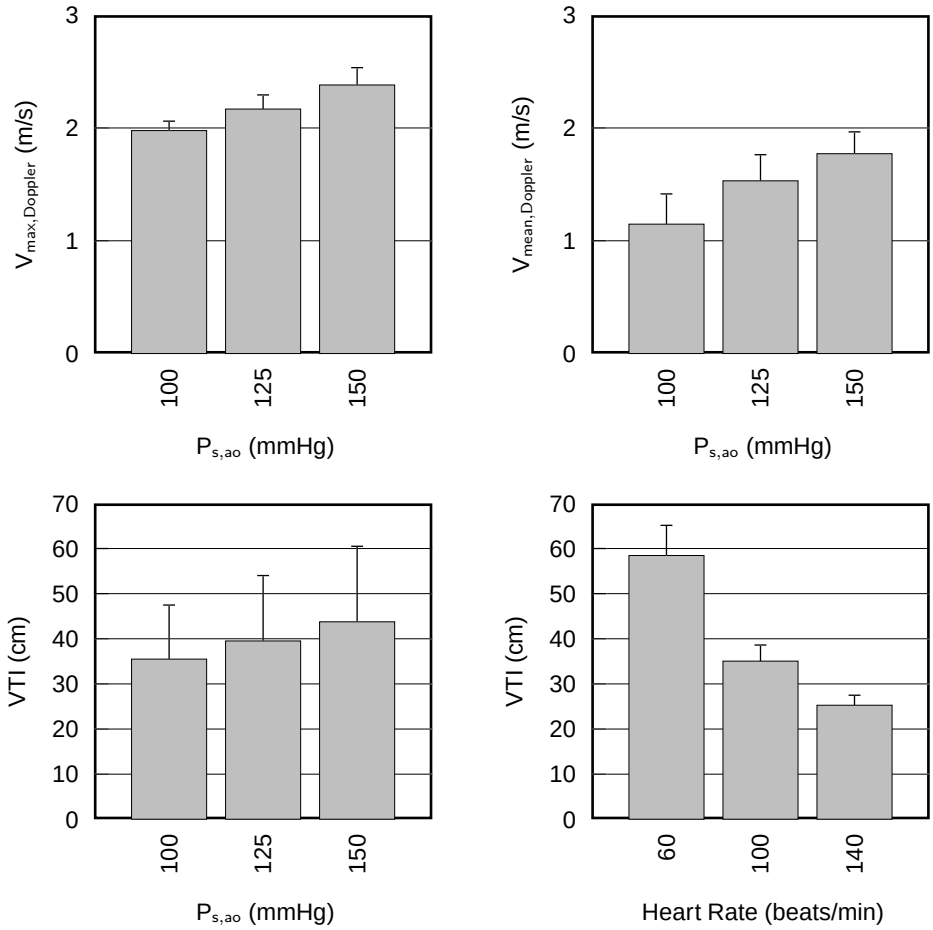

Figure V.6.: Velocity data calculated from the Continuous Wave Doppler measurements and Velocity Time Integral averaged per heart rate and per pressure level, respectively.

equation" approach, EOA is 1.31 ± 0.08 cm^2; the Gorlin equation yields a somewhat lower value of 1.27 ± 0.08 cm^2. The performance index is 0.74 ± 0.04 using the actual geometric orifice area, and 0.38 ± 0.02 using the tissue annulus diameter.

V.4. Discussion

This study is, to our knowledge, the first to combine directly measured pressure and volume flow data, with Doppler echocardiographic data to assess the hydrodynamic performance of the Omnicarbon valve. This allowed us to simultaneously assess hydrodynamic performance as well as valve leakage information. This was achieved

in an *in vitro* set-up designed to test heart valves in aortic and mitral position.
Overall, our data demonstrate an excellent hydrodynamic performance for the Omnicarbon aortic cardiac valve and confirm findings reported in earlier *in vitro* and clinical studies.[173, 175, 176, 178, 179, 180] During forward flow conditions, measured mean pressure gradients are between 4.5 and 20.2 mmHg (11.9 ± 4.4 mmHg) for cardiac outputs between 3.6 and 5.3 l/min (4.5 ± 0.4 l/min) under various systolic pressures and beats/min frequency conditions. Doppler-derived mean pressure gradients are between 2.0 and 17.0 mmHg (9.3 ± 3.9 mmHg) for the same flow conditions. Doppler gradients are lower than the value reported by Fehske et al.[173] and Messner-Pellenc et al..[176] This discrepancy between our *in vitro* experiments and *in vivo* data are, at least in part, due to the specific character of the Pulse Duplicator System. The valves were mounted in a short tube and this influences the flow pattern through the valves. The velocity in this tube stays high and impeded "pressure recovery" distal to the valve. This is different than in the real aorta, where the pressure can and will rise due to pressure recovery. The absence of pressure recovery is also a possible explanation for the difference in the Doppler derived and measured pressure gradients that we observed in our data.[181] In addition the accuracy of the LV pressure measurements (6 French pigtail catheter connected to a piezoelectric pressure transducer: Ohmeda, Ghent, Belgium) is a limitation for the measured pressure data. The maximum deviation of the pressure transducers, due to the total effects of nonlinearity, hysteresis and sensitivity variation is no more than 2% of the reading.
Tilting disc and bileaflet aortic valve substitutes have an optimal orientation yielding favorable haemodynamics and smallest pressure gradients.[182, 183] We compared the $\Delta P_{fwd,mean}$-$Q_{fwd,mean}$ curves for two orientations of the valves, i.e. the valve mounted in a vertical or a horizontal orientation (figure V.2). There is a trend for a higher pressure drop for the vertical position of the valve (figure V.4), but our data do not allow to demonstrate its statistical significance. This is due to the rather limited number of valves tested and to the variability in the measurements induced by manipulation of the Pulse Duplicator System (opening the system and changing the valve or its orientation) and/or variation on certain control parameters of the model, such as cardiac output, total arterial compliance and resistance and pressure level.
The effective orifice area (table V.2), calculated with the continuity equation was 1.31 ± 0.08 cm^2. This value is in agreement with *in vivo* patient data: 1.36 ± 0.1 cm^2 found by Messner-Pellenc et al.[176] and between 1.2 and 1.7 cm^2 found by Carrier et

al..[180] Although it has been reported that methods to calculate effective orifice area are not interchangeable (Chambers et al.[168]) we found quite good agreement using the Gorlin equation (1.27 ± 0.08 cm^2).
The value of the performance index (PI) strongly depends on how the geometric valve area is defined. Using the actual geometric orifice area, we found a PI_{geo} of 0.74 ± 0.04. Using the tissue annulus diameter, however, the PI_{tissue} is 0.38 ± 0.02. This value is close to the performance index given by Peter et al.[175] (0.35), knowing that the PI was calculated using the available tissue annulus. It should be noted that this Omnicarbon model is intended for intra-annular implantation and hence, its outside diameter (including the compressed suture ring) closely matches the stated nominal size of the tissue annulus diameter (21 mm).[184]
The total regurgitating volume was lower than 3 ml, the closing volume being the most important contributor. As expected leak volume decreased with increasing heart rate (less time available to leak) and increasing with systolic pressure level (higher pressure gradient over closed valve). The average percent regurgitation was 4.5 ± 1.8 %.

V.5. Study limitations

The reported data includes echocardiographic and complete haemodynamic data, but only for 1 valve size.

V.6. Conclusions

In conclusion, the Omnicarbon aortic cardiac valve prosthesis shows an excellent hydrodynamic performance. Effective orifice area is 1.31 ± 0.08 cm^2 and the performance index is 0.74 ± 0.04, using the actual geometric orifice area, and 0.38 ± 0.02, using the tissue annulus diameter, for a cardiac output of about 4.5 ± 0.4 l/min. Regurgitation volumes are below 3 ml. There is a trend to a slight effect of valve orientation on haemodynamics. Data are in agreement with reported *in vitro* and clinical data.

Chapter VI

Design of a new pulsatile bioreactor for tissue engineered aortic heart valve formation

The contents of this chapter is published in Artif Organs 2002;26(8):710-714.
Design of a new pulsatile bioreactor for tissue engineered aortic heart valve formation
Dumont K, Yperman J, Verbeken E, Segers P, Meuris B, Vandenberghe S, Flameng W, Verdonck P

Abstract

Evidence has been gathered that biomechanical factors have a significant impact on cell differentiation and behavior in *in vitro* cell cultures. The aim of this bioreactor is to create a physiological environment in which tissue engineered (TE) aortic valves, seeded with human cells, can be cultivated and conditioned during a period of several days. The bioreactor consists of two major parts: (i) the left ventricle (LV) and (ii) the afterload consisting of a compliance, representing the elastic function of the large arteries, and in series a resistance, mimicking the arterioles and capillaries. Between the LV and the compliance the TE aortic valve is placed. A mechanical valve in mitral position ensures the uni-directional flow in the closed circuit. With controllable resistance, compliance, stroke volume, and frequency, hydrodynamic conditions can be changed over a wide physiological range. This study resulted in a biocompatible prototype of a compact pulsatile flow system.

VI.1. Introduction

Valvular heart disease is an important cause of morbidity and mortality. Currently available substitutes for failing heart valves have serious limitations. Mechanical heart valves require lifelong anticoagulation and are unable to grow. Currently used biological heart valves are known to have superior haemodynamics, but they have limited durability. A new promising alternative to overcome these shortcomings is tissue engineering of heart valves. Tissue engineering is a new domain in which techniques are being developed to transplant autologous cells onto a cell matrix, which can be a biodegradable scaffold, or an acellularized heterograft cell matrix. Ultimately this promising technique could lead to the creation of new functional autologous tissue.[84, 92, 110, 185, 186, 187] An important obstacle to the creation of implantable tissue engineered heart valves is the fact that tissue engineered valves show inadequate mechanical properties to withstand haemodynamic stresses on the valve in aortic position.[188, 189] This is especially important for aortic valves where transvalvular pressure differences of 80 mmHg may exist during diastole, with high mechanical stresses on the leaflet. Evidence has been gathered that the application of pulsatile fluid flow stimulates the tissue engineered heart valve to develop structural integrity prior to implantation.[97, 110, 189, 190] For this purpose, a new bioreactor is developed, in which the seeded cells can grow under physiological aortic pressure and flow conditions. The aim of this bioreactor is to create a physiological environment in which tissue engineered aortic valves can be cultivated and conditioned during a period of several days.

VI.2. Basic demands of a bioreactor

A bioreactor tries to mimic the complex *in vivo* environment,[97, 191, 192] including all natural stimuli that have impact on cell growth and differentiation. In a classic general cell culture-bioreactor system, these stimuli can be divided into 4 basic categories:[84, 95, 97] (i) growth matrix in or on which cells can grow; (ii) the chemical and physiological composition of the medium; (iii) the composition of the gas phase in the incubator; (iv) the incubation temperature (including heat transport). However a modern approach to certain cell cultures is to create an *in vitro* environment that not only embodies the 4 above-mentioned aspects but also includes mechanical

stimuli as pressure and shear stress.[84,97] The bioreactor has to meet several other requirements: compact in size, sterility, low volume, easy refreshment of the medium, access to the TE-valve and visualization of the TE-valve. The use of a pump (heat production) may not disturb the climate in the incubator. The medium should be exposed to the controlled atmosphere (diffusion of O_2, CO_2, N_2) of the incubator. This way, a micro-environment is created with sufficient nutrients and without accumulation of metabolites. The bioreactor should allow testing of entire valves as well as parts of it. From haemodynamic point of view, the bioreactor should be able to mimic different haemodynamic conditions, within certain physiological limits (transvalvular pressure gradient, flow, frequency).

VI.3. Materials and methods

VI.3.1. Bioreactor design

The bioreactor design (Figure VI.1) is based on the experience obtained with a pulsatile mock loop of the left heart[130](14) and a two-element windkessel model[132](15). It consists of two major parts: the left ventricle and the afterload consisting of a compliance chamber and a resistance. The first part is the left ventricle (LV) made of silicone rubber (Wilsor, the Netherlands). For the prototype, we chose a maximum stroke volume of 80 ml. From this value the diameter of a spherical ventricle was calculated as

$$\sqrt[3]{6/\pi \cdot 8 \cdot 10^{-5} m^3} = 5.35cm. \tag{VI.1}$$

This LV is compressed and decompressed by the movement of a piston by means of an external circuit (E), which allows varying the stroke volume and the frequency. It is thus possible to create different pulsatile flow conditions. An air filled chamber is used as a compliance (C), representing the elastic function of the large arteries. The air volume (and compliance) is easily varied by pumping air in and out of the chamber. As a constant volume V of air is compressed and relaxed at low pressures P, the compliance can be mathematically described by the gas law. This means that the process can be assumed isothermal and described by Boyle's law: P.V = constant. This also allows approximating the size of the air chamber. For standard diastolic and systolic pressures of 80 and 120 mmHg, atmospheric pressure 105 Pa, conversion factor 133 Pa/mmHg (mmHg to Pa) and a stroke volume of 50 ml, the

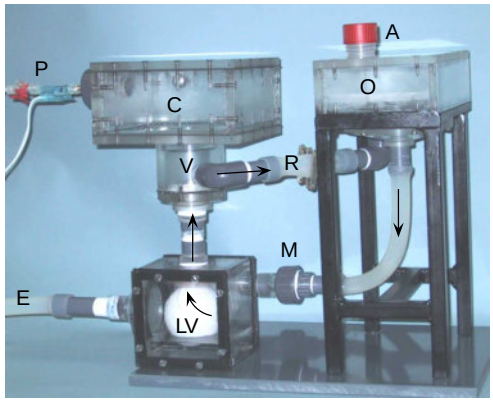

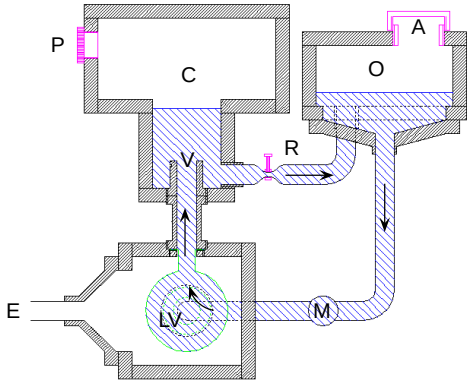

Legend:	
C	Compliance
R	Resistance
O	Reservoir
V	TE valve
M	Mechanical valve
A	Aerator
LV	Left ventricle
E	External circuit
P	Pressure transducer

Figure VI.1.: Basic design of prototype of the pulsatile bioreactor.

air chamber volume V_C can be calculated as:

$$\frac{V_C}{V_C - 50} = \frac{(120 \cdot 133) + 10^5}{(80 \cdot 133) + 10^5} \Rightarrow V_C = 1024ml \cong 1l \qquad \text{(VI.2)}$$

The TE aortic valve (V) is placed between the LV (LV) and the compliance (C). Distal to this compliance chamber is a non-linear resistance (R), mimicking the arterioles and capillaries. As a resistance we used a variable clamp, which controls the diameter of the tubing. Downstream aeration is regulated (A). The mechanical valve (M) ensures the flow in one direction.

VI.3.2. Hydrodynamic study

With controllable resistance, compliance, stroke volume and frequency, it is possible to change the hydrodynamic conditions over a wide physiological range. The

hydraulic properties of the bioreactor were tested by using a mechanical valve as well as a cadaveric ovine aortic valve (OAV) in aortic position. Flow was measured with a Transonic flow probe positioned between the LV and the aorta valve. Aortic pressure in the compliance chamber was measured with an Ohmeda pressure transducer. During this hydraulic evaluation, heart rate (40-100 BPM), stroke volume (35-76 ml), resistance (0.98-4.70 mmHg.s/ml) and compliance (0.4-1.2 ml/mmHg) parameters were varied.

VI.3.3. Biocompatibility study

The ISO 10993-1 gives a guideline of the characteristics, which should be examined in order to prove biocompatibility of certain materials. Taking into account that no blood will be used in the bioreactor during *in vitro* tests, only cyto-toxicity was investigated. A cell line of endothelial cells (EA. hy 926) was used for these experiments. The bioreactor contains 8 different materials: 1) silicone tubing, 2) silicone ventricle (Wilsor, the Netherlands), 3) rubber sealing, 4) Teflon sealing, 5) plexiglass, 6) glue (Acrifix 192 Rhm GmbH Germany, glued pieces of plexiglass and/or PVC), 7) PVC tubes, 8) PVC angles. Of each material, one piece was sterilized by ethylene oxide (EtO) and one by glutaraldehyde (2%) (GA). The materials were leaching in cell medium (Dulbeccos's modified eagle medium DMEM supplemented with 10% fetal bovine serum, 100 units/ml penicillin, 100 μg/ml streptomycin and 0.25 μg/ml amphotericin B) for two weeks. As a reference, two samples of cell medium without any material were added to this series. These different media were used to start up the cell cultures. The cell cultures were evaluated after one and three days of growth. The cells were evaluated quantitatively by cell counts after staining with trypan blue; only living cells were counted. Cell numbers of the cultures corresponding to each of the 8 test materials are reported as the ratio living cell number divided by the cell number observed in the reference culture at t=0. The results are thus expressed as a relative cell number. The cells were qualitatively evaluated with immunocytochemical stainings for endothelial cells: Von Willebrand factor and CD 31. As an index for proliferation KI 67 was used. Degenerating or dead cells do not express the endothelial antibodies. We scored the cell cultures based on the intensity of the staining. A score between 0 (no dye visible) and 5 (very intense) was attributed. The lower the quality factor, the less healthy or proliferating the cells are.

VI.4. Results

VI.4.1. Hydraulic evaluation of the bioreactor

The four controllable parameters are easily managed and the system adapts to a change within some seconds and then remains stable. Figure VI.2 shows the open

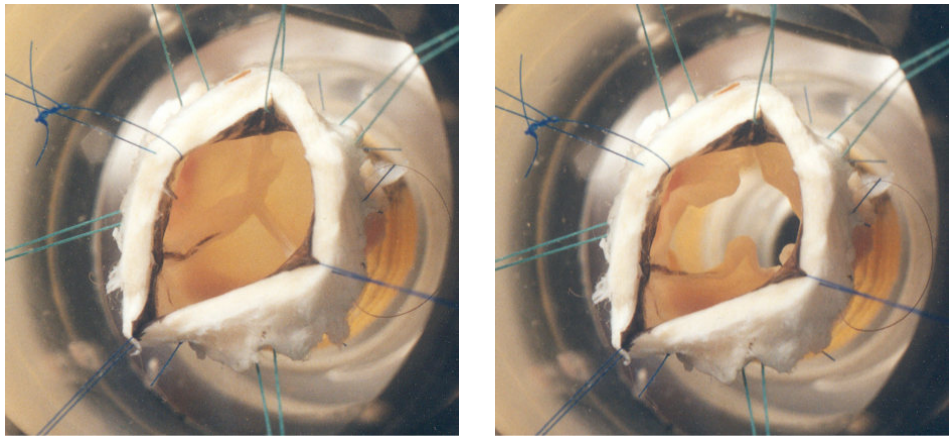

(a) Closed during diastole. (b) Open during systole.

Figure VI.2.: Ovine aorta valve in the bioreactor.

and closed aortic ovine valve during the cardiac cycle. Figure VI.3 shows as example aortic pressure and flow for 2 different settings of the 4 controllable parameters. Adapting the parameters it is possible to start with low flow conditions (e.g. cardiac output of 1.68 l/min or even lower) and thus according physiological low shear stress on the endothelial surface of the valve leaflets. Later on, the flow and pressure conditions can be progressively increased (e.g. cardiac output of 3,44 l/min) until normal physiological conditions are reached. The results show the ability of the bioreactor to perform a wide range of physiological conditions.

VI.4.2. Biocompatibility results

There are no important differences in cell numbers between the two sterilization methods (figure VI.4). For cultures on medium in which EtO sterilized materials had leached, cell counts are slightly higher in 6, slightly lower in 7 and the same in 2 cases compared to cultures in which GA sterilized materials are leached. Regarding the silicone ventricle, cell counts are seriously lower when EtO sterilization is used.

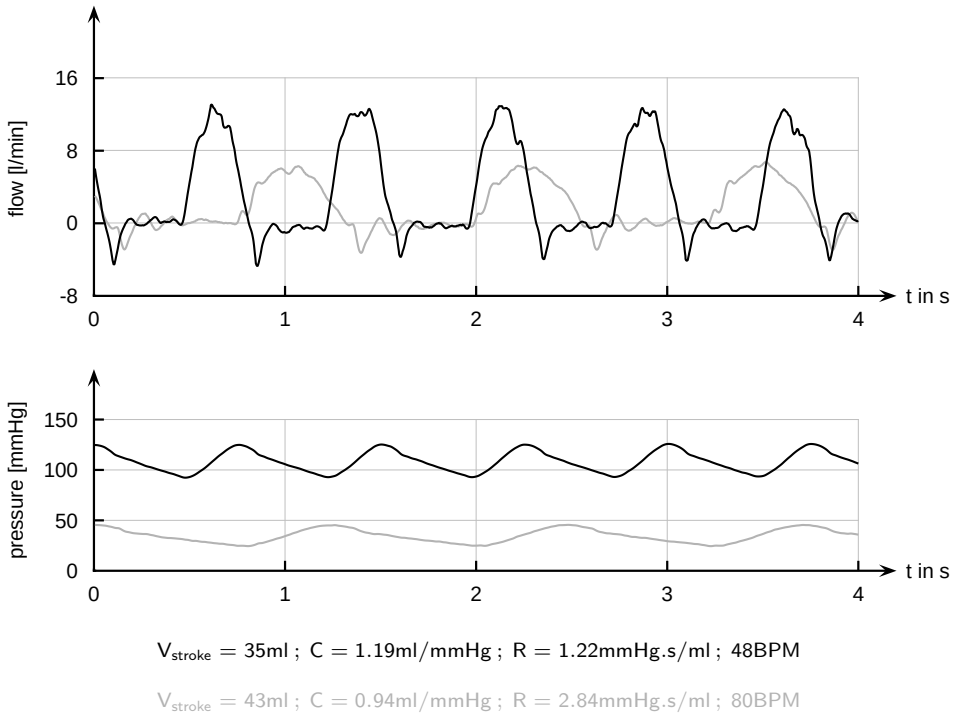

Figure VI.3.: Aortic pressure and flow curves for two (low flow: 1.68 l/min, high flow: 3.44 l/min) different parameter settings: stroke volume (V_{stroke}), compliance (C), resistance (R) and, heart rate (BPM).

Both GA and EtO sterilized rubber have very lethal effects within hours. The cells degenerate and detach from the bottom of the flask, resulting in medium containing dead cell remnants (figure VI.5-VI.6). In addition, cell counts indicate that the silicone ventricle is also harmful to cells although not to the same extent as rubber (figure VI.5). Quantitatively, only the EtO sterilized silicone ventricle results are very low, but qualitatively the GA sterilized silicone ventricle has low CD 31-score (table VI.1). The scores of all other materials are analogue to these of the reference cultures as well for the KI, CD-31 as the Von Willebrand factor staining.

VI.5. Discussion and conclusion

This study resulted in a prototype of a compact, biocompatible pulsatile flow system that fits in an incubator. Safe and easy handling of the bioreactor is ensured by its simple design. Although the ideal hydrodynamic conditions for the *in vitro*

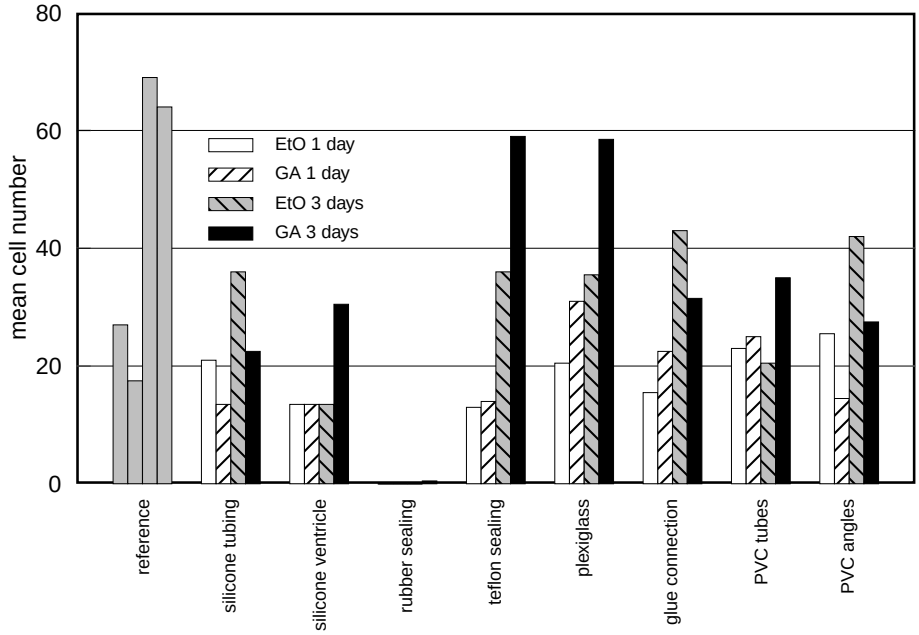

Figure VI.4.: Comparison mean amount of cells after 1 and 3 days for the different sterilization techniques (glutaraldehyde (2%) GA and ethylene oxide EtO).

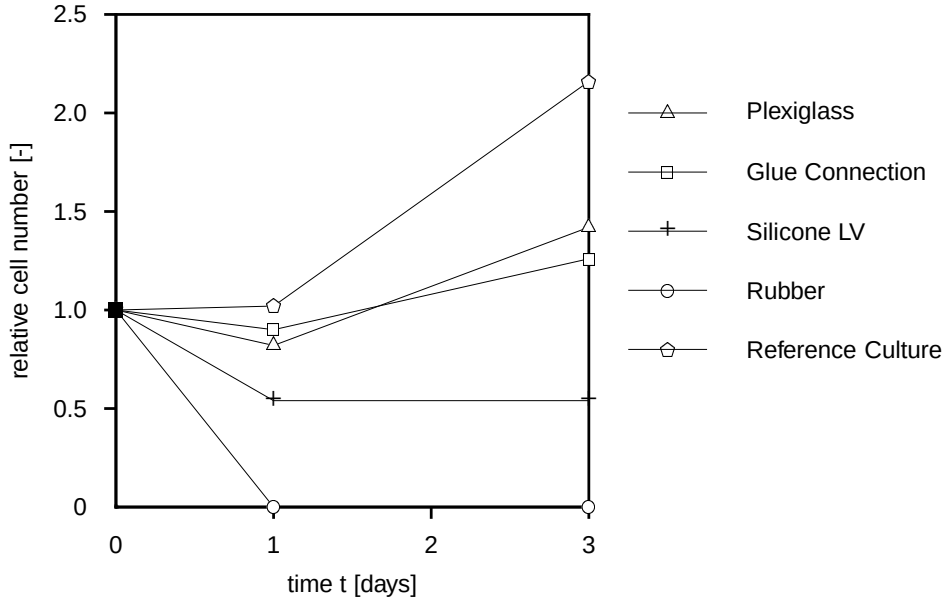

Figure VI.5.: Evolution in time of cellgrowth: relative cell number.

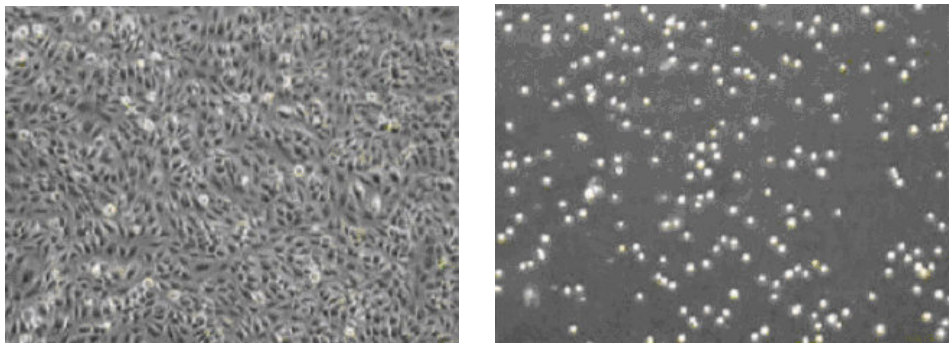

(a) Control. (b) Exposure to rubber for 3 days.

Figure VI.6.: (a) healthy reference culture, (b) lethal effect of rubber.

Table VI.1.: Qualitative evaluation with cytochemical dyes: KI 67, CD 31, Von Willebrand factor for the silicone ventricle and rubber sealing after sterilization with glutaraldehyde (2%) GA and ethylene oxide (EtO).

Material	Sterilization Technique	KI 67		CD 31		Von Willebrand Factor	
		Day 1	Day 2	Day 1	Day 2	Day 1	Day 2
Reference		2	4	4	3	2	4
Silicone Ventricle	GA	3	4	2	1	3	4
	EtO	0	2	3	4	0	4
Rubber Sealing	GA	0	0	0	0	0	0
	EtO	0	0	0	0	0	0

formation of a haemodynamically and mechanically competent tissue are at yet unknown,[193] recent publications reveal the positive effects of flow and shear stress for the generation of cardiovascular tissue engineered constructs.[95,97,110,190] Thus, the cultivation of tissue engineered heart valves can potentially be achieved using our biomimetic flow culture system. The result of the biocompatibility tests showed the highly cytotoxic effects of the sealing material and to a minor extent the negative influence of the silicone material used to construct the left ventricle. Data in table VI.1 show that rubber should be removed from the bioreactor. The KI 67 and Von Willebrand factor staining results yield a low quality number for the EtO sterilized silicone ventricle and the CD-31 staining yield a low quality score for the GA sterilized silicone ventricle. Considering both qualitative and quantitative studies, an analogous but more biocompatible material should be used to construct the flexi-

ble ventricle. Future research includes the numerical research of the pulsatile flow conditions, shear stress distribution and pressure distribution in the vicinity of the aortic valve. Numerical simulation in combination with experimental studies in the bioreactor will allow to quantify the mechanical load and to study its impact on the seeded cells.

Part C.

Computational fluid dynamics and fluid-structure interaction of heart valves

Chapter VII

Stabilization of a fluid-structure coupling procedure for rigid body motion

---

The contents of this chapter is published as proceeding AIAA-2003-3720 and submitted for publication in the AIAA journal.

Stabilization of a Fluid-Structure Coupling Procedure for Rigid Body Motion

Vierendeels J, Dumont K, Dick E and Verdonck P

Abstract

Fluid-structure interaction computations in geometries where different chambers are almost completely separated from each other by a movable rigid body but connected through very small gaps, can encounter stability problems when a standard explicit coupling procedure is used for the coupling of the fluid flow and the movement of the rigid body. An example of such kind of flows is the opening and closing of valves, when the valve motion is driven by the flow. In this paper, a stability analysis is performed for the coupling procedure of the movement of a cylinder in a cylindrical tube, filled with fluid. Between the moving cylinder and the tube a small gap is present, so that two chambers are formed. It is shown that a standard explicit coupling procedure or an implicit coupling procedure with explicit coupling in the subiterations steps can lead to unstable motion depending on the size of the gaps, the density of the rigid body and the density of the fluid. It is proven that a reduction of the time step size cannot stabilize the coupling procedure. An implicit coupling procedure with implicit coupling in the subiterations has to be used. An illustration is given on how such a coupling procedure can be implemented in a commercial CFD software package. The CFD package Fluent (Fluent Inc.) is used. As an application, the opening and the closing of a prosthetic aortic valve is computed.

VII.1. Introduction

Fluid-structure interaction (FSI) problems with moving valves are popular in biomedical applications where the simulation of the flow in the heart during the cardiac cycle is one of the goals to be achieved. Different coupling methods for this FSI problem have been used. Both in the immersed boundary method[145,194] and in the fictitious domain method[29,30,150] a fixed grid is used for the flow calculation. The influence of the structure is introduced by momentum sources in the momentum equations of the flow. However, if details of the flow around the valves are of interest (e.g. shear stresses), it would be more appropriate to use an arbitrary Lagrangean-Eulerean (ALE) method because the accuracy of the latter method is better in the vicinity of the moving boundaries for a given mesh density. Makhijani et al. presented a real 3D simulation of a pericardial bioprosthetic aortic valve during the complete cardiac cycle.[166] They used an implicit 'influence coefficient' technique to couple the flow with the motion of the structure.
In this paper, different coupling procedures for the motion of a rigid body in a moving fluid are analyzed analytically and numerically. Different time integration schemes for the motion of the valve are compared. First, a stability analysis is performed for the coupling procedure of the movement of a cylinder in a cylindrical tube, filled with fluid. Between the moving cylinder and the tube a small gap is present, so that two chambers are formed. It is shown that the coupling procedure for this kind of problem is representative for the rigid valve motion during opening and closing. The valve motion is coupled with the flow motion computed with the commercial CFD software package Fluent (Fluent Inc.). The dynamic mesh model of Fluent 6.1 has been used for the ALE computations.

VII.2. Stability analysis for a generic 1D test case

VII.2.1. Definition of the test case

As a generic 1D test case for the kind of FSI problem treated in this paper, a moving cylinder is considered in a cylindrical tube (figure VII.1). Between the cylinder and the tube there exists a small gap which connects the fluid in front at the front and the back of the cylinder. There exists an analogy between the moving valve problem and the 1D test case because during certain phases of the valve motion also

a small gap is present that connects the fluid on both sides of the valve. Also, both problems are described with one degree of freedom. For this generic test case, the

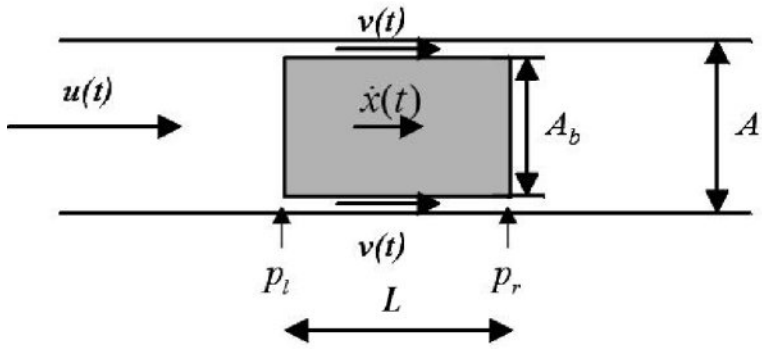

Figure VII.1.: Motion of a rigid body in a tube, generic 1D test case. $u(t)$ is the velocity of the oncoming fluid, $v(t)$ is the velocity in the gaps, $\dot{x}$ is the velocity of the rigid body, A and A_b are the cross sectional area of the tube and the front area of the rigid body respectively, L is the length of the gap .

conservation of mass is given by:

$$Au(t) = A_b\dot{x}(t) + (A - A_b)v(t) \tag{VII.1}$$

or

$$v(t) = \frac{1}{a}\left(u(t) - (1-a)\dot{x}(t)\right), \tag{VII.2}$$

with $a = A_g/A$, $A_g = A - A_b$.

The conservation of momentum in the gap is:

$$\frac{\partial v}{\partial t} + \frac{1}{\rho_f}\frac{\partial p}{\partial x} = 0 \tag{VII.3}$$

for inviscid flow. ρ_f denotes the density of the fluid, p is the pressure. In the analysis the influence of the viscous terms is neglected. The driving force for the rigid body motion is given by the pressure difference between the left and right wall of the cylinder. This pressure difference is:

$$p_l - p_r = \frac{\partial v}{\partial t} L\rho_f, \tag{VII.4}$$

with L the length of the gap. The force on the solid body is then given by

$$F = A_b(p_l - p_r) = (1-a)A(p_l - p_r). \tag{VII.5}$$

The equation of motion for the solid body becomes:

$$m\ddot{x} = F \tag{VII.6}$$

or using equation (VII.2),(VII.4),(VII.5) and $m = A_b L \rho_s$

$$\ddot{x} = \frac{\partial u}{\partial t}\frac{\rho_f}{\rho_s}\frac{1}{a} - \ddot{x}\frac{1-a}{a}\frac{\rho_f}{\rho_s}, \tag{VII.7}$$

with ρ_s the density of the solid.

VII.2.2. Discretization

Since a commercial package is used for the fluid calculation, the interface characteristics of this software have to be taken into account. The fluid solver uses an ALE algorithm. Thus starting from a known state at time level n, the new position of the boundary at time level $n+1$ has to be provided. With the other boundary conditions given as a function of the time (e.g. at inlet and outlet), the software computes a new state on timelevel $n+1$. The only time discretization scheme that can be selected for the ALE calculations in Fluent is the backward Euler scheme. Therefore the fluid discretization part of the generic 1D test case problem is also done with a backward Euler approach. It is important to notice that the only variable that is passed through the interface between the solid and the fluid problem is the position x, which is common for both problems. It means that both problems have their own variables for the other state variables (e.g. velocity). With a backward Euler discretization, the force F^{n+1} is given by

$$\begin{aligned} F^{n+1}/m &= \frac{\rho_f}{\rho_s}\frac{v^{n+1}-v^n}{\Delta t} \\ &= \frac{\rho_f}{\rho_s}\left(\frac{1}{a}\frac{u^{n+1}-u^n}{\Delta t} - \frac{1-a}{a}\frac{\dot{x}_{NS}^{n+1}-\dot{x}_{NS}^n}{\Delta t}\right). \end{aligned} \tag{VII.8}$$

Remark that the velocity used in the Navier-Stokes solver is denoted as $\dot{x}_{NS}$. This velocity can be related to the position vector x as

$$\dot{x}_{NS}^{n+1} = \frac{x^{n+1} - x^n}{\Delta t}, \tag{VII.9}$$

again using the backward Euler discretization of the Navier-Stokes solver. The force is then passed to the solid problem and used in the equation of motion:

$$m\ddot{x}^{n+1} = F^{n+1}. \tag{VII.10}$$

Here $\ddot{x}$ denotes the acceleration variable in the solid problem. The equation of motion can be integrated to obtain the velocity $\dot{x}^{n+1}$ of the solid problem and the position x^{n+1}. We consider a class of integration schemes given by

$$\begin{aligned} \dot{x}^{n+1} &= \dot{x}^n + (1-\beta)\,\ddot{x}^n\Delta t + \beta\ddot{x}^{n+1}\Delta t \\ x^{n+1} &= x^n + \dot{x}^n\Delta t + \gamma\ddot{x}^n\Delta t^2 + \alpha\ddot{x}^{n+1}\Delta t^2. \end{aligned} \tag{VII.11}$$

For γ=1/2-α this corresponds to the class of Newmark schemes. For γ=0 and $\alpha = \beta = 1$ this corresponds to the backward Euler scheme. Indeed, with the latter choice, the scheme can be rewritten as

$$\begin{aligned} \dot{x}^{n+1} &= \dot{x}^n + \ddot{x}^{n+1}\Delta t \\ x^{n+1} &= x^n + \dot{x}^{n+1}\Delta t. \end{aligned} \tag{VII.12}$$

From eqs. (VII.8), (VII.9), (VII.10) and (VII.11), F^{n+1} and the variable x^n and x^{n+1} can be eliminated easily. The resulting equations can be written in matrix

form:

$$\begin{bmatrix} 0 & 1 & -\alpha \\ 1 & 0 & -\beta \\ 0 & K & 1 \end{bmatrix} \begin{bmatrix} \dot{x}\Delta t \\ \dot{x}_{NS}\Delta t \\ \ddot{x}\Delta t^2 \end{bmatrix}^{n+1} = \begin{bmatrix} 1 & 0 & \gamma \\ 1 & 0 & 1-\beta \\ 0 & K & 0 \end{bmatrix} \begin{bmatrix} \dot{x}\Delta t \\ \dot{x}_{NS}\Delta t \\ \ddot{x}\Delta t^2 \end{bmatrix}^{n} + \begin{bmatrix} 0 \\ 0 \\ \dfrac{K}{1-a}\left(u^{n+1}-u^n\right)\Delta t \end{bmatrix} \tag{VII.13}$$

where K is given by

$$K = \frac{\rho_f}{\rho_s}\frac{1-a}{a}. \tag{VII.14}$$

Eq. (VII.13) can be rewritten is condense form as

$$A\phi^{n+1} = B\phi^n + D. \tag{VII.15}$$

VII.2.3. Stability of the time integration scheme

The time integration scheme (VII.15) is stable if the amplitude of all eigenvalues of the matrix $C = A^{-1}B$ is not larger than one. The characteristic equation for the eigenvalues λ_i of C is given by

$$(\lambda - 1)\left(\lambda^2 - \frac{(\alpha-\beta-\gamma)K}{1+\alpha K}\lambda + \frac{(1-\beta-\gamma)K}{1+\alpha K}\right) = 0. \tag{VII.16}$$

The eigenvalues λ_i are

$$\begin{aligned} \lambda_1 &= 1, \\ \lambda_{2,3} &= \frac{(\alpha-\beta-\gamma)K \pm \sqrt{(\alpha+\beta+\gamma)^2K^2 - 4K(1+\alpha K-\beta-\gamma)}}{2(1+\alpha K)}. \end{aligned} \tag{VII.17}$$

The eigenvector corresponding to the eigenvalue 1 is $[1\ 1\ 0]^T$. It is seen, if u is constant in time ($D = [0\,0\,0]^T$), that the solution of the generic test case corresponds with a motion at constant speed. This solution corresponds to the eigenmode with

eigenvalue 1, i.e.

$$\begin{bmatrix} \dot{x} \\ \dot{x}_{NS} \\ \ddot{x} \end{bmatrix}^{n+1} = \begin{bmatrix} \dot{x} \\ \dot{x}_{NS} \\ \ddot{x} \end{bmatrix}^{n} \tag{VII.18}$$

if $\dot{x}^n = \dot{x}^n_{NS}$ and $\ddot{x}^n = 0$. The other modes are spurious and should be damped. They are formed by a linear combination of e.g. a mode corresponding with a different speed in the solid and the fluid problem and no acceleration ($[1\ -1\ 0]^T$) and a mode with velocity zero and an acceleration different from zero ($[0\ 0\ 1]^T$). It should be noted that the two latter modes are not neccessarily eigenmodes, but form a span for these eigenmodes. So, in order to damp the spurious modes, the amplitude of the eigenvalues λ_2 and λ_3 must be strictly smaller than one and for good damping close to zero.

With the transformation

$$\lambda_i = \frac{1+z_i}{1-z_i}, \tag{VII.19}$$

the inner part of the unit circle in the λ-plane is transformed into the left half plane of the z-plane. After elimination of the factor $(\lambda - 1)$ in eq. (VII.16), the transformation gives

$$(1+K(1+2\alpha-2\beta-2\gamma))z^2 + 2(1+K(\alpha+\beta+\gamma-1))z + 1 + K = 0. \tag{VII.20}$$

or

$$a_2 z^2 + a_1 z + a_0 = 0 \tag{VII.21}$$

The conditions for stability are now that $\Re(z_i) \leq 0$ (Routh-Hurwitz conditions). For a quadratic polynomial, these are fulfilled if a_0, a_1 and a_2 have the same sign. The stability conditions are given by

$$\begin{aligned} 1+K(1+2\alpha-2\beta-2\gamma) &> 0 \\ 1+K(\alpha+\beta+\gamma-1) &> 0 \end{aligned} \tag{VII.22}$$

For large, but finite values of K, the conditions are

$$\begin{aligned} \beta+\gamma &\leq \alpha+1/2 \\ \alpha+\beta+\gamma &\geq 1. \end{aligned} \tag{VII.23}$$

Note that solutions can be found only if $\alpha \geq 1/4$.

VII.2.4. Choice of the time integration scheme

An explicit scheme for the motion of the solid is obtained for $\alpha = \beta = 0$. Conditions for γ can then only be fulfilled if $K < 3$. This means that for large K an explicit scheme is unstable and cannot be used.
A Newmark scheme is obtained if $\gamma = 1/2 - \alpha$. For large K, the stability conditions are $2\alpha \geq \beta \geq 1/2$. A Newmark scheme is second order accurate in time[195] if $\beta = 1/2$. The product of the eigenvalues λ_2 and λ_3 are given by the constant in eq. (VII.16) after elimination of the factor $(\lambda - 1)$. For the second order Newmark scheme this constant is equal to $\alpha K/(1+\alpha K)$, which is very close to one for large values of K. So, the second order Newmark scheme has almost no damping for the spurious modes arising in the generic test case problem. A typical choice for α for a second order Newmark scheme is $\alpha = 1/4$. The eigenvalues are then given by

$$\lambda_{2,3} = \frac{-K \pm 2i\sqrt{K}}{K+4}, \tag{VII.24}$$

which are close to -1 for large K. So, for this choice of parameters (α=1/4, β=1/2, γ=1/4), the scheme is second order accurate in time, but weakly damped π-oscillations of the spurious modes are present.
A typical choice for a first order Newmark method is the scheme with parameters (α=1/2, β=1, γ=0). This scheme is the fully implicit Newmark scheme. The eigenvalues are then $\lambda_2 = 0$ and $\lambda_3 = -K/(K+2)$. Again, one of the spurious modes has weakly damped π-oscillations.
Let us consider now the schemes for which $\beta + \gamma = 1$. The eigenvalues for these schemes are $\lambda_2 = 0$ and $\lambda_3 = (\alpha-1)K/(1+\alpha K)$ which reduces to $\lambda_3 = (\alpha-1)/\alpha$ for large values of K. One of the spurious modes is damped immediately. For $\alpha < 1/2$ the scheme is unstable. For $1/2 \leq \alpha < 1$, the other spurious mode is oscillatory damped. For $\alpha = 1$, all spurious modes are immediately damped. For

$\alpha > 1$, the other spurious mode is supercritically damped (without oscillations). Several schemes are tested out in the results section to show the validity of this analysis. The scheme with $\alpha = \beta = 1$ and $\gamma = 0$ will finally be used for the computations. This scheme corresponds to the first order backward Euler scheme and corresponds to the time integration scheme for the fluid problem. It should be pointed out that for another choice of the time integration scheme for the fluid problem, the analysis should be repeated and will have an impact on the choice of the integration scheme for the solid problem. A second remark is that for small K, close to zero, the spurious modes are damped very well, independent of the choice of α, β and γ. So, if only a weak coupling exists between the fluid and the solid problems, the matching of the time integration scheme for both problems is of less importance.

VII.2.5. Stability of the subiteration process

In more general applications, the system given by eq. (VII.13) is solved in an iterative way because no closed expression for the force in function of the solid variables is available. The force is obtained from a CFD computation, as is done for the valve motion, shown later in this paper. A subiteration process can be set up as follows. Starting from an approximation for the new acceleration $\ddot{x}^{n+1,k}$ a new value for the velocity $\dot{x}^{n+1,k}$ and the position $x^{n+1,k}$ are computed with the time integration scheme for the solid. Here k denotes the subiteration index, starting at 0. The new position is then passed to the fluid problem, where the force $F^{n+1,k}$ is computed. From the equation of motion (VII.6) a newer value for the acceleration $\ddot{x}^{n+1,k+1}$ is then computed and the cycle is repeated until convergence is achieved.
Let us first consider only schemes for which, when entering the fluid problem, the velocity computed in the fluid problem $\dot{x}_{NS}$ is equal to the velocity in the solid problem $\dot{x}$. From eqs. (VII.11) and (VII.9) can be deduced that the conditions for the parameters are $\beta + \gamma = 1$ and $\alpha = \beta$. The backward Euler scheme belongs to this family of schemes, but none of the schemes of the Newmark family does. For these particular schemes we can write the equation of motion for the generic test case (VII.10) as

$$\ddot{x}^{n+1} = K\left(\frac{1}{1-a}\frac{u^{n+1}-u^n}{\Delta t} - (\alpha\ddot{x}^{n+1} + \gamma\ddot{x}^n)\right), \qquad \text{(VII.25)}$$

so that the discrete solution of the acceleration on the new time level is given by

$$\ddot{x}^{n+1} = \frac{K}{1+\alpha K}\frac{1}{1-a}\frac{u^{n+1}-u^n}{\Delta t} - \frac{\gamma K}{1+\alpha K}\ddot{x}^n. \tag{VII.26}$$

However, eq. (VII.25) can not be solved directly for $\ddot{x}^{n+1}$ in a more general application as explained above, but has to be solved iteratively.

VII.2.5.1. Explicit coupling in the subiterations

If explicit coupling in the subiteration process is used, $\ddot{x}^{n+1,k+1}$ is computed as

$$\ddot{x}^{n+1,k+1} = (1-\omega)\ddot{x}^{n+1,k} + \omega K\left(\frac{1}{1-a}\frac{u^{n+1}-u^n}{\Delta t} - (\alpha\ddot{x}^{n+1,k} + \gamma\ddot{x}^n)\right). \tag{VII.27}$$

with ω the underrelaxation factor. With $\ddot{x}^{n+1,k} = \ddot{x}^{n+1} + \ddot{\varepsilon}^{n+1,k}$, where $\varepsilon^{n+1,k}$ represents the error in the subiteration process with respect to the discrete solution $\ddot{x}^{n+1}$, eq. (VII.27) can be written as

$$\ddot{\varepsilon}^{n+1,k+1} = -(1-\omega-\omega\alpha K)\ddot{\varepsilon}^{n+1,k}. \tag{VII.28}$$

The amplification of the error is determined by

$$\left|\frac{\varepsilon^{n+1,k+1}}{\varepsilon^{n+1,k}}\right| = |1-\omega-\omega\alpha K|. \tag{VII.29}$$

The amplification factor is less than one if

$$\omega < \frac{2}{1+\alpha K}. \tag{VII.30}$$

For small gaps, an unusual small ω is required, close to zero. The amplification factor is zero for ω given by

$$\omega = \frac{1}{1+\alpha K}. \tag{VII.31}$$

The error is then equal to zero after one subiteration. However, this approach is not suitable for flows where the dimension of the gap changes with time as for opening

and closing valves. Then it would be more appropriate to use an implicit coupling method in the subiterations.

VII.2.5.2. Implicit coupling in the subiterations

A way to have implicit coupling in the subiterations, is to compute $\ddot{x}^{n+1,k+1}$ from

$$\begin{aligned} m\ddot{x}^{n+1,k+1} &= F^{n+1,k+1} \\ &\approx F^{n+1,k} + \frac{\partial F}{\partial \ddot{x}} \left(\ddot{x}^{n+1,k+1} - \ddot{x}^{n+1,k} \right). \end{aligned} \tag{VII.32}$$

For the generic test case, the derivative $\dfrac{\partial F}{\partial \ddot{x}}$ is given by $\dfrac{\partial F}{\partial \ddot{x}} = -mK$. The error $\ddot{\varepsilon}^{n+1,k+1}$ is defined by

$$\ddot{\varepsilon}^{n+1,k+1} = -K\ddot{\varepsilon}^{n+1,k} - K\left(\ddot{\varepsilon}^{n+1,k+1} - \ddot{\varepsilon}^{n+1,k} \right) \tag{VII.33}$$

which result in $\ddot{\varepsilon}^{n+1,k+1} = 0$. So, the amplification factor is equal to zero, independent of the gap size and the fluid and solid densities.

The derivative has to be evaluated numerically in more general applications. This can be done as follows:

$$\frac{\partial F}{\partial \ddot{x}} = \frac{F_{NS}(\ddot{x}^{n+1,0} + \Delta\ddot{x}) - F_{NS}(\ddot{x}^{n+1,0})}{\Delta\ddot{x}}. \tag{VII.34}$$

Two extra Navier-Stokes (NS) evaluations per time step are needed with this approach to evaluate the derivative. It should be noted that the acceleration variables in this equation are those of the solid problem, because the acceleration variables are first used to compute new positions x with the time integration scheme and the forces F_{NS} are evaluated with these positions. So, the latter approach can be used to converge the subiterations for any value of the parameters α, β and γ. This approach is used with success for the moving valve problem, as is shown later.

VII.3. FSI of an aortic valve

VII.3.1. Problem definition

In order to verify the numerical behavior of the coupling procedure a two-dimensional representation of the aortic valve configuration is considered (figure VII.2). The model contains an inflow tract (inlet = left ventricle), a sinus of Valsalva (aortic valve), an outflow tract (outlet = aorta) and a rigid leaflet. The dimensions of the model are l_1 = 4 cm, l_2 = 4 cm, r_1 = 2 cm, r_2 = 0.7 cm, h = 2 cm, θ_{initial} = 0.384 rad = 22 degrees. The flow during the ejection phase (systole) is computed. As boundary conditions (figure VII.3) a pulsatile aortic flow in x-direction is given as a function of time at the inlet:

$$u_{\text{inlet}} = u_{\text{mean}} + 0.5 u_{\text{amp}} sin\left(\frac{2\pi\left((t-t_o)/T_p + 0.26\right)}{1.26}\right) \quad \text{for} \quad 0 < t < t_o \text{ and } t_o + 0.37\, T_p < t < T_p, \tag{VII.35}$$

$$u_{\text{inlet}} = u_{\text{mean}} + u_{\text{amp}} sin\left(\frac{2\pi(t-t_o)/T_p}{0.74}\right) \quad \text{for} \quad t_o < t < t_o + 0.37\, T_p. \tag{VII.36}$$

The parameters in this formula are T_p = 2.45 s, t_o = 0.4 s, u_{mean} = 0.04 m/s, u_{amp} = 0.11 m/s. The tangential velocity at the inlet is set equal to 0 m/s. At the outlet a constant gauge pressure of 0 Pa is assumed. On all the other walls *no slip* conditions are defined. The unknown variables of the problem are the velocity components

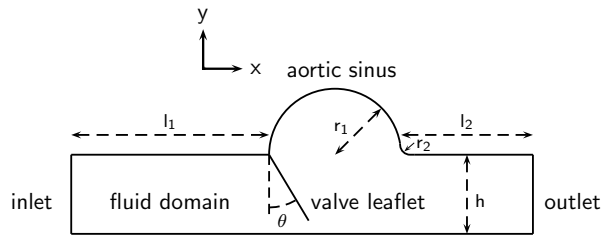

Figure VII.2.: Geometry of 2D aortic valve model.

in x- and y-direction and the pressure p, together with the coordinates (x, y) of the valve nodes determined by the angle θ.

The 2D Navier-Stokes equations for unsteady flow written in a conservative ALE

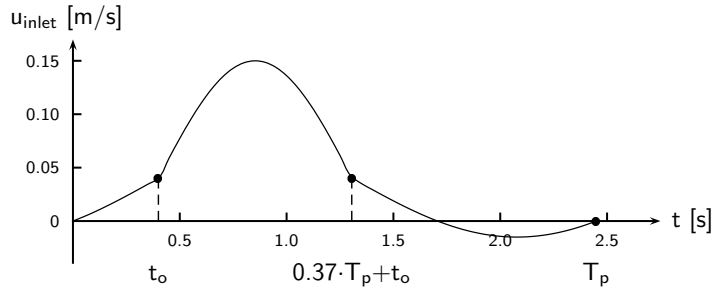

Figure VII.3.: Velocity boundary condition at the inlet as a function of time t.

formulation for incompressible laminar fluid flow are solved together with the continuity equation for each moving grid cell in the flow domain. Water (ρ_f=1000 kg/m^3, dynamic viscosity μ=1 mPa s) and blood (ρ_f=1000 kg/m^3, dynamic viscosity μ=4 mPa s) are used in the calculations. Both are treated as a Newtonian fluid. The computation is performed with the dynamic mesh model in the CFD software package Fluent (Fluent Inc.). As input the new position of the boundary nodes of the moving valve have to be prescribed at the beginning of a time step. The dynamic mesh model assumes that grid nodes are connected with springs and an equilibrium equation for the spring forces determines the position of the nodes at the new time level. Between time steps a local remeshing technique is used in order to keep a sufficient grid density during the movement of the valve. The positions of the boundary nodes at the new time level are prescribed through a user defined function (UDF) that can be coupled with the code. Since these positions depend on the FSI solution, a straightforward calculation is not possible. Therefore a journal file with commands to be executed, is used to drive the computation.
It is necessary to include read and write commands for the geometry and data files in this journal file, since it should be possible to start over each time step several times during the coupling procedure.
The equation of motion for the stiff valve leaflet is written as

$$M = I\ddot{\theta} \tag{VII.37}$$

with M the moment resulting from the forces acting on the surface of the leaflet, I the moment of inertia and θ the angle that determines the position of the leaflet as indicated in figure VII.2. For the valve leaflet, the moment of inertia I with the

rotational axis at the end of the leaflet is given by:

$$I = (1/3)ml^2 \tag{VII.38}$$

with $m = \rho lt$ the mass of the leaflet per unit length, ρ the density of the leaflet (1100 kg/m^3), t the thickness of the leaflet (1 mm and 0.5 mm) and l the length of the leaflet (22 mm). A reference length of 1 m is used in the third dimension, corresponding to the reference length used in the CFD package to calculate the moments. Both values for the moment of inertia $I = 3.909$ kg mm^2 and $I = 1.9545$ kg mm^2 are used.

VII.3.2. Implementation of the FSI

Figure VIII.3 presents a flow diagram of the coupling of the flow computations and the movement of the leaflet. The flow diagram corresponds to the method with implicit coupling in the subiterations. In the following paragraphs the different steps of the implementation are explained. First all UDF variables t, Δt, n, k, I, θ, $\dot{\theta}$, $\ddot{\theta}$ are initialized. The subsequent position of the valve leaflet on the new time level is calculated by coupling the time integration scheme for the solid with the CFD code. The time integration scheme for the solid is given by

$$\begin{aligned} \dot{\theta}^{n+1} &= \dot{\theta}^n + (1-\beta)\Delta t\ddot{\theta}^n + \beta\Delta t\ddot{\theta}^{n+1}, \\ \theta^{n+1} &= \theta^n + \Delta t\dot{\theta}^n + \gamma\Delta t^2\ddot{\theta}^n + \alpha\Delta t^2\ddot{\theta}^{n+1}. \end{aligned} \tag{VII.39}$$

The indices $n+1$ and n correspond with time levels $t+\Delta t$ and t respectively.
In order to obtain the position θ^{n+1} at $t+\Delta t$ an iterative approach is used. For each timestep there are k subiterations performed in order to reach sufficient convergence of eq. (VIII.6).
At the beginning of each time step, the derivative $dM/d\ddot{\theta}$ has to be estimated. A first estimation ($k = 0$) of the new position $\theta^{n+1,k=0}$ is computed with the old value of the angular acceleration $\ddot{\theta}^n$. This value of the acceleration is used to calculate the position using the equation eq. (VII.39). With this initial guess of the new position at $t + \Delta t$, Fluent is called to adapt the mesh with the dynamic mesh model and to solve the Navier-Stokes equations. After convergence of the Navier-Stokes equations, $M^{n+1,k=0}$ is calculated. A second estimation ($k = 1$) of the new position

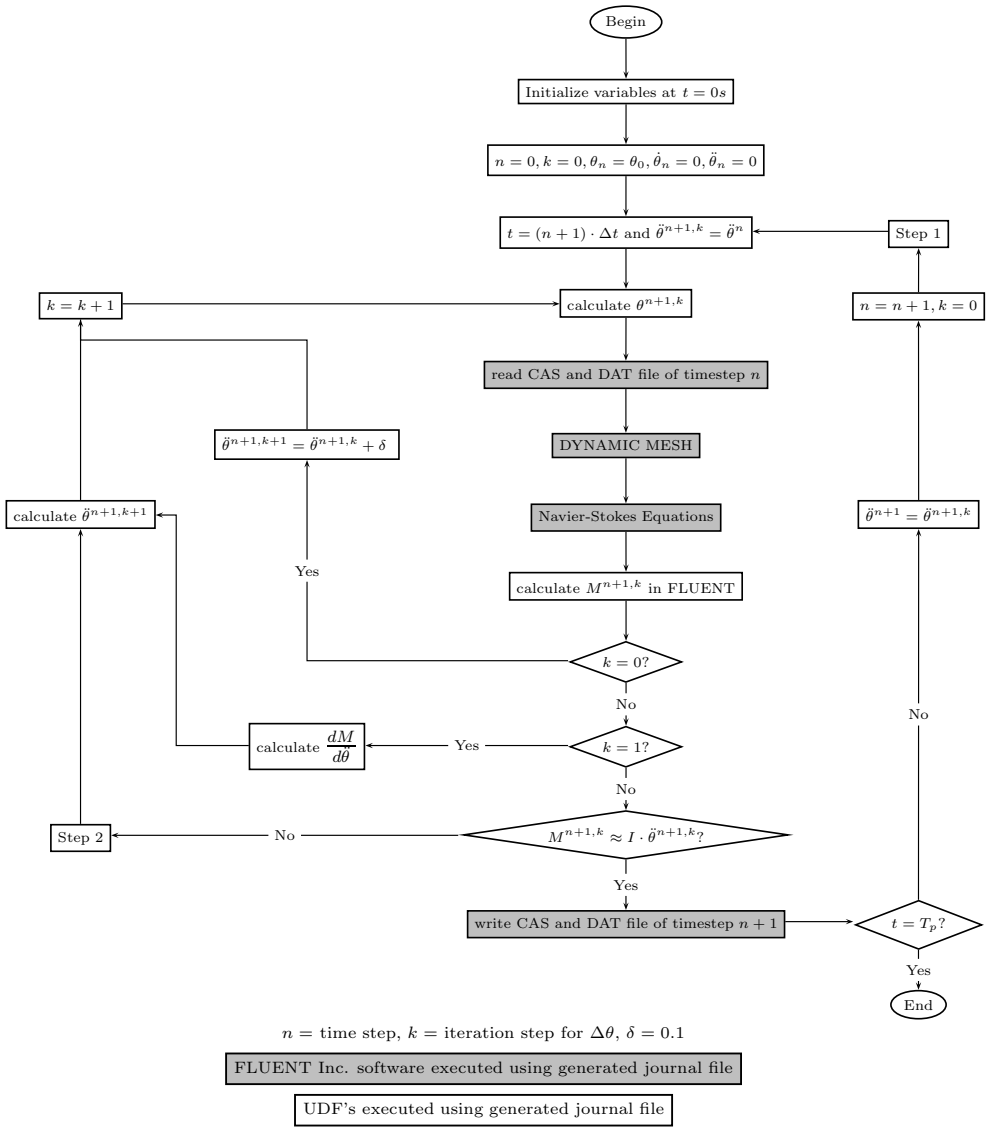

Figure VII.4.: Flow diagram of the coupling of fluid and structure in FLUENT.

$\theta^{n+1,k=1}$ is computed with the old value of the angular acceleration increased with a constant δ=0.1 rad/s^2. This value is about 1/100 of the maximum angular acceleration, which can be estimated from the inlet profile. It is shown that the choice of this value is not very sensitive. After convergence of the fluid problem, $M^{n+1,k=1}$

and the derivative $dM/d\ddot{\theta}$ is calculated as follows:

$$\begin{aligned} \ddot{\theta}^{n+1,k=0} &= \ddot{\theta}^{n} \\ \ddot{\theta}^{n+1,k=1} &= \ddot{\theta}^{n} + \delta \\ \frac{dM}{d\ddot{\theta}} &= \frac{M^{n+1,k=1} - M^{n+1,k=0}}{\ddot{\theta}^{n+1,k=1} - \ddot{\theta}^{n+1,k=0}} = \frac{M^{n+1,k=1} - M^{n+1,k=0}}{\delta}. \end{aligned} \tag{VII.40}$$

The derivative $dM/d\ddot{\theta}$ can now be used to calculate a better approximation of the position of the valve leaflet:

$$\begin{gathered} M^{n+1,k+1} = I\ddot{\theta}^{n+1,k+1} \\ \Downarrow \\ M^{n+1,k} + \frac{dM}{d\ddot{\theta}}\left(\ddot{\theta}^{n+1,k+1} - \ddot{\theta}^{n+1,k}\right) = I\ddot{\theta}^{n+1,k+1} \\ \Downarrow \\ \ddot{\theta}^{n+1,k+1} = \frac{\left(M^{n+1,k} - \frac{dM}{d\ddot{\theta}}\ddot{\theta}^{n+1,k}\right)}{\left(I - \frac{dM}{d\ddot{\theta}}\right)} \end{gathered} \tag{VII.41}$$

With this better approximation of the angular acceleration the new position is calculated, the mesh is adapted and the Navier-Stokes equations are solved. After convergence of the Navier-Stokes equations, $M^{n+1,k}$ is calculated and convergence of the inner loop is checked:

$$M^{n+1,k} \approx I\ddot{\theta}^{n+1,k}$$

The inner loop is repeated until convergence is achieved. A convergence criterium of a residual drop of 3 orders of magnitude is used. Then the next time step is computed. If only one cycle is computed, the simulation ends at t=T_p.

VII.4. Results and discussion

VII.4.1. Solution of the problem

Figure VII.5 shows the meshed geometry. It is shown in this figure that the ALE remeshing requires at least one cell in the gap between the valve leaflet and the

wall. Thus, the valve will never close completely. However, the gap can be made as small as required by local refinement of the mesh. The backward Euler time integration scheme for the solid has been used, unless stated otherwise. First a grid

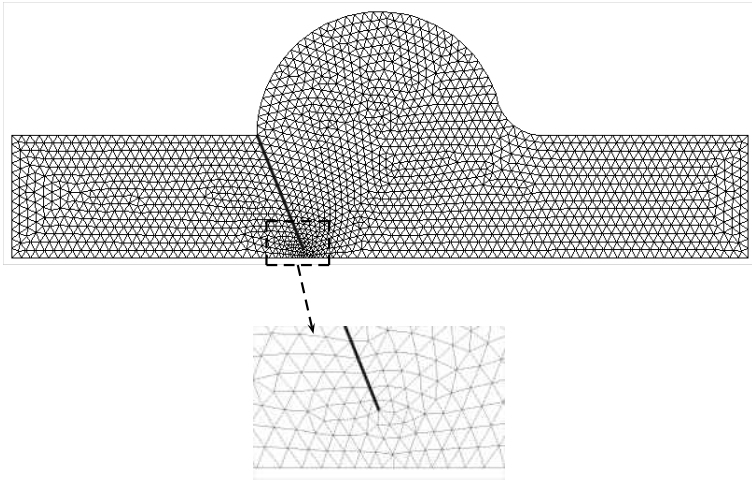

Figure VII.5.: ALE grid of the 2D aortic valve model.

convergence study is performed. This study is done with water as fluid, with a time step of 1 ms and with a moment of inertia I=3.909 kg mm^2. Three grids are considered. The angle of the valve is plotted as a function of time for the first cycle in figure VII.6. The finest grid is further used for all computations. The influence of the magnitude of the time step is shown in figure VII.7. Both computations are done for blood as fluid and for a moment of inertia $I = 1.9545$ kg mm^2. A time step equal to 1/1000 of the interval of the cycle (Δt = 2.45 ms) is compared with a time step of 1 ms for the coarse mesh. Both computations give the same result for the movement of the valve. A time step of Δt = 2.45 ms is further used for all computations, unless specified otherwise. A convergence study for the cycle is shown in figure VII.8. The positions of the valve at the beginning and the end of the third cycle correspond to each other, and the positions of the valve during the second half of the second cycle correspond with those of the third cycle. The pressure differences between inlet and outlet are also shown as a function of time in this figure. No differences can be seen between the different cycles. This pressure difference is however less sensitive, because it is mainly determined by the velocity profile applied at the inlet and this is the same for all cycles. The pressure difference plot shows two discontinuities at $t = t_o$ and at $t = t_o + 0.37T_p$. This is due to the

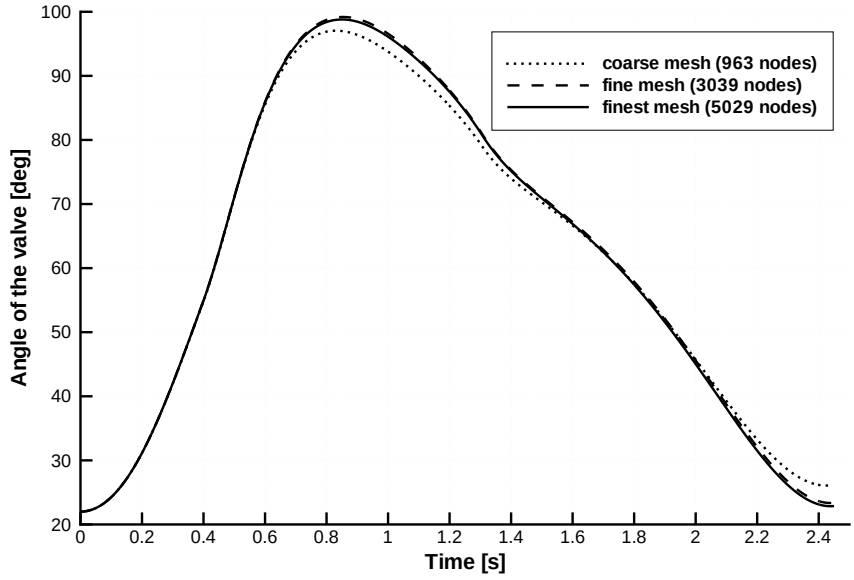

Figure VII.6.: Comparison of the evolution of the angle of the valve for different grids densities. The fluid is water, the moment of inertia of the valve I=3.909 kg mm^2 and the time step is 1 ms.

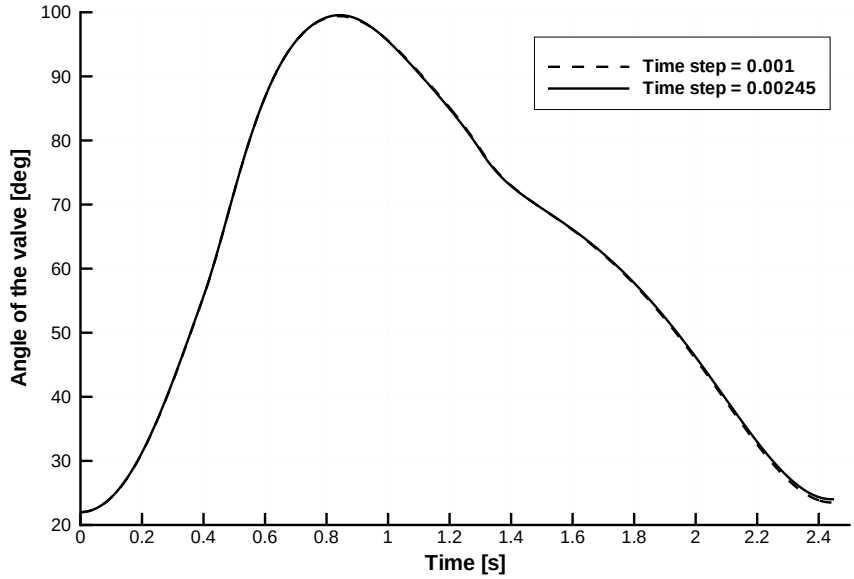

Figure VII.7.: Comparison of the evolution of the angle of the valve for two different time steps. The fluid is blood, the moment of inertia of the valve I=1.9545 kg mm^2.

fact that the inlet velocity has also this discontinuity in its derivative (figure VII.3). We conclude that from the third cycle on, the differences between the cycles can be assumed to be negligible. This discontinuity wouldn't have been present for a smoother inlet profile. However, if a strong acceleration would be present in the inlet profile during a short time interval and if a time step is used that does not resolve this time interval the same problem would arise. At this point spurious modes can enter the solution. These should be damped immediately. The inlet profile that is used introduces a spurious mode independent of the size of the time step. So, with this inlet profile the damping behavior for spurious modes of the different numerical schemes can be tested. Figure VII.9 demonstrates the velocity vectors at five different moments in time during the flow cycle. The arrows show how the vortices are changing during the cardiac cycle. These figures show that the opening and closing of the valve can be computed with the presented method. It is clear that the backflow plays an important role in the closing of the aortic valve: in the converged cycle the valve reaches the closed state because of the presence of a period during which backflow is present at the inlet boundary. We will further focus on the numerical behavior of the FSI problem, the application itself is not further discussed.

VII.4.2. Stability of the time integration scheme

The conclusions of the stability analysis on the generic 1D test case are numerically verified with the moving valve problem. The analogy between the two problems is already mentioned. The main difference of the 1D test case and this 2D problem is the difference in the length of the gap. In the 1D test case is assumed that only the acceleration of the fluid in the gap is responsible for the pressure difference across the solid. The influence of the 2D effects at both ends of the gap is neglected. In the 2D problem of the valve, the length of the gap is negligible. The pressure difference between both sides of the valve is now not only due to the acceleration of a small amount of fluid in the gap, but also the acceleration of fluid in front of and behind the gap, must be taken into account. This influence can not be quantified easily, but it is not necessary. It is clear that the mass of the fluid that must be accelerated is much more than only the mass of the fluid in the gap. This means that the factor K is not equal anymore to the expression given in eq. (VII.14), but much larger. It must also be remarked that when the valve reaches the open state, a gap exists

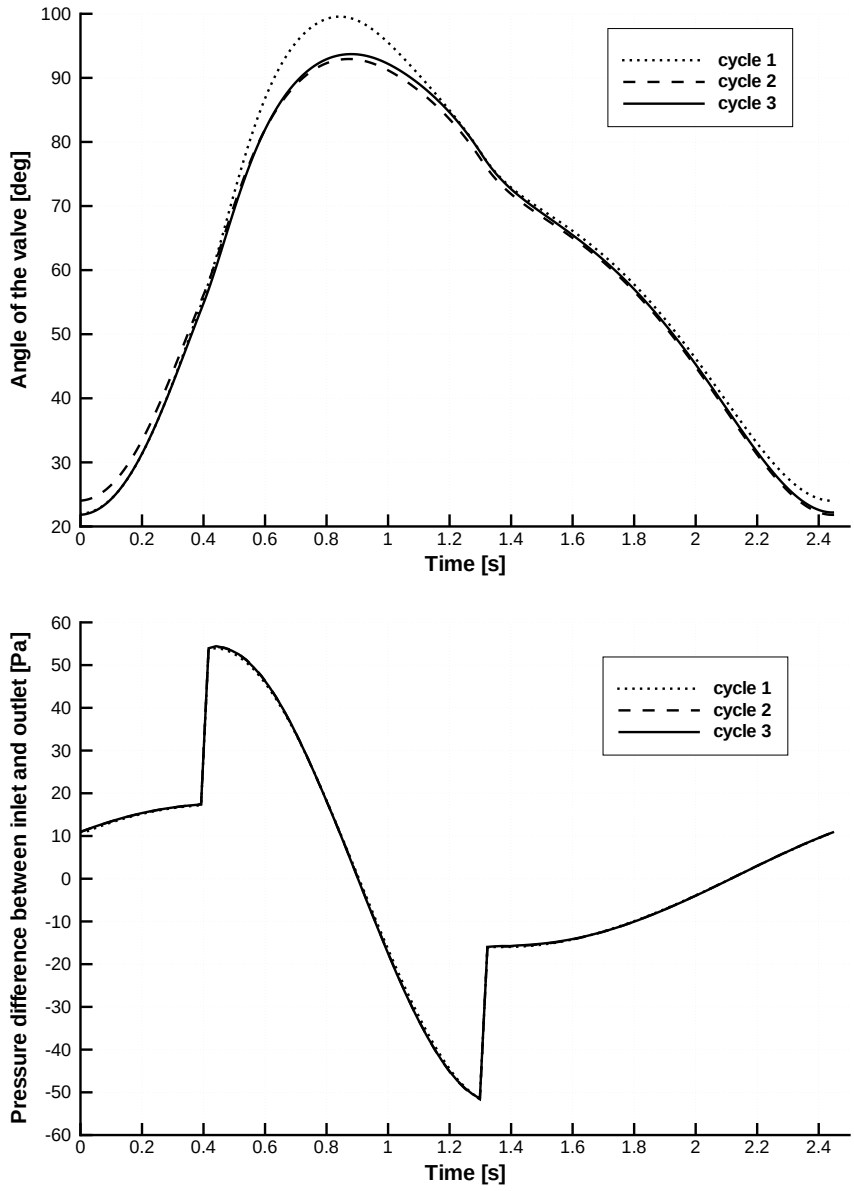

Figure VII.8.: Evolution of the angle of the valve and the pressure difference between the inlet and outlet for the first three cycles. The fluid is blood, the moment of inertia of the valve I=1.9545 kg mm^2.

between the main flow and the fluid in the sinus of Valsalva. Therefore, the 1D test case problem is representative for most of the cycle during opening and closing of the valve, and especially in the completely closed and open positions.

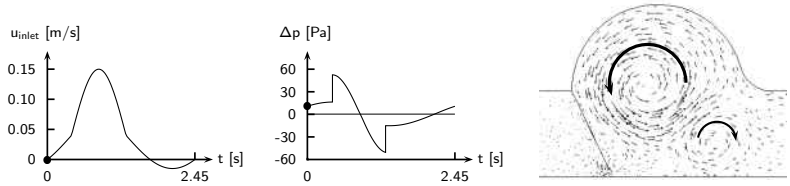

(a) t = 0.00s

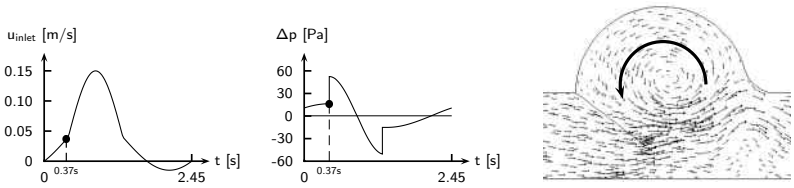

(b) t = 0.37s

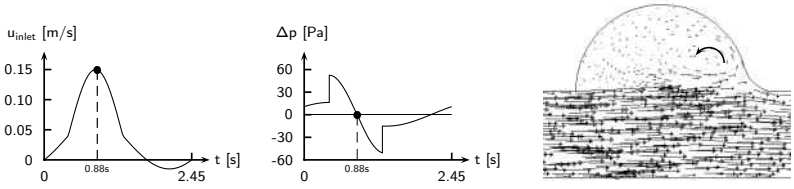

(c) t = 0.88s

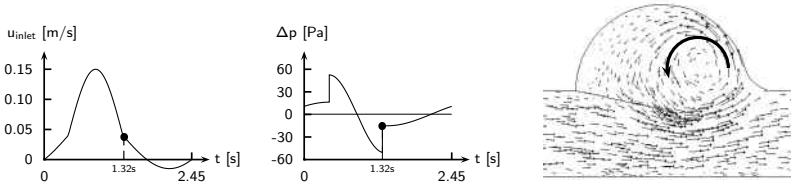

(d) t = 1.32s

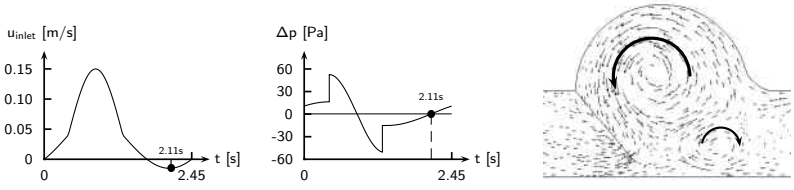

(e) t = 2.11s

Figure VII.9.: Velocity vectors for t = 0.00s, t = 0.37s, t = 0.88s, t = 1.32s, t = 2.11s.

Tables VII.1 and VII.2 show the evolution of the angle, the angular velocity and the angular acceleration during the first four time steps of the first cycle for an explicit time integration scheme ($\alpha = \beta = \gamma = 0$) for the motion of the solid. Two time

steps are compared: Δt=1 ms and Δt=0.01 ms. Blood is used as fluid and the moment of inertia I=3.909 kg mm^2.

Time	θ [rad]	$\dot{\theta}$ [rad/s]	$\ddot{\theta}$ [rad/s^2]
0.000	0.3840	0.00	0.00
0.001	0.3840	0.00	284.91
0.002	0.3841	0.28	-4971.54
0.003	0.3819	-4.69	96525.94
0.004	0.4255	91.84	-5054412.89

Table VII.1.: Explicit stepping $\alpha = \beta = \gamma = 0$, Δt = 0.001 s.

Time	θ [rad]	$\dot{\theta}$ [rad/s]	$\ddot{\theta}$ [rad/s^2]
0.00000	0.383972000	0.000000	0.00
0.00001	0.383972000	0.000000	269.71
0.00002	0.383972013	0.002697	-4319.77
0.00003	0.383971824	-0.040501	71972.37
0.00004	0.383975018	0.679223	-1193827.07

Table VII.2.: Explicit stepping $\alpha = \beta = \gamma = 0$, Δt = 0.00001 s.

The explicit scheme is unstable. The spurious modes are more or less amplified in the same way in both calculations independent of the time step. This behavior is predicted by the stability analysis.

For the calculations in the rest of this paragraph, blood is used as fluid, a time step Δt=2.45 ms and a moment of inertia I=1.9545 kg mm^2 are used.

In table VII.3, some Newmark schemes, the backward Euler scheme and some of the other (β=1, γ=0) schemes are tried out. The angular acceleration of the first three time steps of the first cycle are given. The backward Euler scheme gives a critically damped behavior and can be treated as a reference for the other schemes. In figures VII.10-VII.12, the angle, the angular velocity and the angular acceleration computed with the backward Euler scheme, the second order Newmark scheme ($\alpha = 1/4$, $\beta = 1/2$), the fully implicit Newmark scheme ($\alpha = 1/2$, $\beta = 1$) and a damping Newmark scheme ($\alpha = 0.4$, $\beta = 0.6$) are shown as a function of time for

the complete first cycle. With this table and these figures, part of the conclusions

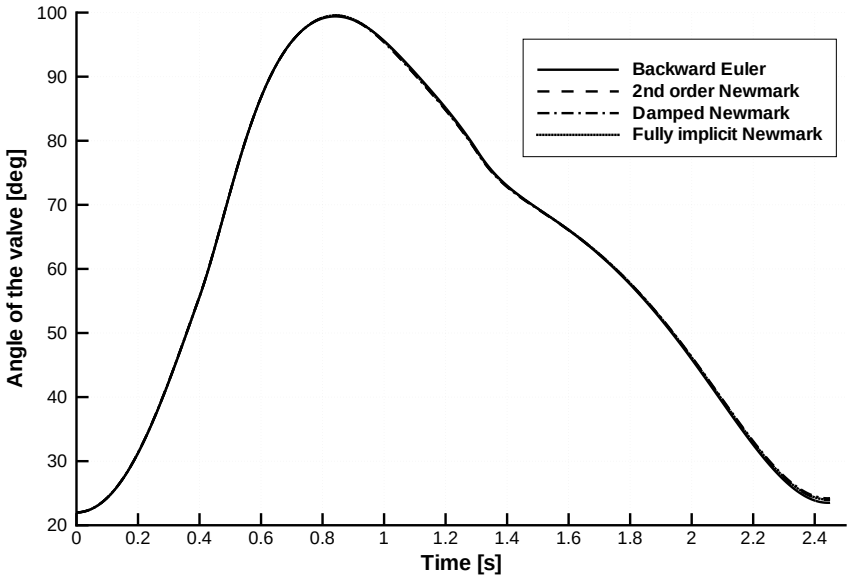

Figure VII.10.: Comparison of the evolution of the angle of the valve for the first cycle computed with the backward Euler scheme, the second order Newmark scheme, the fully implicit Newmark scheme and a damping Newmark scheme ($\alpha = 0.4, \beta = 0.6$). The fluid is blood, the time step Δt is 2.45 ms and the moment of inertia of the valve I=1.9545 kg mm^2.

Class	Scheme	$\ddot{\theta}$ [rad/s^2] t=0.00245 s	$\ddot{\theta}$ [rad/s^2] t=0.00490 s	$\ddot{\theta}$ [rad/s^2] t=0.00735 s
Newmark	α=1/4, β=1/2	29.201	-26.191	51.106
$\gamma = 1/2 - \alpha$	α=1/2, β=1	14.963	0.413	14.577
	α=0.4, β=0.6	18.604	5.101	1.415
	α=0.4	18.604	-8.418	30.842
	α=0.5	14.963	0.413	14.577
β=1, $\gamma = 0$	α=0.6	12.533	4.354	9.706
	α=0.8	9.449	7.121	7.709
	Backward Euler α=1	7.576	7.587	7.592
	α=1.5	5.077	6.751	7.312

Table VII.3.: Damping of the spurious modes for different schemes. $\ddot{\theta}$ is converged in the subiterations.

of the stability analysis for the generic 1D test case is verified. The second order Newmark and the fully implicit Newmark scheme show almost no damping. The

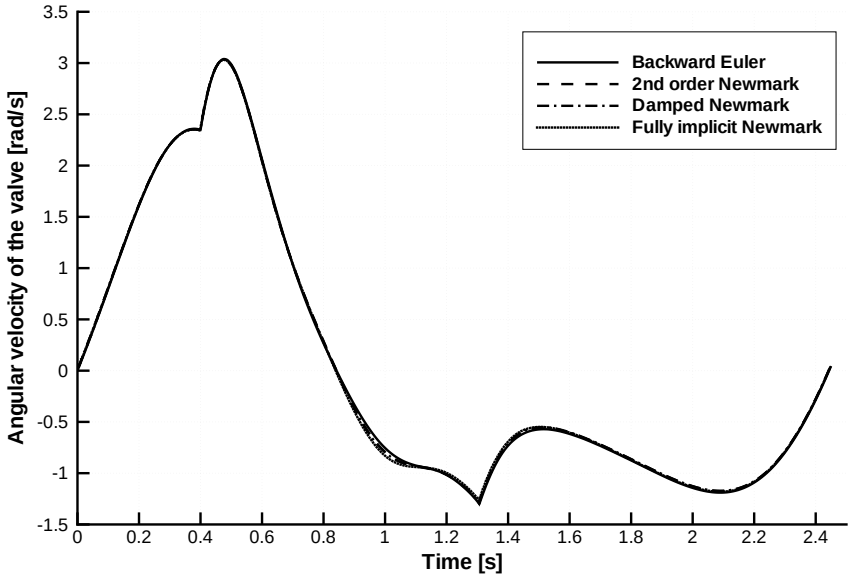

Figure VII.11.: Comparison of the evolution of angular velocity of the valve for the first cycle computed with the backward Euler scheme, the second order Newmark scheme, the fully implicit Newmark scheme and a damping Newmark scheme ($\alpha = 0.4, \beta = 0.6$). The fluid is blood, the time step Δt is 2.45 ms and the moment of inertia of the valve I=1.9545 kg mm^2.

damping of the (β=1, γ=0) schemes behaves also as was predicted. For α=0.4 the scheme is unstable, for α=1/2, the scheme is weakly damped, for α=0.6 and α=0.8 the scheme gives subcritical damping for the spurious modes with an oscillatory behavior. For α=1, the backward Euler scheme, is obtained which gives critical damping for the spurious modes. They are damped immediately. For α=1.5, a supercritical damping behavior is seen. Agreement with the stability analysis is obtained for all these tests.

In table VII.4 the convergence of the subiteration process is analyzed for one time step of the backward Euler scheme. The analysis is done at time level $t = 2.695$ s. This time level is chosen because at this point the convergence behavior of the subiteration process is the worst compared with the rest of the cycle. At this time level the angle of the valve is 0.6612 rad or 37.89 degrees. The difference between the moment computed with the CFD software and $I\ddot{\theta}$ is given for the first 4 subiterations. When the implicit approach is used in the subiterations, the first two subiterations are used to calculate the derivative.

With explicit coupling in the subiterations, no convergence could be obtained.

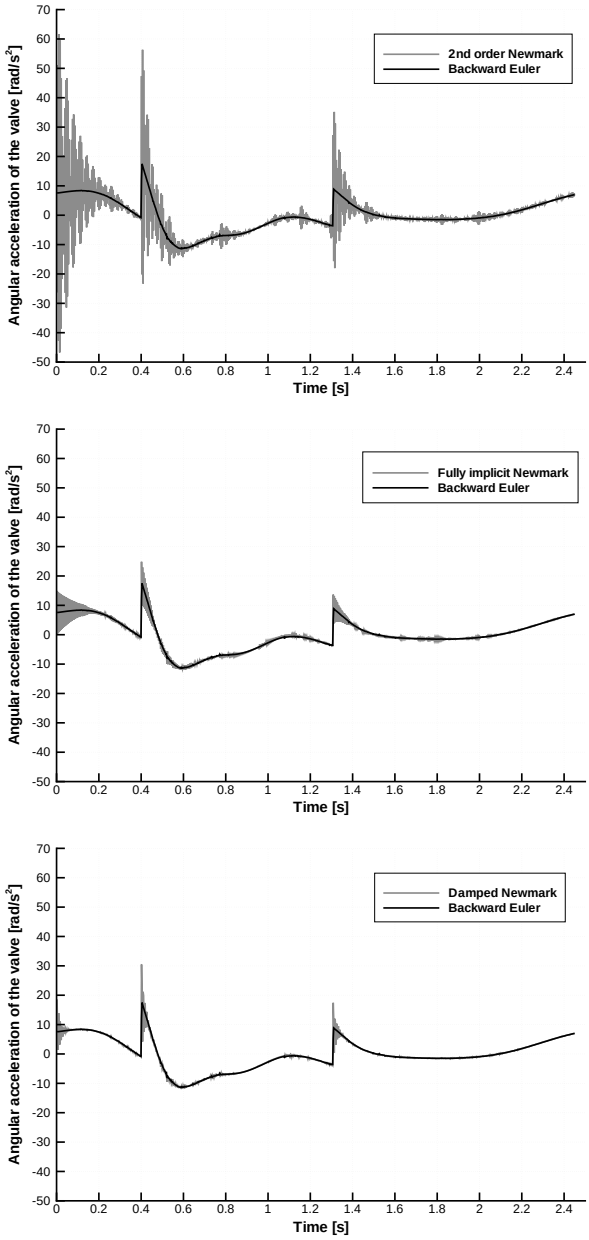

Figure VII.12.: Comparison of the evolution of the angular acceleration of the valve for the first cycle computed with the backward Euler scheme, the second order Newmark scheme, the fully implicit Newmark scheme and a damping Newmark scheme ($\alpha = 0.4, \beta = 0.6$). The fluid is blood, the time step Δt is 2.45 ms and the moment of inertia of the valve I=1.9545 kg mm^2.

Method	$M_{CFD} - I\ddot{q}$ [Nm] Subiter 1	$M_{CFD} - I\ddot{q}$ [Nm] subiter 2	$M_{CFD} - I\ddot{q}$ [Nm] subiter 3	$M_{CFD} - I\ddot{q}$ [Nm] subiter 4	Remark
Explicit	4.918E-04	1.177E-02	3.378E-01	Crash	Diverging
ω = 0.05	1.119E-05	1.583E-05	2.313E-05	3.360E-05	Diverging
ω = 0.025	1.121E-05	2.431E-06	5.2670E-07	1.148E-07	
ω = 0.005	1.123E-05	8.493E-06	6.428E-06	4.865E-06	Very slow
$\delta = 10^{-7}$ rad/s^2	Calculation of $\partial F/\partial\ddot{\theta}$		1.2944E-05	6.2502E-04	Diverging
δ = 0.001 rad/s^2	Calculation of $\partial F/\partial\ddot{\theta}$		1.3294E-05	3.0894E-08	
δ = 0.1 rad/s^2	Calculation of $\partial F/\partial\ddot{\theta}$		1.122E-05	3.740E-07	
δ = 1 rad/s^2	Calculation of $\partial F/\partial\ddot{\theta}$		1.122E-05	7.142E-07	
δ = 100 rad/s^2	Calculation of $\partial F/\partial\ddot{\theta}$		1.3294E-05	3.0894E-08	
δ = 100000 rad/s^2	Calculation of $\partial F/\partial\ddot{\theta}$ crashes				Crash

Table VII.4.: Behavior of the error of the subiterations for the backward Euler scheme ($\alpha = \beta = 1, \gamma = 0$) at time level t=2.695 s. Different subiteration strategies are compared.

For an underrelaxation factor ω=0.025, a good damping is obtained, a value ω=0.05 leads to divergence and for a value ω=0.005 almost no damping of the subiteration process is obtained. This shows the sensitivity to the underrelaxation factor. As the factor K changes during the opening and the closing process, a good value for the whole cycle could not be obtained.

The implicit method uses the derivative of the force with respect to the angular acceleration and shows good damping for a broad range of values of δ, defined in eq. VIII.9. This value determines the displacement of the valve in the second step of the subiteration cycle. This displacement should be less than the size of the grid cells in the vicinity of the valve. We used a value of δ=0.1 rad/s^s, because it is almost 1/100 of the maximum acceleration present in the problem. This maximum acceleration can be estimated from the inlet boundary condition in our application. Another way to choose δ is to use a fraction of the current angular acceleration. The value must then be prohibited to become too small if the angular acceleration becomes close to zero. For too small values of δ, the difference between the two moments from which the derivative is computed becomes too small and is of the same size or even smaller than the error on the computed moments. The magnitude of this error depends on the accuracy of the solution of the Navier-Stokes problem. We used a residual drop of three orders of magnitude as a convergence criterium for the fluid solver. In the table it is shown that a too small value of δ leads to a crash of the calculation, because of this reason. If δ is taken too large, the displacement that

corresponds with it is also too large and the moving mesh solver diverges, which explains the crash in this situation. The choice of δ is application dependent but not very sensitive, which makes the method robust.

The behavior of the subiteration process also matches the behavior predicted in the generic 1D test problem.

VII.5. Conclusions

This study shows a stability analysis for FSI problems where different fluid zones are almost separated by a moving rigid body, but connected through gaps in the vicinity of the moving rigid body. A FSI calculation procedure is constructed that couples the movement of a rigid body with the flow calculations performed in a commercial CFD package. The procedure is succesfully applied to the opening and closing of a two dimensional model for the aortic valve.

From the stability analysis and the numerical experiments, it can be concluded that the matching of the time integration scheme for the fluid and the solid problem is very important for these kind of FSI problems. It has been shown that for a backward Euler scheme used in the fluid problem, a backward Euler scheme for the solid problem damps all the spurious modes of the coupling procedure immediately. The second order Newmark scheme and the fully implicit Newmark scheme show a weakly damped behavior. Other schemes with good damping behavior can be constructed. The stability analysis showed also that for loosely coupled FSI problems, the matching of the numerical scheme for the fluid and the solid problem is much less important to damp the spurious modes.

A second conclusion is that also the convergence of the subiteration process deserves a lot of attention for these kind of FSI problems. A standard underrelaxation technique does not work well because the choice of the underrelaxation factor is very sensitive to the amount of stiffness of the coupling. Since this stiffness is not necessarily constant during a calculation, such a method is not robust. The use of an implicit coupling procedure in the subiterations, with the use of a numerically computed derivative, which acts as a sensitivity parameter, leads to a robust method to tackle these stiff FSI problems.

Chapter VIII

Validation of a fluid-structure interaction model of a heart valve using the dynamic mesh method in Fluent

The contents of this chapter is published in Computer Methods in Biomechanics and Biomedical Engineering 2003;7(3):139-146.
Validation of a fluid-structure interaction model of a heart valve using the dynamic mesh method in Fluent
Dumont K, Stijnen J, Vierendeels J, van de Vosse F, Verdonck P

Abstract

Simulations of coupled problems such as fluid-structure interaction (FSI) are becoming more and more important for engineering purposes. This is particularly true when modeling the aortic valve, where the fluid-structure interaction between the blood and the valve determines the valve movement and the valvular haemodynamics. Nevertheless only a few studies are focusing on the opening and closing behavior during the ejection phase (systole). In this paper we present the validation of a FSI model using the dynamic mesh method of Fluent for the two-dimensional (2D) simulation of mechanical heart valves during the ejection phase of the cardiac cycle. The FSI model is successfully validated by comparing simulation results to experimental data obtained from *in vitro* studies using a CCD camera.

VIII.1. Introduction

The interaction between blood and structure plays an important role in many biofluid dynamic flow problems such as blood flow in the heart, vessels, heart valves, cardiac assist devices and in artificial organ design.[134,156] The opening and closing of a heart valve during systole involves a strong interaction between blood and the surrounding tissue. Only a few numerical models[29,30,81,141,159,166,196,197] have been made to analyze the valve kinematics during systole using numerical fluid-structure interaction models.

Different numerical techniques have been used to tackle this fluid-structure interaction (FSI) problem. Immersed boundary techniques were already used from the late seventies by Peskin and McQueen[145] and Yellin *et al*.[198] Widespread is the Arbitrary Lagrangian-Eulerian ALE method,[199] commonly used for modeling blood flow in arteries.[200] The ALE method requires continuously updating the fluid mesh to accommodate for the motion of the structural domain. In contrast, the fictitious domain formulation[150] circumvents the fluid mesh updating: the fluid is described using a fixed mesh in an Eulerian setting, the coupling of fluid and structure is taken care of by so called Lagrange multipliers.

These numerical techniques can be used to calculate details or features of the flow field that are important to know, but impossible to measure. One such feature is wall shear stress. Shear stress is an important biomechanical modulator of endothelial function and vascular tissue remodeling,[201] and thus a critical parameter that requires precise control in various tissue engineering applications, among which the cultivation of (aortic) valve prosthesis in bioreactor systems.

Recently, Fluent Inc. (New Hampshire, US) released the dynamic mesh model for the simulation of flows where the shape of the domain is changing with time due to the motion of the domain boundaries. The dynamic mesh model makes use of an ALE and local remeshing approach to adapt the mesh in FSI problems. The motion of a boundary is then described using user-defined functions (UDFs).

In this work, we describe a numerical model to simulate aortic valve haemodynamics making use of Fluent software, but implementing a user-defined iterative procedure to simulate valve motion. For the validation of our code, we run simulations using the 2D geometry and boundary conditions as used in *in vitro* experiments by the group of F.N. van de Vosse of the Eindhoven University of Technology.[196,197]

As such, we can directly compare the FSI model to experimental data obtained via a CCD Camera in a pulse duplicator.

VIII.2. Methods

VIII.2.1. Experimental method

In order to validate the results obtained by the computational model, experiments were performed in an *in vitro* setup. The experimental setup, shown in figure VIII.1(a), is a two-dimensional representation of a cross section of the aortic valve. The valve section of the setup (figure VIII.1(b)) consists of a plexiglass channel,

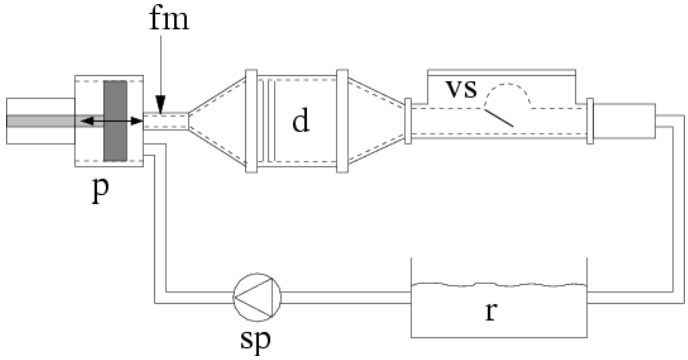

(a) Schematic drawing of the pulse duplicator setup. (p) piston, (d) diffuser, (vs) the valve section, (r) reservoir, (sp) stationary pump and (fm) flow meter.

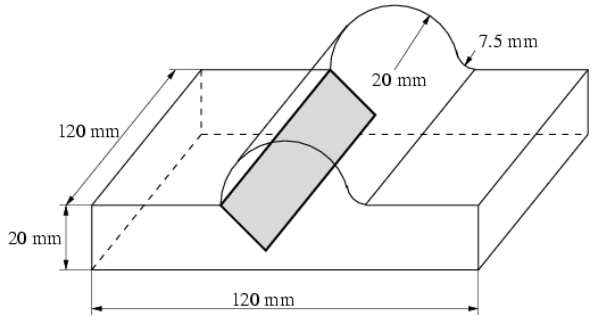

(b) Schematic representation of the valve compartiment of the experimental setup.

Figure VIII.1.: Experimental setup of TUEindhoven.

with a heigth of 20 mm and length of 120 mm. In order to obtain a two-dimensional flow field in the center of the channel, the width of the channel is taken 120 mm.

Located in the middle of the length of the channel, is a cilindrical cavity with a radius of 20 mm, representing the aortic sinus. At the downstream side of the cavity, the transition of the cavity to the outflow channel is rounded, with a radius of 7.5 mm. At the upstream transition of the channel to the cavity a stiff strip of lexane, representing the leaflet, is attached to the top of the channel using three strips of water resistant adhesive tape, one in the center of the cavity and two near the side walls. In order to keep the bending stiffness of the tape low, the width of the strips of adhesive tape was 5 mm. The valve section was mounted in a pulse duplicator setup, as shown in figure VIII.1(a). The pulse duplicator setup consists of a steady pump (sp), a computer controlled piston (p), a diffusor (d), the valve section (vs) and reservoir (r). The flow downstream the piston was measured using an electromagnetic flow meter (fm). In order to obtain physiologically relevant fluid flow parameters, the fluid used was a mixture of 36% by volume of glycerol in water, having a dynamic viscosity μ of 4 mPa $\cdot$ s.

The generated flow pulse resembles the aortic flow in the sense that there is a large flow peak lasting approximately 37 % of the cardiac cycle which is due to the blood being ejected from the heart, while during the rest of the cardiac cycle the flow rate is low. The flow pulse was obtained by a stationary flow rate, delivered by the stationary pump, to which a pulsating flow is added by the computer controlled motion of the piston. With an average peak inflow velocity (V) of 0.15 m/s, a density (ρ) of 1090 kg/m^3, a channel heigth (h) of 20 mm, a viscosity (μ) of 4 mPa·s = 4·10^{-3}kg/(m $\cdot$ s) and a period time T_p of 2.45 s, the flow pulse is characterized by the Reynolds number of 750 and the Strouhal number of 0.055, where Reynolds and Strouhal are defined as:

$$Re = \frac{\rho V h}{\mu} \qquad\qquad Sr = \frac{h}{T_p V} \tag{VIII.1}$$

The position of the valve leaflet was recorded by a CCD camera (Kodak ES-1.0) at 50 instants in the flow cycle. The opening angle of the valve is derived from the position of the valve in the camera images.

VIII.2.2. Geometry and mesh of the numerical aortic valve model

The two-dimensional geometry (figure VIII.2) consists of an inflow tract (inlet = left ventricle), a sinus of Valsalve (aortic valve) and an outflow tract (outlet = aorta). The dimensions of the geometry are l_1 = 4 cm, l_2 = 4 cm, r_1 = 2 cm, r_2 = 0.75 cm, h = 2 cm, $\theta_{initial}$ = 0.384 rad = 22 degrees.
An example of the computational mesh is shown in figure VIII.2(b). First a grid convergence study is performed. Three different grid densities, e.g. ±1000, ±3000 and ±5000 nodes, were studied. The finest mesh showed to give grid independent results. Because of the limitations in the dynamic mesh model, there is at least one cell required to cover the gap between the valve leaflet and the wall. This one cell needs to ensure that the fluid domain is preserved as one entity. Furthermore, to increase the accuracy of the flow calculations, the mesh at the gap is made even more dense, as can be seen in figure VIII.2(b). As such, it is not possible to simulate perfectly closing devices using the remeshing technique, which could be seen as a limitation of the technique. As we are interested in studying aortic valve hydrodynamics during systole (ejection phase), we assume that this does not influence our study. Furthermore the diastolic phase is not taken into account.

VIII.2.3. Governing equations of the numerical model

The unknown variables are the velocity component u in x-direction, the velocity component v in y-direction, the pressure p and the coordinates (x, y) of the valve nodes determined by the angle θ.
The continuity equation in integral form Eq(VIII.2) is given by

$$\frac{\partial}{\partial t}\int_V \rho dV + \int_S \rho(\overrightarrow{\boldsymbol{v}} - \overrightarrow{\boldsymbol{v}_b}) \cdot \overrightarrow{\boldsymbol{n}}\, dS \;=\; 0 \qquad \text{(VIII.2)}$$

where $\int_V ...dV$ is the integral over a control "volume", $\int_S ...dS$ is the integral over a control "surface", $\overrightarrow{\boldsymbol{n}}$ is the outwardly directed vector normal to dS, ρ is the density of the fluid, $\overrightarrow{\boldsymbol{v}}$ = (u,v) is the velocity vector of the fluid, $\overrightarrow{\boldsymbol{v}_b}$ = (u_b,v_b) is the velocity vector of the moving boundary. For each face j of the control volume $\overrightarrow{\boldsymbol{v}_{b,j}} \cdot \overrightarrow{\boldsymbol{n}}\, dS_j$ is computed from $\frac{\delta V_j}{\Delta t}$ where δV_j is the volume swept out by the control volume face j over the time step Δt. With this definition of $\overrightarrow{\boldsymbol{v}_{b,j}}$ the so called space conservation

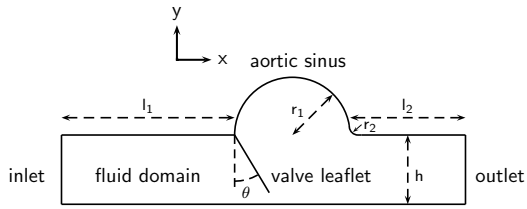

(a) Geometry of 2D aortic valve model.

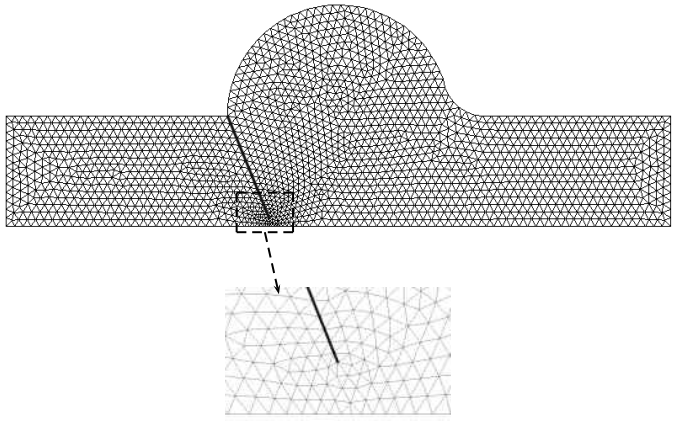

(b) ALE Grid of the 2D aortic valve model.

Figure VIII.2.: Geometry and mesh of the 2D valve model.

law Eq(VIII.3) is fulfilled for each control volume.

$$\frac{\partial}{\partial t}\int_V dV \;=\; \int_S \vec{\boldsymbol{v}_b}\cdot\vec{\boldsymbol{n}}\,dS \tag{VIII.3}$$

The momentum equation in integral form is given by Eq(VIII.4)

$$\frac{\partial}{\partial t}\int_V \rho\vec{\boldsymbol{v}}\,dV + \int_S \rho\vec{\boldsymbol{v}}(\vec{\boldsymbol{v}}-\vec{\boldsymbol{v}_b})\cdot\vec{\boldsymbol{n}}\,dS \;=\; -\int_S p\vec{\boldsymbol{n}}\,dS + \int_S \underline{\overline{\boldsymbol{\tau}}}\cdot\vec{\boldsymbol{n}}\,dS \tag{VIII.4}$$

where $\underline{\overline{\boldsymbol{\tau}}}$ is the stress tensor. Body forces were neglected. The density of the rigid leaflet (1100 kg/m^3) is almost equal to the fluid density (1090 kg/m^3), therefore the buoyancy force can be neglected. The stress tensor $\underline{\overline{\boldsymbol{\tau}}}$ is given by Eq(VIII.5)

$$\underline{\overline{\boldsymbol{\tau}}} = 2\mu\underline{\overline{\boldsymbol{\gamma}}} = 2\mu\begin{bmatrix} \dfrac{\partial u}{\partial x} & \dfrac{1}{2}\left(\dfrac{\partial u}{\partial y}+\dfrac{\partial v}{\partial x}\right) \\ \dfrac{1}{2}\left(\dfrac{\partial u}{\partial y}+\dfrac{\partial v}{\partial x}\right) & \dfrac{\partial v}{\partial y} \end{bmatrix} \tag{VIII.5}$$

where $\overline{\underline{\gamma}}$ is the strain rate tensor. Flow is assumed laminar and a constant dynamic viscosity μ of 4 mPa·s for the fluid is used. Finally, the equation of motion Eq(VIII.6) for the leaflet can be written as

$$M = I \cdot \ddot{\theta} \tag{VIII.6}$$

with M the torque per unit length on a stiff valve leaflet, I the moment of inertia per unit length and θ the opening angle of the leaflet as indicated in figure VIII.2(a). For the valve leaflet the moment of inertia I with the rotational axis along the edge of the leaflet can be calculated as Eq(VIII.7):

$$I = (1/3) \cdot m \cdot l^2 \tag{VIII.7}$$

with $m = \rho_{leaflet} \cdot l \cdot t$ the mass of the leaflet per unit length, $\rho_{leaflet}$ the density of the leaflet (1100 kg/m^3), t the thickness of the leaflet (1 mm) and l the length of the leaflet (22 mm). This results in $I = 3.9{\cdot}10^{-6}$ kg·m^2/m.
The continuity Eq(VIII.2), space conservation Eq(VIII.3) and momentum Eq(VIII.4) equations for incompressible laminar flow are solved for each moving grid cell in the fluid domain. The CFD software package Fluent (Fluent Inc.) is used to solve the governing equations. Fluent is based on the finite volume method, where the domain is discretized into a finite set of control volumes or cells. A backward Euler 1st order implicit scheme is used for the time integration of the fluid flow. The implementation of these equation in the Fluent package is out of the scope of this paper.
Our FSI model uses the dynamic mesh method of the CFD software package. This method uses a user defined function (UDF) that can be coupled with the code. As input of the UDF the position of the boundary nodes of the moving valve have to be prescribed at the beginning of a new time step. Since these positions depend on the FSI solution, a straightforward calculation is not possible and an iteration strategy is necessary. Therefore journal files are generated and then used to drive the computation.

VIII.2.4. Implementation of the interaction between fluid and structure

Figure VIII.3 presents a flow diagram of the solution strategy. In the following paragraphs the different steps of the scheme are explained.
First all UDF variables t, Δt, n, k, I, θ, $\dot{\theta}$, $\ddot{\theta}$ are initialized. The subsequent position in function of time of the valve leaflet is calculated with a backward Euler scheme (figure VIII.3). This in accordance with the scheme used in Fluent.

$$\begin{aligned} \dot{\theta}^{n+1} &= \dot{\theta}_n + \Delta t \cdot \ddot{\theta}^{n+1} \\ \theta^{n+1} &= \theta_n + \Delta t \cdot \dot{\theta}^{n+1} \end{aligned} \tag{VIII.8}$$

In this way a full implicit scheme is obtained. The indices $n+1$ and n correspond with time levels $t + \Delta t$ and t respectively. In order to obtain the position θ^{n+1} at $t + \Delta t$ an iterative approach is used. For each timestep there are k iterations performed in order to reach sufficient convergence of Eq(VIII.6).

VIII.2.4.1. Step 1

Two initial steps are done in order to estimate the derivative $dM/d\ddot{\theta}$ (Eq(VIII.9)). A first estimation ($k = 0$) of the new position $\theta^{n+1,k=0}$ is computed with the old value of the angular acceleration $\ddot{\theta}_n$. This value of the acceleration is used to calculate the position using equation Eq(VIII.8). With this initial guess of the new position at $t + \Delta t$ the mesh is adapted with the dynamic mesh model. After adaptation of the mesh, Fluent is used to solve the continuity and momentum equations. After convergence of the Navier-Stokes equations, $M^{n+1,k=0}$ is calculated. A second estimation ($k = 1$) of the new position $\theta^{n+1,k=1}$ is computed with the old value of the angular acceleration increased with a constant δ=0.1rad/s^2. This iteration step results in the value of $M^{n+1,k=1}$ and the derivative $dM/d\ddot{\theta}$ can be calculated.

$$\begin{aligned} \ddot{\theta}^{n+1,k=0} &= \ddot{\theta}^{n} \\ \ddot{\theta}^{n+1,k=1} &= \ddot{\theta}^{n} + \delta \\ \frac{dM}{d\ddot{\theta}} &= \frac{M^{n+1,k=1} - M^{n+1,k=0}}{\ddot{\theta}^{n+1,k=1} - \ddot{\theta}^{n+1,k=0}} = \frac{M^{n+1,k=1} - M^{n+1,k=0}}{\delta} \end{aligned} \tag{VIII.9}$$

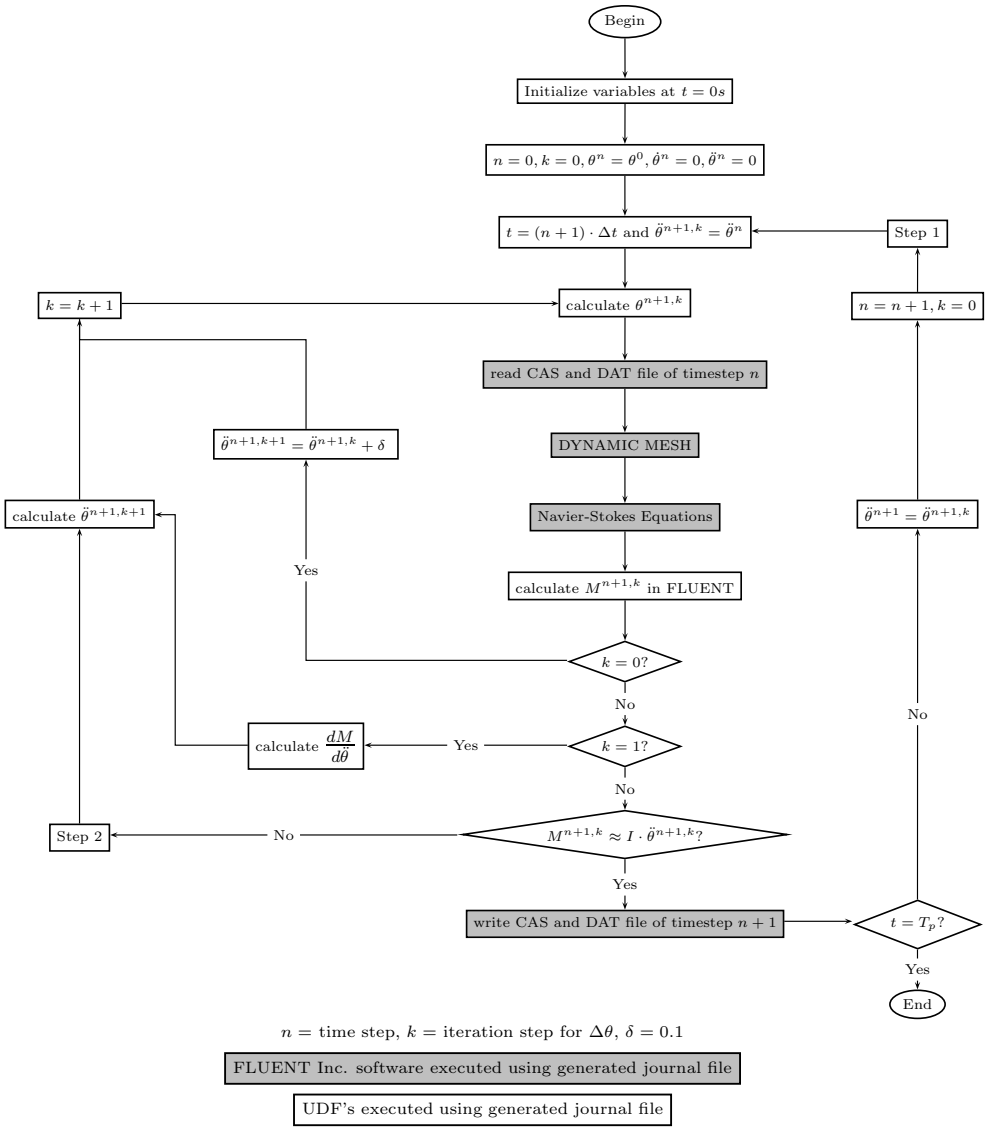

Figure VIII.3.: Flow diagram of the coupling of fluid and structure in FLUENT.

The derivative is only computed once for each timestep and held constant during the iteration cycle. The value of this derivative only affects the convergence of the iteration proces.[140]

VIII.2.4.2. Step 2

The derivative $dM/d\ddot{\theta}$ can now be used the calculate more correct position of the valve leaflet (Eq(IX.7)).

$$\begin{aligned} M^{n+1,k+1} &= I \cdot \ddot{\theta}^{n+1,k+1} \\ &\Downarrow \\ M^{n+1,k} + \frac{dM}{d\ddot{\theta}} \cdot \left(\ddot{\theta}^{n+1,k+1} - \ddot{\theta}^{n+1,k}\right) &= I \cdot \ddot{\theta}^{n+1,k+1} \\ &\Downarrow \\ \ddot{\theta}^{n+1,k+1} &= \frac{\left(M^{n+1,k} - \frac{dM}{d\ddot{\theta}} \cdot \ddot{\theta}^{n+1,k}\right)}{\left(I - \frac{dM}{d\ddot{\theta}}\right)} \end{aligned} \tag{VIII.10}$$

With this better approximation of the angular acceleration the new position is calculated, the mesh is adapted and the Navier-Stokes equations are solved. After convergence of the Navier-Stokes equations, $M^{n+1,k}$ is calculated and convergence of the Eq(VIII.11) is checked.

$$\begin{aligned} M^{n+1,k} &\approx I \cdot \ddot{\theta}^{n+1,k} \\ &\Downarrow \\ |M^{n+1,k} &- I \cdot \ddot{\theta}^{n+1,k}| < \epsilon \end{aligned} \tag{VIII.11}$$

Step 2 will be repeated until convergence of Eq(VIII.11) is achieved. The simulation ends at $t = T_p$ with T_p the time period.

VIII.2.5. Boundary conditions

As boundary conditions for the computer model (figure VIII.4) pulsatile aortic flow is used. The velocity component u in x-direction (m/s) is given in function of the time t at the inlet. This flow pulse was derived from the experimental flow data as shown in figure VIII.4.

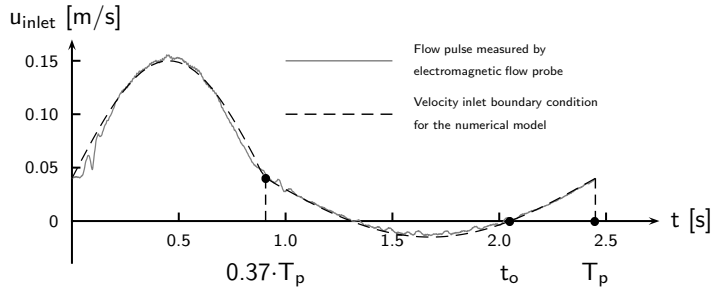

Figure VIII.4.: Boundary conditions for the computational model and the experimental model.

$$
\begin{aligned}
u_{inlet} &= u_{mean} + u_{ampl} \cdot sin\left(\frac{2 \cdot \pi \cdot \frac{t}{T_p}}{0.74}\right) \\
&for \quad 0s < t < 0.37 \cdot T_p, \\
u_{inlet} &= u_{mean} + 0.5 \cdot u_{ampl} \cdot sin\left(\frac{2 \cdot \pi \cdot \left(\frac{t}{T_p} + 0.26\right)}{1.26}\right) \\
&for \quad 0.37 \cdot T_p < t < T_p
\end{aligned}
\tag{VIII.12}
$$

The flow pulse consists of two sinus functions (Eq(VIII.12)). The parameters in this formula are T_p = 2.45 s = the time period, u_{mean} = 0.04 m/s = mean velocity during T_p, u_{ampl} = 0.11 m/s = the velocity amplitude. Velocity component v in y-direction at the inlet is set to 0 m/s. At the outlet a constant gauge pressure of 0 Pa is assumed. On all the other walls *no slip* conditions are defined. In order to apply the *no slip* condition on the moving leaflet, the boundary fluxes are computed with the leaflet face velocities which are computed from the space conservation law Eq(VIII.3). The calculation in Fluent is started at t_o = 2.05 s corresponding with zero flow or u_{inlet} = 0 m/s. Three subsequent cycles are calculated in order to obtain a solution which is independent of the initial position of the valve leaflet. The solution is calculated with Δt = 0.00245 s. It was verified that further reduction of the timestep did not alter the solution.

VIII.3. Results

Figure VIII.5 demonstrates the flow at five different instants of time in the flow cycle. Also the pressure difference between inlet and outlet of the geometry is

shown in this figure. In these figures the boundary flow pulse is shifted in time, so that the curves starts with v=0m/s at t=0s (figure VIII.5(a)) corresponding with the beginning of the acceleration. The figures are the result from the third of the three subsequent cycles that were simulated. The first cycle is initialized with zero flow in the whole fluid domain. Three subsequent cycles are thus necessary in order to obtain results independent of the previous cycle. During the acceleration of the aortic flow (figure VIII.5(a) t=0s and figure VIII.5(b) t=0.37s), the valve leaflet is pushed towards the aortic sinus. Two vortices are observed. A large vortex is present in the sinus cavity and a smaller secondary vortex is shown at the bottom wall downstream of the leaflet. The angle of the valve leaflet reaches his maximum value at t=0.88 s (figure VIII.5(c) and VIII.6). The large vortex is reduced to a small vortex in the sinus cavity. At t=1.32s (figure VIII.5(d)) the vortex is almost filling the complete sinus cavity. Thus, during the closure of the valve the vortex in the sinus is growing. During the further closure of the valve, a second small vortex rotating clockwise has developed downstream the large vortex (figure VIII.5(e)). During the acceleration the vortices get smaller and the secondary vortex is even disappearing. The pressure difference Δp over the valve model shows two discontinuities corresponding with the discontinuities in $\frac{\partial v}{\partial t}$. Furthermore the pressure difference is zero at t=0.88s (figure VIII.5(c)) and t=2.11s (figure VIII.5(e)). These moments in time correspond with the maximum and minimum flow rate respectively.
Figure VIII.6 shows the comparison for the valve leaflet excursion between the simulations and experiments. The data is plotted for the same shifted boundary flow pulse as used in figure VIII.5. There is a good qualitative and quantitative agreement, although figure VIII.6 demonstrates that the numerical leaflet angles are systematically higher than the experimental values. The simulations showed a maximum opening angle of $\theta_{simulation,max}$=93.2 degrees at t=0.88s. The experimental maximum opening angle $\theta_{experiments,max}$ is lower, e.g. 85.5 degrees, and later in the cycle at t=0.95s.

VIII.4. Discussion

A two-dimensional fluid-structure interaction (FSI) model of the aortic valve is developed, which is based on the dynamic mesh method of the Fluent software. To

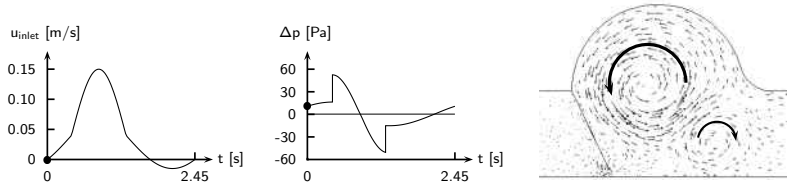

(a) t = 0.00s

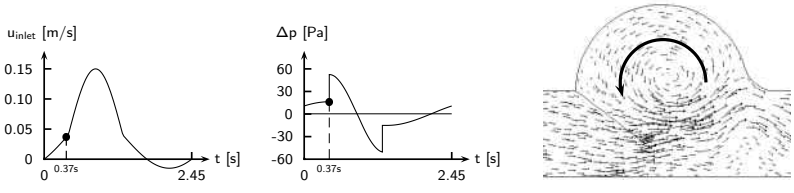

(b) t = 0.37s

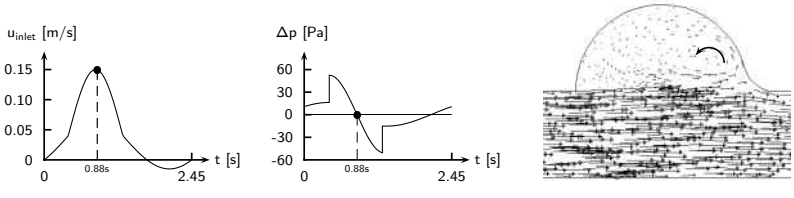

(c) t = 0.88s

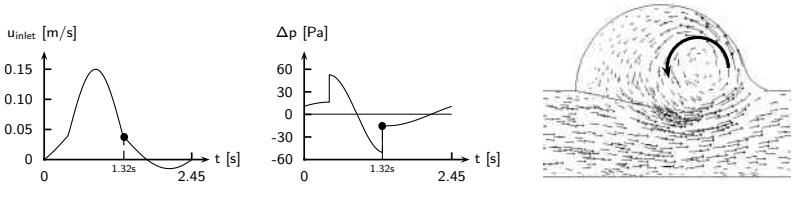

(d) t = 1.32s

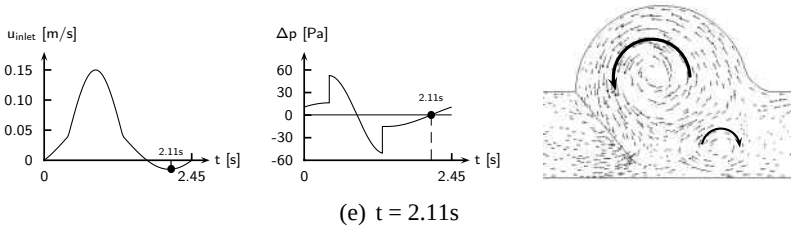

(e) t = 2.11s

Figure VIII.5.: Velocity vectors and pressure difference Δp of the last of the three calculated subsequent cycles.

the best of our knowledge, this numerical model is the first using the Fluent software for the simulation of the FSI of heart valve dynamics. The results presented in figure VIII.5 indicate that the opening and closing of the valve during the ejection

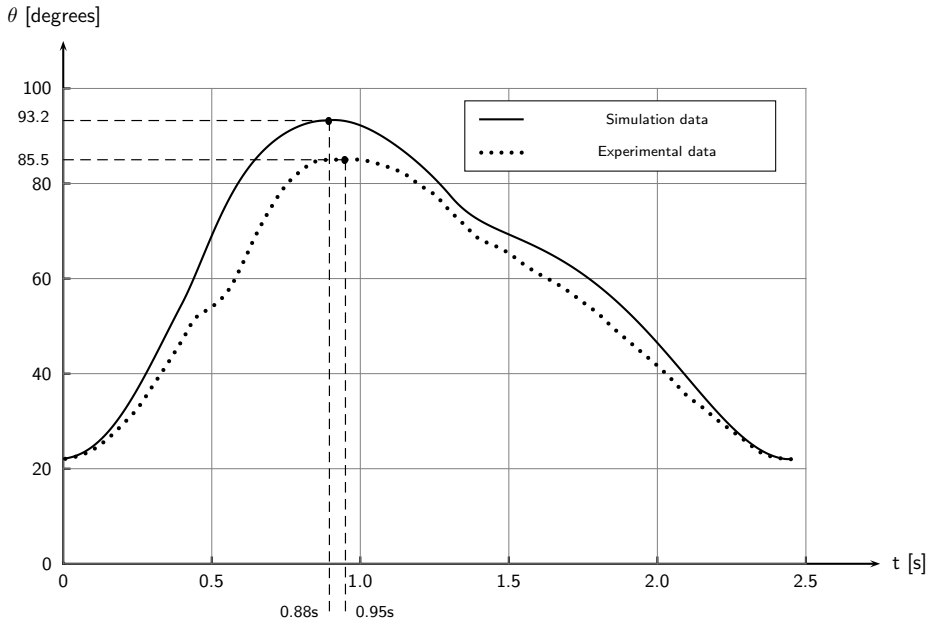

Figure VIII.6.: Comparison of experimental data with simulation data.

phase of the cardiac cycle is modeled quite well using the presented method. The observed vortices are essential for the efficient closure of the aortic valve and were also observed in experiments done by De Hart *et al*[29] and Van Steenhoven *et al*.[202] Furthermore the results demonstrate the effect of the regurgitation (negative inlet velocity) on the closing of the aortic valve. It must be stated that the regurgitant flow is a prescribed quantity in our numerical model. Without this regurgitation the valve would unable to close fully, as the closing of the valve has not yet finished at t = 2.11 s (figure VIII.5).

The computational model has been validated with experiments using a CCD camera (Kodak ES-1.0) to record the valve positions at 50 instants in the flow cycle. The opening angles are used for comparison, since this quantity is a direct result of the fluid-structure interaction. Although a good qualitative and quantitative agreement is shown in figure VIII.6, the numerical leaflet positions are systematically larger than the experimental positions. A few reasons for this difference between the CFD simulations and experimental setup (figure VIII.6) can be found. The CFD simulations are done in two dimensions, although the experimental setup is of course three-dimensional. Due to these three dimensions, there are instationary boundary layer flows near the side walls interacting with the leaflet. These instationary bound-

ary layers are of course not modeled in the numerical two-dimensional model, but they certainly influence the movement of the leaflet in the *in vitro* experiments. Furthermore, since the valve is fixed to the top of the inflow channel using three strips of adhesive tape, a small amount of fluid can leak over the top of the valve between the strips of tape. When the valve is closed and the fluid starts to move forward, the fluid passing underneath the valve will push the valve open. Since some of the fluid will leak over the valve, the valve will possibly not open as far as without the leakage. Another factor is the gap in the computer model between the leaflet and the boundary of the domain. Because this gap isn't present in the experimental setup, it can also induce some errors on the computational results of the leaflet movement.
Our final aim is to calculate wall shear stress on the valve leaflets during a complete cardiac cycle, fully accounting for the delicate interaction between blood flow and stiffness properties of the valve leaflets, and to asses in this way the impact of leaflet properties on the shear stress distribution and the potential impact in tissue-engineered heart valve applications. The ALE method in combination with remeshing allows the accurate calculation of these wall shear stresses.

VIII.5. Conclusions

We have presented a 2D numerical model of the aortic valve haemodynamics in Fluent, making use of ALE and remeshing techniques. Typical aortic flow phenomena were observed in our simulations. Furthermore, our CFD results are in good agreement with experimental observations (CCD Camera), where the same geometry and boundary conditions were applied. From the results it is concluded that our new developed fluid-structure interaction method can be used to describe the fluid-leaflet interaction of the aortic valve.

Chapter IX

Blood-Leaflet interaction in a mechanical heart valve

The contents of this chapter is accepted for publication in Journal of Biomechanical Engineering
Blood-Leaflet Interaction in a Mechanical Heart Valve
Dumont K, Vierendeels J, Segers P, Van Nooten G, Verdonck P

Abstract

Background: *In vitro* studies on the ATS heart valve have shown that the valve opens to the maximum opening angle when it is placed in a straight conduit, but that valve opening is less than maximum when placed in an expanding conduit. This unexpected behaviour can only be due to fluid-structure interaction (FSI) of the valve leaflets in a diverging flow, and is an interesting test case for our newly developed numerical FSI code.

Method of approach: The computational FSI model makes use of Fluent software for solving the flow problem, extended with a dedicated user-defined function to account for the FSI. A 3D model of the ATS valve was created and studied in 2 geometries, simulating the valve in a straight conduit and an expanding conduit. For both geometries, the same velocity inflow profile, with a peak velocity of 1 m/s was applied.

Results: In the straight conduit, the ATS valve opens to the maximum opening angle and remains in that position until closing. Peak transvalvular pressure difference is 3.5 mmHg (465.5 Pa). In the expanding conduit, the valve opens to the maximum opening angle but remains in this position only for 0.092 seconds, after which it moves toward less than maximum opening. Peak pressure difference is 2.8 mmHg (371.4 Pa). We further calculated shear stress distribution on the valve leaflets.

Conclusions: Our numerical study thus confirms that valve opening and haemodynamics depend on the geometrical conditions of the valve. The presence of a diverging flow opens the valve to less than maximum opening and reduces the shear stresses on the leaflets.

IX.1. Introduction

Actual prosthetic bileaflet heart valves are generally considered to be safe and efficient as replacements for malfunctioning natural valves, although complications such as thrombosis and thromboembolism are still unsolved problems. These problems are directly related to valve design characteristics and haemodynamics. The ATS valve (ATS Medical, Minneapolis, MN, USA) is a pyrolytic carbon, open pivot, low-profile cardiac prosthesis. The theoretical opening angle of the ATS valve is 85° (Fig. IX.1(a)) with 60° angle of travel. Compared with conventional mechanical bileaflet valves, its open pivot structure is expected to induce less thrombolytic events. However, it was noticed that normally functioning ATS valves in both the

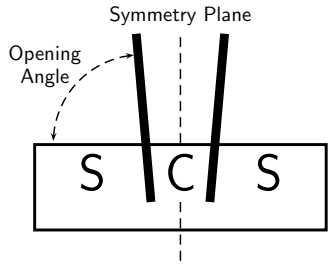

(a) Opening angle and symmetry plane. Side (S) and central (C) flow orifice.

(b) The ATS AP valve as implemented in the numerical model.

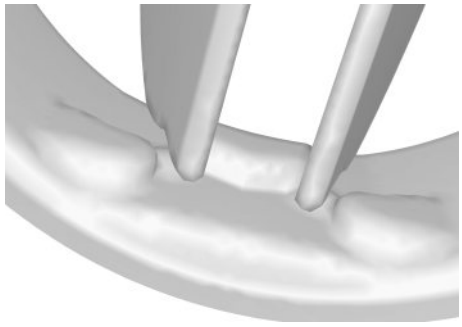

(c) The ATS open pivot hinge in close-up as implemented in the numerical model.

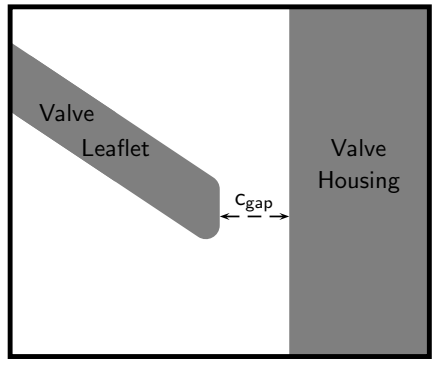

(d) Gap at leaflet tip c_{gap}.

Figure IX.1.: ATS valve.

aortic and the mitral position open to less than maximum angle in clinical situations.[203] In order to clarify ATS valve opening more in detail, *in vitro* tests have been conducted.[73,204] It was found that in a straight outlet, the ATS valve opened to maximum opening angle. However, the opening angle was less than maximum in the expanding conduit.[73,204] These studies confirmed to some degree the clinical finding that the ATS valve did not open to maximum opening angle except when the outflow was straight, and when the leaflet did not extend into an expanding downstream chamber. Design characteristics of the ATS valve, such as its axis being located close to the leaflet straight edge and its leaflets extending further downstream from the ring orifice, may cause this valve behavior.

The literature on computational three dimensional studies of heart valve dynamics is still limited, possibly due to the difficulties associated with the modeling of the complex mechanical heart valve geometry, flow unsteadiness, and the interaction between the blood flow and the leaflet motion. Several studies have been reported on the computation of the flow in the pivot region[127,156] and shear stresses in the clearance region[157] with the leaflets of the mechanical valve in a fixed position. These studies neglected the interplay between the blood flow field and the leaflet motion. In other studies, however, the fluid flow was coupled with the leaflet motion using prescribed valve motion in a simplified flow domain.[155] This prescription of the leaflet motion avoids the complex problem of the blood-leaflet interaction during the valve closure. Only recently, more realistic simulations have become possible, modeling the leaflet motion including the blood-leaflet interaction.[140,141]

We previously developed a robust computational fluid-structure interaction model,[140] capable of calculating the leaflet motion together with the flow field. The algorithm was tested and validated on a two dimensional (2D) model.[142] Since the peculiar behavior of the ATS valve leaflets can only result from the interaction between the flow field and the leaflet, we thought this valve to be an excellent 3D test case for our numerical model. The aim of this study was therefore to simulate the 3D leaflet motion of the ATS valve during the complete cardiac cycle and to gain insight into the complex interplay between valve leaflet motion and the geometrical conditions of the heart valve in situ.

IX.2. Methods

IX.2.1. Valve and conduit geometries

The model is based on the 22mm AP ATS Open Pivot™ heart valve shown in figure IX.1(b). The inside diameter of the valve orifice is 20.8 mm with a geometric orifice area of 3.17 cm^2. Specific to this valve is its open pivot design (figure IX.1(c), in which the convex pivot and stops are located on the inner circumference and extended in the flow field. Figure IX.1 defines the opening angle of leaflets (Fig. IX.1(a)), the side and central flow orifice of the valve (Fig. IX.1(a)) and the gap c_{gap} between the leaflet tips and the housing of the closed valve (Fig. IX.1(d)).
The first geometry in which the valve haemodynamics is computed is a straight conduit (Fig. IX.2(a)) with a diameter of 21.9 mm. The second geometry (Fig.

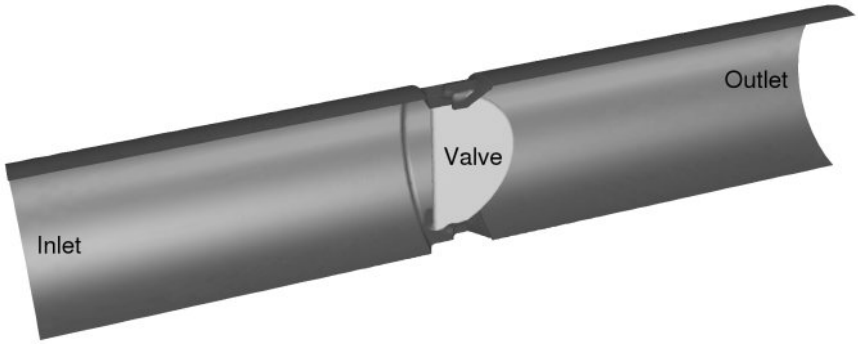

(a) the straight conduit: ATS valve positioned in a straight conduit.

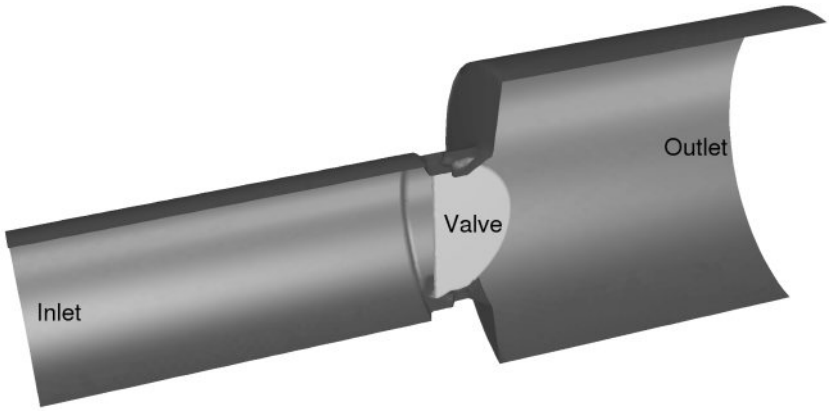

(b) the expanding conduit: ATS valve positioned in an expanding conduit.

Figure IX.2.: The straight and expanding geometries as used in the computational study.

IX.2(b)) has an enlargement downstream of the valve and thus the leaflets extend into an expanding downstream chamber during the opening of the valve, further referred as expanding conduit. The diameter is 21.9 mm for the inflow conduit and 40.0 mm for the outflow conduit. The length of the in- and outflow conduits is 50.0 mm for both geometries.

IX.2.2. CFD package and remeshing

Meshing the geometries was achieved with Gambit 2.1 (Fluent Inc.). The valve motion is coupled with the blood flow. The latter is computed with the commercial CFD software package Fluent (Fluent Inc.). The dynamic mesh model of Fluent 6.1 has been used for the arbitrary Lagrangian-Eulerian (ALE) computations.
Because of computational time efficiency reasons, there are some limitations on the mesh density when the valve is near and in its closed position. Given that c_{gap} is of the order of $5 \cdot 10^{-5}$m,[155] the volume of the cells of the mesh at the gap are of the order $c_{gap}^3 = 1.25 \cdot 10^{-13}m^3$. Meshing of the inflow and outflow conduit with larger cells and the valve section with these small cells would lead to hundreds of millions of cells. A coarser mesh with refinements of the mesh at the gap of the leaflet tip, still resulted in Gambit in more than 5 million cells. Also this number is quite high, taking into account the fact that unsteady calculations will be performed with an ALE remeshing at every subiteration.
A second limitation concerns the remeshing capability of Fluent. The displacement of the leaflet tip in one calculation timestep should not exceed the length of the smallest boundary of neighboring cells, because otherwise this would result in negative cell volumes. This can be avoided with a decrease of the used timestep. The length of the smallest boundary is proportional to c_{gap}. Knowing that the leaflet tip velocity v_{tip} is in the order of magnitude of 2.1m/s[155] during opening and closing, the required timestep is $c_{gap}/v_{tip} = 2.5 \cdot 10^{-5}$s. With the total time for opening and closing of 0.066s,[155] more than 2600 timesteps need to be calculated for one cardiac cycle. In this, it is assumed that the valve is in the maximum open or closed position during the remaining time of the cycle, a condition which is not necessarily fulfilled, as will be shown further in this work. Converging of 1 timestep (with 4 subiterations for the fluid-structure interaction problem) for 500.000 elements takes about 2 hours on an Intel Xeon Pentium PC (1.7 GHz with 2GB RAM). This would result in a total calculation time of more than half a year!

To avoid such excessive computing times, we had to make simplifications to the meshed geometry. Firstly we take advantage of the symmetry of the bileaflet geometry and simulate only one half of the valve. We further reduced the leaflet dimensions to 95% of their original size. This results in a gap of $25 \cdot 10^{-5}$m = $5c_{gap}$. Furthermore the maximum opening angle of the leaflets is restricted to 80°. This should avoid contact of the leaflet with the pivot stops, which would result in squeezed cells and bad convergence of the Fluent solver. These adaptations result still in a total number of grid cells used in the computation of about 500.000 for both geometries.

IX.2.3. Governing Equations

The unknown variables are the velocity component u in the x-direction, the velocity component v in the y-direction, the velocity component w in z-direction, the pressure p and the coordinates (x, y, z) of the valve nodes determined by the angle θ. The continuity equation in integral form Eq(IX.1) is given by

$$\frac{\partial}{\partial t}\int_V \rho dV + \int_S \rho(\overrightarrow{\boldsymbol{v}} - \overrightarrow{\boldsymbol{v_b}}) \cdot \overrightarrow{\boldsymbol{n}} dS \;=\; 0 \qquad \text{(IX.1)}$$

where $\int_V ...dV$ is the integral over a control "volume", $\int_S ...dS$ is the integral over a control "surface", $\overrightarrow{\boldsymbol{n}}$ is the outwardly directed vector normal to dS, ρ is the density of the fluid, $\overrightarrow{\boldsymbol{v}}$ = (u,v,w) is the velocity vector of the fluid, $\overrightarrow{\boldsymbol{v_b}}$ = (u_b,v_b,w_b) is the velocity vector of the moving boundary. For each face j of the control volume $\overrightarrow{\boldsymbol{v}_{b,j}} \cdot \overrightarrow{\boldsymbol{n}} dS_j$ is computed from $\frac{\delta V_j}{\Delta t}$ where δV_j is the volume swept out by the control volume face j over the time step Δt. With this definition of $\overrightarrow{\boldsymbol{v}_{b,j}}$ the so called space conservation law Eq(IX.2) is fulfilled for each control volume.

$$\frac{\partial}{\partial t}\int_V dV \;=\; \int_S \overrightarrow{\boldsymbol{v_b}} \cdot \overrightarrow{\boldsymbol{n}} dS \qquad \text{(IX.2)}$$

The momentum equation in integral form is given by Eq(IX.3)

$$\frac{\partial}{\partial t}\int_V \rho \overrightarrow{\boldsymbol{v}} dV + \int_S \rho \overrightarrow{\boldsymbol{v}} (\overrightarrow{\boldsymbol{v}} - \overrightarrow{\boldsymbol{v_b}}) \cdot \overrightarrow{\boldsymbol{n}} dS \;=\; -\int_S p \overrightarrow{\boldsymbol{n}} dS + \int_S \underline{\overline{\boldsymbol{\tau}}} \cdot \overrightarrow{\boldsymbol{n}} dS \qquad \text{(IX.3)}$$

where $\underline{\overline{\tau}}$ is the stress tensor. Body and buoyancy forces were neglected. Finally, the equation of motion Eq(IX.4) for the leaflet can be written as

$$M = I \cdot \ddot{\theta} \tag{IX.4}$$

with M the torque on a stiff valve leaflet, I the moment of inertia = 4.0· 10^{-9}kg·m^2 and θ the opening angle of the leaflet as indicated in figure IX.1(a).
The continuity Eq(IX.1), space conservation Eq(IX.2) and momentum Eq(IX.3) equations for incompressible laminar flow are solved in the fluid domain. Since the calculations are unsteady and performed in 3D, the large scale turbulence, with scale larger than the mesh size, is completely captured by the flow solver and thus needs no modeling. The fluid is assumed to be Newtonian with the density of 1050 kg/m^3 and viscosity of 0.004 kg/m·s, which is representative of human blood properties at 37°C. The CFD software package Fluent (Fluent Inc.) is used to solve the governing equations. Fluent is based on the finite volume method, where the domain is discretised into a finite set of control volumes or cells. A backward Euler 1st order implicit scheme is used for the time integration of the fluid flow. The implementation of these equation in the Fluent package is out of the scope of this paper.
Our FSI model uses the dynamic mesh method of the CFD software package. This method uses a user defined function (UDF) that can be coupled with the code. As input of the UDF the position of the boundary nodes of the moving valve have to be prescribed at the beginning of a new time step. Since these positions depend on the FSI solution, a straightforward calculation is not possible and an iterative approach is necessary. Therefore command files are generated and then used to drive the computation.

IX.2.4. Blood-Leaflet interaction model

Figure IX.3 shows a flow diagram of the coupling of the flow computations and the movement of the leaflet. A partitioned approach is used but strong coupling is achieved through implicit coupling in the subiterations. Implicit coupling is obtained through the derivative of the moment M to the angular acceleration $\ddot{\theta}$ which is derived numerically. In the following paragraphs the different steps of the imple-

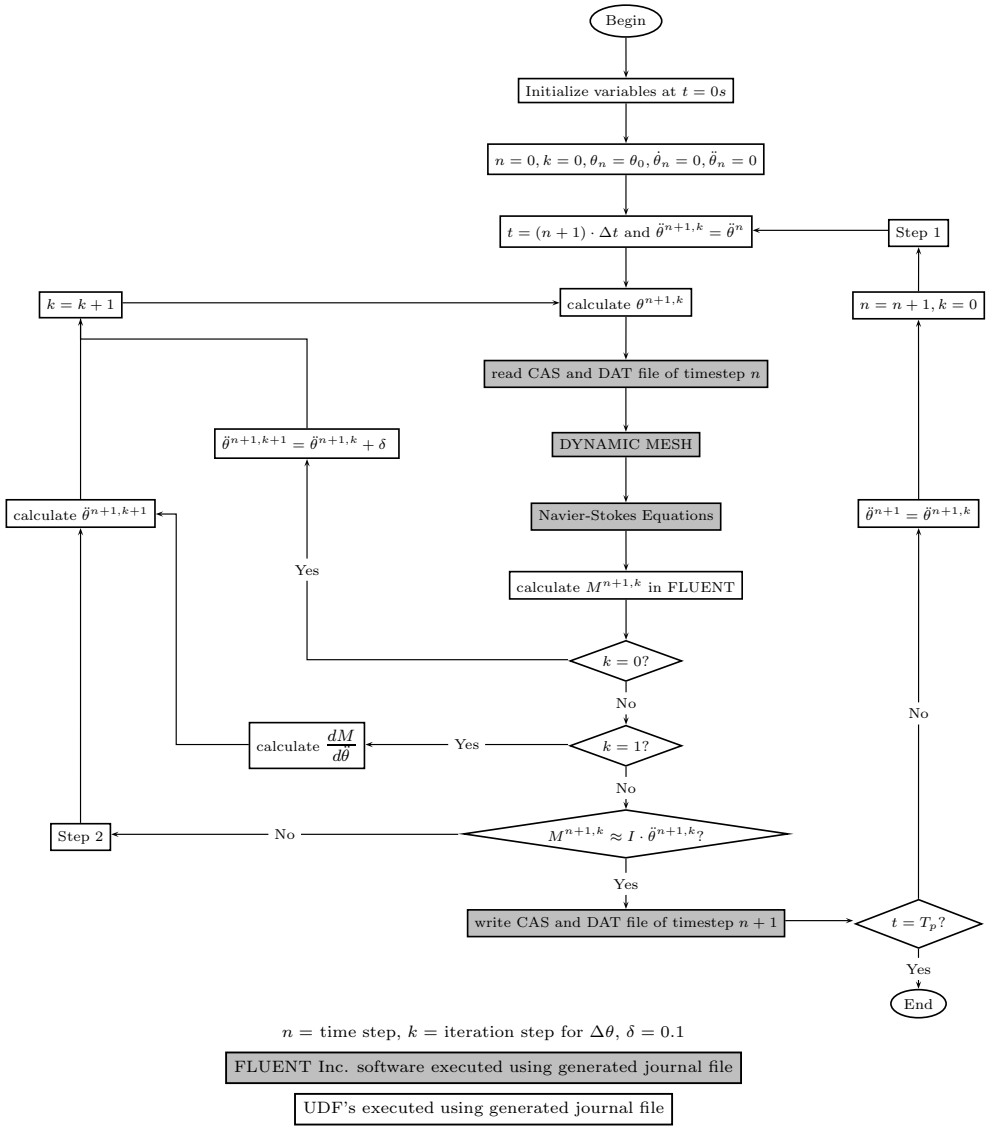

Figure IX.3.: Flow diagram of the coupling of fluid and structure in FLUENT.

mentation are explained. First all UDF variables t, Δt, n, k, I, θ, $\dot{\theta}$, $\ddot{\theta}$ are initialized. The subsequent position of the valve leaflet on the new time level is calculated by coupling the backward Euler time integration scheme for the solid with the CFD code. The backward Euler scheme for the solid is given by

$$\begin{aligned} \dot{\theta}^{n+1} &= \dot{\theta}^n + \Delta t \ddot{\theta}^{n+1}, \\ \theta^{n+1} &= \theta^n + \Delta t \dot{\theta}^{n+1}. \end{aligned} \tag{IX.5}$$

The indices $n+1$ and n correspond with time levels $t+\Delta t$ and t respectively.
In order to obtain the position θ^{n+1} at $t+\Delta t$ an iterative approach is used. For each timestep there are k subiterations performed in order to reach sufficient convergence of eq. (IX.4).
At the beginning of each time step, the derivative $dM/d\ddot{\theta}$ is computed numerically. A first estimation ($k=0$) of the new position $\theta^{n+1,k=0}$ is computed with the old value of the angular acceleration $\ddot{\theta}^n$. This value of the acceleration is used to calculate the position using the equation eq. (IX.5). With this initial guess of the new position at $t+\Delta t$, Fluent is called to adapt the mesh with the dynamic mesh model and to solve the Navier-Stokes equations. After convergence of the Navier-Stokes equations, $M^{n+1,k=0}$ is calculated from the flow field. A second estimation ($k=1$) of the new position $\theta^{n+1,k=1}$ is computed with the old value of the angular acceleration increased with a constant δ=0.1 rad/s^2. This value is about 1/100 of the maximum angular acceleration, which can be estimated from the inlet profile. Tests have demonstrated that the convergence of the algorithm is not very sensitive to the choice of this value. After convergence of the fluid problem, $M^{n+1,k=1}$ and the derivative $dM/d\ddot{\theta}$ is calculated as follows:

$$\begin{aligned} \ddot{\theta}^{n+1,k=0} &= \ddot{\theta}^n \\ \ddot{\theta}^{n+1,k=1} &= \ddot{\theta}^n + \delta \\ \frac{dM}{d\ddot{\theta}} &= \frac{M^{n+1,k=1} - M^{n+1,k=0}}{\delta}. \end{aligned} \tag{IX.6}$$

The derivative $dM/d\ddot{\theta}$ can now be used to calculate an approximation of the angular acceleration of the valve leaflet in an implicit way:

$$\begin{gathered} M^{n+1,k+1} = I\ddot{\theta}^{n+1,k+1} \\ \Downarrow \\ M^{n+1,k} + \frac{dM}{d\ddot{\theta}}\left(\ddot{\theta}^{n+1,k+1} - \ddot{\theta}^{n+1,k}\right) = I\ddot{\theta}^{n+1,k+1} \\ \Downarrow \\ \ddot{\theta}^{n+1,k+1} = \frac{\left(M^{n+1,k} - \frac{dM}{d\ddot{\theta}}\ddot{\theta}^{n+1,k}\right)}{\left(I - \frac{dM}{d\ddot{\theta}}\right)} \end{gathered} \tag{IX.7}$$

With this approximation of the angular acceleration the new position is calculated, the mesh is adapted and the Navier-Stokes equations are solved. After convergence of the Navier-Stokes equations, $M^{n+1,k+1}$ is calculated and convergence of the inner loop is checked:

$$M^{n+1,k+1} \approx I\ddot{\theta}^{n+1,k+1}$$

The inner loop is repeated until convergence is achieved. A convergence criterium of a residual drop of 3 orders of magnitude is used. Then the next time step is computed. The simulation ends at t=T_p. The developed FSI code belongs to the class of partitioned but strongly coupled methods, also known as iterative methods for fluid-structure interaction,[148,147] i.e. separate solvers are used for the fluid and the structure, but strongly coupling is achieved.[149,205,206]

IX.2.5. Boundary conditions

The inlet velocity profile is given in Fig. IX.4(a). The spatial velocity distribution is shown in Fig. IX.4(b)[127] with r the radial position and R the conduit radius. At the outlet of the conduit in both geometries a constant pressure is assumed. The absolute value of the outlet pressure is of no importance because only the transvalvular pressure difference between inlet and outlet, computed with the incompressible solver, is important for the simulation of the leaflet motion. The remaining boundaries are solid walls, and the standard no-slip velocity condition is used. Simulations are performed during the whole cycle starting from the closed valve assuming zero velocity over the whole fluid domain. One and a half cycle are simulated. In this way the opening of the valve is independent of the initial zero flow conditions. The computations advances in time with a time step ranging between 0.001s and 0.00025s, dependent on the angular velocity of the valve.

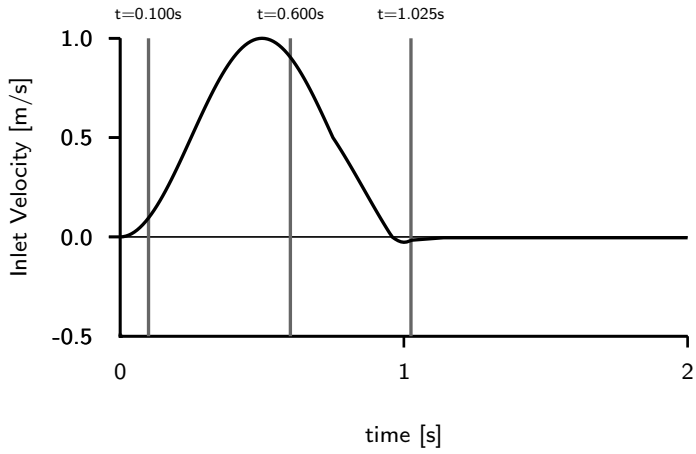

(a) Inlet velocity.

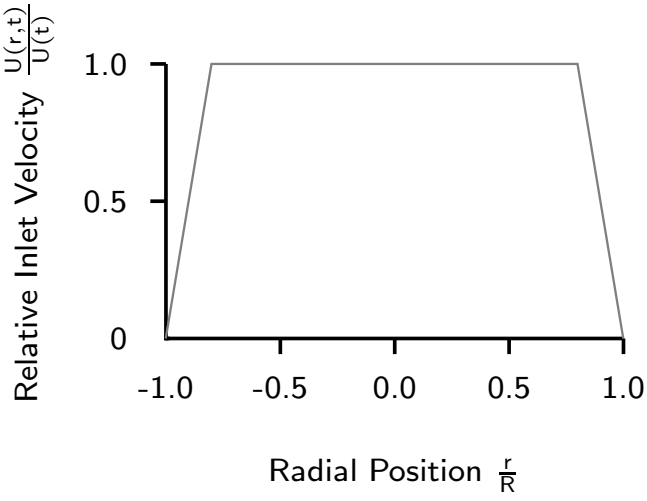

(b) Inlet profile.

Figure IX.4.: Velocity boundary condition used at the inlet of both geometries.

IX.2.6. Derived parameters

The following parameters are calculated from the simulation results:

$\Delta t_{opening}$ = the time period during which the valve is moving towards the open position

$\Delta t_{maximum\ opening}$ = the time period during which the valve is at maximum opening angle, θ=80°

$\Delta t_{closing}$ = the time period during which the valve is moving towards the closed position

$\Delta t_{cycle} = \Delta t_{opening} + \Delta t_{maximum\ opening} + \Delta t_{closing}$

$\theta_{mean,fwd\ flow}$ = mean leaflet angle during forward flow

$\theta_{mean,\Delta t_{maximum\ opening}^{the\ straight\ conduit}}$ = mean leaflet angle during $\Delta t_{maximum\ opening}$ of the straight conduit (Fig. IX.5(a))

Δp_{max} = the maximum transvalvular pressure difference between inlet and outlet

SS_{avg} = the spatial average of the shear stress on the leaflet at a certain timestep

$maxSS_{avg}$ = the maximum value of the SS_{avg} curve

SS_{max} = the local maximum shear stress

The parameters are summarized in table IX.1.

IX.3. Results

Opening angles, opening times, transvalvular pressure differences, flow pathlines and shear stresses are compared for the two geometries and discussed below.
Figure IX.5(a) and table IX.1 compare the angle of the leaflets during the whole cycle. At the beginning of inflow the time behavior of the opening angles are similar for both geometries. The opening time $\Delta t_{opening}$ for the straight conduit is 0.147s compared to 0.200s for the expanding conduit. In the straight conduit the valve opens to the maximum opening angle (80°) during 0.702s. In contrast, the leaflet

Table IX.1.: Summarized time, angle, pressure and shear stress data.

Results: time, angle, pressure and shear stress data		
	the straight conduit	the expanding conduit
$\Delta t_{opening}$ [s]	0.147	0.200
$\Delta t_{maximum\ opening}$ [s]	0.702	0.092
$\Delta t_{closing}$ [s]	0.344	0.726
Δt_{cycle} [s]	1.193	1.018
$\theta_{mean,fwd\ flow}$ [degrees]	74.0	69.7
$\theta_{mean,\Delta t^{the\ straight\ conduit}_{maximum\ opening}}$ [degrees]	80.0	74.7
Δp_{max} [mmHg]	3.5	2.8
SS_{max} [Pa]	44.4	44.6
$maxSS_{avg}$ [Pa]	26.6	17.8

in the expanding conduit opens to the maximum opening angle for a very short period of 0.092s. From this timelevel on the leaflets are moving slowly towards the closed leaflet position. In the expanding conduit the streamlines diverge from the axis of the conduit, and the leaflets respond to this divergent flow. In the straight conduit $\Delta t_{closing}$ takes 0.344s while 0.726s in the expanding conduit. This results in Δt_{cycle} of 1.193s for the straight conduit and 1.018s for the expanding conduit. The mean angle during forward flow in the straight conduit is 74.0° and 68.7° in the expanding conduit. The mean angle θ_{mean} during $\Delta t^{the\ straight\ conduit}_{maximum\ opening}$ (Fig. IX.5(a)) is 80.0° in the straight conduit and 74.7° in the expanding conduit.

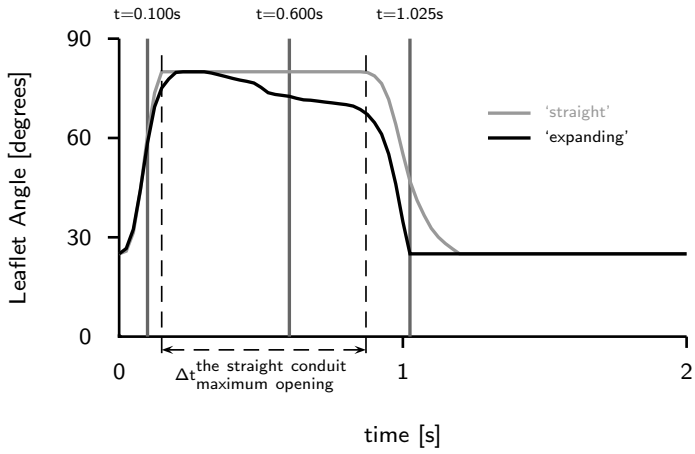

(a) Opening angle of the valve [degrees].

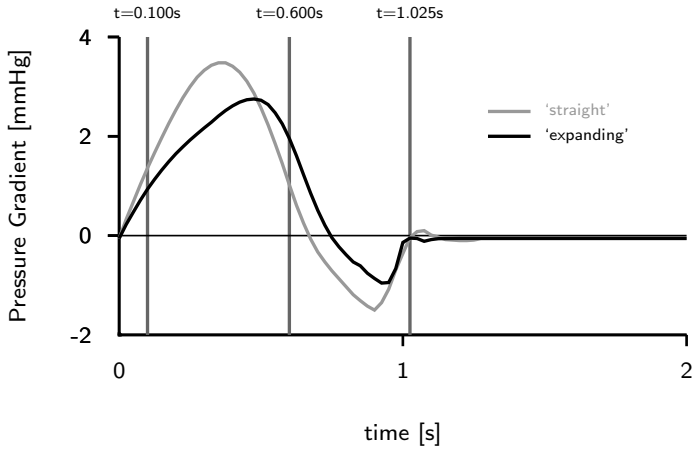

(b) Transvalvular pressure difference [mmHg].

Figure IX.5.: Comparison of opening angle and transvalvular pressure difference in both geometries.

The simulations can also be used to calculate transvalvular pressure differences between inlet and outlet (Fig. IX.5(b)). The maximum pressure difference is 3.5mmHg in the straight conduit and 2.8mmHg in the expanding conduit (table IX.1).
Figure IX.6 shows flow pathlines for both geometries at three different timesteps of the cycle. Figures IX.6(a) and IX.6(b) show the flow pathlines during the opening of the valve. The flow pathlines in figures IX.6(a) are streamlined, while they are more diverging downstream the valve in the expanding conduit (Fig. IX.6(c)). This indicates the presence of the diverging flow which is guiding the valve leaflet motion. At a later stage in the flow cycle the flow pathlines in the straight conduit

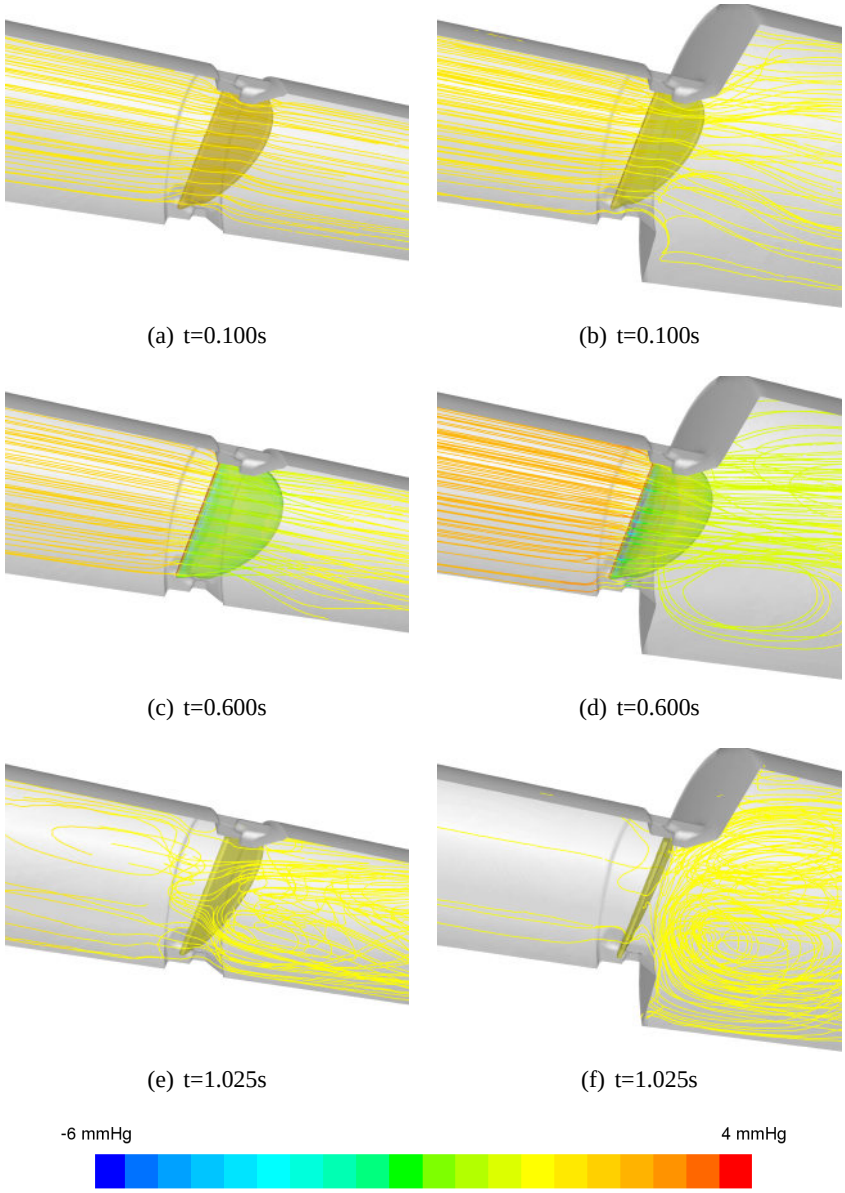

(a) t=0.100s (b) t=0.100s

(c) t=0.600s (d) t=0.600s

(e) t=1.025s (f) t=1.025s

(g) Pressure Values [mmHg].

Figure IX.6.: Flow pathlines colored with respect to pressure values in both geometries.

are still streamlined (Fig. IX.6(c)), while large circular flow pathlines are present in the expanding conduit (Fig. IX.6(d)). These circular flow pathlines remain present during complete closing phase of the valve (Fig. IX.6(f)). In the straight conduit also less streamlined flow pathlines are present during valve closure (Fig. IX.6(e)).

Average shear stress on the leaflet is lower in the expanding conduit with a maximum value equal to 17.8 Pa, compared to a maximum value of 26.6 Pa in the straight conduit (Fig. IX.7(a)).

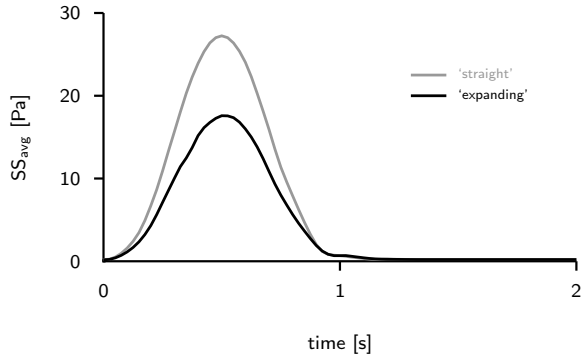

(a) Average shear stress on the leaflet.

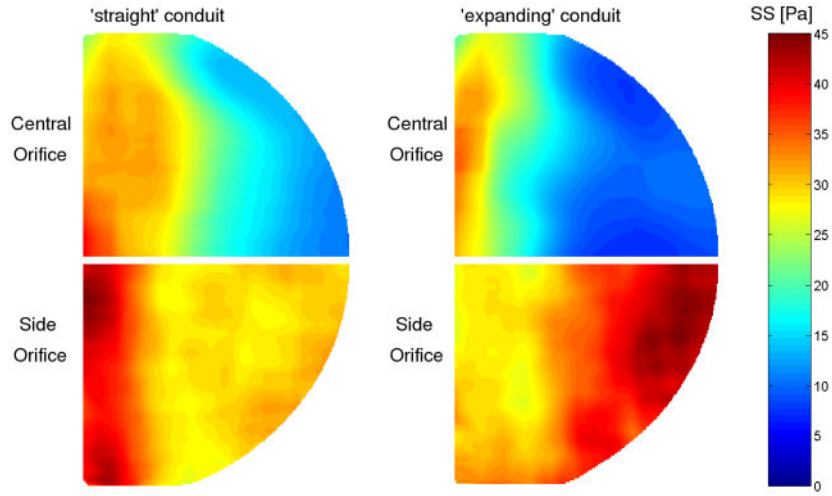

(b) Shear stress distribution on the leaflet at t=0.500s.

Figure IX.7.: Shear stress on the valve leaflets.

Figure IX.7(b) compares the shear stress distribution on the leaflet for the two geometries and for the side and central orifice (Fig. IX.1(a)). The figure shows the shear stress at t=0.5s for a peak inlet velocity of 1.0m/s. Although the maximal shear stress was in both cases around 44.5Pa, the location of the high shear stresses on the leaflets differs in both geometries: proximal of the leaflet in the straight con-

duit compared to distal of the leaflet in the expanding conduit, especially for the shear stress at the side orifices.

IX.4. Discussion

We simulated the ATS valve opening and closing in two geometries, a straight conduit and a expanding conduit. In both cases we used the same boundary conditions. Results confirm earlier *in vitro* observations of the ATS valve leaflet motion, i.e. the leaflet motion is dependent on geometrical conditions.[73,203,204] The opening angle in the straight conduit is larger than in the expanding conduit.

The impact of geometrical conditions on the ATS valve leaflet motion was studied *in vitro* by Feng et al.,[73,204] confirming earlier published *in vivo* results reported by Aoyagi et al.[203] They[73,204] reported less than maximum opening of the valve in an expanding conduit under mitral flow conditions. Their results are in qualitative agreement with our numerical simulations.

In our simulations, using the inlet profile as shown in Fig. IX.4(a), the valve actually reached the maximal possible opening angle, which was restricted to 80°. Due to open pivots, even if the leaflets do not go to maximum opening angle, it does not compromise the function of the valve: the trend towards less than maximum opening reduces shear stresses on the leaflets. Also the pressure difference was lower in the calculation with the expanding conduit, but here the pressure recovery due to the expansion can be the cause of this. Therefore we compared pressure differences in the expanding conduit for a leaflet angle of 75°and 80°using steady flow calculations. These calculations showed that there is almost no difference in pressure drop due to the less than maximum opening of the ATS valve.

Obviously, the leaflet motion is also highly dependent on the applied boundary condition which was, in this case, an inflow profile adopted from a previous study in which we validated the algorithm in a 2D setting.[142] This 2D validation study showed the robustness and accuracy of the FSI algorithm and thus it could be used in 3D. It is, however, at the same time acknowledged that further experimental measurements are needed to validate the agreement between the measured and calculated complex 3D flow phenomena around the moving valve leaflet.

At this point, we can only state that the application of a flow profile to an ATS-like valve in 2 different geometrical constraints yields a different behaviour of the

leaflets. In order to match our findings to clinical data (i.e., a valve in aortic and mitral position), more physiological flow profiles are to be prescribed. Although we could not demonstrate an incomplete opening of the valve in the expanding conduit, we could prove a strong difference in the leaflet behavior in both geometries. In the straight conduit the valve is open at the maximum opening angle for a long period of time (0.702s). The leaflet in the expanding conduit is open at the maximum opening angle for only 0.092s of the total flow cycle. From this timelevel on the leaflets are moving towards a less open position. The leaflet responds to the divergent flow in the expanding conduit. The mean opening angle during forward flow is 74.0° in the straight conduit, but only 68.65° in the expanding conduit. Even during $\Delta t_{\text{maximum opening}}^{\text{the straight conduit}}$ the mean angle in the expanding conduit is only 74.7°. This value is close to the reported 75.5°.[73, 155, 204] Another interesting observation is the fact that $\Delta t_{\text{cycle}}^{\text{the straight conduit}}$=1.193s is larger than $\Delta t_{\text{cycle}}^{\text{the expanding conduit}}$=1.018s. Thus, although the boundary conditions and the amount of regurgitation are the same in both geometries, the valve in the expanding conduit is closing earlier. The valve leaflet responds to the divergent flow in the expanding conduit, resulting in an earlier closing of the valve.

With our CFD model, we not only obtain information on the motion of the valve leaflets, but also detailed haemodynamic data such as, for instance, the transvalvular pressure difference between inlet and outlet. The transvalvular pressure differences $\Delta p_{\text{max}}^{\text{the straight conduit}}$ = 3.5mmHg and $\Delta p_{\text{max}}^{\text{the expanding conduit}}$ = 2.8mmHg are of the same order of magnitude as found in the Feng studies.[73, 204] Due to the leaflet reduction the negative transvalvular pressure difference over the closed valve could not be shown. Either flow or pressure has to be imposed as boundary conditions. Since the gap size is larger, a small pressure difference is needed to obtain the imposed regurgitation flow. This follows from the computations. If pressure differences were imposed as boundary conditions, the regurgitation flow that would come out of the simulations, would have been very high due to the enlarged gap size. We therefore do not report the regurgitation data, as this issue requires further exploration in future studies. Also, reducing the leaflet size will have an impact on flow phenomena during closing of the valve, i.e. cavitation and rebound of the leaflet.[141, 51]

Another important haemodynamic variable, impossible to measure directly *in vivo* and *in vitro*, is the shear stress on the valve leaflet. The maximum shear stress is in both cases around 44.5Pa for a peak blood flow of 1m/s and are far lower than

hemolytic threshold (<200Pa).[124,126,207] These values are comparable to what is found in the literature.[44,125,51] The average shear stress on the leaflet is 17.8Pa in the expanding conduit compared to a larger value of 26.6Pa in the straight conduit (Fig. IX.7(a)). The location of the higher shear stress on the leaflet at the side orifice in the straight conduit is located at the upstream edge of the leaflet. In the expanding conduit the diverging flow interacts with the leaflet, causing a different location of the high shear stress on the leaflet as can be seen in Fig. IX.7(b). At the center orifice, there is only a minor difference between the 2 geometries. The location of the high shear stress is almost the same at the center orifice. Our numerical study unravels that the presence of a diverging flow reduces the shear stress distribution on the leaflets.

This new FSI model will be a major tool to study the haemodynamics associated with thrombolytic and hemolytic events of existing and new mechanical heart valves. Although our CFD model has revealed its potential as a tool to study valve dynamics in a much more detailed way than possible with any *in vitro* technique, there are still some limitations. The shear stress during the leakage flow[125,141] could not be accounted for because of the enlarged gap. In the simulations, valve excursions reached 80°. It is not clear whether the valve would have reached the maximum open position (85°) of the ATS valve if it would have been included in the model.

Although it is reported by Liang et al.[158] that grid density should be $5{\cdot}10^{6}$ grid points in order to simulate the symmetry-breaking instabilities and flow fields in heart valve modeling, we could not achieve this goal because of limited available PC power. It is also stated in the same study that the high Reynolds numbers of the flow could result in symmetry-breaking instability. In spite of this remark, we still assume symmetrical flow through the leaflet in order to save computer CPU time.

Perhaps the most challenging obstacle is the development of turbulence models capable of simulating pulsatile flows periodically undergoing transition to turbulence and laminarization.[158] Since our laminar calculations are unsteady and performed in 3D, the large scale turbulence, with scale larger than the mesh size, is completely captured by the flow solver and thus the large scale turbulence needs no modeling. Successful application of laminar or more advanced turbulence models to mechanical heart valve flows, however, will require detailed experimental measurements,

i.e. PIV measurements, and validation.[158]

IX.5. Conclusion

We have studied the dynamic behavior of a mechanical ATS bileaflet heart valve in 2 different geometries. In agreement with *in vitro* studies, our simulations demonstrate a trend to less than maximum opening of the valve leaflets in an expanding geometry. This new FSI algorithm will be a major engineering tool available to unravel the haemodynamics associated with thrombolytic and hemolytic events of existing and new mechanical heart valves. Although improvements could be made concerning the mesh of the closed valve and more physiological boundary conditions, the computer model has shown its ability of modeling the dynamic behavior of mechanical heart valves.

Chapter X

Predicting ATS Open Pivot™ heart valve performance with computational fluid dynamics

---

The contents of this chapter is accepted for publication in Journal of Heart Valve Disease
Predicting ATS Open Pivot™ Heart Valve Performance with Computational Fluid Dynamics
Dumont K, Vierendeels J, Segers P, Van Nooten G, Verdonck P

Abstract

In vitro studies on the ATS heart valve have observed that valve opening is less in an expanding conduit compared to opening in a straight conduit.
We have studied bileaflet valve behavior using a new computational fluid-structure interaction model. A 3D model of the ATS valve was studied in two geometries, simulating the valve in a geometry with a sudden expansion downstream of the valve and in a straight conduit. Mitral and aortic flow patterns are simulated. The computer model was used to study standard clinical performance parameters.
The ATS valve in the expanding geometry showed opening to a maximum angle of 77.5°. This finding was confirmed by earlier clinical and *in vitro* studies. The mean and maximum transvalvular pressure gradients are 2.1 mmHg and 4.6 mmHg. The effective orifice area is 2.5 cm^2. The maximum shear stress calculated on the leaflet is 25 Pascal.
Maximum opening of the valve is achieved in the straight conduit. The mean and maximum pressure gradients are 1.1 mmHg and 4.3 mmHg. The effective orifice area is 2.3 cm^2. The maximum shear stress calculated on the leaflet is 35 Pascal.
Our numerical study confirms that valve haemodynamics and leaflet motion are dependent on the geometrical conditions of the valve: the presence of a diverging flow influences the maximum opening angle of the valve leaflets. The model can be used to predict pressure gradients, effective orifice area, and shear stress loading of mechanical heart valves. This model will be a major research tool in the future to unravel the haemodynamics of existing and new mechanical heart valves.

X.1. Introduction

Important design criteria of heart valves are related to the behavior of the valve in the flow field. In particular, pressure gradients should be as low as possible. Stagnation, recirculation zones[127,156] and shear stresses in the clearance region[157] are to be minimized in order to prevent initiation of coagulation.

Traditionally, the behavior of the valve (leaflets) is tested in *in vitro* mock circulations,[73,130,133,204] which implies that prototypes of the valves are already available at the time of testing. In the course of the design process, however, valves are computer designed, and virtual valve prototypes are available in an early stage of the design process. The challenge remains, however, to test the haemodynamic performance of these virtual prototypes. To do so, advanced computational algorithms, which take into account the continuous and full interaction between the flow and the valve leaflets are required.[140,141,155]

Several attempts have been made to assess heart valve kinematics using numerical fluid-structure interaction (FSI) models. Peskin and McQueen et al.[145] developed a three-dimensional model including the heart and vessel walls based on the immersed boundary method. Mechanical heart valve dynamics were studied only in two dimensions using the fictitious domain method by van de Vosse et al.[197] Although these methods have the advantage that they avoid the mesh movement, they are less accurate at the interface between the blood and the leaflet. As such, shear stress values on heart valve leaflets can not be estimated with these methods.

Using the arbitrary Lagrangian-Eulerian ALE-remeshing approach,[153] shear stress values on heart valve leaflets can be estimated more accurate. There are different ways to tackle the coupled interaction problem. One possibility is to develop new software and solution methods for each of these coupled applications. This is referred to as the monolithical approach or the direct method.[146] On the other hand, one can make use of existing methods and software packages which have been developed for either fluid or structural applications and consider iterative methods[147] - also known as partitioned methods[148] for fluid-structure interaction. As such, separate solvers are used for the fluid and the structure problem. The coupling between both, with an exchange of updated meshes and boundary conditions, is done in an iterative way.

We have recently developed a new numerical code that fulfils these requirements, and validation studies have demonstrated the accuracy of the numerical simula-

tions.[140,142] Our FSI code belongs to the class of partitioned but strongly coupled methods.[140,142,205] In this study, we apply this numerical code on a computer model of the ATS bileaflet valve. The motivation for choosing this particular valve is based on the observation that in some conditions, the valve opening angle does not reach the maximum opening position.[203] *In vitro* experiments[73,204] seem to suggest that this behavior is related to the geometrical conditions in which the valve functions: the maximum opening angle is achieved in a straight conduit, but not when the valve is placed in a expanding conduit.
In the following, we will simulate the flow pattern through the ATS valve and the motion of the valve leaflets in two conditions: (i) in a straight geometry subjected to a nominal aortic flow profile; (ii) in an expanding geometry, subjected to a nominal mitral flow profile. To further illustrate the possibilities of numerical simulations as 'virtual haemodynamic bench tests', we will use the simulated data (pressure, velocity fields) to calculate well known indices, traditionally calculated in *in vitro* and clinical studies,[73,203,204,208,209] and characterizing valve performance. In addition this allows us to calculate the shear stress distribution on the valve leaflets.

X.2. Materials and methods

X.2.1. Valve specifications

The model is based on the 22mm AP ATS Open Pivot™ heart valve. The inside diameter of the valve orifice is 20.8 mm with a geometric orifice area of 3.17 cm^2. Specific to this valve is its open pivot design, in which the convex pivot point and stops are located on the inner circumference and extended in the flow field. The opening angle of the leaflets and the side and central orifice of the valve are defined in Figure X.1.

X.2.2. Geometrical and boundary conditions

Two different configurations are studied and referred to as the 'straight' and 'expanding' geometry. Only one half of the valve is studied assuming symmetry of the flow. The straight geometry (Figure X.2(b)) is a conduit of 100 mm length and a diameter of 21.9 mm. The outflow conduit of the expanding geometry (Figure X.2(a)) is increased to 40 mm.

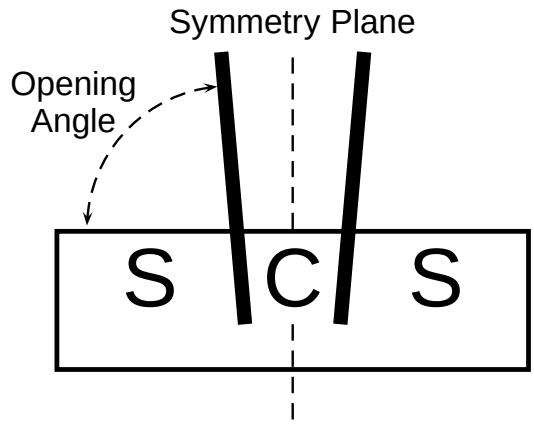

Figure X.1.: Opening angle, symmetry plane, side (S) and central (C) orifice of the ATS valve.

Inflow conditions are set 5 cm proximal to the valve. The applied flow profiles are nominal mitral and aortic flow profiles (Figure X.2(c) and X.2(d)), with the duration

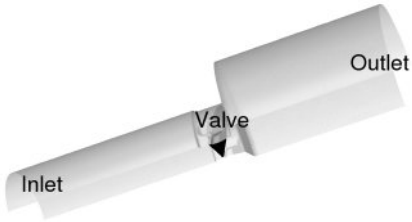

(a) 'Expanding' geometry.

(b) 'Straight' geometry.

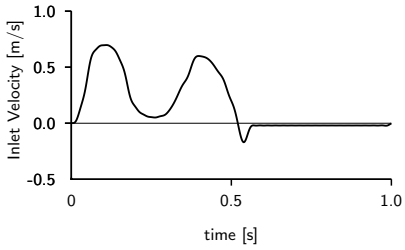

(c) 'Mitral' inlet velocity profile.

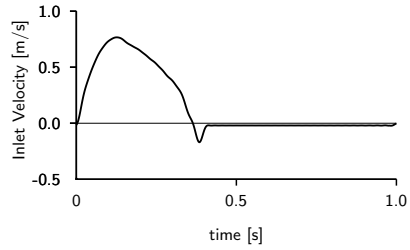

(d) 'Aortic' inlet velocity profile.

Figure X.2.: Studied geometries and velocity profiles.

of one cardiac cycle being 1 second (60 beats/minute). The cardiac output for both flow profiles is 4 l/min.

X.2.3. Clinical relevant parameters derived from the model

Numerical simulations produce pressure and velocity in each node of the numerical grid, and the position of the valve leaflet at any moment during the cardiac cycle. We calculated the velocity in the central V_{CO} and side orifice V_{SO} , and the pressure 1.5 cm and 5 cm proximal and distal to the valve. From these pressure data, we derived two transvalvular pressure gradients. The pressure gradient $\Delta P_{\Delta x=10cm}$ is defined as the pressure difference between points 5cm proximal and distal to the valve. Likewise, the pressure gradient $\Delta P_{\Delta x=3cm}$ is defined as the pressure difference between points 1.5cm proximal and distal to the valve. Mean and maximum transvalvular pressure gradients are calculated: ΔP_{mean} is the mean pressure gradient during forward flow, ΔP_{max} is the maximum pressure gradient during the cardiac cycle. Furthermore the pressure gradient ΔP_{Feng} as defined by Feng et al. is calculated.[73,204] The ΔP_{Feng} is defined as the mean pressure difference during acceleration phase.
Velocity profiles are simulated at the center orifice V_{CO} and side orifice V_{SO} of the valve. The velocity profile at the center orifice represents the velocity that would be measured by an ultrasound machine and is referred to here as the 'Doppler' velocity profile. The simplified Bernoulli equation is used to estimate the maximum forward pressure gradient $\Delta P_{doppler,max}$:

$$\Delta P_{doppler,max} = 4 \cdot V_{max}^2 \tag{X.1}$$

and the mean forward pressure gradient $\Delta P_{doppler,mean}$:

$$\Delta P_{doppler,mean} = 4 \cdot V_{mean}^2 \, . \tag{X.2}$$

The effective orifice area ($EOA_{continuity}$ [cm^2]) is calculated as the ratio of the forward stroke volume SV and velocity time integral VTI:

$$EOA_{continuity} = \frac{SV}{VTI} \, . \tag{X.3}$$

Besides the continuity equation, the Gorlin equation provides an alternative formula to calculate the effective orifice area (EOA_{Gorlin}):

$$EOA_{Gorlin} = \frac{\frac{SV}{t_{fwd}}}{51.6 \cdot \sqrt{\Delta P_{doppler,mean}}} \tag{X.4}$$

with t_{fwd} the time period of forward flow.
From the simulated velocities we were able to calculate the shear stress distribution on the leaflet assuming a constant blood viscosity. Shear stress is recognized as the primary biomechanical trigger for thrombolytic and hemolytic events.[124, 126, 207] From the shear stress distribution we calculated:

- For each timestep the spatial average shear stress on the leaflet: SS_{avg}
- The time variation of SS_{avg} during the cardiac cycle with a maximum value: $maxSS_{avg}$
- Maximum value of shear stress during the cardiac cycle on the leaflet: SS_{max}

X.3. Results

X.3.1. 'Expanding' geometry

The time course of leaflet opening is given in Figure X.3(a). The valve opening angle initially reaches 76.2°, moves toward a more closed position during diastasis (59.6°), and reopens during atrial contraction to an angle of 77.5°. The valve thus never reaches the maximum opening position.
Figure X.3(c) shows the velocity profiles as observed at the center orifice V_{CO} and side orifice V_{SO} of the valve compared to the inlet velocity profile. Then V_{CO} and V_{SO} are used to calculate $\Delta P_{doppler,max}$, $\Delta P_{doppler,mean}$ and the VTI as given in Table X.1. The maximum Doppler gradient $\Delta P_{doppler,max}$ is 4.27 mmHg and the mean value $\Delta P_{doppler,mean}$ is 1.11 mmHg. The mean pressure gradients derived from the numerical simulations are $\Delta P_{mean,\Delta x=10cm}$ = 0.49 mmHg and $\Delta P_{mean,\Delta x=3cm}$ = 0.71 mmHg. The maximum pressure gradients derived from the numerical simulations are $\Delta P_{max,\Delta x=10cm}$ = 9.20 mmHg and $\Delta P_{max,\Delta x=3cm}$ = 4.10 mmHg. The pressure gradient as defined by Feng et al. ΔP_{Feng} is 2.79 mmHg.
The effective orifice area (Table X.1), calculated with the continuity equation, is

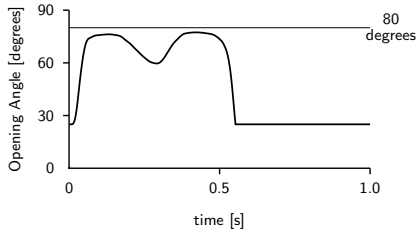

(a) 'Expanding' geometry: valve opening angle.

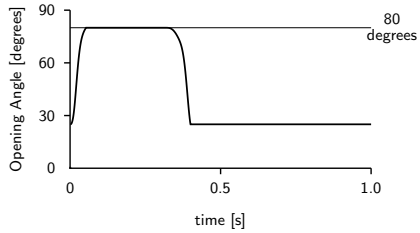

(b) 'Straight' geometry: valve opening angle.

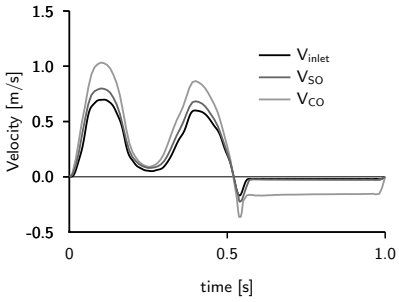

(c) 'Mitral' velocity profiles.

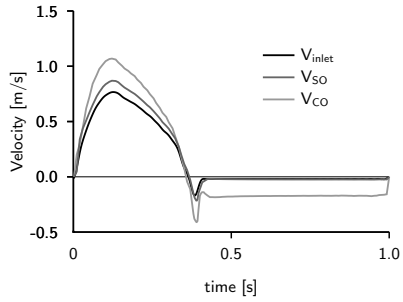

(d) 'Aortic' velocity profiles.

Figure X.3.: Valve opening angle and velocity profiles.

2.36 cm^2 and that with the Gorlin equation is 2.23 cm^2.

The flow pathlines are given in Figure X.4. These figures demonstrate some of the capabilities of the numerical model. The flow pathlines are diverging into the enlargement downstream of the valve (Figure X.4(a) and X.4(b)) guiding the valve leaflet motion. Circular pathlines are furthermore present during complete closing phase of the valve (Figure X.4(c)).

X.3.2. 'Straight' geometry

The valve opening with time for the straight geometry is given in Figure X.3(b). The valve opens fully and reaches the model maximum of 80°.

Figure X.3(d) shows the velocity profiles that are used to calculate $\Delta P_{doppler,max}$, $\Delta P_{doppler,mean}$ and the VTI as given in Table X.1. The maximum Doppler gradient $\Delta P_{doppler,max}$ is 4.58 mmHg and the mean value $\Delta P_{doppler,mean}$ is 2.06 mmHg. The mean pressure gradients derived from the numerical simulations are $\Delta P_{mean,\Delta x=10cm}$ = 0.70 mmHg and $\Delta P_{mean,\Delta x=3cm}$ = 0.76 mmHg. The maximum pressure gradients derived from the numerical simulations are $\Delta P_{max,\Delta x=10cm}$ = 9.79 mmHg and

Table X.1.: Summarized haemodynamic data.

Haemodynamic Flow and Pressure Data			
		'Expanding' Geometry	'Straight' Geometry
$\Delta P_{mean,Feng}$	[mmHg]	2.79	3.29
$\Delta P_{mean,\Delta x=10cm}$	[mmHg]	0.49	0.70
$\Delta P_{max,\Delta x=10cm}$	[mmHg]	9.20	9.79
$\Delta P_{mean,\Delta x=3cm}$	[mmHg]	0.71	0.76
$\Delta P_{max,\Delta x=3cm}$	[mmHg]	4.10	3.74
$\Delta P_{doppler,mean}$	[mmHg]	1.11	2.06
$\Delta P_{doppler,max}$	[mmHg]	4.27	4.58
VTI	[cm]	28.19	26.5
$EOA_{continuity}$	[cm^2]	2.36	2.52
EOA_{Gorlin}	[cm^2]	2.23	2.50

$\Delta P_{max,\Delta x=3cm}$ = 3.74 mmHg. The pressure gradient ΔP_{Feng} is 3.29 mmHg.
The effective orifice area (Table X.1), calculated with the continuity equation, is 2.52 cm^2 and that with the Gorlin equation is 2.50 cm^2.
The flow pathlines are given in Figure X.5. The flow pathlines in Figures X.5(a) and X.5(b) are more streamlined compared to the pathlines during the closure of the of the valve (Figure X.5(c)).

X.3.3. Shear stress distribution

We calculated shear stress distribution on the valve leaflet in the two geometries. The time variation of average shear stress SS_{avg} is shown (Figure X.6(a)). Average shear stress SS_{avg} is higher in the straight geometry than in the expanding geometry (Figure X.6(a)). The $maxSS_{avg}$ is calculated 10.4 Pa for the expanding geometry and 19.3 Pa for the straight geometry. Figure X.6(b) compares the shear stress distribution on the leaflet for the two geometries and for the side and central orifice

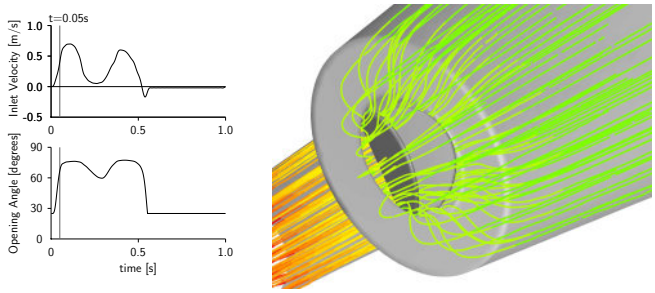

(a) t=0.05s, θ =66°, V_{inlet}=0.40m/s

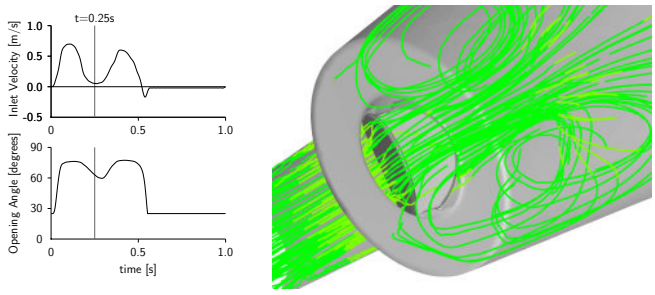

(b) t=0.25s, θ =63°, V_{inlet}=0.05m/s

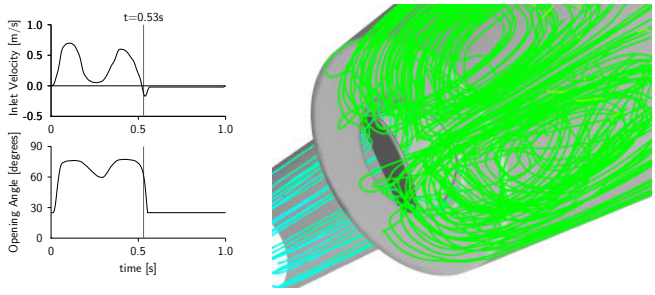

(c) t=0.53s, θ =61°, V_{inlet}=-0.12m/s

(d) Pressure values colorbar.

Figure X.4.: 'Expanding' geometry: pathlines colored with reference to pressure.

(Figure X.1). The figure shows the shear stress distribution corresponding with the time of maxSS_{avg} in figure X.6(a). The SS_{max} is 25 Pa for of the expanding geometry and 35 Pa for the straight geometry.

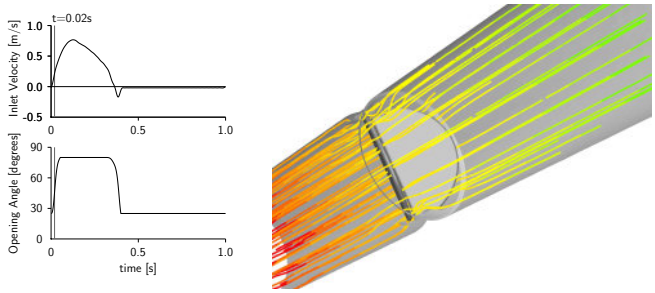

(a) t=0.02s, θ =45°, V_{inlet}=0.22m/s

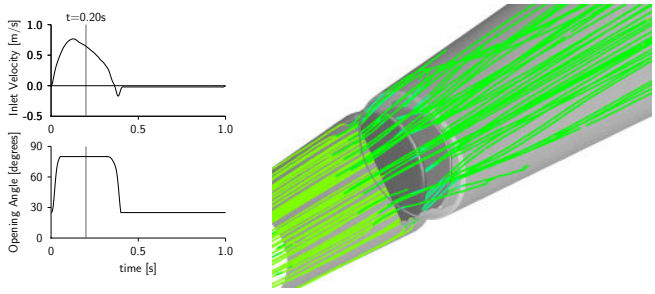

(b) t=0.20s, θ =80°, V_{inlet}=0.64m/s

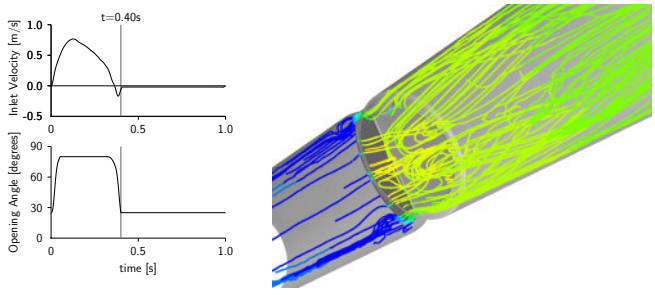

(c) t=0.40s, θ =25°, V_{inlet}=-0.06m/s

(d) Pressure values colorbar.

Figure X.5.: 'Straight' position: pathlines colored with reference to pressure.

X.4. Discussion

We simulated the opening and closing of the ATS Open Pivot™ heart valve in two geometries, a 'expanding' conduit and a 'straight' conduit. In both cases we used the physiological inflow pattern corresponding to a cardiac output of 4 l/min. Clin-

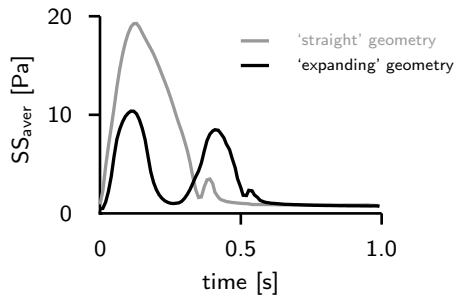

(a) SS_{avg} [Pa] on the leaflet.

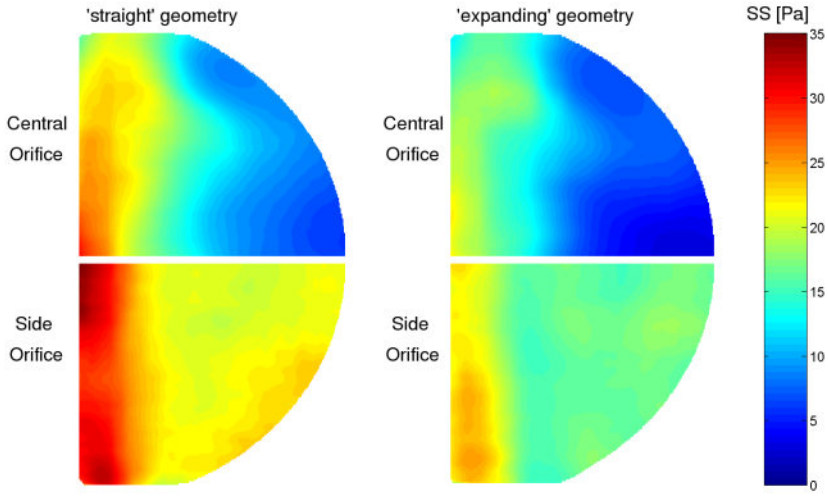

(b) Shear stress distribution [Pa] on the leaflet corresponding with the time of maxSS_{avg}.

Figure X.6.: Shear stress [Pa] on the valve leaflets.

ical relevant parameters were investigated from the numerical simulations.
We have recently developed a numerical code that accounts for the complex blood-leaflet interaction, and a 2D validation study has demonstrated the accuracy of the numerical simulations.[140,142] Based on these observations we applied the algorithm in a 3D setting. It is however acknowledged that further experimental measurements are needed to validate the agreement between the measured and calculated complex 3D flow phenomena around the moving valve leaflet. During forward flow conditions, mean pressure gradients remain below 3.3 mmHg for a cardiac output of 4.0 l/min. The mean forward pressure gradients $\Delta P_{doppler,mean}$ are 1.11 mmHg in case of mitral flow conditions and 2.06 mmHg for aortic flow pattern. These values are

in the same range as reported by Laske et al.[210] The maximum forward pressure gradients are in good agreement with the maximum pressure gradients $\Delta P_{\Delta x=3cm}$ for both geometries. The maximum pressure gradients $\Delta P_{\Delta x=10cm}$ are higher than $\Delta P_{\Delta x=3cm}$. In order to compare the calculated pressure gradients with published experimental data, we calculated the mean pressure gradient as defined by Feng et al.[73] Our calculated values are 2.79 mmHg for the expanding conduit and 3.29 mmHg for the straight compared to 4.8 mmHg for the same cardiac output as reported by Feng et al.[73]

The effective orifice area, calculated with the continuity equation, is 2.36 cm^2 for the expanding conduit and 2.52 cm^2 for the straight conduit. The effective orifice area, calculated with the Gorlin equation is 2.23 cm^2 for the expanding conduit and 2.50 cm^2 for the straight conduit. The ATS FDA submission[72] reported an effective orifice area of 2.1 cm^2 for the same valve size.

The impact of geometrical conditions on the ATS valve leaflet motion was studied *in vitro* by Feng et al.,[73,204] which confirms earlier published *in vivo* results reported by Aoyagi et al.[203] in mitral position. They[73,204] reported less than maximum opening of the valve in an expanding conduit under mitral flow conditions. Their results are in qualitative agreement with our numerical simulations. The ATS valve in the expanding geometry showed opening to a maximum angle of 77.5°, which closely resembles the 75.5 ± 1.7° reported by Feng at al.[73,204]

Another important haemodynamic parameter, impossible to measure directly *in vivo* and *in vitro*, is the shear stress distribution. The SS_{max} on the valve leaflet is 25 Pa for the expanding geometry and 35 Pa for the straight geometry. These values are comparable to what can be found in literature.[44] The average SS_{avg} on the leaflet is 10.4 Pa in the expanding geometry compared to 19.3 Pa in the straight geometry (Figure X.6(a)). In the expanding geometry the diverging flow interacts with the valve opening, reducing shear stress on the leaflets as shown in Figures X.6(a) and X.6(b). Thus, less than maximum opening of the valve and alignment of the leaflets with the streamlines, improve the shear stress distribution and reduce potential for damage to platelets and blood cells.

The aim of the study was to apply our computational fluid dynamics code on a realistic 3D geometry of the ATS valve using relevant geometrical and physiological conditions. Our results are in qualitative agreement with *in vivo* and *in vitro* observations.[44,72,73,203,204,210]

X.5. Conclusion

Our numerical simulation confirms that valve haemodynamics and leaflet motion depend on the geometrical conditions of the valve: the diverging flow caused by the expanding conduit combined with the valve design characteristics lead to less than maximum valve opening, but results in reduced shear stresses on the leaflets.
The computer model can be used to predict pressure gradients, shear stress distribution and effective orifice area of mechanical heart valves. The calculated haemodynamic performances of the ATS medical valve are in agreement with published data. This new numerical model will be a major research tool to unravel the haemodynamics associated with thrombolytic and hemolytic events of new and existing mechanical heart valves.

Chapter XI

Fluid-structure interaction modeling of a tissue engineered heart valve leaflet

---

The contents of this chapter is submitted for publication in Computers in Biology & Medicine.
Feasibility Study of Fluid-Structure Interaction of a Flexible Heart Valve Leaflet in Fluent
Dumont K, Vierendeels J, Segers P and Verdonck P

Abstract

A new method for the computational analysis of fluid-structure interaction with highly flexible bodies is presented. Methods and software systems which have been developed for either fluid or structural applications are used separately. The goal of this study was to show the feasibility of a new innovative algorithm for the strongly coupling of a commercial available computational fluid dynamics code (Fluent) with a in-house coded structural solver. Fluent (Fluent Inc, New Hampshire, US) uses a dynamic mesh approach for the simulation of flows where the shape of the domain is changing with time due to the motion of the domain boundaries. The dynamic mesh model makes use of an arbitrary Lagrangian Eulerian (ALE) formulation of the Navier-Stokes equations with local remeshing. A full implicit iteration scheme is developed in order to obtain a stable algorithm. The strong response of the pressure distribution to the displacement is represented by a Jacobian matrix and is added to the structural solver in order to obtain a stable iteration scheme. The method is demonstrated for the opening and closing of a 2D model of a flexible aortic valve leaflet during the complete cardiac cycle. Futhermore the model is used to calculate the shear stress on the leaflet applicable for the development of tissue engineered constructs.

XI.1. Introduction

Detailed knowledge of the flow field and forces acting upon the heart valve apparatus is critical for the design of prosthetic heart valves, and for a better understanding of biomechanical actors in heart valve disease. This is particularly true for tissue engineered aortic valves. It is still problematic to transplant an *in vitro* cultured valve into the aorta, where it is subjected to high pressures and shear forces acting on the newly seeded cells. Measuring these forces in a direct way is impossible, but numerical techniques may be used to assess them. Ideally the numerical computation fully accounts for the interaction between the fluid and the leaflet moving within the fluid, without predefining the fluid field or the leaflet motion.

Several attempts have been made to assess heart valve kinematics using numerical fluid-structure interaction (FSI) models. Horsten et al.[167] modeled the interaction of a flexible two-dimensional valve leaflet with a rigid channel flow. Peskin and McQueen et al.[145] developed a three-dimensional model including the heart and vessel walls based on the immersed boundary method. A fluid-structure simulation of a bioprosthetic aortic valve functioning was performed by Makhijani et al.,[166] but the leaflet structure had a much higher resistance to bending compared to the natural leaflets. A physiological more realistic fluid-structure interaction model of the natural valve, has been developed by De Hart et al. using the fictitious domain method.[30,81,143]

Another method often applied to fluid-structure interaction simulations is the arbitrary Lagrangian-Eulerian (ALE) formulation.[153,154] This method combines the Eulerian formulation, describing the fluid using a fixed mesh, and the Lagrangian formulation, where the numerical grid follows the motion of the structure. Using the ALE-remeshing approach, there are different ways to tackle a coupled interaction problem. One possibility is to develop new software and solution methods for each of these coupled applications. This is referred to as the monolithical approach or the direct method.[146,147] On the other hand, one can make use of existing methods and software packages which have been developed for either fluid or structural applications and consider iterative methods[148] - also known as partitioned methods[147] for fluid-structure interaction. As such, separate solvers are used for the fluid and the structure problem.[149] The coupling between both, with an exchange of updated meshes and boundary conditions, is done in an iterative way.

Recently, Fluent Inc. (New Hampshire, US) released the dynamic mesh model for

the simulation of flows where the shape of the domain is changing with time due to the motion of the domain boundaries. The dynamic mesh model uses an ALE and local remeshing approach to adapt the mesh to a described motion, which can be described using user-defined functions (UDFs).[211] Using Fluent, a structural solver has to be coupled to the fluid solver in an iterative way.[147]

In this study, we apply a newly developed FSI algorithm to solve the problem of a flexible valve leaflet in 2D flow. Furthermore, we believe that one of the potential applications of the FSI model is the estimation on shear stress forces exerted by the fluid flow on the endothelial cell surface of a tissue engineered heart valve. Therefore, to demonstrate the feasibility of calculating detailed flow directed features in the vicinity of the moving valve leaflets, we calculated shear stresses (SS) on the leaflets over the complete cardiac cycle.

XI.2. Methods

XI.2.1. A 2D structural model of a flexible heart valve leaflet

Figure XI.1 illustrates how the 2D flexible heart valve leaflet with a length l is modeled. The leaflet consists of N equidistant segments with length $\Delta l = \frac{l}{N}$ connected to each other with frictionless pivots and with torsional springs, characterized by the constant $k_s = \frac{EI}{\Delta l}$. The material model is based on earlier studies done by David et al.[212] and Horsten et al.[167] If the pressure distribution $\underline{p}$ on the leaflet is given by the fluid solver Fluent, the unknown variables are the positions $\underline{X}$ of the segment centers, the angles $\underline{\theta}$ defining the position of the leaflet, and the reaction forces $\underline{R}_x$ and $\underline{R}_y$ in the x-direction and the y-direction, respectively.

$$\underline{p} = \begin{bmatrix} p_1 \\ \vdots \\ p_i \\ \vdots \\ p_N \end{bmatrix}, \quad \underline{X} = \begin{bmatrix} x_1 \\ y_1 \\ \vdots \\ x_i \\ y_i \\ \vdots \\ x_N \\ y_N \end{bmatrix}, \quad \underline{\theta} = \begin{bmatrix} \theta_1 \\ \vdots \\ \theta_i \\ \vdots \\ \theta_N \end{bmatrix}, \quad \underline{R}_x = \begin{bmatrix} R_{x,1} \\ \vdots \\ R_{x,i} \\ \vdots \\ R_{x,N} \end{bmatrix}, \quad \underline{R}_y = \begin{bmatrix} R_{y,1} \\ \vdots \\ R_{y,i} \\ \vdots \\ R_{y,N} \end{bmatrix} \tag{XI.1}$$

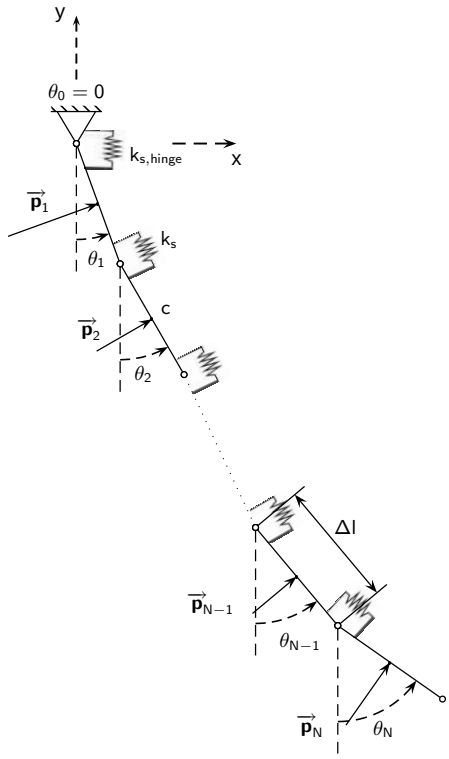

(a) Scheme for flexible leaflet: segments are connected with frictionless pivots and angular stiffness.

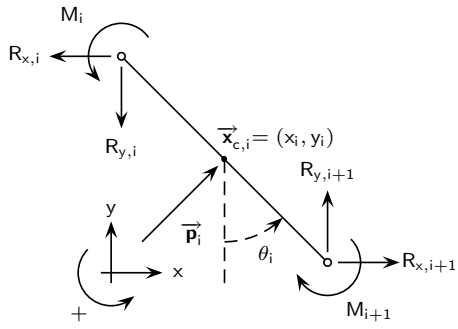

(b) Forces acting on a single segment of the flexible leaflet.

Figure XI.1.: Schematic overview of the implemented material model: total leaflet length (top panel), single segment (bottom panel).

The equation describing the material model is written as

$$\underline{G}(\underline{p}, \underline{X}, \underline{\theta}, \underline{R}_x, \underline{R}_y) = 0 \tag{XI.2}$$

Two equations (2 dimensional model) will express that the length of the leaflet segments is a constant value Δl. Furthermore, Newton's 2nd Law of Motion states that the acceleration of a particle is equal to the vector sum of forces acting upon that particle. This Conservation of Momentum results in an equilibrium equation of the forces in the x-direction, and the y-direction and the rotational equilibrium equation.

$$\left\{\begin{array}{l} G_{i,1} = 0\,, \\ G_{i,2} = 0\,, \\ G_{i,3} = 0\,, \\ G_{i,4} = 0\,, \\ G_{i,5} = 0 \end{array}\right. = \left\{\begin{array}{l} x_i = x_{i-1} + \frac{\Delta l}{2} \cdot sin(\theta_{i-1}) + \frac{\Delta l}{2} \cdot sin(\theta_i)\,, \\ y_i = y_{i-1} - \frac{\Delta l}{2} \cdot cos(\theta_{i-1}) - \frac{\Delta l}{2} \cdot cos(\theta_i)\,, \\ m \cdot \ddot{x}_i = -R_{x,i} + R_{x,i+1} + p_i \cdot cos(\theta_i)\,, \\ m \cdot \ddot{y}_i = -R_{y,i} + R_{y,i+1} + p_i \cdot sin(\theta_i)\,, \\ I \cdot \ddot{\theta}_i = M_i - M_{i+1} + \frac{\Delta l}{2} \cdot (R_{x,i} + R_{x,i+1}) \cdot cos(\theta_i) \\ \qquad\qquad + \frac{\Delta l}{2} \cdot (R_{y,i} + R_{y,i+1}) \cdot sin(\theta_i) \end{array}\right. \tag{XI.3}$$

The equations are linearized with Newton linearization and solved iteratively upon convergence. The index n indicates the timestep and s denotes the subiterations of the structural model.

$$
\begin{aligned}
x_i^{n+1,s+1} &= x_{i-1}^{n+1,s+1} && \text{(XI.4)}\\
&+ \tfrac{\Delta l}{2}\cdot(sin(\theta_{i-1}^{n+1,s})+sin(\theta_i^{n+1,s}))\\
&+ \tfrac{\Delta l}{2}\cdot cos(\theta_{i-1}^{n+1,s})\cdot(\theta_{i-1}^{n+1,s+1}-\theta_{i-1}^{n+1,s})\\
&+ \tfrac{\Delta l}{2}\cdot cos(\theta_i^{n+1,s})\cdot(\theta_i^{n+1,s+1}-\theta_i^{n+1,s})\ ,\\
y_i^{n+1,s+1} &= y_{i-1}^{n+1,s+1} && \text{(XI.5)}\\
&- \tfrac{\Delta l}{2}\cdot(cos(\theta_{i-1}^{n+1,s})+cos(\theta_i^{n+1,s}))\\
&+ \tfrac{\Delta l}{2}\cdot sin(\theta_{i-1}^{n+1,s})\cdot(\theta_{i-1}^{n+1,s+1}-\theta_{i-1}^{n+1,s})\\
&+ \tfrac{\Delta l}{2}\cdot sin(\theta_i^{n+1,s})\cdot(\theta_i^{n+1,s+1}-\theta_i^{n+1,s})\ ,\\
\tfrac{m}{\Delta t^2}\cdot x_i^{n+1,s+1} &= \tfrac{m}{\Delta t^2}\cdot(x_i^n+\dot{x}_i^n\cdot\Delta t) && \text{(XI.6)}\\
&- R_{x,i}^{n+1,s+1}+R_{x,i+1}^{n+1,s+1}+p_i\cdot cos(\theta_i^{n+1,s})\ ,\\
\tfrac{m}{\Delta t^2}\cdot y_i^{n+1,s+1} &= \tfrac{m}{\Delta t^2}\cdot(y_i^n+\dot{y}_i^n\cdot\Delta t) && \text{(XI.7)}\\
&- R_{y,i}^{n+1,s+1}+R_{y,i+1}^{n+1,s+1}+p_i\cdot sin(\theta_i^{n+1,s})\ ,\\
\tfrac{I}{\Delta t^2}\cdot\theta_i^{n+1,s+1} &= \tfrac{I}{\Delta t^2}\cdot(\theta_i^n+\dot{\theta}_i^n\cdot\Delta t) && \text{(XI.8)}\\
&+ \tfrac{EI}{\Delta l}(\theta_{i-1}^{n+1,s+1}-\theta_i^{n+1,s+1}-\Delta\theta_{i,no\ stress})\\
&- \tfrac{EI}{\Delta l}(\theta_i^{n+1,s+1}-\theta_{i+1}^{n+1,s+1}-\Delta\theta_{i+1,no\ stress})\\
&+ \tfrac{\Delta l}{2}\cdot(R_{x,i}^{n+1,s+1}+R_{x,i+1}^{n+1,s+1})\cdot cos(\theta_i^{n+1,s})\\
&- \tfrac{\Delta l}{2}\cdot(R_{x,i}^{n+1,s}+R_{x,i+1}^{n+1,s})\cdot sin(\theta_i^{n+1,s})\cdot(\theta_i^{n+1,s+1}-\theta_i^{n+1,s})\\
&+ \tfrac{\Delta l}{2}\cdot(R_{y,i}^{n+1,s+1}+R_{y,i+1}^{n+1,s+1})\cdot sin(\theta_i^{n+1,s})\\
&+ \tfrac{\Delta l}{2}\cdot(R_{y,i}^{n+1,s}+R_{y,i+1}^{n+1,s})\cdot cos(\theta_i^{n+1,s})\cdot(\theta_i^{n+1,s+1}-\theta_i^{n+1,s})
\end{aligned}
$$

The equations look slightly different for the outer segments i=1 and i=N of the leaflet: $M_1 = k_{s,hinge}\cdot(\theta_1-\theta_0)$ and $x_0 = y_0 = 0$ m, $M_{N+1} = 0$ Nm, $R_{x,N+1} = R_{y,N+1} = 0$ N. The structural equations are solved for a certain imposed pressure distribution $\underline{p}$. This gives the displacements $\underline{X}^{n+1}$ as a result. The angles and reaction forces can be seen as internal variables for the structural solver. In the sequel we can thus write the structural solver as

$$\underline{G}(\underline{X}^{n+1},\underline{p}) = 0\ . \qquad \text{(XI.9)}$$

As explained, the structural problem will be solved in an iterative manner, with $s+1$ the new subiteration and s the previous subiteration.

$$\underline{G}(\underline{X}^{s+1}, \underline{p}) = 0 = \underline{G}(\underline{X}^{s}, \underline{p}) + \left.\frac{\partial \underline{G}}{\partial \underline{X}}\right|_{s} \cdot \Delta \underline{X} \tag{XI.10}$$

If $A = \left.\frac{\partial \underline{G}}{\partial \underline{X}}\right|_{s}$, we can solve $\Delta \underline{X}$ from the equation:

$$A \cdot (-\Delta \underline{X}) = \underline{G}(\underline{X}^{s}, \underline{p}) \tag{XI.11}$$

This scheme is solved iteratively until $\Delta \underline{X}$ equals zero, so that the Conservation of Momentum is fulfilled in all the nodes. The position of the nodes $\underline{X}$ is then in equilibrium with the pressure distribution $\underline{p}$. From now on we drop the index s as notation.

XI.2.2. The implicit iteration scheme

To achieve implicit time integration with the partioned (fluid and structural) solvers, an iterative coupling is needed per timestep. To obtain a coupled solution of both fluid and structural solver, an explicit coupling procedure can be used, consisting of subsequent calls of both solvers. An estimated pressure distribution $\underline{p}^{n+1,k}$ is used in the structural model $\underline{G}(\underline{X}^{n+1,k+1}, \underline{p}^{n+1,k}) = 0$ to estimate the new positions of the valve leaflet $\underline{X}^{n+1,k+1}$. Here k denotes the subiteration level of the coupling of the fluid and the structural solver. A new pressure distribution $\underline{p}^{n+1,k+1}$ is then estimated by solving the flow equation in Fluent $\underline{F}(\underline{X}^{n+1,k+1}, \underline{p}^{n+1,k+1}) = 0$ for this new position of the valve leaflet $\underline{X}^{n+1,k+1}$. This new pressure distribution will then again be used to estimate the new positions of the flexible valve leaflet.

$$\begin{cases} \underline{G}(\underline{X}^{n+1,k+1}, \underline{p}^{n+1,k}) = 0, \\ \underline{F}(\underline{X}^{n+1,k+1}, \underline{p}^{n+1,k+1}) = 0\ . \end{cases} \tag{XI.12}$$

However, this explicit procedure is not stable, because the displacements $\Delta \underline{X}$ of the structural solver are highly sensitive to variations of the imposed pressure distribution $\Delta \underline{p}$ from Fluent on the valve leaflet. The pressure distribution $\Delta \underline{p}$ calculated in Fluent, on the other hand, is reacting very sensitively on variations of the displace-

ments $\Delta\underline{X}$ from the structural solver. The problems with this explicit scheme, is that the equations $\underline{G}$ are not solved with $\underline{p}^{n+1,k+1}$, but with $\underline{p}^{n+1,k}$. Thus, in the iterative procedure the pressure distribution of the previous Fluent subiteration is used. Because the valve leaflet is highly flexible and the structural problem is not accounting for the influence $\frac{\partial p}{\partial \underline{X}}$ of the displacements $\underline{X}$ on the pressure distribution $\underline{p}$, it is overreacting to the pressure forces from Fluent. Earlier studies on mechanical heart valves with stiff leaflets and thus only one degree of freedom, e.g. the angle of the valve leaflet, showed the importance of this derivative for the stabilization of the iteration scheme.[140,142,213] The iterative scheme becomes stable and fully implicit if we could predict in the structural solver how the pressure distribution would react on changes in the positions of the leaflet nodes. The implicit formulation of the equation for the flexible leaflet becomes

$$\underline{G}(\underline{X}^{n+1,k+1}, \underline{p}^{n+1,k+1}) = 0 \; . \tag{XI.13}$$

An approximation of $\underline{p}^{n+1,k+1}$ (Equation XI.14) can be obtained from a **R**educed **O**rder **M**odel $\underline{F}_{ROM}$ which predicts the behavior of the fluid solver to the prescribed displacements of the leaflet.

$$\underline{p}^{n+1,k+1} = \underline{F}_{ROM}(\underline{X}^{n+1,k+1}) = \underline{p}^{n+1,k} + A_{ROM}(\underline{X}^{n+1,k+1} - \underline{X}^{n+1,k}) \tag{XI.14}$$

Since the pressure distribution on the leaflet is not longer a constant value, but changing with the leaflet position, the equation XI.10 needs to be rewritten:

$$\begin{aligned} 0 = \underline{G}(\underline{X}^{n+1,k+1}, \underline{p}^{n+1,k+1}) \approx \quad & \underline{G}(\underline{X}^{n+1,k+1}, \underline{p}^{n+1,k}) \\ & + \left.\frac{\partial \underline{G}}{\partial \underline{p}}\right|^{n+1,k} \cdot (\underline{p}^{n+1,k+1} - \underline{p}^{n+1,k}) \; . \end{aligned} \tag{XI.15}$$

With equation XI.14 this becomes

$$\begin{aligned} 0 = \underline{G}(\underline{X}^{n+1,k+1}, \underline{p}^{n+1,k+1}) \approx \quad & \underline{G}(\underline{X}^{n+1,k+1}, \underline{p}^{n+1,k}) \\ & + \left.\frac{\partial \underline{G}}{\partial \underline{p}}\right|^{n+1,k} \cdot A_{ROM}(\underline{X}^{n+1,k+1} - \underline{X}^{n+1,k}) \end{aligned} \tag{XI.16}$$

where $\underline{p}^{n+1,k}$ and $\underline{X}^{n+1,k}$ are solutions of $\underline{F}(\underline{X}^{n+1,k}, \underline{p}^{n+1,k}) = 0$ and A_{ROM} is the Jacobian matrix of a reduced order model of the response of the fluid solver.

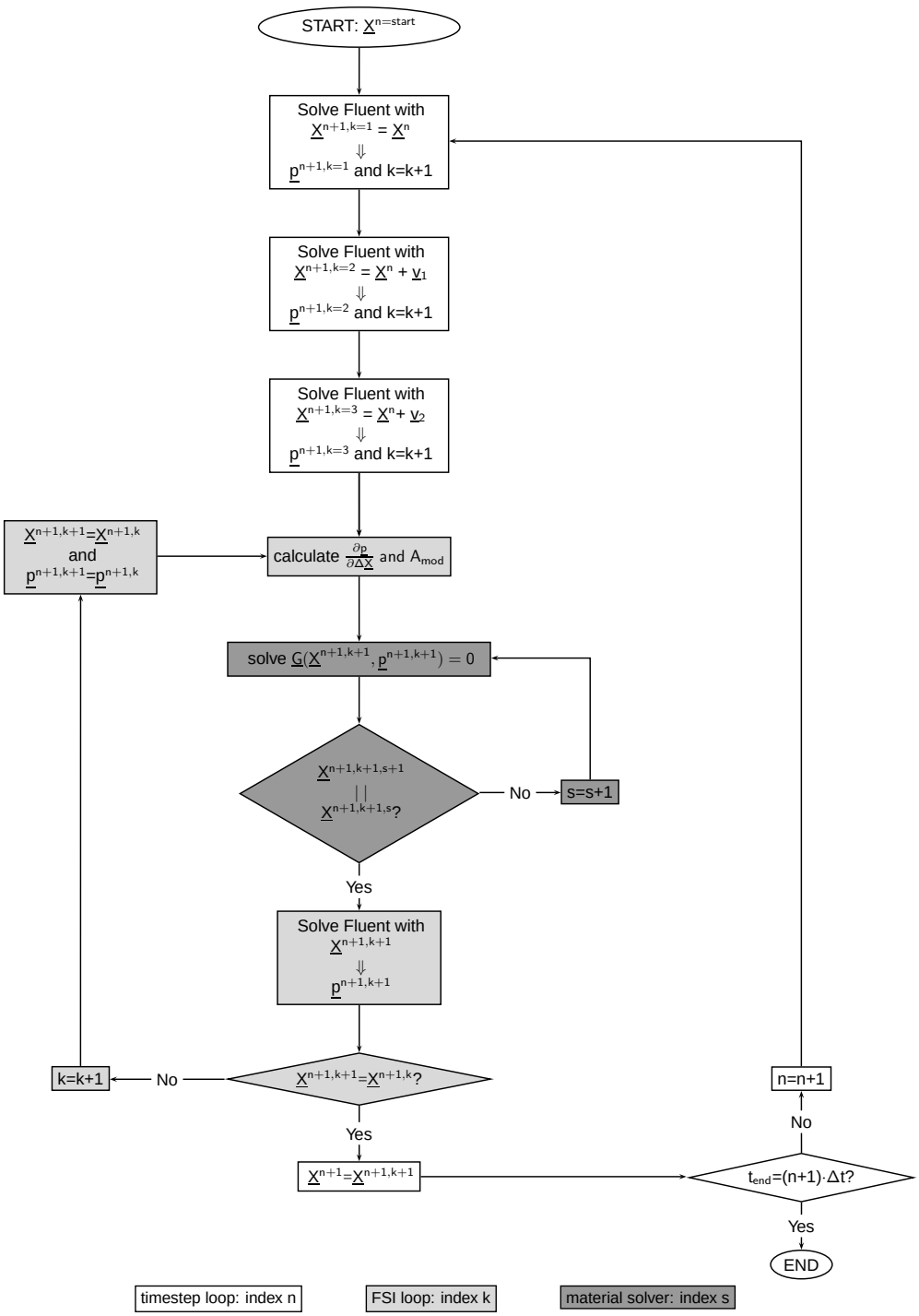

Figure XI.2.: Iterative scheme of the 2D flexible leaflet fluid-structure interaction model.

With $A_{mod} = \left.\frac{\partial \underline{G}}{\partial \underline{p}}\right|^{n+1,k} \cdot A_{ROM}$, this results in

$$0 = \underline{G}(\underline{X}^{n+1,k+1}, \underline{p}^{n+1,k+1}) \approx \quad \underline{G}(\underline{X}^{n+1,k+1}, \underline{p}^{n+1,k}) + A_{mod} \cdot (\underline{X}^{n+1,k+1} - \underline{X}^{n+1,k}) \; . \tag{XI.17}$$

This equation is solved iteratively in the same way as equation XI.11. The index mod of the matrix A_{mod} is based on the use of "displacements modes", which is further explained in paragraph "**Calculation of** A_{mod}".
Finally, figure XI.2 shows how the three iterations loops fit into the flow diagram: the smallest loop with index s is the iteration loop for the structural leaflet model, the middle loop with index k is the iteration loop for the coupling of Fluent with the structural solver and the outer loop with index n is the timestep loop.

XI.2.2.1. Calculation of A_{mod}

To calculate the matrix A_{mod} we remark that the force on one single segment is only function of the pressure on that segment and is independent on the pressure distribution on the other segments. With this simplification the calculation of $\frac{\partial \underline{G}}{\partial \underline{p}}$ is relatively simple.

$$\frac{\partial \underline{G}}{\partial \underline{p}} = \begin{bmatrix} 0 & & & & & & & & \\ 0 & & & & & & & & \\ \partial G_{1,3}/\partial p_1 & & & & & & & & \\ \partial G_{1,4}/\partial p_1 & & & & & & & & \\ 0 & & & & & & & & \\ & \ddots & & & & & & & \\ & & 0 & & & & & & \\ & & 0 & & & & & & \\ & & \partial G_{i,3}/\partial p_i & & & & & & \\ & & \partial G_{i,4}/\partial p_i & & & & & & \\ & & 0 & & & & & & \\ & & & \ddots & & & & & \\ & & & & 0 & & & & \\ & & & & 0 & & & & \\ & & & & \partial G_{N,3}/\partial p_N & & & & \\ & & & & \partial G_{N,4}/\partial p_N & & & & \\ & & & & 0 & & & & \end{bmatrix} \tag{XI.18}$$

The calculation of A_{ROM} is more complicated. A_{ROM} represents the relation between $\Delta\underline{p}$ and $\Delta\underline{X}$ within one timestep. The proposed method uses "displacement modes" or possible displacements of the valve leaflet. As the leaflet has $2 \cdot N$ degrees of freedom, there are maximum $2 \cdot N$ linear independent modes. By using these modes, we can calculate an approximation of $\frac{\partial p}{\partial \underline{X}}$.
The process is started from the initial positions $\underline{X}^{n+1,k}$ and the pressure distribution $\underline{p}^{n+1,k}$. Small perturbations with reference to $\underline{X}^{n+1,k}$ are introduced in the model and the correspondent pressure distribution is calculated with the Fluent solver. When using m displacement modes $\underline{v}_j$, Fluent gives us correspondingly m pressure distributions $\underline{p}_j$. By doing so, we can construct the matrix with the pressure responses to the applied displacements modes.

$$\begin{bmatrix} \Delta\underline{p}_1 & \cdots & \Delta\underline{p}_j & \cdots & \Delta p_m \end{bmatrix} \tag{XI.19}$$

with $\Delta\underline{p}_j = \underline{p}^{n+1,j} - \underline{p}^{n+1,k-1}$ for $k > 3$, $j = 1 \ldots k-2$ and with $\underline{p}_j$ the pressure distribution resulting from the perturbation $\underline{v}_{j-1}$ ($\underline{v}_0 = \underline{0}$). An arbitrary displacement $\Delta\underline{X}$ can now be written as the sum of $2.N$ perturbation modes:

$$\Delta\underline{X} = \begin{bmatrix} \Delta x_1 \\ \Delta y_1 \\ \Delta x_2 \\ \Delta y_2 \\ \vdots \\ \Delta x_N \\ \Delta y_N \end{bmatrix} = \alpha_1.\underline{v}_1 + \alpha_2.\underline{v}_2 + \alpha_3.\underline{v}_3 + \ldots + \alpha_{2.N}.\underline{v}_{2.N} \tag{XI.20}$$

where the scalars α_j represent the weighting factor of the perturbation modes. As it is not necessarily required to use all $2.N$ modes, we can rewrite the above equation for m modes.

$$\Delta\underline{X} \approx \alpha_1.\underline{v}_1 + \ldots + \alpha_j.\underline{v}_j + \ldots + \alpha_m.\underline{v}_m \tag{XI.21}$$

Multiplying to the left with $\underline{v}_1^T$, gives:

$$\underline{v}_1^T \cdot \Delta\underline{X} \approx \alpha_1 . \langle \underline{v}_1, \underline{v}_1 \rangle + \ldots + \alpha_j . \left\langle \underline{v}_1, \underline{v}_j \right\rangle + \ldots + \alpha_m . \langle \underline{v}_1, \underline{v}_m \rangle \qquad \text{(XI.22)}$$

with $\left\langle \underline{v}_j, \underline{v}_j \right\rangle = \underline{v}_j^T \cdot \underline{v}_j$. If this is done for every mode, this results in:

$$\begin{bmatrix} \alpha_1 \\ \vdots \\ \alpha_j \\ \vdots \\ \alpha_m \end{bmatrix} \approx \begin{bmatrix} \langle \underline{v}_1, \underline{v}_1 \rangle & \ldots & \left\langle \underline{v}_1, \underline{v}_j \right\rangle & \ldots & \langle \underline{v}_1, \underline{v}_m \rangle \\ \vdots & & \vdots & & \vdots \\ \langle \underline{v}_l, \underline{v}_1 \rangle & \ldots & \left\langle \underline{v}_l, \underline{v}_j \right\rangle & \ldots & \langle \underline{v}_l, \underline{v}_m \rangle \\ \vdots & & \vdots & & \vdots \\ \langle \underline{v}_m, \underline{v}_1 \rangle & \ldots & \left\langle \underline{v}_m, \underline{v}_j \right\rangle & \ldots & \langle \underline{v}_m, \underline{v}_m \rangle \end{bmatrix}^{-1} \cdot \begin{bmatrix} \underline{v}_1^T \\ \vdots \\ \underline{v}_j^T \\ \vdots \\ \underline{v}_m^T \end{bmatrix} \cdot \begin{bmatrix} \Delta x_1 \\ \Delta y_1 \\ \vdots \\ \Delta x_i \\ \Delta y_i \\ \vdots \\ \Delta x_N \\ \Delta y_N \end{bmatrix}$$

$$\approx \underline{V} \cdot \begin{bmatrix} \Delta x_1 \\ \Delta y_1 \\ \vdots \\ \Delta x_i \\ \Delta y_i \\ \vdots \\ \Delta x_N \\ \Delta y_N \end{bmatrix} \qquad \text{(XI.23)}$$

The calculated α's represent the 'contribution' of each mode to the total displacement $\Delta\underline{X}$ and thus we can write:

$$\frac{\partial \underline{G}}{\partial \underline{p}} \cdot \Delta \underline{p} \approx \frac{\partial \underline{G}}{\partial \underline{p}} \cdot \left[\Delta \underline{p}_1 \quad \cdots \quad \Delta \underline{p}_j \quad \cdots \quad \Delta \underline{p}_m \right] \cdot \begin{bmatrix} \alpha_1 \\ \vdots \\ \alpha_j \\ \vdots \\ \alpha_m \end{bmatrix} \tag{XI.24}$$

The matrix A_{mod} is thus defined and is given by:

$$A_{mod} = \frac{\partial \underline{G}}{\partial \underline{p}} \cdot \left[\Delta \underline{p}_1 \quad \cdots \quad \Delta \underline{p}_j \quad \cdots \quad \Delta \underline{p}_m \right] \cdot \underline{V} \tag{XI.25}$$

With this knowledge, one can solve the equation XI.17. During the subiterations the modes are subsequently calculated and added to the model. Only a few subiterations are needed for convergence (3 to 4 orders of magnitude). In practice minimally one mode needs to be prescribed to get started. The other modes are then the result from the calculated displacements with the structural model. In other words, the structural model generates the additional modes itself. These new modes fasten the convergence of the algorithm. Experience learned that better convergence can be obtained if two or more modes are prescribed. This is also reflected in figure XI.2 where the FSI loop starts with the computation of the pressure responses on prescribed modes v_1 and v_2. Figure XI.3 shows as an example the shape of the two prescribed modes. These quadratic functions of the form $A \cdot (s/l)^2 + B \cdot (s/l) = 0$, with $0 < s < l$ the distance along the leaflet, are based on the structural analysis theory of an elastic beam. For v_1 we used $A = 2$ and $B = -2$ and for v_2 the parameters are chosen $A = -2.5$ and $B = 2$. The final result is independent of the prescribed modes, although the chosen shape can influence the convergence speed of the procedure.

XI.2.3. Geometry, meshes and boundary conditions

The two-dimensional geometry used for the actual simulation (figure XI.4(a)) consists of an inflow tract (inlet = left ventricular outflow tract), a sinus of Valsalve

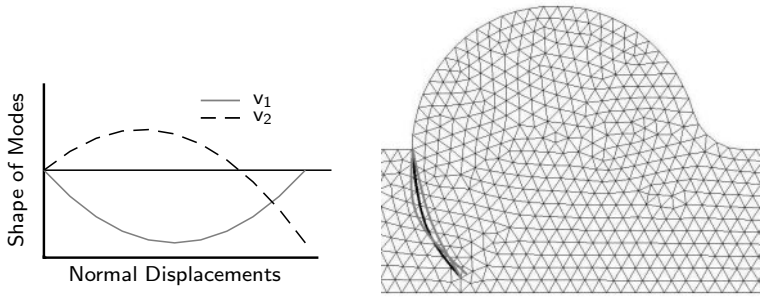

(a) Shape of prescribed modes.

(b) Example of imposed prescribed modes.

Figure XI.3.: Prescribed modes.

(aortic valve) and an outflow tract (outlet = aorta). The dimensions of the geometry are l_1 =4cm, l_2=6cm, r_1=2cm, r_2=0.75cm and h=2cm.
A physiological aortic inflow pattern (Q_{ao}) (figure XI.4(b)) is imposed as boundary condition. An example of the computational mesh is shown in figure XI.4(c). Because of the limitations in the dynamic mesh model, there is at least one cell required to cover the gap between the valve leaflet and the wall. This one cell needs to ensure that the fluid domain is preserved as one entity.

XI.2.3.1. Stability of the algorithm

Firstly a grid convergence study was performed. Two different grid densities, i.e. ±2100 cells with the leaflet divided in N=10 segments and ±4650 cells with the leaflet divided in N=15 segments, were studied with Δt=0.001s. Secondly it is verified whether solutions were timestep independent with variations in the timestep from Δt=0.001s to Δt=0.0005s for the coarse mesh. Two subsequent cycles were calculated in order to have results independent of the initial zero flow in the entire fluid domain fluid. The stiffness EI_{normal} of the aortic valve leaflet used in this model is $2.7 \cdot 10^{-5}\ N \cdot m^2$. The modulus of Young E for normal aortic valve leaflets found in literature is between $1 \cdot 10^6\ N/m^2$ and $2 \cdot 10^6\ N/s^2$.[29,30,31,32] We chose E equal to $1.5 \cdot 10^6\ N/m^2$. The thickness of the leaflet varies between 0.2 and $1.4\ mm$,[29,33] but as most researchers, we use about $0.6\ mm$ as the leaflet thickness for aortic valve.[31,32,34] With the moment of inertia $I = \frac{b \cdot h^3}{12}$, h = thickness of the leaflet and b = $1m$ the reference width of the 2D model, the above mentioned value of $2.7 \cdot 10^{-5}\ N \cdot m^2$ is obtained. As proposed by David at al.[212] the stiffness of

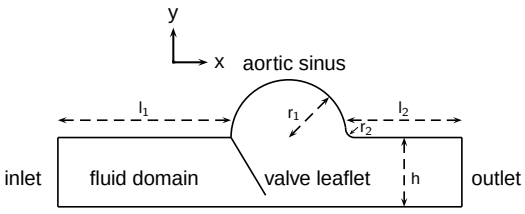

(a) Geometry of the 2D aortic valve.

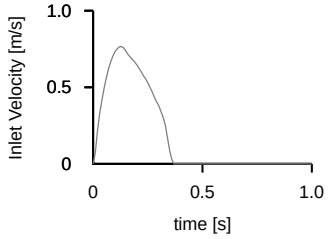

(b) Aortic flow boundary condition.

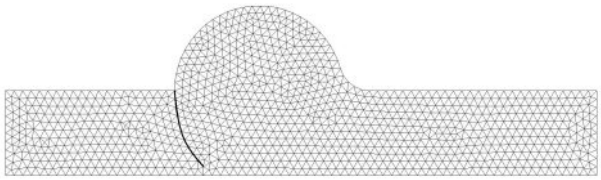

(c) Example of a mesh.

Figure XI.4.: 2D flexible aortic valve model.

the hinge $k_{s,hinge}$ is somewhat lower than the leaflet stiffness. For both meshes the same value for $k_{s,hinge}$ = $0.0075N \cdot m/rad$ is used.

XI.2.3.2. Application: shear stress on flexible valve leaflets

One of the potential applications of the FSI model is the estimation of shear stress (SS) forces exerted by the the fluid flow on the endothelial cell surface of a tissue engineered heart valve. We calculate the spatial average SS on the ventricular and aortic side of the leaflet over time. First of all, the influence of a low flow rate with Q_{low}=$\frac{Q_{ao}}{10}$ on the SS was investigated for the same leaflet stiffness properties as used in the stability analysis. Furthermore, the SS was estimated on a stiffer leaflet with EI_{high} four times higher, thus EI_{high} = $1.08 \cdot 10^{-4}$ $N \cdot m^2$ and $k_{s,hinge,high}$ = $0.03N \cdot m/rad$.

XI.3. Results

XI.3.1. Flow fields and leaflet motion

Figure XI.5 demonstrates the behavior of the flexible valve leaflet during the opening phase of the aortic valve. The fluid flow is accelerating and initially pushes the leaflet towards the outlet. Due to the flexible properties, the leaflet shows a bump

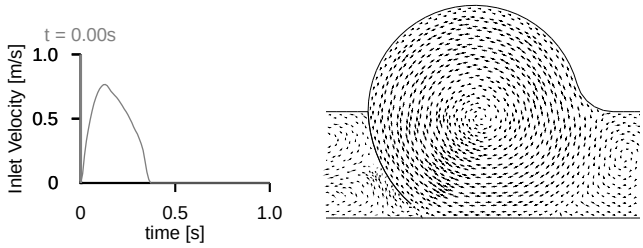

(a) t=0.00s.

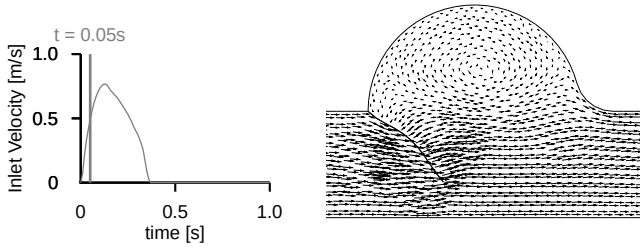

(b) t=0.05s.

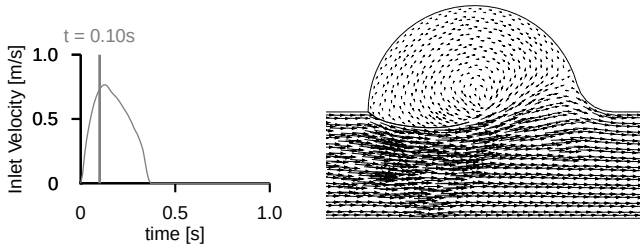

(c) t=0.10s.

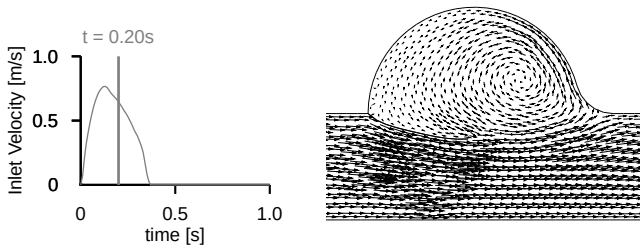

(d) t=0.20s.

Figure XI.5.: Aortic flow vector plots during the opening phase of the valve motion.

(figure XI.5(b) because of the forward flow at t=0.05s. At t=0.10s the leaflet is almost moving into the sinus cavity. In figure XI.5(d) at t=0.20s, the leaflet is guided by the flow and the vortex in the sinus cavity is responsible for the curving of the leaflet.

Figure XI.6 demonstrates the flexible behavior of the valve leaflet during the clos-

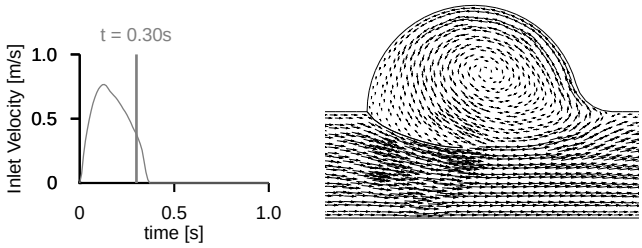

(a) t=0.30s.

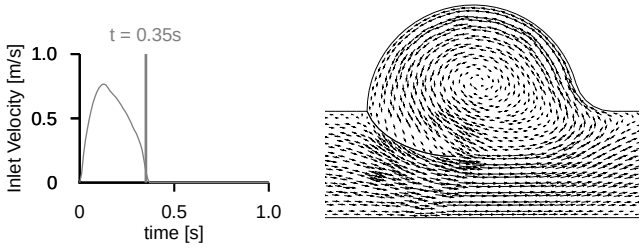

(b) t=0.35s.

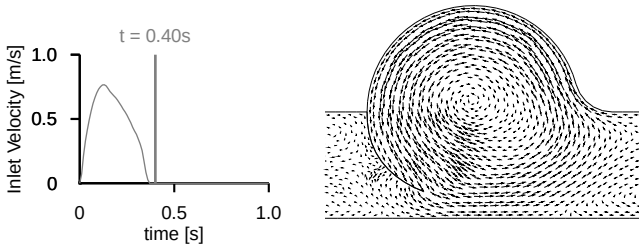

(c) t=0.40s.

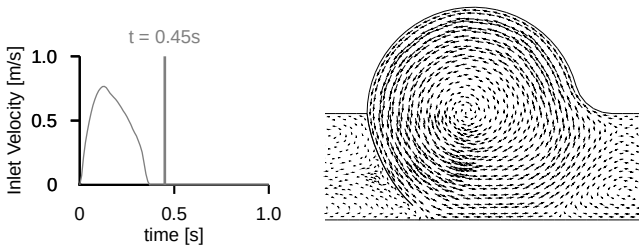

(d) t=0.45s.

Figure XI.6.: Aortic flow vector plots during the closing phase of the valve motion.

ing phase of the aortic valve, where the flow is decelerating. The vortex in the aortic sinus is enlarging, forcing the leaflet to move downwards (figures XI.6(b) and XI.6(c)). In figure XI.6(d) the large vortex in the sinus is guiding and curving the flexible valve leaflet.

XI.3.2. Grid dependence study

The FSI problem was solved on two different grids: a dense grid with approximately 4650 cells and N=15 segments for the valve leaflet and a coarse grid with approximately 2100 cells and N=10 segments for the valve leaflet. Figures XI.7 show results which are virtually grid independent. The biggest difference exists at t=0.09s (figure XI.7(a)). Figure XI.7(a) shows an "overshoot" of the valve leaflet almost into the aortic sinus. Eventually the leaflet is moving downwards to a more stable position. During closure of the valve small differences are shown in figure XI.7(b). It is important to mention that the $k_{s,hinge}$ needs to be the same value for both the values of N, with N representing the number of segments of the valve leaflet. The stiffness $\frac{EI}{\Delta l} = \frac{EI}{l/N}$ of the other springs is dependent on N.

XI.3.3. Timestep dependence study

Figure XI.8 shows the results obtained with the two timesteps used: Δt=0.001s (dashed lines) and Δt=0.0005s (dotted line). They are qualitatively and quantitatively the same. The small difference in "overshoot" of the valve leaflet at t=0.09s is not influencing the closure of the valve, as shown in figure XI.8(b).

XI.3.4. Application: shear stress on flexible valve leaflets

Figure XI.9 shows the average SS on the ventricular and aortic leaflet side during the complete cardiac cycle. Figure XI.9(a) shows lower SS at the aortic side of the valve leaflet compared to the ventricular side (figure XI.9(b)). The higher stiffness (EI_{high}=$4 \cdot EI_{normal}$), results in higher SS values, especially at the ventricular side of the valve leaflet. A lower flow rate (Q_{low}=$\frac{Q_{ao}}{10}$) results in a similar decrease in SS.

XI.4. Discussion and Conclusion

A novel fluid-structure interaction algorithm has been developed to study the interaction between the flow and highly flexible structures such as heart valves. The available Fluent software was extended with dedicated User Defined Functions (UDFs) and coupled with a customized structural solver with an iterative algorithm. The

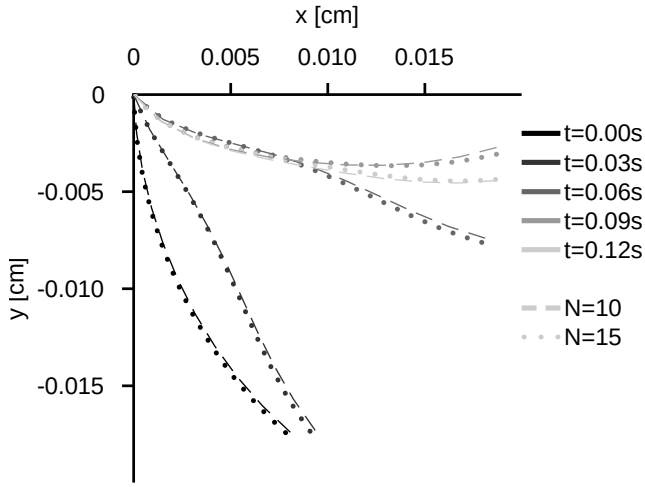

(a) Grid dependence study during the opening phase of the valve motion.

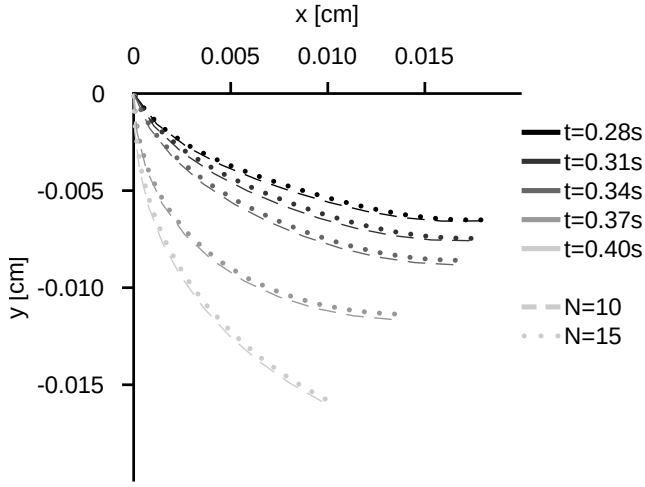

(b) Grid dependence study during the closing phase of the valve motion.

Figure XI.7.: Grid dependence study.

structural solver is based on a model previously studied by Horsten et al.[167] and by David et al.[212] Several studies demonstrated the behavior of a flexible heart valve[29,167,202,212] in settings similar to the one we used. The leaflet moves towards the aortic sinus, and tends to move into this sinus.[29] After this “overshoot” of the valve leaflet, the leaflet starts moving downwards. The vortex is present during the complete cardiac cycle. This vortex helps and guides the closure and movement of the aortic valve leaflet during the closure of the valve.[202]

A grid and timestep dependence study was performed, in order to demonstrate the

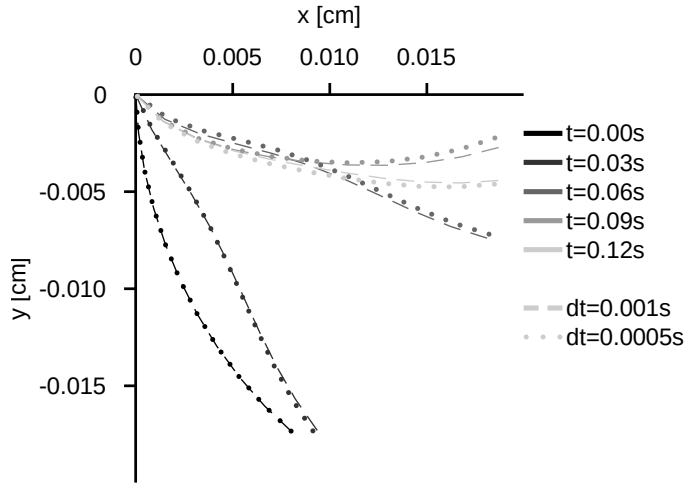

(a) Timestep dependence study during the opening phase of the valve motion.

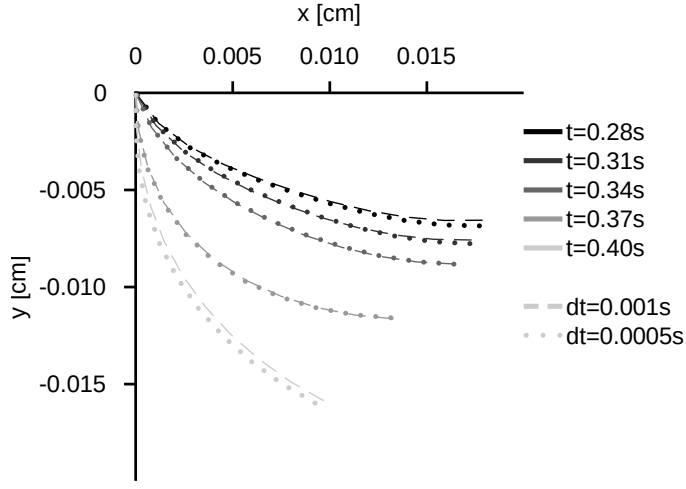

(b) Timestep dependence study during the closing phase of the valve motion.

Figure XI.8.: Timestep dependence study.

robustness of the newly developed FSI code. Figure XI.7 shows that grid independence is achieved. The same study was performed to assess timestep independence. In both cases small differences are shown in figures XI.8 and XI.7 concerning the valve leaflet “overshoot”, but this difference does not influence the valve closure of the flexible leaflet as shown in figure XI.8(b). Thus figures XI.7 and XI.8 give qualitative and quantitative good results, and it proves the robustness of the new FSI algorithm.

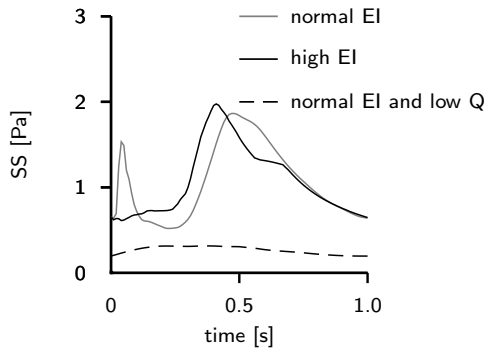

(a) SS in Pa on the aortic sinus valve side.

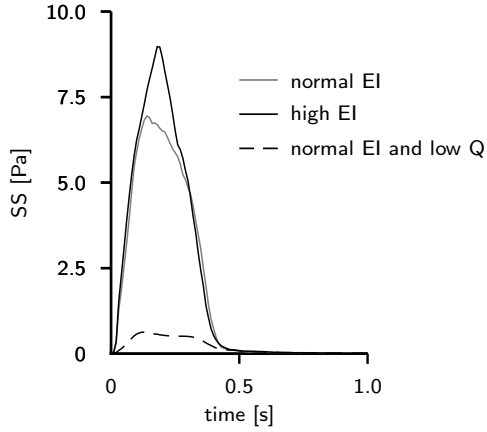

(b) SS in Pa on the left ventricular side.

Figure XI.9.: Shear stress SS in Pa on the 2D valve leaflet.

The final goal of the flexible leaflet study is to use the model in the development of guidelines for bioreactor and tissue engineering studies of aortic heart valve leaflets. An important haemodynamic parameter influencing the endothelial cell layer is the shear stress (SS). Cells seeded on TE constructs are matured and conditioned in a bioreactor. Although flow and pressure can be regulated in a bioreactor, the magnitude of SS on the cells is unknown. Maturing them in a bioreactor requires a gradual increase of shear stress.[96,97,110] Little is known about how a protocol for these TE constructs needs to look like, and there is a need for standardization.[96,110] This FSI-CFD algorithm should allow to assess SS exerted on the valve inside the bioreactor and could thus help to develop a protocol with gradually increasing shear stress. In this way, the endothelial cells would be able to adapt to the flow and gradually orientate in the direction of the flow.[118]

A stable FSI code was obtained, through our experience with the 2D and 3D modeling of mechanical heart valves.[140,142,213] Although the modeling of mechanical heart valves requires the FSI algorithm to solve only for one variable θ, the angle of the *stiff* leaflet, a similar iterative approach was necessary. This approach was extended for the simulation of flexible heart valve leaflets. Because there are more degrees of freedom the problem is more difficult to solve in a stable way. Therefore a matrix A_{mod} is included in the structural model. Our newly developed FSI code has the advantage that current available and widely used CFD codes could be coupled to arbitrary structural code.[147,149]

Our goal was to study the feasibility of the iterative coupling of Fluent with a structural solver. The used method implies that commercial structural solver need to be highly open source when used for iterative coupling with CFD packages. This open source allows the user to add the variations of the pressure forces in function of the found displacements. In this way a fully implicit iteration scheme can be obtained. The method is demonstrated on the opening and closing of the aortic valve during the complete cardiac cycle in 2D and has potential for shear stress estimation on tissue engineered leaflet constructs.

XI.5. Model limitations and future developments

This study has some inherent limitations. Firstly, the study is restricted to two dimensions and a simple structural model for the leaflets is used. This will have to be extended to three dimensions with incorporation of the layered structure of native heart valves. Secondly, although a stability study was performed, the code should be validated further, comparing calculated flow fields and valve movement with measured data in an *in vitro* setup.

XI.6. Aknowledgements

Dr. M. Nakamura is thanked for his effort to check the presented model and equations.

Conclusion

Surgical replacement of diseased human heart valves by mechanical and tissue valve substitutes is now commonplace. Still, new valves are designed to improve the biocompatibility and haemodynamics, optimizing the transvalvular flow with special attention to prevent stagnation and excess (shear) forces on the valve. Different techniques can be used to assess the haemodynamic performance of these heart valves. In this dissertation both *in vitro* testing and numerical simulation have been described.

Two different types of mechanical heart valves (On-X bileaflet valve and Omnicarbon monoleaflet valve) were tested in a Pulse Duplicator Mock loop. More important than the assessment of the performance of these specific valves, these experiments allowed us to get insight in the requirements associated with haemodynamic valve testing, and to get an overview of parameters which are currently in use to quantify valve functioning. In addition, the knowhow gathered with the mock loop enabled us to design mechanical parts of the bioreactor and to create a system allowing the generation of versatile and diverse haemodynamic conditions, necessary for the conditioning of tissue engineered heart valves.

From CFD perspective, the challenging task was not only to calculate the flow through the valve, but especially to model the dynamic interaction of the aortic valve with the surrounding blood, and finally to calculate the local deformations and stresses in the structure. In this thesis, we have presented a model based on the available commercial fluid solver Fluent (Fluent Inc.), which makes use of an ALE (arbitrary Lagrange-Euler) approach. The software allows for the simulation of flows where the shape of the structure is changing with time. Although, this software is capable of solving a wide range of engineering and biomedical problems, it is not accounting for the interaction between the fluid and the structure. For that reason, we developed an iterative methodology based on the available Fluent software. To reduce complexity of the iterative model in the initial phase, the flexible properties of the leaflet were neglected and an aortic valve with stiff leaflet was studied. The stability and accuracy of the new model was investigated with a 2D model of the aortic valve.

The potential of this model as a research and development tool for mechanical heart valves has been demonstrated in this dissertation. For instance, the above mentioned *in vitro* techniques imply that prototypes of the valves are already available at the time of testing. In the course of the development process, however, valves are computer designed, and virtual valve prototypes are available in an early stage of the design process. We have shown that our numerical model is capable of testing the haemodynamic performance of these virtual prototypes, as we simulated a commercially available 3D bileaflet mechanical heart valve (ATS valve). Although the size of the leaflet and the maximum opening angle had to be reduced due to the mentioned remeshing and/or CPU-time limitations, the model was able to reproduce reported *in vitro* and clinical results. It is clear that the model can be used to predict shortcomings of available and new mechanical heart valves. Future work may include the numerical comparison of currently available mechanical heart valves in different geometries and for different inflow conditions and, obviously, virtual prototype testing in the early stage of new mechanical heart valve design.

Current available heart valves are non-viable valves and all have disadvantages in one way or another. Most of the shortcomings of current valves could be solved by tissue engineering, where it is theoretically possible to grow a valve with patient-specific biological material, consisting of viable tissue. Until now, most research efforts failed in the final stage of implantation of the valve in aortic position, which seems to indicate that preconditioning of the valve should be optimized to train the valve in withstanding the high forces *in vivo*. The developed bioreactor is capable of providing a physiological environment for growing and testing these tissue engineered heart valve constructs with a high degree of flexibility in creating pulsatile flow conditions, though further attention should be paid improving the biocompatibility of the design.

There is overwhelming evidence that the function and integrity of cells exposed to flow is highly dependent on the nature of the flow regime, which determines the magnitude and direction of the shear forces exerted on the cells. Therefore, in order to set up a protocol for cultivating, maturing and growing a tissue engineered cardiovascular device, it is important to assess and to control the shear forces exerted on the fragile freshly seeded cells. These shear stresses can be easily calculated in

simple flow geometries, as in cell culture devices, but not in the more complex *in vivo* environment or inside a bioreactor. This is where numerical (CFD) techniques can help.

To tackle this type of problem, the stiff leaflet model needed to be extended to a flexible leaflet model, as one of the goals was to predict the shear stresses on a tissue engineered valve construct, cultivated in a bioreactor. Adding the flexibility of the valve leaflet resulted in an innovative complex iteration procedure, embedded, however, within available software code, demonstrating that fluid-structure interaction of the flexible heart valve is feasible in this setting. The robustness (grid and time step independence) of the model has been demonstrated, but further validation with comparison to *in vitro* experiments is mandatory. The model will allow to estimate shear stress not only for different flow rates, but also for different stiffness properties of the flexible leaflet model. At this stage, a relatively simple material model is used, which does not account for the layered structure of the natural heart valves. A first extension could be the implementation of a layered material model and a detailed parameter study of the internal stresses and the shear stresses. Furthermore, only a 2D model is developed in this dissertation, but the extension to 3D is, though more complex (due to more complex 3D deformation modes), straightforward.

Bibliography

[1] Price, S. and Wilson, L. (1992) *Pathophysiology, clinical concepts of disease processes (4th ed.).*, Mosby-Year Book inc, Philadelphia.

[2] Darovic, G. (1995) *Hemodynamic monitoring: Invasive and noninvasive clinical application.*, 2nd ed. Philadelphia: W.B. Saunders Company.

[3] Vandenberghe, S. (2004) *Modeling the Interaction between Cardiac Assist Devices and the Left Ventricle*, Phd thesis, Ghent University.

[4] Yellin, E. (1995) *The momentum of mass, the momentum of ideas, and diastolic function.*, Amsterdam: IOS Press.

[5] Matthys, K. (2004) *Assessment of Vascular Hemodynamics: Investigation of non-invasive and minimally invasive methods for assessment of vascular function at rest and during cardiovascular challenge*, Phd thesis, Ghent University.

[6] Bender, J. (1992) *YALE UNIVERSITY School of Medicine HEART BOOK*, chapter Heart Valve Disease, William Morrow and Company, Inc., ISBN 0-688-09719-7.

[7] De Hart, J. (2002) *Fluid-Structure Interaction in the Aortic Heart Valve: a three-dimensional computational analysis*, Phd thesis, Technische Universiteit Eindhoven.

[8] Thubrikar, M., Bosher, L. and Nolan, S. (1979) "Mechanism of opening of the aortic-valve.", *Journal of thoracic and cardiovascular surgery* **77**(6), 863–870.

[9] Vesely, I. (2000) "Aortic root dilation prior to valve opening explained by passive hemodynamics.", *Journal of Heart Valve Disease* **9**(1), 16–20.

[10] Cooper, T., Napolitano, L., Fitzgerald, M., Moore, K., Daggett, W., Willman, V., Sonnenblick, E. and Hanlon, C. (1966) "Structural basis of cardiac valvar function", *Arch Surg* **93**, 767–771.

[11] Yacoub, M., Kilner, P., Birks, E. and Misfeld, M. (1999) "The aortic outflow and root: a tale of dynamism and crosstalk", *Annals of Thoracic Surgery* **68**(3), S37–S43.

[12] Fenoglio, J., Pham, T., Wit, A., Bassett, A. and Wagner, B. (1972) "Canine mitral complex: ultrastructure and electromechanical properties", *Circulation Research* **31**, 417–430.

[13] Hibbs, R. and Ellison, J. (1973) "The atrioventricular valves of the guinea-pig: Ii. an ultrastructural study.", *Am J Anat* **138**, 347–369.

[14] Filip, D., Radu, A. and Simionescu, M. (1986) "Interstitial cells of the heart valves possess characteristics similar to smooth muscle cells.", *Am J Anat* **59**(3), 310–320.

[15] Schneider, P. and Deck, J. (1981) "Tissue and cell renewal in the natural aortic valve of rats: an autoradiographic study.", *Cardiovascular Research* **15**(4), 181–189.

[16] Henney, A., Parker, D. and Davies, M. (1982) “Collagen biosynthesis in normal and abnormal human heart valves.”, *Cardiovascular Research* **16**(11), 624–630.

[17] Rabkin, E. and Schoen, F. (2002) “Cardiovascular tissue engineering”, *Cardiovascular Pathology* **11**(6), 305–317.

[18] Bachetti, T. and Morbidelli, L. (2000) “Endothelial cells in culture: A model for studying vascular functions.”, *Pharmacological Research* **42**(1), 9–19.

[19] Frater, R., Gong, G., Hoffman, D. and Liao, K. (1992) “Endothelial covering of biological artificial heart valves.”, *Annals of Thoracic Surgery* **53**(3), 371–372.

[20] Kunzelman, K., Cochran, R., Murphree, S., Ring, W., Verrier, E. and R.C., E. (1993) “Differential collagen distribution in the mitral valve and its influence on biomechanical behaviour.”, *Journal of Heart Valve Disease* **2**, 236–244.

[21] Vesely, I. (1998) “The role of elastin in aortic valve mechanics.”, *Journal of Biomechanics* **31**(2), 115–123.

[22] Flanagan, T. and Pandit, A. (2003) “Living artificial heart valve alternatives: a review.”, *European-cells-and-materials-[electronic-resource]* **6**, 28–45; discussion 45.

[23] Gross, L. and Kugel, M. (1931) “Topographic anatomy and histology of the valves in the human heart.”, *American Journal of Pathology* **7**, 445–456.

[24] Hoffman-Kim, D. (2002) “Tissue engineering: Heart valves.”, *Science & Medicine* **8**(2), 62–64.

[25] Culav, E., Clark, C. and Merrilees, M. (1999) “Connective tissues: matrix composition and its relevance to physical therapy.”, *Physical Therapy* **79**(3), 308–319.

[26] Scott, M. and Vesely, I. (1995) “Aortic-valve cusp microstructure - the role of elastin”, *Annals of Thoracic Surgery* **60**(2), S391–S394.

[27] Lee, T., Midura, R., Hascall, V. and Vesely, I. (2001) “The effect of elastin damage on the mechanics of the aortic valve”, *Journal of Biomechanics* **34**(2), 203–210.

[28] Adamczyk, M., Lee, T. and Vesely, I. (2000) “Biaxial strain properties of elastase-digested porcine aortic valves”, *Journal of Heart Valve Disease* **9**(3), 445–453.

[29] De Hart, J., Peters, G. W. M., Schreurs, P. J. G. and Baaijens, F. P. T. (2000) “A two-dimensional fluid-structure interaction model of the aortic value”, *Journal of Biomechanics* **33**(9), 1079–1088.

[30] De Hart, J., Peters, G. W. M., Schreurs, P. J. G. and Baaijens, F. P. T. (2003) “A three-dimensional computational analysis of fluid-structure interaction in the aortic valve”, *Journal of Biomechanics* **36**(1), 103–112.

[31] Sripathi, V., Kumar, R. and Balakrishnan, K. (2004) “Further insights into normal aortic valve function: Role of a compliant aortic root on leaflet opening and valve orifice area .”, *Annals of Thoracic Surgery* **77**(3), 844–851.

[32] Stradinsa, P., Lacisa, R., Ozolantab, I., Purinab, B., Oseb, V., Feldmanea, L. and Kasyanovb, V. (2004) “Comparison of biomechanical and structural properties between human aortic and pulmonary valve.”, *European Journal of Cardio-thoracic Surgery* **0**(0), 0–0.

[33] Li, J., Luo, X. and Kuang, Z. (2001) “A nonlinear anisotropic model for porcine aortic heart valves.”, *Journal of Biomechanics* **34**(10), 1279–1289.

[34] Yoganathan, A., Lemmon, J. and Ellis, J. (2000) *The Biomedical Engineering Handbook, Second Edition.*, chapter Heart Valve Dynamics., CRC Press LLC, ISBN 0-849-38594-6.

[35] Pries, A., Neuhaus, D. and Gaehtgens, P. (1992) "Blood-viscosity in tube flow - dependence on diameter and hematocrit.", *American Journal of Physiology* **263**(6), H1770–H1778.

[36] Fahraeus, R. and Lindqvist, T. (1931) "The viscosity of blood in narrow capillary tubes.", *American Journal of Physiology* **96**, 562–568.

[37] Gijsen, F. (1998) *Modeling of Wall Shear Stress in Large Arteries.*, Phd thesis, Eindhoven University of Technology.

[38] Chien, S., Usami, S., Dellenback, R. and Gregersen, M. (1970) "Shear-dependent deformation of erythrocytes in rheology of human blood.", *American Journal of Physiology* **219**, 85–107.

[39] Caro, C., Pedley, T. and Schroter, R. (1978) *The Mechanics of Circulation*, Oxford University Press.

[40] Hofer, M., Rappitsch, G., Perktold, K., Trubel, W. and Schima, H. (1996) "Numerical study of wall mechanics and fluid dynamics in end-to-side anastomoses and correlation to intimal hyperplasia.", *Journal of Biomechanics* **29**(10), 1297–1308.

[41] King, M., Corden, J., David, T. and Fisher, J. (1996) "A three-dimensional, time-dependent analysis of flow through a bileaflet mechanical heart valve: comparison of experimental and numerical results.", *Journal of Biomechanics* **29**(5), 609–618.

[42] Rappitsch, G., Perktold, K. and Pernkopf, E. (1997) "Numerical modelling of shear-dependent mass transfer in large arteries.", *International Journal for Numerical Methods in Fluids* **25**(7), 847–857.

[43] Leuprecht, A., Perktold, K., Prosi, M., Berk, T., Trubel, W. and Schima, H. (2002) "Numerical study of hemodynamics and wall mechanics in distal end-to-side anastomoses of bypass grafts.", *Journal of Biomechanics* **35**(2), 225–236.

[44] Bluestein, D., Li, Y. and Krukenkamp, I. (2002) "Free emboli formation in the wake of bi-leaflet mechanical heart valves and the effects of implantation techniques", *Journal of Biomechanics* **35**(12), 1533–1540.

[45] Gijsen, F., van de Vosse, F. and Janssen, J. (1998) "Wall shear stress in backward-facing step flow of a red blood cell suspension", *Biorheology* **35**(4-5), 263–279.

[46] Cross, M. (1958) "Rheology of non-newtonian fluids: a new flow equation for pseudo-plastic systems.", *J. Colloid.* **20**, 417–437.

[47] Carreau, P. (1972) "Rheological equations from molecular network theories.", *Trans. Soc. Rheol.* **16**(1), 99–127.

[48] Yasuda, R. and Cohen, R. (1981) "Shear-flow properties of concentrated-solutions of linear and star branched polystyrenes.", *Rheol. Acta* **20**, 163–178.

[49] Gijsen, F., van de Vosse, F. and Janssen, J. (1999) "The influence of the non-newtonian properties of blood on the flow in large arteries: unsteady flow in a 90°curved tube", *Journal of Biomechanics* **32**(7), 705–713.

[50] Gijsen, F., van de Vosse, F. and Janssen, J. (1999) "The influence of the non-newtonian properties of blood on the flow in large arteries: steady flow in a carotid bifurcation model", *Journal of Biomechanics* **32**(6), 601–608.

[51] Choi, C., Kim, C. and Choi, M. (2001) “Characteristics of transient blood flow in mhvs with different maximum opening angles using fluid-structure interaction method.”, *Korean Journal of Chemical Engineering* **18**(6), 809–815.

[52] Cho, Y. and Kensey, K. (1991) “Effects of the non-newtonian viscosity of blood on flows in a diseased arterial vessel. part 1: steady flows.”, *Biorheology* **28**(3-4), 241–262.

[53] Johnston, B., Johnston, P., Corney, S. and Kilpatrick, D. (2004) “Non-newtonian blood flow in human right coronary arteries: steady state simulations.”, *Journal of Biomechanics* **37**(5), 709–720.

[54] “Heart disease and stroke statistics, 2003 update”, Technical report, American Heart Association, Dallas, Texas, US.

[55] Yoganathan, A. P. (2000) *The Biomedical Engineering Handbook, Volume I: Second Edition.*, chapter Cardiac Valve Prostheses., CRC Press LLC, ISBN 0-849-38594-6.

[56] Vongpatanasin, W., LD, L. H. and Lange, R. (1996) “Medical progress - prosthetic heart valves.”, *New England Journal of Medicine* **335**(6), 407–416.

[57] Bonow, R., Carabello, B., de Leon, A., Edmunds, L., Fedderly, B., Freed, M., Gaasch, W., McKay, C., Nishimura, R., O’Gara, P., O’Rourke, R. and Rahimtoola, S. (1998) “ACC/AHA guidelines for the management of patients with valvular heart disease”, *JACC* **32**(5), 1486–1588.

[58] Gardin, J., Davidson, D., Rohan, M., Butman, S., Knoll, M., Garcia, R., Dubria, S., Gardin, S. and Henry, W. (1987) “Relationship between age, body size, gender, and blood-pressure and doppler flow measurements in the aorta and pulmonary artery”, *American Heart Journal* **113**(1), 101–109.

[59] Takenaka, K., Dabestani, A., Waffarn, F., Gardin, J. and Henry, W. (1987) “Effect of left ventricular size on early diastolic left-ventricular filling in neonates and in adults.”, *American Journal of Cardiology* **59**(1), 138–141.

[60] Lange, R. and Hillis, L. (2003) “CARDIOLOGY PATIENT PAGE diagnostic cardiac catheterization”, *Circulation* **107**(17), e111–113.

[61] Turi, Z. (2004) “CARDIOLOGY PATIENT PAGE mitral valve disease”, *Circulation* **109**(6), e38–41.

[62] Kisslo, J. and Adams, D. (Accessed 15 july 2004), “Doppler evaluation of valvular regurgitation”, http://www.echoincontext.com/index.asp, Duke University Medical Center.

[63] Kisslo, J. and Adams, D. (Accessed 15 july 2004), “Doppler evaluation of valvular stenosis”, http://www.echoincontext.com/index.asp, Duke University Medical Center.

[64] Nishimura, R. (2002) “CARDIOLOGY PATIENT PAGE aortic valve disease”, *Circulation* **106**(7), 770–772.

[65] Hufnagel, C., Valkgas, P. and Nahas, H. (1958) “Experiences with new types of aortic valvular prostheses.”, *Ann. Surg.* **147**, 636–645.

[66] Starr, A. (1960) “Total mitral valve replacement: fixation and trombosis.”, *Surg. Forum* **11**, 258–60.

[67] Starr, A. and Edwards, M. (1961) “Mitral replacement: the shielded ball valve prosthesis.”, *J. Thorac. Cardiovasc. Srug.* **42**, 673–682.

[68] Bettadapur, M., Griffin, B. and Asher, C. (2002) "Caring for patients with prosthetic heart valves.", *Cleveland Clinic Journal of Medicine* **69**(1), 75–87.

[69] Fraund, S., Pethig, K., Wahlers, T., Harringer, W., Wiebe, K., Struber, M., Karck, M., Mehler, D. and Haverich, A. (1998) "On-X bileaflet valve in aortic position–early experience shows an improved hemodynamic profile", *Thorac Cardiovasc Surg* **46**(5), 293–7.

[70] Hwang, N. H., Reul, H. and Reinhard, P. (1998) "In vitro evaluation of the long-body On-X bileaflet heart valve", *J Heart Valve Dis* **7**(5), 561–8.

[71] Hwang, N. H. (1998) "Mitral regurgitation of the On-X size 23 valve is comparable to or less than the size 27 sjm, which has the same geometric orifice area", *Asaio J* **44**(3), 238.

[72] ATS Medical Inc., Pre-Market Approval Application - Summary of Safety and Effectiveness: 200. Washington D.C., U.S. Food and Drug Administration. 2000. P990046.

[73] Feng, Z., Nakamura, T., Fujimoto, T. and Umezu, M. (2002) "In vitro investigation of opening behavior and hydrodynamics of bileaflet valves in the mitral position", *Artificial Organs* **26**(1), 32–39.

[74] Westaby, S. (1995) *Stenltess Bioprostheses*, chapter Pulmonary autograft (Ross) operation., 130–138, edited by A. Piwnica and S. Westaby, Isis Medical Media Ltd.

[75] Bloomfield, P. (2002) "Valve disease: Choice of heart valve prosthesis", *Heart* **87**(6), 583–589.

[76] Silberman, S., Shaheen, J., Merin, O., Fink, D., Shapira, N., Liviatan-Strauss, N. and Bitran, D. (2001) "Exercise hemodynamics of aortic prostheses: Comparison between stentless bioprostheses and mechanical valves.", *Annals of Thoracic Surgery* **72**(4), 1217–1221.

[77] Westaby, S., Horton, M., Jin, X., Katsumata, T., Ahmed, O., Saito, S., Li, H. and Grunkemeier, G. (2000) "Survival advantage of stentless aortic bioprostheses.", *European Journal of Cardio-Thoracic Surgery* **70**(3), 785791.

[78] Jin, X. and Pepper, J. (2002) "Do stentless valves make a difference?", *European Journal of Cardio-Thoracic Surgery* **22**(1), 95100.

[79] Angell, W., Pupello, D., Bessone, L., Hiro, S. and Brock, J. (1991) "Effect of stent mounting on tissue valves for aortic replacement.", *J Cardiac Surg* **6**(Suppl 4), 595599.

[80] Broom, N. (1978) "Fatigue induced damage in glutaraldehyde preserved heart valve tissues.", *J Thorac Cardiovasc Surg* **76**(2), 202–211.

[81] De Hart, J., Baaijens, F. P. T., Peters, G. W. M. and Schreurs, P. J. G. (2003) "A computational fluid-structure interaction analysis of a fiber-reinforced stentless aortic valve", *Journal of Biomechanics* **36**(5), 699–712.

[82] Mirsch, W. (1995) *Stenltess Bioprostheses*, chapter Toronto SPV^{TM} valve: the engineer's standpoint., 43–47, edited by A. Piwnica and S. Westaby, Isis Medical Media Ltd.

[83] Nugent, H. and Edelman, E. (2003) "Tissue engineering therapy for cardiovascular disease", *Circulation Research* **92**(10), 1068–1078.

[84] Vacanti, J. P. and Langer, R. (1999) "Tissue engineering: the design and fabrication of living replacement devices for surgical reconstruction and transplantation", *Lancet* **354**, SI32–SI34.

[85] Shinoka, T., Breuer, C. K., Tanel, R. E., Zund, G., Miura, T., Ma, P. X., Langer, R., Vacanti, J. P. and Mayer, J. E. (1995) "Tissue engineering heart valves: Valve leaflet replacement study in a lamb model", *Ann. Thorac. Surg.* **60**(6), S513–S516.

[86] Heath, C. (2000) "Cells for tissue engineering.", *Trends in Biotechnology* **18**(1), 17–19.

[87] Nerem, R. and Seliktar, D. (2001) "Vascular tissue engineering.", *Annual Review of Biomedical Engineering* **3**(1), 225–243.

[88] Chapekar, M. (2000) "Tissue engineering: Challenges and opportunities.", *Journal of Biomedical Materials Research* **53**(6), 617–620.

[89] Hoerstrup, S. P., Zund, G., Ye, Q., Schoeberlein, A., Schmid, A. C. and Turina, M. I. (1999) "Tissue engineering of a bioprosthetic heart valve: Stimulation of extracellular matrix assessed by hydroxyproline assay", *Asaio J.* **45**(5), 397–402.

[90] Sodian, R., Sperling, J. S., Martin, D. P., Stock, U., Mayer, J. E. and Vacanti, J. P. (1999) "Tissue engineering of a trileaflet heart valve - early in vitro experiences with a combined polymer", *Tissue Eng.* **5**(5), 489–493.

[91] Shum-Tim, D., Stock, U., Hrkach, J., Shinoka, T., Lien, J., Moses, M. A., Stamp, A., Taylor, G., Moran, A. M., Landis, W., Langer, R., Vacanti, J. P. and Mayer, J. E. (1999) "Tissue engineering of autologous aorta using a new biodegradable polymer", *Ann. Thorac. Surg.* **68**(6), 2298–2304.

[92] Bader, A., Schilling, T., Teebken, O. E., Brandes, G., Herden, T., Steinhoff, G. and Haverich, A. (1998) "Tissue engineering of heart valves - human endothelial cell seeding of detergent acellularized porcine valves", *Eur. J. Cardio-Thorac. Surg.* **14**(3), 279–284.

[93] Barron, V., Lyons, E., Stenson-Cox, C., McHugh, P. and Pandit, A. (2003) "Bioreactors for cardiovascular cell and tissue growth: A review.", *Annals of Biomedical Engineering* **31**(9), 1017–1030.

[94] Freed, L. and Vanjak-Novakovic, G. (2000) *Principles of Tissue Engineering*, chapter Tissue engineering bioreactors., 143–156, edited by J. P. Vacanti. San Diego, CA: Academic.

[95] Niklason, L. E., Gao, J., Abbott, W. M., Hirschi, K. K., Houser, S., Marini, R. and Langer, R. (1999) "Functional arteries grown in vitro", *Science* **284**(5413), 489–493.

[96] Dumont, K., Yperman, J., Verbeken, E., Segers, P., Meuris, B., Vandenberghe, S., Flameng, W. and Verdonck, P. (2002) "Design of a new pulsatile bioreactor for tissue engineered aortic heart valve formation.", *Artificial Organs* **26**(8), 710–714.

[97] Hoerstrup, S. P., Sodian, R., Sperling, J. S., Vacanti, J. P. and Mayer, J. E. (2000) "New pulsatile bioreactor for in vitro formation of tissue engineered heart valves", *Tissue Eng.* **6**(1), 75–79.

[98] Goldstein, S. and Black, K. S. (1999) "Pulsatile flow system for developing heart valves.", *United States Patent. Kennesaw, GA Cryolife* .

[99] Sikavitsas, V., Bancroft, G. and Mikos, A. G. (2002) "Formation of three-dimensional cell/polymer constructs for bone tissue engineering in a spinner flask and a rotating wall vessel bioreactor.", *J. Biomed. Mater. Res.* **62**(1), 136–148.

[100] Freed, L. and Vanjak-Novakovic, G. (2002) *Methods of Tissue Engineering*, chapter Culture environments: cell polymer bioreactor systems., 97–110, edited by R. P. Lanza. San Diego, CA: Academic.

[101] Carrier, R., Papadaki, M., Rupnick, M., Schoen, F. J., Bursac, N., Langer, R., Freed, L. E. and Vunjak-Novakovic, G. (1999) "Cardiac tissue engineering: cell seeding, cultivation parameters, and tissue construct characterization.", *Biotechnol. Bioeng.* **64**(5), 580589.

[102] Duray, P., Hatfill, S. J. and Pellis, N. R. (1997) "Tissue culture in microgravity.", *Sci. Med. (Phila)* **4**(3), 4655.

[103] Freed, L., Langer, R., Martin, I., Pellis, N. and Vunjak-Novakovic, G. (1997) "Tissue engineering of cartilage in space.", *Proc. Natl. Acad. Sci. U.S.A.* **94**(25), 1388513890.

[104] Freed, L., Pellis, N., Searby, N., de Luis, J., Preda, C., Bordonaro, J. and Vunjak-Novakovic, G. (1999) "Microgravity cultivation of cells and tissues.", *Gravit. Space Biol. Bull.* **12**(2), 57–66.

[105] Unsworth, B. and Lelkes, P. (1998) "Growing tissues in microgravity.", *Nat. Med.* **4**(8), 901907.

[106] Vunjak-Novakovic, G., Searby, N., De Luis, J. and Freed, L. (2002) "Microgravity studies of cells and tissues.", *Ann. N.Y. Acad. Sci.* **974**, 504517.

[107] Carrier, R., Rupnick, M., Langer, R., Schoen, F. J., Freed, L. E. and Vunjak-Novakovic, G. (2002) "Perfusion improves tissue architecture of engineered cardiac muscle.", *Tissue Engineering* **8**(2), 175188.

[108] Carrier, R., Rupnick, M., Langer, R., Schoen, F. J., Freed, L. E. and Vunjak-Novakovic, G. (2002) "Effects of oxygen on engineered cardiac muscle.", *Biotechnol. Bioeng.* **78**(6), 617625.

[109] Rabkin, E., Hoerstrup, S., Aikawa, M., Mayer, J. and Schoen, F. (2002) "Evolution of cell phenotype and extracellular matrix in tissue-engineered heart valves during in vitro maturation and in vivo remodeling.", *Journal of Heart Valve Disease* **11**(3), 308–314.

[110] Hoerstrup, S. P., Sodian, R., Daebritz, S., Wang, J., Bacha, E. A., Martin, D. P., Moran, A. M., Guleserian, K. J., Sperling, J. S., Kaushal, S., Vacanti, J. P., Schoen, F. J. and Mayer, J. E. (2000) "Functional living trileaflet heart valves grown in vitro", *Circulation* **102**(19), 44–49.

[111] Mann, B. K. and West., J. L. (2001) "Tissue engineering in the cardiovascular system: Progress toward a tissue engineered heart.", *Anatomical Record* **263**(4), 367–371.

[112] Sodian, R., Hoerstrup, S. P., Sperling, J. S., Daebritz, S. H., Martin, D. P., Schoen, F. J., Vacanti, J. P. and Mayer, J. E. (2000) "Tissue engineering of heart valves: In vitro experiences", *Ann. Thorac. Surg.* **70**(1), 140–144.

[113] Neuenschwander, S. and Hoerstrup, S. P. (2004) "Review: Heart valve tissue engineering", *Transplant Immunology* **12**(3-4), 359–365.

[114] Schmailz, K. and Ormerod, O., editors (1998) *Ultrasound in Cardiology*, Blackwell Science.

[115] Yoganathan, A. and Chatzimavroudis, G. (2002) *PanVascular Medicine: Integrated Clinical Management*, chapter Chapter 7: Hemodynamics., Springer.

[116] Welty, J., Wicks, C., Wilson, R. and Rorrer, G. (2000) *Fundamentals of Momentum, Heat, and Mass Transfer*, Wiley Text Books; 4 edition, ISBN 0471381497.

[117] Malek, A., Alper, S. and Izumo, S. (1999) "Hemodynamic shear stress and its role in atherosclerosis", *Journal of the American Medical Association (JAMA)* **282**(21), 2035–2042.

[118] Malek, A. and Izumo, S. (1996) “Mechanism of endothelial cell shape change and cytoskeletal remodeling in response to fluid shear stress”, *Journal of Cell Science* **109**, 713–726.

[119] Ruggeri, Z. (1993) “Mechanisms of shear-induced platelet adhesion and aggregation.”, *Thrombosis and Haemostasis* **70**(1), 119123.

[120] Kroll, M., Hellums, J., McIntire, L., Schafer, A. and Moake, J. (1996) “Platelets and shear stress.”, *Blood* **88**(5), 1525–1541.

[121] Yoganathan, A., Wick, T. and Reul, H. (1992) *Current Issues in Heart Valve Disease*, chapter Thrombosis, Embolism and Bleeding., 123–148, London: ICR.

[122] Hellums, J. and Hardwick, R. (1981) *The Rheology of Blood, Blood Vessels and Associated Tissues*, chapter Response of Platelets to Shear Stress - a Review, 160–183, Sijthoff & Noordhoff, Alphen aan den Rijn.

[123] Blackshear, P., Dorman, F. and Steinbach, E. (1966) “Shear, wall interaction and hemolysis”, *Transactions of the American Society of Artificial Internal Organs* **12**, 113–120.

[124] Nevaril, C., Lynch, E., Alfrey, C. and Hellums, J. (1968) “Erythrocyte damage and destruction induced by shearing stress”, *Journal of Laboratory and Clinical Medicine* **71**(5), 781–790.

[125] Ellis, J., TM, T. W. and Yoganathan, A. (1998) “Prosthesis-induced hemolysis: Mechanisms and quantification of shear stress”, *Journal of Heart Valve Disease* **7**(4), 376–386.

[126] Goubergrits, L. and Affeld, K. (2004) “Numerical estimation of blood damage in artificial organs”, *Artificial Organs* **28**(5), 449–507.

[127] Kelly, S., Verdonck, P., Vierendeels, J., Riemslagh, K., Dick, E. and Nooten, G. V. (1999) “A three-dimensional analysis of flow in the pivot regions of an ATS bileaflet valve”, *International Journal of Artificial Organs* **22**(11), 754–763.

[128] Tillmann, W., Reul, H., Herold, M., Bruss, K. and van Gilse, J. (1984) “In vitro wall shear measurements in aortic valve prostheses.”, *Journal of Biomechanics* **17**(4), 263–279.

[129] A.P. Yoganathan, Y. W. and Sung, H. (1986) “Turbulent shear stress measurements in aortic valve prostheses.”, *Journal of Biomechanics* **19**(6), 433–442.

[130] Verdonck, P., Kleven, A., Verhoeven, R., Angelsen, B. and Vandenbogaerde, J. (1992) “Computer-controlled in vitro model of the human left heart”, *Med. Biol. Eng. Comput.* **30**(6), 656–659.

[131] Fisher, J., Jack, G. and Wheatley, D. (1986) “Design of a function test apparatus for prosthetic heart valves. initial results in the mitral position”, *Clinical Physiology and Functional Imaging* **7**(1), 63–73.

[132] Westerhof, N., Elzinga, G. and Sipkema, P. (1971) “An artificial arterial system for pumping hearts”, *J. Appl. Physiol* **31**(5), 776–81.

[133] Verdonck, P., Van Nooten, G. and Van Belleghem, Y. (1997) “Pulse duplicator hydrodynamics of four different bileaflet valves in the mitral position”, *Cardiovasc Surg* **5**(6), 593–603.

[134] Verdonck, P., Dumont, K., Segers, P., Vandenberghe, S. and Van Nooten, G. (2002) “Mock loop testing of On-X prosthetic mitral valve with doppler echocardiography.”, *Artificial Organs* **26**(10), 872–878.

[135] Dumont, K., Segers, P., Vandenberghe, S., Van Nooten, G. and Verdonck, P. (2002) "Omnicarbon^{tm} 21 mm aortic valve prosthesis: In vitro hydrodynamic and echo-doppler study.", *International Journal of Artificial Organs* **25**(8), 783–790.

[136] Vandervoort, P. M., Greenberg, N. L., Pu, M., Powell, K. A., Cosgrove, D. M. and Thomas, J. D. (1995) "Pressure Recovery in Bileaflet Heart Valve Prostheses : Localized High Velocities and Gradients in Central and Side Orifices With Implications for Doppler-Catheter Gradient Relation in Aortic and Mitral Position", *Circulation* **92**(12), 3464–3472.

[137] Garcia, D., Dumesnil, J., Durand, L., Kadem, L. and P., P. (2003) "Discrepancies between catheter and doppler estimates of valve effective orifice area can be predicted from the pressure recovery phenomenon: Practical implications with regard to quantification of aortic stenosis severity", *Journal of the American College of Cardiology (JACC)* **41**(3), 435–442.

[138] Bech-Hanssen, O., K., C., I., W., P., A. and B., W. (2001) "Assessment of effective orifice area of prosthetic aortic valves with doppler echocardiography: An in vivo and in vitro study", *The Journal of Thoracic and Cardiovascular Surgery* **122**(2), 287–295.

[139] Wu, Z., Gao, B., Slonin, J. and Huang, N. (1996) "Bileaflet mechanical heart valves at low cardiac output.", *ASAIO Journal* **42**(5), 747–749.

[140] Vierendeels, J., Dumont, K. and Verdonck, P. (2003) "Stabilization of a fluid-structure coupling procedure for rigid body motion", *33rd AIAA Fluid Dynamics Conference and Exhibit* AIAA–2003–3720, 23–26 june 2003, Orlando, US.

[141] Cheng, R., Lai, Y. and Chandran, K. (2003) "Two-dimensional fluid-structure interaction simulation of bileaflet mechanical heart valve flow dynamics", *Journal of Heart Valve Disease* **12**(6), 772–780.

[142] Dumont, K., Stijnen, J., Vierendeels, J., van de Vosse, F. and Verdonck, P. (2004) "Validation of a fluid-structure interaction model of a heart valve using the dynamic mesh method in fluent", *Computer Methods in Biomechanics and Biomedical Engineering* **7**(3), 139–146.

[143] De Hart, J., Peters, G., Schreurs, P. and Peters, G. (2004) "Collagen fibers reduce stresses and stabilize motion of aortic valve leaflets during systole.", *Journal of Biomechanics* **37**(3), 303–311.

[144] Versteeg, H. and Malalasekera, W. (1995) *An introcution to Computational Fluid Dynamics: the Finite Volume Method.*, Longman Group Ltd.

[145] Peskin, C. S. and McQueen, D. M. (1980) "Modeling prosthetic heart-valves for numerical-analysis of blood-flow in the heart", *Journal of Computational Physics* **37**(1), 113–132.

[146] Blom, F. (1998) "A monolithical fluid-structure interaction algorithm applied to the piston problem", *Computer methods in applied mechanics and engineering* **167**(3-4), 369–391.

[147] Zhang, H. and Bathe, K. (2001) *Computational Fluid and Solid Mechanics*, chapter Direct and iterative computing of fluid flows fully coupled with structures., KJ Bathe, editor, Amsterdam: Elsevier.

[148] Piperno, S., Farhat, C. and Larrouturou, B. (1995) "Partitioned procedures for the transient solution of coupled aeroelastic problems: Model problem, theory and 2-dimensional application.", *Computer methods in applied mechanics and engineering* **124**(1-2), 79–112.

[149] Matthies, H. and Steindorf, J. (2001) *Computational Fluid and Solid Mechanics*, chapter How to make weak couplings strong., KJ Bathe, editor, Amsterdam: Elsevier.

[150] Baaijens, F. P. T. (2001) “A fictitious domain/mortar element method for fluid-structure interaction”, *International Journal For Numerical Methods in Fluids* **35**(7), 743–761.

[151] Bertrand, F., Tanguy, P. and Thibault, F. (1997) “A three-dimensional fictitious domain method for incompressible fluid flow problems”, *International Journal For Numerical Methods in Fluids* **25**(6), 719–736.

[152] van Loon, R., Anderson, P., van de Vosse, F. and Baaijens, F. (2004) “A fictitious domain method combined with adaptive meshing for enhanced modelling of blood-heart valve interaction.”, *Proceedings of the Congress of the European Society of Biomechanics* (ESB 2004, ’s-Hertogenbos, the Netherlands).

[153] Chu, H. (1980) “Arbitrary lagrangian-eulerian method for transient fluid-structure interactions.”, *Nuclear Technology* **51**(3), 363–377.

[154] Donea, J., Giuliani, S. and J.P., H. (1982) “An arbitrairy lagrangian-eulerian finite element method for transient dynamic fluid-structure interactions.”, *Compter Methods in Applied Mechanics and Engineering* **33**(1-3), 689–723.

[155] Lai, Y., Chandran, K. and Lemmon, J. (2002) “A numerical simulation of mechanical heart valve closure fluid dynamics”, *Journal of Biomechanics* **35**(7), 881–892.

[156] Kelly, S. G. D. (2002) “Computational fluid dynamics insights in the design of mechanical heart valves”, *Artificial Organs* **26**(7), 608–613.

[157] Lee, C. and Chandran, K. (1995) “Numerical simulation of instantaneous backflow through central clearance of bi-leaflet mechanical heart valve at closure: shear stresses and pressure fields”, *Medical and Biological Engineering and Computing* **33**(3), 257–263.

[158] Liang, G., Jones, S., Sotiropoulos, F., Healy, T. and Yoganathan, A. (2003) “Numerical simulation of flow in mechanical heart valves: Grid resolution and the assumption of flow symmetry”, *Journal of Biomechanical Engineering* **125**(6), 709–718.

[159] David, T. and Hsu, C. (1996) “The integrated design of mechanical bi-leaflet prosthetic heart valves.”, *Med. Eng. Phys.* **18**(6), 452–462.

[160] King, M., David, T. and Fisher, J. (1997) “Three-dimensional study of the effect of two leaflet opening angles on the time-dependent flow through a bileaflet mechanical heart valve.”, *Med. Eng. Phys.* **19**(3), 235–241.

[161] Black, M., Howard, I., Huang, X. and Patterson, E. (1991) “A 3-dimensional analysis of a bioprosthetic heart-valve”, *Journal of Biomechanics* **24**(9), 793–801.

[162] De Hart, J., Cacciola, G., Schreurs, P. and Peters, G. (1998) “A three-dimensional analysis of a fibre-reinforced aortic valve prosthesis”, *Journal of Biomechanics* **31**(7), 629–638.

[163] Grande-Allen, K., Cochran, R., Reinhall, P. and Kunzelman, K. (1999) “Mechanisms of aortic valve incompetence in aging: A finite element model”, *Journal of Heart Valve Disease* **8**(2), 149–156.

[164] Grande-Allen, K., Cochran, R., Reinhall, P. and Kunzelman, K. (2001) “Mechanisms of aortic valve incompetence: Finite-element modeling of marfan syndrome”, *Journal of Thoracic and Cardiovascular Surgery* **122**(5), 946–954.

[165] Gnyaneshwar, R., Kumar, R. and Balakrishnan, K. (2002) “Dynamic analysis of the aortic valve using a finite element model”, *Annals of Thoracic Surgery* **73**(4), 1122–1129.

[166] Makhijani, V. B., Yang, H. Q., Dionne, P. J. and Thubrikar, M. J. (1997) "Three-dimensional coupled fluid-structure simulation of pericardial bioprosthetic aortic valve function", *ASAIO Journal* **43**(5), M387–M392.

[167] Horsten, J. (1990) *On the analysis of moving heart valves: a numerical Fluid-Structure Interaction model*, Phd thesis, Technische Universiteit Eindhoven.

[168] Chambers, J. and Ely, J. (2000) "A comparison of the classical and modified forms of the continuity equation in the On-X prosthetic heart valve in the aortic position", *J Heart Valve Dis* **9**(2), 299–301; discussion 301–2.

[169] Chambers, J. and Ely, J. L. (1998) "Early postoperative echocardiographic hemodynamic performance of the On-X prosthetic heart valve: a multicenter study", *J Heart Valve Dis* **7**(5), 569–73.

[170] Van Nooten, G., Ozaki, S., Herijgers, P., Segers, P., Verdonck, P. and Flameng, W. (1999) "Distortion of the stentless porcine valve induces accelerated leaflet fibrosis and calcification in juvenile sheep", *J. Heart Valve Dis.* **8**(1), 34–41.

[171] Laczkovics, A., Heidt, M., Oelert, H., Laufer, G., Greve, H., Pomar, J. L., Mohr, F. W., Haverich, A., Birnbaum, D., Regensburger, D., Palatianos, G. and Wolner, E. (2001) "Early clinical experience with the On-X prosthetic heart valve", *J Heart Valve Dis* **10**(1), 94–9.

[172] Walther, T., Falk, V., Tigges, R., Kruger, M., Langebartels, G., Diegeler, A., Autschbach, R. and Mohr, F. W. (2000) "Comparison of On-X and SJM HP bileaflet aortic valves", *J Heart Valve Dis* **9**(3), 403–7.

[173] Fehske, W., Kessel, D., Kirchhoff, P. G., Omran, H., Manz, M. and Luderitz, B. (1994) "Echocardiographic profile of the normally functioning omnicarbon valve.", *Journal of Heart Valve Disease* **3**(3), 263–274.

[174] Iguro, Y., Moriyama, Y., Yamaoka, A., Yamashita, M., Shimokawa, S., Toyohira, H. and Taira, A. (1999) "Clinical experience of 473 patients with the omnicarbon prosthetic heart valve", *J. Heart Valve Dis.* **8**(6), 674–679.

[175] Peter, M., Weiss, P., Jenzer, H. R., Hoffmann, A., Dubach, P., Roth, J., Bertschmann, W., Stulz, P., Gradel, E. and Burckhardt, D. (1993) "The omnicarbon tilting-disc heart-valve prosthesis - a clinical and doppler-echocardiographic follow-up", *J. Thorac. Cardiovasc. Surg.* **106**(4), 599–608.

[176] Messnerpellenc, P., Wittenberg, O., Leclercq, F., Albat, B., Ximenes, C., Grolleau, R. and Thevenet, A. (1993) "Doppler-echocardiographic evaluation of the omnicarbon cardiac- valve prostheses", *J. Cardiovasc. Surg.* **34**(3), 195–202.

[177] Dewall, R. A., Raggio, J. M. C., Dittrich, H., Guilmet, D., Morea, M. and Thevenet, A. (1989) "The omni design - evolution of a valve", *J. Thorac. Cardiovasc. Surg.* **98**(5), 999–1007.

[178] Kleine, P., Hasenkam, M. J., Nygaard, H., Perthel, M., Wesemeyer, D. and Laas, J. (2000) "Tilting disc versus bileaflet aortic valve substitutes: Intraoperative and postoperative hemodynamic performance in humans", *J. Heart Valve Dis.* **9**(2), 308–311.

[179] Plehn, J. F., Arbuckle, B. E., Southworth, J., Nugent, W., Plume, S. and Marrin, C. A. S. (1996) "A hemodynamic comparison of omniscience and medtronic hall aortic prostheses", *J. Heart Valve Dis.* **5**(3), 328–336.

[180] Carrier, M., Martineau, J. P., Bonan, R. and Pelletier, L. C. (1987) "Clinical and hemodynamic assessment of the omniscience prosthetic heart-valve", *J. Thorac. Cardiovasc. Surg.* **93**(2), 300–307.

[181] Stewart, S. F. C., Nast, E. P., Arabia, F. A., Talbot, T. L., Proschan, M. and Clark, R. E. (1991) "Errors in pressure-gradient measurement by continuous wave doppler ultrasound - type, size and age effects in bioprosthetic aortic valves", *J. Am. Coll. Cardiol.* **18**(3), 769–779.

[182] Laas, J., Kleine, P., Hasenkam, M. J. and Nygaard, H. (1999) "Orientation of tilting disc and bileaflet aortic valve substitutes for optimal hemodynamics", *Ann. Thorac. Surg.* **68**(3), 1096–1099.

[183] Wurzel, D., Panidis, I. and Gonzales, R. . (1991) "In vitro continuous wave doppler gradients of mechanical valves in less than optimal orientations.", *ASAIO Trans* **37**(3), 448–51.

[184] Christakis, G. T., Buth, K. J., Goldman, B. S., Fremes, S. E., Rao, V., Cohen, G., Borger, M. A. and Weisel, R. D. (1998) "Inaccurate and misleading valve sizing: A proposed standard for valve size nomenclature", *Ann. Thorac. Surg.* **66**(4), 1198–1203.

[185] Steinhoff, G., Stock, U., Karim, N., Mertsching, H., Timke, A., Meliss, R. R., Pethig, K., Haverich, A. and Bader, A. (2000) "Tissue engineering of pulmonary heart valves on allogenic acellular matrix conduits - in vivo restoration of valve tissue", *Circulation* **102**(19), 50–55.

[186] Ye, Q., Zund, G., Benedikt, P., Jockenhoevel, S., Hoerstrup, S. P., Sakyama, S., Hubbell, J. A. and Turina, M. (2000) "Fibrin gel as a three dimensional matrix in cardiovascular tissue engineering", *Eur. J. Cardio-Thorac. Surg.* **17**(5), 587–591.

[187] L'Heureux, N., Germain, L. and Auger, L. A. (1999) "Tissue engineering", *Science* **284**(5420), 1621–1622.

[188] L'Heureux, N., Paquet, S., Labbe, R., Germain, L. and Auger, F. A. (1998) "A completely biological tissue-engineered human blood vessel", *Faseb J.* **12**(1), 47–56.

[189] Rademacher, A., Paulitschke, M., Meyer, R. and Hetzer, R. (2001) "Endothelialization of PTFE vascular grafts under flow induces significant cell changes", *Int. J. Artif. Organs* **24**(4), 235–242.

[190] Zeltinger, J., Landeen, L. K., Alexander, H. G., Kidd, I. D. and Sibanda, B. (2001) "Development and characterization of tissue-engineered aortic valves", *Tissue Eng.* **7**(1), 9–22.

[191] Zulliger, M., Montorzi-Thorell, G., Friedez, P., Kretzers, L., Larik, V., Meister, J. J. and Stergiopulos, N. (2000) "Arterial wall remodeling using an ex vivo artery support system", *Arch. Physiol. Biochem.* **108**(1-2), 31–31.

[192] Bardy, N., Karillon, G. J., Merval, R., Samuel, J. L. and Tedgui, A. (1995) "Differential-effects of pressure and flow on DNA and protein-synthesis and on fibronectin expression by arteries in a novel organ-culture system", *Circ. Res.* **77**(4), 684–694.

[193] Stock, U. A. and Vacanti, J. P. (2001) "Cardiovascular physiology during fetal development and implications for tissue engineering", *Tissue Eng.* **7**(1), 1–7.

[194] Lemmon, J. and Yoganathan, A. (2000) "Three-dimensional computational model of left heart diastolic function with fluid-structure interaction", *Journal of Biomechanical Engineering* **122**, 109–117.

[195] Wood, W. (1990) *Practical time-stepping schemes*, Oxford University Press, iSBN 0-19-859677-4.

[196] van de Vosse, F. (2003) "Mathematical modelling of the cardiovascular system", *Journal of Engineering Mathematics* **47**(3-4), 175–183.

[197] van de Vosse, F., de Hart, J., van Oijen, C., Bessems, D., Gunther, T., Segal, A., Wolters, B., Stijnen, J. and Baaijens, F. (2003) "Finite-element-based computational methods for cardiovascular fluid-structure interaction", *Journal of Engineering Mathematics* **47**(3-4), 335–368.

[198] Yellin, E. L., Peskin, C. S., Yoran, C., Koenigsberg, M., Matsumoto, M., Laniado, S., McQueen, D. M., Shore, D. and Frater, R. W. M. (1981) "Mechanisms of mitral-valve motion during diastole", *Amarican journal of physiology* **241**(3), H389–H400.

[199] Hughes, T. J. R., Liu, W. K. and Zimmerman, T. K. (1991) "Lagragian-eulerian finite element formulation in incompressible viscous flows", *Computer Methods in Applied Mechanics and Engineering* **29**, 329–349.

[200] Perktold, K., Hofer, M., Rappitsch, G., Loew, M., Kuban, B. D. and Friedman, M. H. (1998) "Validated computation of physiologic flow in a realistic coronary artery branch", *Journal of Biomechanics* **31**(3), 217–228.

[201] Adel, M., Seth, L. and Seigo, I. (1999) "Hemodynamic shear stress and its role in atherosclerosis", *JAMA* **282**(21), 2035–2042.

[202] Van Steenhoven, A. and van Dongen, M. (1979) "Model studies of the closing behaviour of the aortic valve", *Journal of Fluid Mechanics* **90**(1), 21–32.

[203] Aoyagi, S., Kawara, T., Fukunaga, S., Mizoguchi, T., Nishi, Y., Kawano, H. and Arinaga, K. (1997) "Cineradiographic evaluation of ATS open pivot bileaflet valves", *Journal of Heart Valve Disease* **6**(3), 258–263.

[204] Feng, Z., Umezu, M., Fujimoto, T., Tsukahara, T., Nurishi, M. and Kawaguchi, D. (2000) "In vitro hydrodynamic characteristics among three bileaflet valves in the mitral position", *Artificial Organs* **24**(5), 346–354.

[205] Matthies, H. and Steindorf, J. (2003) "Partitioned strong coupling algorithms for fluid-structure interaction", *Comput. Struct.* **81**, 805–812.

[206] Fernández, M. and Moubachir, M. (2004) "A newton method using exact jacobians for solving fluid-structure coupling", *Comput. Struct.* **To appear**.

[207] Grigioni, M., Daniele, C., Morbiducci, U. and D'Avenio, G. (2004) "The power-law mathematical model for blood damage prediction: Analytical developments and physical inconsistencies", *International Journal of Artificial Organs* **28**(5), 467–475.

[208] Karpuz, H., Jeanrenaud, X., Hurni, M., Aebischer, N., Koerfer, J., Fischer, A., Ruchat, P., Stumpe, F., Sadeghi, H. and Kappenberger, L. (1996) "Doppler echocardiographic assessment of the new ATS medical prosthetic valve in the aortic position", *American Jounral of Cardiovascular Imaging* **10**(4), 254–260.

[209] Emery, R., Nooten, G. V. and Tesar, P. (2003) "The initial experience with the ATS medical mechanical cardiac valve prosthesis", *Annals of Thoracic Surgery* **75**(2), 444,452.

[210] Laske, A., Jenni, R., Maloigne, M., Vassalli, G., Bertel, O. and Turina, M. (1996) "Pressure gradients across bileaflet aortic valves by direct measurement and echocardiography", *Annals of Thoracic Surgery* **61**(1), 48–57.

[211] FLUENT Inc, http://www.fluent.com/ last accessed 15 august 2004.

[212] David, T. (2000) *McDonald's Blood Flow in Arteries.*, chapter Advances in Fluid Dynamics: Intra and Extracorporeal Cardiovascular Fluid Dynamics., 177–208, Verdonck P, Perktold K, eds., 1 ed: WIT Press.

[213] Dumont, K., Vierendeels, J., Segers, P., van de Nooten, G. and Verdonck, P. (2004) “Modeling heart valve dynamics during the complete cardiac cycle: ATS open pivot™ heart valve”, *submitted for publication in the Journal of Biomechanical Engineering (ASME)* .